Seismic Hazard Assessment for the UK offshore Exclusive Economic Zone

Multi-Hazards and Resilience Programme

Open Report OR/24/012

BRITISH GEOLOGICAL SURVEY

MULTI-HAZARDS AND RESILIENCE PROGRAMME

OPEN REPORT OR/24/012

Seismic Hazard Assessment for the UK offshore Exclusive Economic Zone

I Mosca, B Baptie, R Haslam, J Gafeira, G Jenkins

Keywords

Seismic hazard, earthquake catalogue, seismic source model, ground motion, United Kingdom, North Sea.

Bibliographical reference

MOSCA, I, BAPTIE, B, HASLAM, R, GAFEIRA, J, JENKINS, G. 2024. Seismic Hazard Assessment for the UK Offshore Exclusive Economic Zone. *British Geological Survey Open Report*, OR/24/012. 168pp.

Keyworth, Nottingham British Geological Survey 2024

BRITISH GEOLOGICAL SURVEY

The full range of our publications is available from BGS shops at Nottingham, Edinburgh, London and Cardiff (Welsh publications only) see contact details below or shop online at www.geologyshop.com

The London Information Office also maintains a reference collection of BGS publications, including maps, for consultation.

We publish an annual catalogue of our maps and other publications; this catalogue is available online or from any of the BGS shops.

The British Geological Survey carries out the geological survey of Great Britain and Northern Ireland (the latter as an agency service for the government of Northern Ireland), and of the surrounding continental shelf, as well as basic research projects. It also undertakes programmes of technical aid in geology in developing countries.

The British Geological Survey is a component body of UK Research and Innovation.

British Geological Survey offices

Nicker Hill, Keyworth,
Nottingham NG12 5GG
Tel 0115 936 3100

BGS Central Enquiries Desk
Tel 0115 936 3143
email enquiries@bgs.ac.uk

BGS Sales
Tel 0115 936 3241
email sales@bgs.ac.uk

The Lyell Centre, Research Avenue South,
Edinburgh EH14 4AP
Tel 0131 667 1000
email scotsales@bgs.ac.uk

Natural History Museum, Cromwell Road,
London SW7 5BD
Tel 020 7589 4090
Tel 020 7942 5344/45
email bgslondon@bgs.ac.uk

Cardiff University, Main Building, Park Place,
Cardiff CF10 3AT
Tel 029 2167 4280

Maclean Building, Crowmarsh Gifford,
Wallingford OX10 8BB
Tel 01491 838800

Geological Survey of Northern Ireland, 7th Floor,
Adelaide House, 39-49 Adelaide Street, Belfast, BT2 8FD
Tel 0289 038 8462
www2.bgs.ac.uk/gsni/

Natural Environment Research Council, Polaris House,
North Star Avenue, Swindon SN2 1EU
Tel 01793 411500 Fax 01793 411501
www.nerc.ac.uk

UK Research and Innovation, Polaris House,
Swindon SN2 1FL
Tel 01793 444000
www.ukri.org

Website www.bgs.ac.uk
Shop online at www.geologyshop.com

Foreword

This report is the published product of a study by the British Geological Survey (BGS) to develop new seismic hazard maps for the UK offshore Exclusive Economic Zone using a Monte Carlo-based approach. These are intended to update the current maps for UK waters published in 2002. The work done by BGS has been informed at key stages by external experts who have reviewed the main components of the seismic hazard model. The hazard outputs for this work consist of seismic hazard maps for peak ground acceleration (PGA), spectral acceleration at 0.2 s and 1.0 s with 5% damping for the return periods of 95, 475, 1100, 2475, and 5000 years. Site-specific estimates (hazard curves, uniform hazard spectra, and disaggregation analysis) have been computed for three carbon capture storage areas, i.e. Acorn in the Moray Firth Basin, Endurance in the Sole Pit Basin, and the HyNet North West storage area in the southeast Irish Sea. The project was funded by the Industrial Decarbonisation Research and Innovation Centre (IDRIC) under Grant Ref: EP/V027050/1.

Acknowledgements

We thank Storegga for the support of this project and particularly Elle Lashko for fruitful discussions throughout the project.

We are very grateful for the support and input of Associate Director Ziggy Lubkowski (Arup), Dr Chen Huang (NORSAR), and Dr Volker Oye (NORSAR), who reviewed the individual components of the seismic hazard model and the draft report. Their insightful comments helped improve the seismic hazard model and the report.

From BGS, we thank Davie Galloway for his assistance in checking some events of the earthquake catalogue, and Svea Rauterberg for converting Shapefiles into text files and digitising the fault map in Europe. We are grateful to Maarten Krabbendam for internally reviewing the section on tectonics and Richard Luckett and Susanne Sargeant for internally reviewing the report. Finally, we thank the BGS Graphics Team and in particular Calum Ritchie for making the high-resolution seismic hazard maps for the UK offshore Exclusive Economic Zone.

This work is supported by the British Geological Survey and the Industrial Decarbonisation Research and Innovation Centre (IDRIC) under Grant Ref: EP/V027050/1.

Contents

FIGURES

TABLES

List of abbreviations

AKK14	Akkar et al. (2014a)
ASCR	Active shallow crustal region
ASK14	Abrahamson et al. (2014)
BIIS	British Irish Ice Sheet
BIN14	Bindi et al. (2014)
BGS	British Geological Survey
BSSA14	Boore et al. (2014)
CAU15	Cauzzi et al. (2015)
CB14	Campbell and Bozorgnia (2014)
CCS	Carbon Capture and Storage
CENA	Central and Eastern North America
CY14	Chiou and Youngs (2014)
EDR	Euclidean distance-based ranking
EEZ	Exclusive Economic Zone
EQE02	EQE (2002)
ESHM13	2013 European Seismic Hazard Model
ESHM20	2020 European Seismic Hazard Model
ESM	Engineering Strong Motion
EPRI	Electric Power Research Institute
FAS	Fourier amplitude spectrum
FCAT-17	French catalogue of Manchuel et al. (2018)
FMD	Frequency-magnitude distribution
GIA	Glacio-Isostatic Adjustment
GM	Geometric mean
GMC	Ground motion characterisation
GMM	Ground motion model
GMPE	Ground Motion Prediction Equation
HEM	Hybrid-empirical method
HTTA	Host-to-Target Adjustment
IDRIC	Industrial Decarbonisation Research and Innovation Centre
INSN	Irish National Seismic Network
IPE	Intensity Prediction Equation
ISC	International Seismological Centre
KNMI	Royal Netherlands Meteorological Institute
KOT20	Kotha et al. (2020)
LDBFZ	Lake District Boundary Fault Zone
LDG	Laboratoire de Détection et de Géophysique/CEA

LGM	Last Glacial Maximum
LLH	Log-likelihood
MDE	Modified Euclidean Distance
NEHRP	National Earthquake Hazards Reduction Program
NGA	Next Generation of Ground-Motion Attenuation Models
NNSN	Norwegian National Seismic Network
NSRS	North Sea Rift System
PEZ18	Pezeshk et al. (2018)
PGA	Peak ground acceleration
PLF	Pontesford-Linley Fault
PSA	pseudo-spectral acceleration
PSHA	Probabilistic seismic hazard assessment
QNFZ	Quesssoy/Nort-sur-Erdre Fault Zone
RE19	Rietbrock and Edwards (2019)
RS	Response spectra
SA	Spectral acceleration
$SA_{0.2\ s}$	Spectral acceleration at 0.2 s
$SA_{1.0\ s}$	Spectral acceleration at 1.0 s
SCR	Stable continental region
SHARE	Seismic Hazard Harmonisation in Europe
SSC	Seismic source characterisation
SZM	Source zone model
UCC	Royal Observatory of Belgium
UK	United Kingdom
USGS	US Geological Survey
YEN15	Yenier and Atkinson (2015)
WC20	Weatherill and Cotton (2020)
WCF	Watchet-Cothelstone Fault

List of symbols

A	Area of a zone
a	Activity rate
b	b-value
$C_{RS,Vs-\kappa 0}$	$Vs-\kappa_0$ adjustment factor
$\bar{D}$	Observed average distance
Δ	Normalised residual
δB	Between-event residual
$\delta S2S$	Site-to-site residual

δW	Intra-event residual
δWS	Site- and event-corrected intra-event residual
ε	Number of standard deviations above or below the median ground motion prediction
f_1	Lower limit of the frequency range for the HTTA
f_2	Upper limit of the frequency range for the HTTA
φ	Within-event (or intra-event) standard deviation
φ_{s2s}	Site-to-site variability
φ_{ss}	Single-station within-event (or intra-event) standard deviation
κ_0	Near-surface site-specific attenuation parameter
Mc	Completeness magnitude
ML	Local magnitude
Mmax	Maximum magnitude
Ms	Surface wave magnitude
Mw	Moment magnitude
mb	Body wave magnitude
Rjb	Joyner-Boore distance
Rrup	Rupture distance
RotD050	Non-redundant rotation angles
σ	Total standard deviation
$\sigma_{ergodic}$	See σ
σ_{ss}	Single-station total standard deviation
τ	Between-event (or inter-event) standard deviation
Vs	Shear wave velocity
Vs30	Time-averaged shear wave velocity for the top 30 m

Summary

This report presents the new seismic hazard maps for the UK offshore Exclusive Economic Zone (EEZ) developed using a Monte Carlo-based approach. These are intended to update the current maps for UK waters published in 2002. The work done by the BGS team in this project has been informed at key stages by external experts who have reviewed the main components of the seismic hazard model.

The analysis is based on a comprehensive catalogue of earthquake activity across the region developed by combining existing earthquake catalogues and data from regional and local monitoring agencies. Anthropogenic events such as those related to blasting, underwater explosions, mining and hydrocarbon exploration have been removed where possible. We also remove foreshocks and aftershocks to ensure that the catalogue only contains time-independent events. We then use published empirical magnitude conversion relationships to convert different magnitudes to moment magnitude (Mw) to ensure that the catalogue has consistent and homogeneous magnitudes across the region of interest. Finally, we assess catalogue completeness for different time intervals using both published information for the earthquake catalogues from the region and by examining cumulative and annual numbers of earthquakes for specific magnitudes.

We model earthquake occurrence across the region using a seismic source characterisation (SSC) model that consists of a series of zones, where seismicity is considered to be homogeneous. The shape and extent of each zone are based on knowledge of the tectonics, geology and seismicity of the study area. We use four different seismic source zone models within the SSC to capture the epistemic uncertainty in different rupture scenarios but we do not include specific fault sources in the SSC model because of the difficulty relating earthquakes to particular faults. We estimate the rate of earthquake occurrence for each seismic source zone using the earthquake catalogue derived for the study. A logic tree approach was used to account for the epistemic uncertainty in earthquake activity rates, maximum magnitude, earthquake depth distribution, and faulting style.

Ground motions are estimated for different rupture scenarios using a ground motion characterisation (GMC) model that consists of five recently published multiple ground motion prediction equations (GMPEs) considered to be applicable to the region. The GMPEs are included in a logic tree where the weights are informed by the fit between observed and modelled ground motions. The GMC model also includes the host-to-target adjustments (HTTAs) and a single-station sigma model.

We calculate the hazard using Monte Carlo-based simulations to generate artificial catalogues by random sampling of the probability distributions in the SSC model. This follows the same methodology used for the latest national seismic hazard maps for the UK. Hazard is calculated at individual points spaced at 0.125° in latitude and 0.25° in longitude for peak ground acceleration (PGA) and spectral acceleration at 0.2 s ($SA_{0.2\ s}$) and 1.0 s ($SA_{1.0\ s}$) for 5% damping and Vs30 = 800 m/s (rock conditions) as a proportion of g and for the return periods of 95, 475, 1100, 2475, and 5000 years. This is the first time that maps of the seismic hazard at short (0.2 s) and long periods (1.0 s), which are particularly relevant for offshore structures, have been produced for UK waters. Uniform hazard spectra are calculated for two offshore carbon capture and storage sites in the North Sea (Endurance storage site, the Acorn area) and the HyNet North West in the southeast Irish Sea and a disaggregation of the hazard for these sites has also been undertaken to identify the earthquakes that control the hazard for key return periods.

For a return period of 475 years, the PGA hazard is lower than 0.04 g for much of the UK offshore EEZ, except for the Irish Sea close to North Wales, the northern North Sea and the southern North Sea. The hazard is up to 0.05 g in the region offshore North Wales, 0.07 g in the northern North Sea, and 0.05 g in the southern North Sea. A similar spatial pattern in the hazard is observed at 0.2 s with the highest hazard in the northern North Sea (0.16 g) with more pronounced variations. At 1.0 s, the hazard is less than 0.02 g and there is little variation across the UK offshore EEZ.

For 2475 years, the northern North Sea, the offshore area close to western Scotland, the Irish Sea close to Wales, and the southern North Sea are the areas of highest hazard for PGA and $SA_{0.2\ s}$. The highest hazard values (0.19 g for PGA and 0.39 g for $SA_{0.2\ s}$) are observed in the northern North Sea.

The Acorn site has the lowest hazard of the three carbon capture and storage license areas with a PGA hazard value of 0.04 g for a 2475-year return period. The PGA hazard values at Endurance and the HyNet are 0.11 g and 0.07 g for the same return periods. For $SA_{0.2\ s}$ the hazard values for the 2475-year return period increase to 0.10 g at Acorn, 0.23 g at Endurance, and 0.16 g at HyNet. The uniform hazard spectra for return periods of 475 years and 2475 years show the hazard values for different periods of ground motion with an equal probability of exceedance and demonstrate that the hazard values peak between periods of 0.1 to 0.4 s.

The comparison between the maps for the 475-year return period from this study and the previous maps shows a good agreement although the input data and the SSC and GMC models used for the calculations between the two studies are different.

It is important to note that these seismic hazard maps are not a substitute for site-specific hazard assessment and high-consequence-of-failure installations (designated CC4-Highest in the new edition of EN1990, 2002) in particular. The user must take responsibility for checking that use of the results contained in this report is appropriate for the case in question.

The products of this project will be accessible to the public through a dedicated webpage (http://www.earthquakes.bgs.ac.uk/hazard/UKhazard.html) and an interactive mapping tool (https://www.bgs.ac.uk/map-viewers/geoindex-offshore/). The computer code can be made available on request to ukeqs@bgs.ac.uk.

1 Introduction

In the context of the United Kingdom's (UK's) decarbonisation and net zero carbon policy, the UK continental shelf and in particular the North Sea and the Irish Sea has a strategic role in achieving this target with an increasing number of licensed carbon capture and storage (CCS) sites (Figure 1). The presence of historical seismicity, including the largest recorded earthquake in the UK (Versey, 1939; Neilson et al., 1984), near offshore CCS areas suggests that robust estimates of earthquake hazard are essential for the planning and design of offshore critical infrastructure. Although updated seismic hazard maps for the UK were recently published to inform the National Annex to Eurocode 8 (earthquake-resistant design of structures; Mosca et al., 2020, 2022), these maps do not extend offshore and the most recent hazard maps for the offshore regions around the UK were published in 2002 (EQE, 2002). Since then, there have been significant advances in seismic hazard assessment, in particular how to model the ground shaking produced by potential, future earthquakes and capture its uncertainties.

Principia Mechanica Ltd. (1986) carried out one of the earliest studies to assess the seismic hazard in the North Sea for the UK Department of Energy largely motivated by the development of the offshore oil and gas industry. Around the same time, Bungum et al. (1986) assessed seismic hazard in the Norwegian sector of the North Sea. Scientific collaboration between Norway and the UK led to two separate seismic hazard studies for the Norwegian and UK sectors of the North Sea by NORSAR and NGI (1998) and EQE (2002), respectively. Furthermore, Bungum et al. (2000) presented seismic hazard maps for Norway, the North Sea, and the United Kingdom that combined the results of these two studies.

The EQE (2002) seismic hazard model (referred hereto as EQE02) includes UK waters between 49°N to 62°N and 11°W to 3°E but does not include the entire UK offshore Exclusive Economic Zone (EEZ). The model used two equally weighted seismic source models and two ground motion prediction equations (GMPEs; Ambraseys et al., 1996; Toro et al., 1997). The resulting contour maps express the seismic hazard in terms of peak ground acceleration (PGA) on bedrock for return periods of 100, 200, 495, 1000, and 10,000 years. The results suggest that for a 10,000-year return period, PGA can be up to 0.30 g in the northern North Sea, around 0.25 g in the southern North Sea, and around 0.20 g offshore Wales and northwest England.

Following an earthquake in the EkoFisk field in 2001 (Ottemoller et al., 2005), the Offshore Safety Division of the UK Health and Safety Executive commissioned the Mallard Partnership to review existing offshore seismic hazard studies. Mallard et al. (2003) highlight several possible issues with the previous studies including the difficulty in interpolating hazard values, the treatment of uncertainty and the lack of low-frequency ground motion hazard estimates, which are particularly relevant for offshore installations. Mallard et al. (2003) also developed a new hazard map for PGA and a 10,000-year return period, which gives PGA values of 0.3 g in the northern North Sea and around 0.275 g in the southern North Sea and Dogger Bank.

A recent study by Carlton et al. (2022) estimated the seismic hazard for the Sofia Offshore Wind Farm, which is located about 200 km northeast of England in the southern North Sea. The seismic source model consisted of two areal seismic source models and four different smoothed seismicity models, and eight different GMPEs (i.e., Akkar and Cağnan, 2010; Atkinson and Boore, 2011; Akkar et al., 2014a; Bindi et al., 2014; Boore et al., 2014; Chiou and Youngs, 2014; Cauzzi et al., 2015; Rietbrock and Edwards, 2019) selected based on comparisons with regional data. The results show that the variation in seismic hazard across the site is negligible and the PGA values appear to be lower than previous regional studies, with values of 0.025 g, 0.050 g, and 0.089 g for the return periods of 475 years, 2475 years, and 10,000 years, respectively, at the site.

NORSAR carried out a PSHA study for Norway to assess the seismic hazard in the country developing hazard maps for Vs30 =1200 m/s and for PGA and spectral acceleration at 0.1 s and 1.0 s for 5% damping and 475 year return period. The maps cover mainland Norway and the Svalbard archipelago but Norwegian waters were excluded (NORSAR, 2020; Lindholm et al., 2024). Both works are still not publicly available yet.

Building regulations for offshore structures are given in ISO 19901-2 (2022) and DNV (2021) where the seismic design criteria are based on the damage limit state-based approach. The return periods of the damage limit states depend on the hazard curves and the exposure level of the structure. DNV (2021) states the associated return periods for key damage limit states may be inferred in Eurocode 8 and its upcoming revision. For example, the Serviceability and Ultimate Limit State may be associated with a return period of 95 years and 475 years, respectively (Klose et al., 2021; Carlton et al., 2022). ISO 19901-2 (2022) does not consider the seismic design for long return periods, such as 10,000 years. Based on the review of ISO 19901-2 (2022) and DNV (2021), the specifications for the offshore seismic hazard maps follow those in Mosca et al. (2022). We also compute seismic hazard maps for the 5000-year return period, which were not included in the UK national hazard maps (Mosca et al., 2022), because this value can be the upper bound for the exposure level of high-consequence structures (i.e., L1 in ISO 19901-2, 2022).

In this study, we develop a new seismic hazard model and accompanying hazard maps for the current UK offshore EEZ (black polygon in Figure 1) using the latest available data and recent advances in seismic hazard methodology, that robustly capture the uncertainties in the data and our understanding of the earthquake process. The UK offshore EEZ describes the 200-mile EEZ around the UK coastline as defined in the Marine and Coastal Assess Act 2009 (Gibson, 2009). We consider a study area of up to 300 km from the UK offshore EEZ (red polygon in Figure 1) to account for all seismic sources which may influence the hazard in UK waters. Earthquakes beyond 300 km from a site are unlikely to affect the hazard (e.g. IAEA, 2022). Figure 1 shows also the locations of the gas and oil hydrocarbon fields, wind farms, and licensing offshore CCS sites as reported by the North Sea Transition Agency. Coordinates are given in decimal degrees throughout the report.

Section 2 of this report describes the methodology that we use for our probabilistic seismic hazard analysis. Section 3 describes the development of the earthquake catalogue used in the hazard assessment. It also describes how we estimate the magnitude of completeness (i.e., the magnitude above which the earthquake catalogue can be considered to be complete) for different time periods. Section 4 describes the seismo-tectonics of the region including potential sources of crustal deformation, relevant tectonic structures and historical and instrumental seismicity in the study area. Section 5 shows the development of the seismic source characterisation (SSC) model using the information from the previous section. We use four different seismic source zone models to capture the epistemic uncertainty in different rupture scenarios. Each zone is described in terms of the geometry (pairs of latitude and longitude for the zone's boundaries), the earthquake recurrence statistics for the seismicity in the zone, maximum and minimum magnitudes, distribution of the hypocentral depths, and faulting style. Section 6 describes the ground motion characterisation (GMC) model used in this study. We select a suite of five recently published GMPEs, which we consider applicable to the study area. The GMPEs are corrected for the host-to-target adjustments (HTTAs), which account for differences between the host region where the GMPE was derived and the target region where the hazard is being estimated (Douglas and Edwards, 2016). The section also describes the model used to describe the aleatory variability in the predicted ground motions. Section 7 presents the hazard outputs for this work and compares those against the results from previous studies. Finally, we present our conclusions in Section 8.

The individual components of the regional seismic hazard model (development of the earthquake catalogue, the SSC model, and the GMC model) and the first draft of the report have been reviewed by three external experts (Associate Director Ziggy Lubkowski -Arup-, Dr Chen Huang -NORSAR-, and Dr Volker Oye -NORSAR). Specifically, the individual components of the analysis were included in short, informal reports that were extensively reviewed. We included the comments of the three experts in the final model and the present report and did respond to these comments formally.

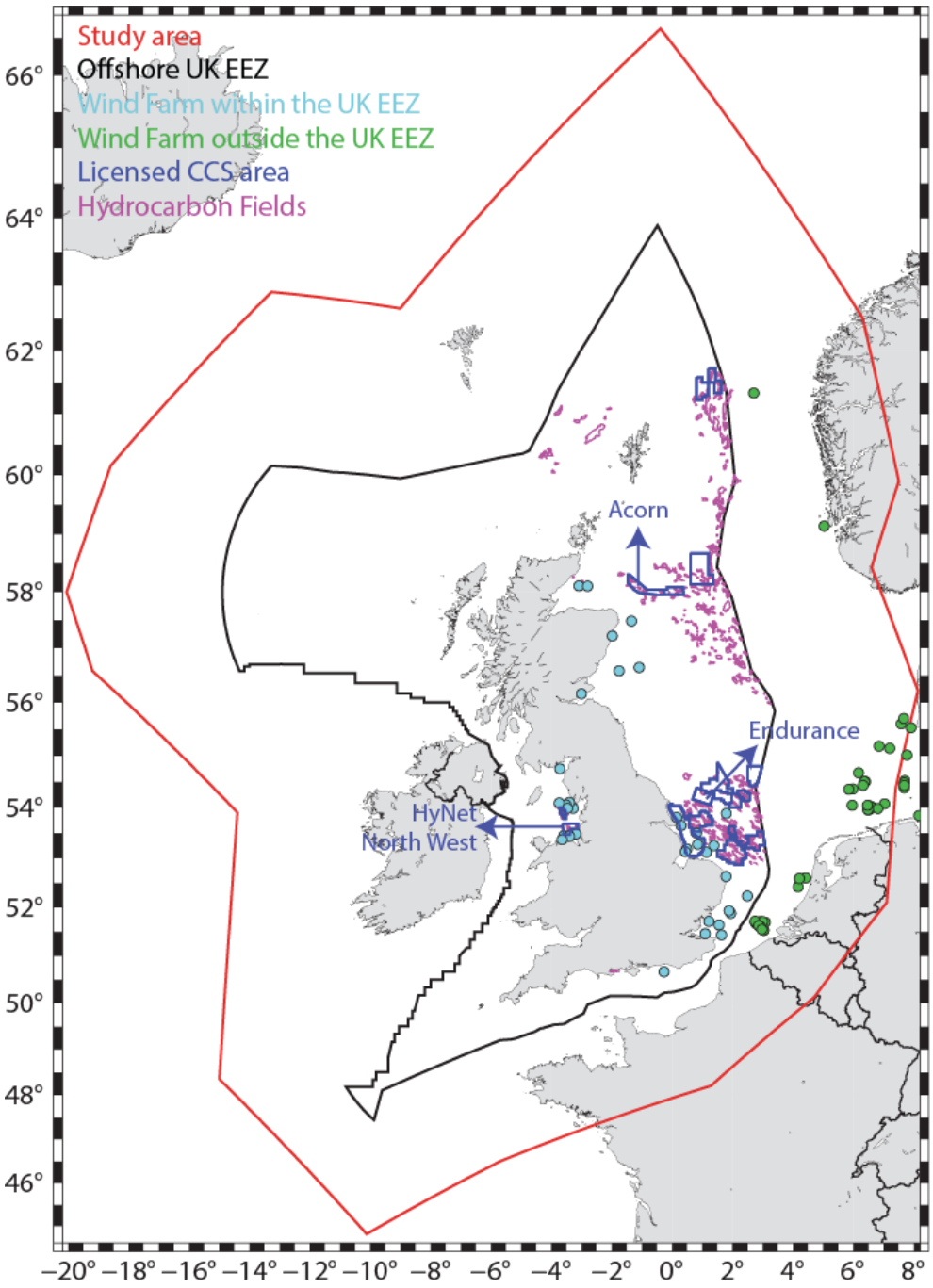

Figure 1: Map of the current UK offshore Exclusive Economic Zone (EEZ; inner polygon), the study area for this project (outer polygon) and the locations of the gas and oil hydrocarbon fields, wind farms, and licensing offshore CCS sites as reported by the North Sea Transition Agency.

2 Methodology

We use a probabilistic seismic hazard analysis (PSHA) framework, which combines seismological, geological and geophysical data to produce a probabilistic description of expected ground shaking that may occur at a site (see Cornell, 1968; Reiter, 1990; McGuire, 2004; Baker et al., 2021). This largely consists of four steps (e.g., Baker et al., 2021).

Step 1: Definition of seismic sources based on knowledge of the tectonics, geology and seismicity of the study area. Such a model may contain both areal sources, where seismicity has an equal probability of occurring anywhere within a given area, and fault sources that account for specific faults, or fault zones, that are considered to be active. A collection of

seismic sources makes up the seismic source zone model. This is often referred to as the SSC model.

Step 2: Quantification of the rate of earthquake occurrence for each seismic source zone using the Gutenberg-Richter frequency-magnitude law (Gutenberg and Richter, 1954) that is commonly expressed as:

$$\log_{10} N = a - b\,M \tag{1}$$

where N is the number of earthquakes above a given magnitude M. The constant *a* describes the seismic productivity in the sample and is known as the activity rate. This is commonly normalised over a period of time, such as per annum. The constant *b* gives the negative slope of the frequency-magnitude curve and expresses the average ratio of exponentially distributed small and large-magnitude earthquakes. This is commonly referred to as the *b*-value. Numerous authors have examined *b*-values using both global (e.g., Frohlich and Davis, 1993) and regional data (e.g., Schlaphorst et al., 2016). In general, the *b*-value lies in a range of 0.5–2.0, with the average value for global seismicity catalogues in the range of 0.79–1.25 (Frohlich and Davis, 1993). Given a *b*-value of 1 in Equation (1), for each unit of magnitude increase, the number of earthquakes reduces tenfold. Cornell and Vanmarcke (1969) define a truncated version of the Gutenberg-Richter law where the range of earthquake magnitudes is limited by a lower and upper bound:

$$N \geq M = 10^{a(Mmin)} \frac{e^{-\beta(M-M_0)} - e^{-\beta(Mmax-M_0)}}{1 - e^{-\beta(Mmax-M_0)}} \tag{2}$$

where β=b*ln(10), M_0 is the minimum magnitude and Mmax is the maximum magnitude.

Step 3: Characterisation of the 'earthquake effect' (Reiter, 1990). This is generally expressed in terms of some instrumental ground motion measure, such as PGA, or seismic intensity. This is often referred to as the GMC model.

Step 4: Estimation of the hazard at the site(s) by analytically integrating over the source models for the location and size of potential future earthquakes (Steps 1 and 2) with expected values of the potential shaking intensity caused by these future earthquakes (Step 3), including the associated variability in each. This is expressed as the probability that a particular ground motion level will be exceeded within a certain period of time. This approach to PSHA is often referred to as Cornell-McGuire PSHA (Cornell, 1968; McGuire, 1974). For the present project, Steps 1 and 2 are described in Section 5, whereas Step 3 is described in Section 6 and the description of the results in Section 7 represents Step 4 of PSHA.

Two types of uncertainties are recognised in PSHA: the aleatory variability that describes the inherent randomness in the seismic process; and the epistemic uncertainty that results from our lack of knowledge about the earthquake process (e.g., Atkinson et al., 2014). Earthquake source parameters and ground motions are associated with both aleatory and epistemic uncertainties. The aleatory variability in PSHA is incorporated by integrating over the distribution of ground-motion amplitudes about the median (e.g., Bommer and Abrahamson, 2006; Atkinson et al., 2014). Epistemic uncertainties can be incorporated through the use of logic trees to capture the centre, body and range of the technically defensible interpretations of the SSC and GMC models (Budnitz et al., 1997; USNRC, 2012). The centre of the distribution is the best estimate of the resulting interpretations, the body describes the shape of the distribution around the best estimate, and the range captures the tails of the distribution (USNRC, 2012). The variability in SSC and GMC models is captured by including alternative models and parameters in the logic tree where weights are assigned to each branch using expert judgement and/or data-driven approaches to reflect the relative confidence in the models and parameters (Coppersmith and Bommer, 2012).

We calculate the hazard using Monte Carlo-based simulations to generate artificial catalogues by random sampling the probability distributions in the SSC model (Musson, 1999, 2000; Assatourians and Atkinson, 2013; Mosca et al., 2020; Baker et al., 2021). This follows the same methodology used for the latest national seismic hazard maps for the UK (Mosca et al., 2020, 2022). Below we describe how Monte Carlo-based PSHA works.

2.1 MONTE CARLO-BASED PSHA

PSHA based on Monte Carlo simulations uses random numbers to sample from the different probability distributions in the SSC model to generate artificial catalogues (e.g., Musson, 1999, 2000; Assatourians and Atkinson, 2013; Baker et al., 2021). Since the SSC model is assumed to completely describe how earthquakes occur in a region, each of the artificial earthquake catalogues represents a version of what could occur in the next N-years, e.g. 50 or 100 years, based on what has previously been observed. This corresponds to Steps 1 and 2 in the Cornell-McGuire PSHA. The ground motion at a specific site is computed for each synthetic catalogue (i.e. Step 3 in the traditional PSHA). This process is iterated R times in order to simulate millions of years of data and therefore resolve the hazard accurately for long return periods. For example, to estimate the hazard for a return period of 10,000 years, the user simulates 100,000 catalogues of 100 years, or 200,000 catalogues of 50 years, giving a total number of 10,000,000 years. To find the ground motion that has an annual probability of being exceeded by 1 in 10,000, the user sorts the values in order of decreasing severity and picks the 1001st value. This has been exceeded 1,000 times out of 10,000,000 and therefore has a 1 in 10,000 probability of being exceeded (Musson, 2000). The process is summarized in Figure 2. Using the same procedure, it is possible to identify ground motions associated with different return periods. The hazard estimate in Monte Carlo-based PSHA differs from Step 4 in Cornell-McGuire PSHA because the hazard results from the analytical integration over the earthquake scenarios in the latter, whereas in the former the hazard is computed from the direct observation of the effects of a very large number of simulations, which randomly sample the earthquake scenarios.

Monte Carlo-based PSHA and Cornell-McGuire-type approaches to PSHA are mathematically equivalent ways of solving the same problem (Baker et al., 2021) and produce the same output given the same initial model (Musson, 2012a; Mosca, 2019). One of the main differences between these two approaches for PSHA is the treatment of epistemic uncertainties. In the Cornell-McGuire approach, the hazard results are performed for every possible combination of branches in the logic tree and the outcome represents a weighted mean (e.g. McGuire, 2004; Musson, 2012a). In a Monte Carlo-based PSHA, not all possible values of the logic tree branches are computed but they are sampled randomly in proportion to their weights and a single hazard calculation is performed (Musson, 2012). For this reason, the Monte Carlo-based PSHA is computationally efficient when a logic tree is complex and contains many branches. There are three clear advantages of the Monte Carlo approach. First, it is very flexible and can be adapted easily by implementing SSC models or new GMPEs when they are published. Second, the process is transparent and therefore it is very easy to halt the simulation process at any point and examine the simulated data. For example, the synthetic catalogues can be inspected to see if the model is reproducing key features of the data. It is also easy to determine which simulated earthquakes are causing high-ground motions. However, while the Monte Carlo approach is an efficient way to assess the hazard in low seismicity areas like the UK, it can be computationally intensive for high seismicity regions.

The Monte Carlo-based approach of Musson (1999, 2000) is encoded in the FORTRAN software M3C, which consists of FORTRAN subroutines for the components of PSHA (e.g. GMPE and generation of synthetic catalogues). The modular structure of the software allows us to incorporate advances in the methodology when they are available. In particular, each ground motion model is implemented as stand-alone functions in their sub-routine. Mosca (2019) checked the implementation of the individual GMPEs in M3C against the ground motion library implemented in the software OpenQuake (Pagani et al., 2014).

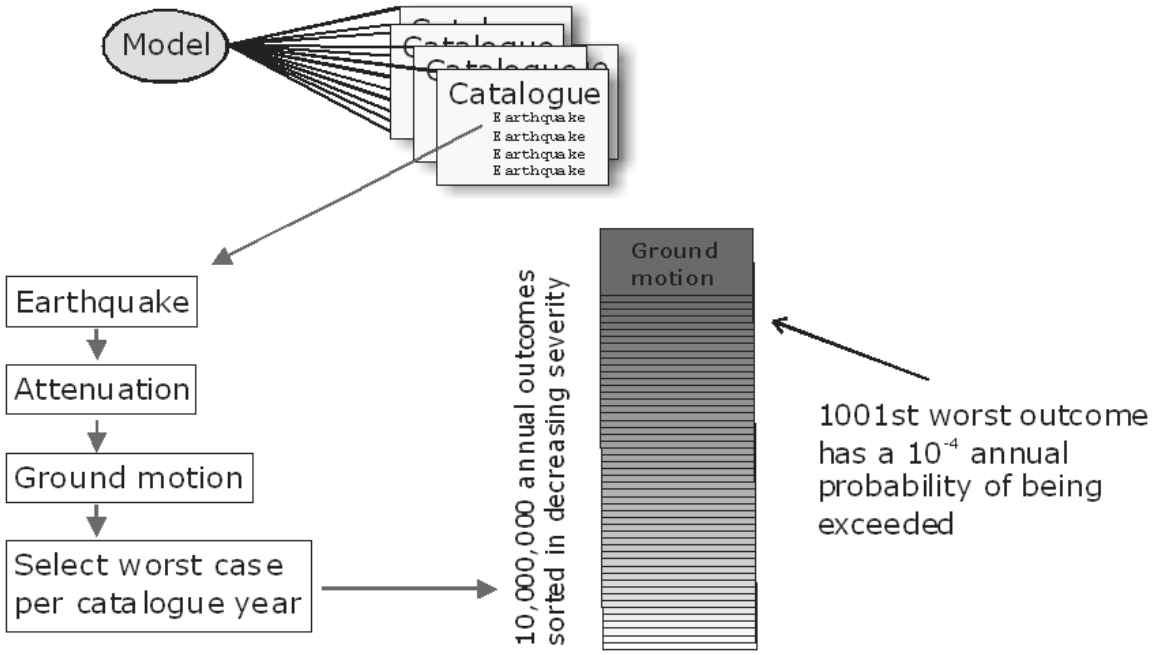

Figure 2: The elements of the Monte Carlo simulation approach to probabilistic seismic hazard assessment (from Musson, 2000). BGS © UKRI 2000

3 Earthquake catalogue

The earthquake catalogue built for this project consists of 4753 tectonic earthquakes with moment magnitude (Mw) ≥ 2.0 from the year 1000 to 31 December 2022 within the study area (Figure 3). It includes data from several sources due to the extent of the study area. To merge the data from different sources and avoid duplicate events, which are presumed to be the same earthquake, we compare events with identical origin times (i.e. year, month, day, hour and minutes) and similar locations (the tolerance in latitude and longitude between two duplicate events is assumed to be ±0.4°) for specific time periods and we assign priority to the data from the local seismic monitoring agencies in each country. Below we describe the sources that are used to build the composite catalogue and how we prioritise the data from these sources. A summary of these sources is also given in Table 1.

For the UK onshore and offshore, including the English Channel, we used the British Geological Survey (BGS) database, which contains historical (before 1970) and instrumental data for the British Isles and surrounding regions.

a. The primary source of data before 1970 is the catalogue of Musson (1994), which is based on historical reports of earthquake effects, and subsequent updates. The location and magnitude of historical events are calculated using the area over which the earthquake was felt as determined from historical accounts and an empirical relationship between felt area and magnitude (Musson, 1996). We did not use the historical earthquake catalogue developed for the 2020 European Seismic Hazard Model (ESHM20; Danciu et al., 2021- see below for more details) for the British Isles for three reasons. First, the BGS catalogue includes small (< 4.0 Mw) events, which are excluded from the ESHM20 catalogue. Second, the magnitude of the earthquakes in the BGS database is in the original scale (i.e. local magnitude -ML), whereas the ESHM20 catalogue does not provide the original magnitude scale. Third, the information on the source parameters of each earthquake in the BGS database is well-documented.
b. The primary source of instrumental data (after 1970) is the annual bulletins of earthquake activity published by the BGS (e.g. Burton and Neilson, 1980; Galloway et

al., 2013). These contain event origin times, locations and local magnitudes determined from instrumental recordings made on the UK seismic monitoring network (e.g. Baptie, 2012). Earthquake size in the BGS database is expressed in terms of ML, which is measured from the maximum amplitude of the recorded ground motion at multiple sites and corrected for distance (Luckett et al., 2019).

Agency/Database	*Code*	*Number of events*	*Time interval*	*Magnitude Range [Mw]*
British Geological Survey	BGS	1606	1122 - 2022	2.0 – 5.9
Catalogue of Manchuel et al. (2018)	FCAT-17	453	1962 - 2009	2.0 – 3.9
Irish National Seismic Network	INSN	24	1980 - 2022	2.0 – 4.1
ESHM20 catalogue	ESHM20	241	1000 - 1966	2.7 – 5.4
Laboratoire de Détection et de Géophysique/CEA	ISC-LDG	737	1975 - 2022	2.0 – 4.4
Royal Netherlands Meteorological Institute	KNMI	42	1932 - 2020	2.0 – 4.2
Other Agencies	ISC-Others	50	1970 - 2019	2.0 – 5.5
Royal Observatory of Belgium	ISC-UCC	153	1986 - 2022	2.0 - 5.5
Norwegian National Seismic Network	NNSN	1447	1900 - 2022	2.0 - 5.3

Table 1: Monitoring agencies used in the earthquake catalogue for this work.

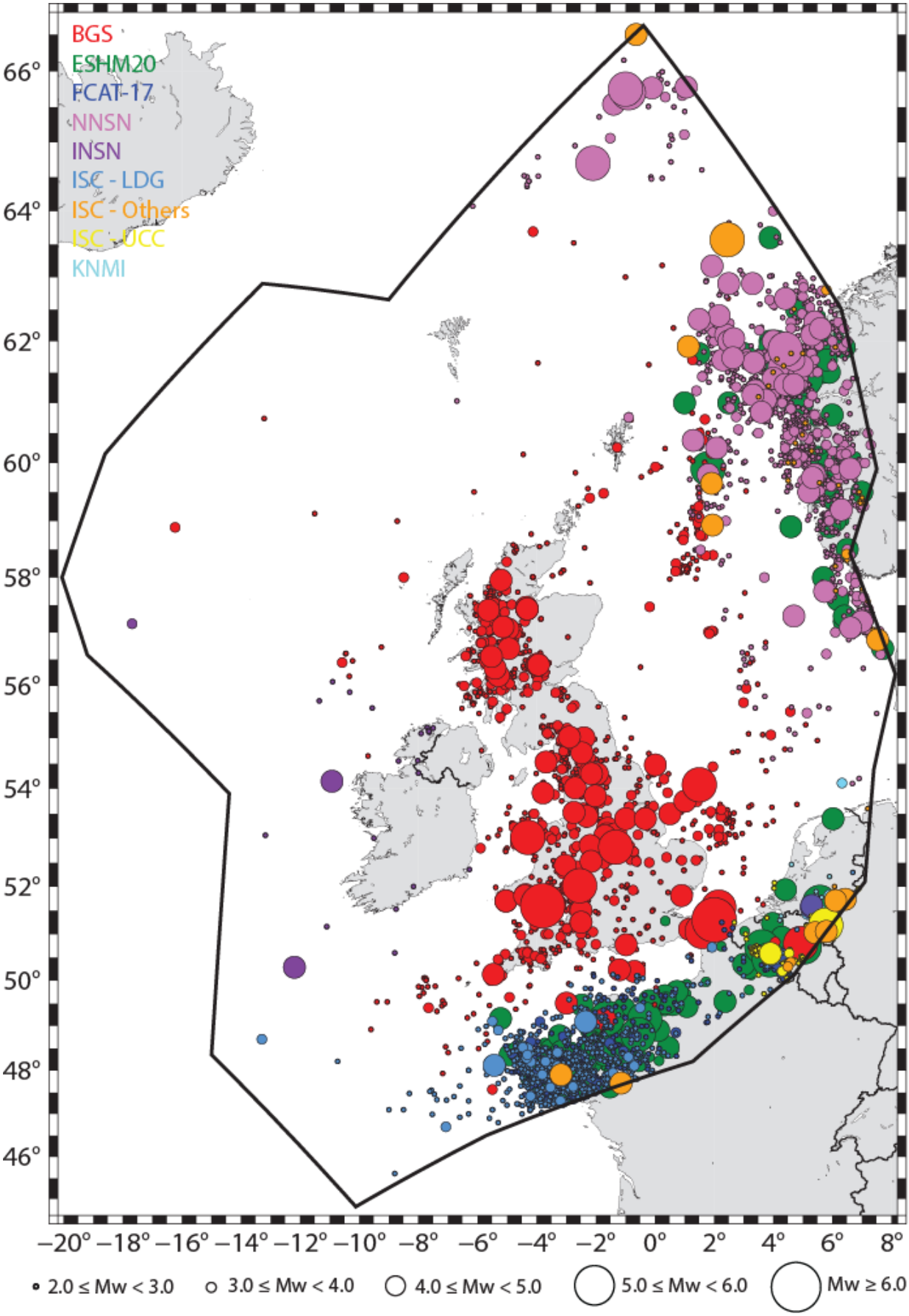

Figure 3: Distribution of earthquakes with Mw ≥ 2.0 in terms of selected agencies within the study area described by the black polygon. The size of the circles is scaled by magnitude. See Table 1 for the acronyms of the agencies.

The prioritisation scheme for northern France is the following.

a. For the historical (before 1970) events, we use the earthquake catalogue developed for the ESHM20 (Danciu et al., 2021). The ESHM20 parametric earthquake catalogue consists of pre-instrumental (from 1000 to 1899) and instrumental parts (from 1900 to December 2014) and covers Europe and the Mediterranean region. The magnitude scale used is Mw and the original magnitude scales are not provided.
b. The primary source of data between 1960 and 2009 is the French earthquake catalogue of Manchuel et al. (2018; referred hereto as FCAT-17), which is a parametric earthquake catalogue that merges the historical and instrumental catalogues for France and covers the period between 500 to December 2009. The magnitude scale used is Mw and the original magnitude scales are not provided. For the historical events in France, we do not use the FCAT-17 because it has a significantly higher number of moderate-to-large earthquakes in the time window 1800-1950 compared to that in instrumental time suggesting a lack of homogeneity between instrumental and historical Mw estimates (Beauval et al., 2020). The procedure for estimating the moment magnitude of historical events in France seems to have resulted in an overestimation of the magnitude of these events as observed also by Mosca et al. (2020).
c. For events that occurred in France after 2009, we use the data from the Laboratoire de Détection et de Géophysique/CEA (LDG) in France that are included in the International Seismological Centre Bulletin (ISC, 2021). These earthquakes are expressed in ML. Note that we use the determination from the BGS database for events that occurred in the English Channel, the Channel Islands and the Cotentin Peninsula after 2009 rather than the LDG's events as reported in the ISC Bulletin. This choice is because the BGS database indicates whether an event is anthropogenic or tectonic (see Subsection 3.1).

The prioritisation scheme for the other regions is the following.

a. We use the ESHM20 catalogue for the historical part of the catalogue.
b. The instrumental part of the project catalogue consists of data from the local monitoring agencies. For the Norwegian region including the Norwegian sector of the North Sea, we use the earthquake catalogue built from the Norwegian National Seismic Network (NNSN) database (https://nnsn.geo.uib.no/nnsn/#/). This is the result of data processing at the University of Bergen with contributions from NORSAR, contains mostly events from instrumental times (1970-now) and a few events from 1060 to 1970. Earthquake size is expressed in terms of ML. The data for the Republic of Ireland are from the Irish National Seismic Network (INSN), which is maintained by the Dublin Institute for Advanced Studies, together with the Geological Survey Ireland (https://www.insn.ie/). The INSN catalogue is a parametric catalogue, which contains event origin times, locations and ML determined from instrumental recordings from 1980 to the present. We use the catalogue from the Royal Netherlands Meteorological Institute (KNMI) for the Netherlands (https://dataplatform.knmi.nl/dataset/aardbevingen-catalogus-1). It contains the location, origin time, magnitude in ML, depth and type of earthquakes in and around the Netherlands.
c. To improve the picture of seismicity in these regions, we use also events from the ISC Bulletin, which contains data from 1904 to the present and is based on bulletin data collected from 515 seismological agencies around the world (ISSC, 2021). Each earthquake is characterised by an origin time, epicentre coordinates, hypocentral depth and any magnitude estimated by the agencies that detected the event. We select the determinations from the main local monitoring agencies in each country (e.g. Royal Observatory of Belgium for Belgium) if possible; otherwise, we use global databases such as the National Earthquake Information Centre online database of the US Geological Survey (USGS, 2017) and the Global Centroid Moment Tensor catalogue (http://www.globalcmt.org). When possible, we prefer to select the events from the database of the local monitoring agencies (e.g. BGS and KNMI) because the ISC database does not discriminate between anthropogenic and tectonic earthquakes.

Figure 3 shows two earthquakes (5.5 Mw 8 September 1692 and 3.0 Mw 13 June 1992) reported in the BGS database that occurred in Belgium (red circles in Figure 3). The 3.0 Mw event is also shown in the ISC database without an estimated magnitude.

3.1 REMOVING ANTHROPOGENIC SEISMICITY

As the first step to have a catalogue of tectonic (natural) earthquakes, we remove all events known to be of anthropogenic (man-made) origin from the catalogue so that these do not bias estimates of activity rate. Also, the physical mechanisms of anthropogenic seismicity are different from those of tectonic earthquakes and may not follow the same Gutenberg-Richter frequency-magnitude law that is used to quantify the rate of occurrence of tectonic earthquakes (e.g. Moein et al., 2023).

Anthropogenic seismicity includes earthquakes induced by oil and gas production such as the 4.1 Mw earthquake on 7 May 2001 in the Ekofisk gas field (Ottemöller et al., 2005; Cesca et al., 2011), and induced seismicity in the north and northeast of the Netherlands, such as the seismicity around the Groningen gas field (van Eijs et al. 2006; van Eck et al. 2006). Similarly, micro-earthquakes of magnitude smaller than 2.0 ML induced by the hydrocarbon production at the Valhall oil field in Central Graben (Kristiansen et al., 2000) are also removed. However, we note that there are also earthquakes (e.g. 3.9 Mw earthquake on 24 September 2019 in the Shearwater Field) that cannot be linked conclusively to production although they are close to operating fields. As a result, we do not remove these events from the catalogue. Note that the induced seismicity in the North Sea is characterised by small (< 4.0 Mw) magnitudes and therefore induced earthquakes, including the Ekofisk and Shearwater earthquakes, would fall outside the completeness thresholds of the catalogue (see Section 3.4). This means that removing these events would not lead to any change in the seismicity rate in the North Sea region.

Mining-induced seismicity in the UK has also been removed. This includes events identified as mining-induced (e.g. Baptie et al., 2016), occurring close to operating mines and with shallow depths (<5 km). Nearly all these events have magnitudes of less than 3 ML. Wilson et al. (2015) reviewed the distribution, timing and probable causes of 1769 seismic events across the UK with ML > 1.5 between 1970 and 2012 suggesting that at least ~21% are of an anthropogenic origin. Events of an explosive origin due to quarrying, mining, weapon testing or disposal, naval exercises, geophysical prospecting and civil engineering have also been excluded where possible. Quarry blasts, which account for the majority of such events, have been removed by checking locations against known quarries and, where possible, confirming blasting times with the relevant quarry. Explosions from the detonation of ordnance or other sources mostly occur offshore and have been removed by analysing the waveform characteristics, which are different from tectonic earthquakes. For ambiguous events, information reported by relevant authorities (e.g. Coastguard) and other seismological agencies is also used to discriminate between natural earthquakes and explosions.

We do not discriminate between tectonic and mining-induced earthquakes in the coal area of the Hainaut province in Belgium and the Pas-De-Calais because we do not have such information. However, this would have a negligible influence on the hazard for the UK offshore EEZ because mining-related earthquakes have a small (< 3 Mw) size and therefore would fall outside the completeness thresholds for the region. From the analysis of the impact and damage of shallow seismic activity that occurred from the end of the 19th century until the late 20th century in the Hainaut province (when the mining area was in operation), Camelbeeck et al. (2022) concluded that only very shallow (up to a depth not exceeding 1km) events suggest a close link to mining activities. Many events, including the largest shallow events in the coal area before 1970, occurred at depths greater than 2 km, which would exclude a direct relationship with mining, but still might imply a triggering causality. Some small earthquakes in the Pas-De-Calais may have a mining origin since there was little seismic activity before the mining activity in the region but there is no conclusive evidence that these events are anthropogenic (Doubre et al., 2021).

3.2 MAGNITUDE HOMOGENISATION

Although Mw is the preferred magnitude scale for seismic hazard assessments, the catalogues compiled by the regional agencies used in this study consider a variety of magnitude scales, primarily ML. We use published empirical magnitude conversion relationships to convert all

magnitudes to moment magnitudes and ensure that the project catalogue has consistent and homogeneous magnitude values across the region of interest.

For the LDG events selected from the ISC Bulletin, we use the ML - Mw equation of Cara et al. (2015), which was derived using earthquakes of ML ≤ 4.0 that occurred in France:

$$Mw = \begin{cases} 0.45 + 0.664ML & if\ ML < 3.1; \\ ML - 0.6 & if\ 3.1 \leq ML \leq 4.0. \end{cases} \quad (3)$$

The standard deviation for this relationship is not reported. For the earthquakes from other sources, including those from the BGS database, we convert ML to Mw using the relation of Grünthal et al. (2009) that was derived from about 8000 earthquakes of 3.5 < ML < 6.5 in Central and Northern Europe:

$$Mw = 0.0376ML^2 + 0.646ML + 0.53. \quad (4)$$

The magnitude-dependent standard deviation in the converted Mw is between 0.29 and 0.34 (see Annex 4 in Grünthal et al., 2009), which we approximate to 0.3 for all magnitudes. The Mw values calculated using Grünthal et al. (2009) do compare relatively well with measured Mw for the UK (see Mosca et al., 2020) although there are very few data for earthquakes larger than 4.0 ML to extend the comparison to larger magnitudes.

The composite catalogue built for this project also contains events with surface wave magnitude (Ms) and body wave magnitude (mb). We use the Ms – Mw and mb – Mw conversion equations of Grünthal et al. (2009):

$$Mw = 10.85 - \sqrt{73.74 - 8.38Ms} \quad for\ Ms < 7.0. \quad (5a)$$

$$Mw = 8.17 - \sqrt{42.04 - 6.42mb} \quad for\ mb < 6.0. \quad (5b)$$

Grünthal et al. (2009) do not report the standard deviation for these two equations.

Figure 4 shows the importance of using different magnitude conversion relationships for each catalogue to avoid an overestimation of Mw in Northern France. If we use Equation 4 to convert the ML(LDG) values into Mw, we would obtain larger Mw estimates than using Equation 3 (see the green stars in the bottom right-hand side plot in Figure 4). The top right-hand side plot in Figure 4 shows that the Mw values in the FCAT-17 catalogue are higher than the converted Mw values for the same events in the BGS database. In contrast, a comparison of the latitudes and longitudes from the three datasets (i.e. BGS, FCAT-17, and ISC-LDG) shows an excellent agreement with a correlation coefficient higher than 0.99.

The total standard deviation in the converted Mw results from two sources of uncertainty. The first is the uncertainty in the original magnitude and the second is related to the conversion from the original magnitude to Mw. The uncertainty in ML is not assessed for historical (before 1970) events in the BGS earthquake catalogue. Furthermore, there is an additional source of uncertainty in the standard deviation of converted Mw for historical events, which is related to the conversion of macroseismic intensity data into ML. The ML uncertainty for instrumental (after 1970) events has been uniformly estimated in the last three years (Baptie, 2022). The standard deviation in ML for the instrumental earthquakes is between 0.0 and 0.9. A value of 0.0 is assigned to events with only one phase, whereas a high standard deviation is mainly associated with events that occurred offshore. The total uncertainty in the converted Mw accounts for the standard deviation in ML and the magnitude-depending standard deviation of 0.3 from the equation of Grünthal et al. (2009). For BGS instrumental events the estimated Mw standard deviation is between 0.3 and 0.9 (see red circles, together with their error bars, in Figure 5).

The earthquake magnitudes in FCAT-17 are given in terms of Mw, together with its standard deviation (Manchuel et al., 2018). Figure 5 compares the standard deviation in Mw between the instrumental events in the BGS database and FCAT-17. The latter appears to be significantly smaller than the former. We could not extend this comparison to the magnitude estimates for events from other sources (e.g., the catalogue of NNSN) because the uncertainty in the original magnitude scale was not reported. This highlights the difficulty of merging catalogues from different regions where different methods of analysis have been used.

Musson (2012b) demonstrates that care should be taken when the magnitude uncertainties are accounted for in the recurrence statistics (Equations 1 and 2), especially when an earthquake catalogue merges many sources and contains more than one original magnitude scale to avoid over- or underestimating the activity rate and the *b*-value in the area under consideration. For this reason, we do not consider the magnitude uncertainty in this work, including the recurrence statistics in Section 5.3.

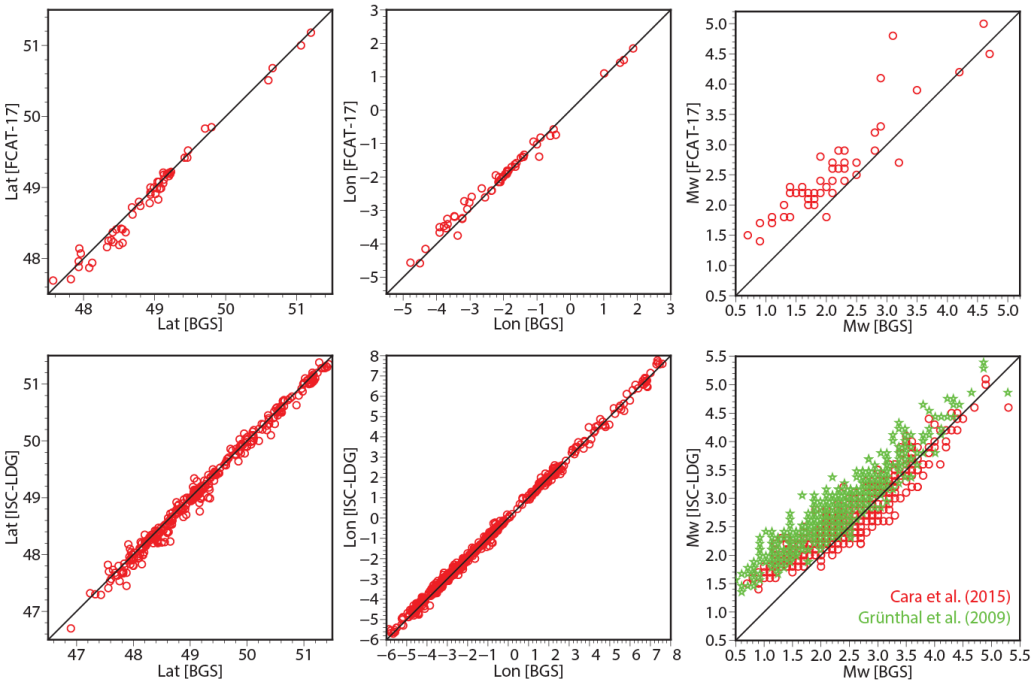

Figure 4: Comparison of latitude, longitude, and converted Mw for common events in the BGS database and the FCAT-17 catalogue (top plots), and the BGS database and LDG as reported in the ISC database (bottom plots). The red and green circles in the right-hand side bottom plot describe the converted Mw values computed from the relationship of Cara et al. (2015) and Grünthal et al. (2009), respectively.

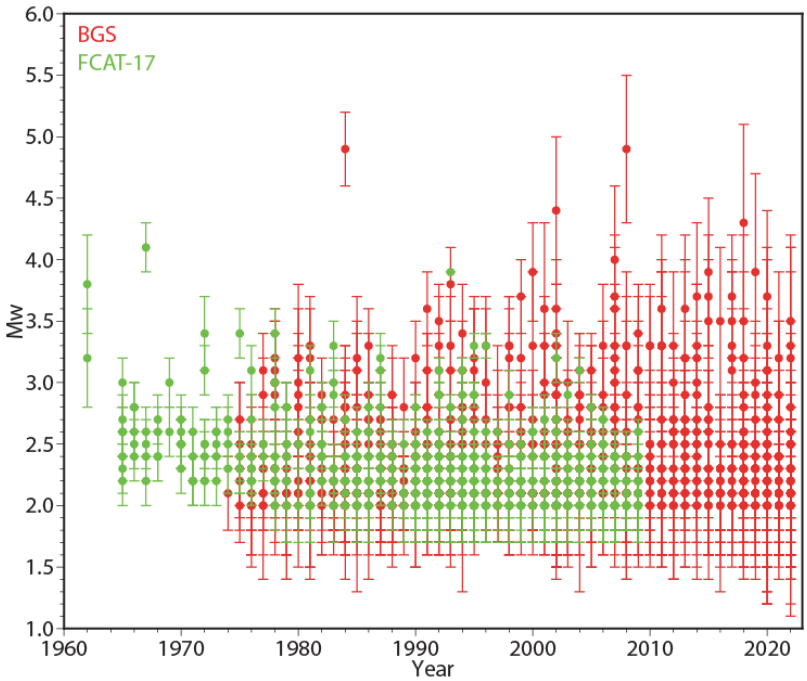

Figure 5: Comparison of the standard deviation in Mw between instrumental events in the BGS database and the FCAT-17.

3.3 DECLUSTERING THE CATALOGUE

The majority of seismic hazard estimations are based on the assumption that the occurrence of an earthquake is independent of the occurrence of any other, i.e. the probability of the occurrence of an earthquake in a given period of time follows a Poisson distribution (Cornell, 1968). Therefore we remove time-dependent earthquakes (i.e. foreshocks and aftershocks) from the catalogue before further analysis.

Following Mosca et al. (2022), we apply the windowing method of Burkhard and Grünthal (2009). This uses magnitude-dependent time and space windows calibrated for the earthquake catalogue in Central Europe but it does not include data in the British Isles. The time windows for foreshocks and aftershocks are:

$$dT_f(Mw) = \begin{cases} exp\left(-4.77 + \sqrt{0.62 + 17.32Mw}\right) \; if \; Mw < 7.8 \\ ex\,p(6.44 + 0.055Mw) \; otherwise; \end{cases} \quad (6a)$$

$$dT_a(Mw) = \begin{cases} exp\left(-3.95 + \sqrt{0.62 + 17.32Mw}\right) \; if \; Mw < 6.6 \\ ex\,p(6.44 + 0.055Mw) \; otherwise; \end{cases} \quad (6b)$$

and the space window is:

$$dR(Mw) = \exp\left(1.77 + \sqrt{0.037 + 1.02Mw}\right) \quad (6c)$$

where dT_f and dT_a are the numbers of days before and after the mainshocks, respectively, and dR is the distance in kilometres of the location of the foreshocks and aftershocks from the mainshock's epicentre. Ideally, the time and space windows of the declustering approach should be calibrated to the local data but this could not be developed within the timescale of the project.

Figure 6 shows the cumulative and annual number of earthquakes of ≥ 2.0 Mw (Figure 6a,c) and ≥ 3.0 Mw (Figure 6b,d) in the catalogue before and after declustering. The black and red lines in Figure 6a display an increase in the cumulative number of earthquakes of Mw ≥ 2.0 after 1980 corresponding to a better detection of small earthquakes by local instrumental monitoring networks. After declustering, the total number of mainshocks of Mw ≥ 2 is 4018 (out of 4753 events of 2 Mw and above before declustering).

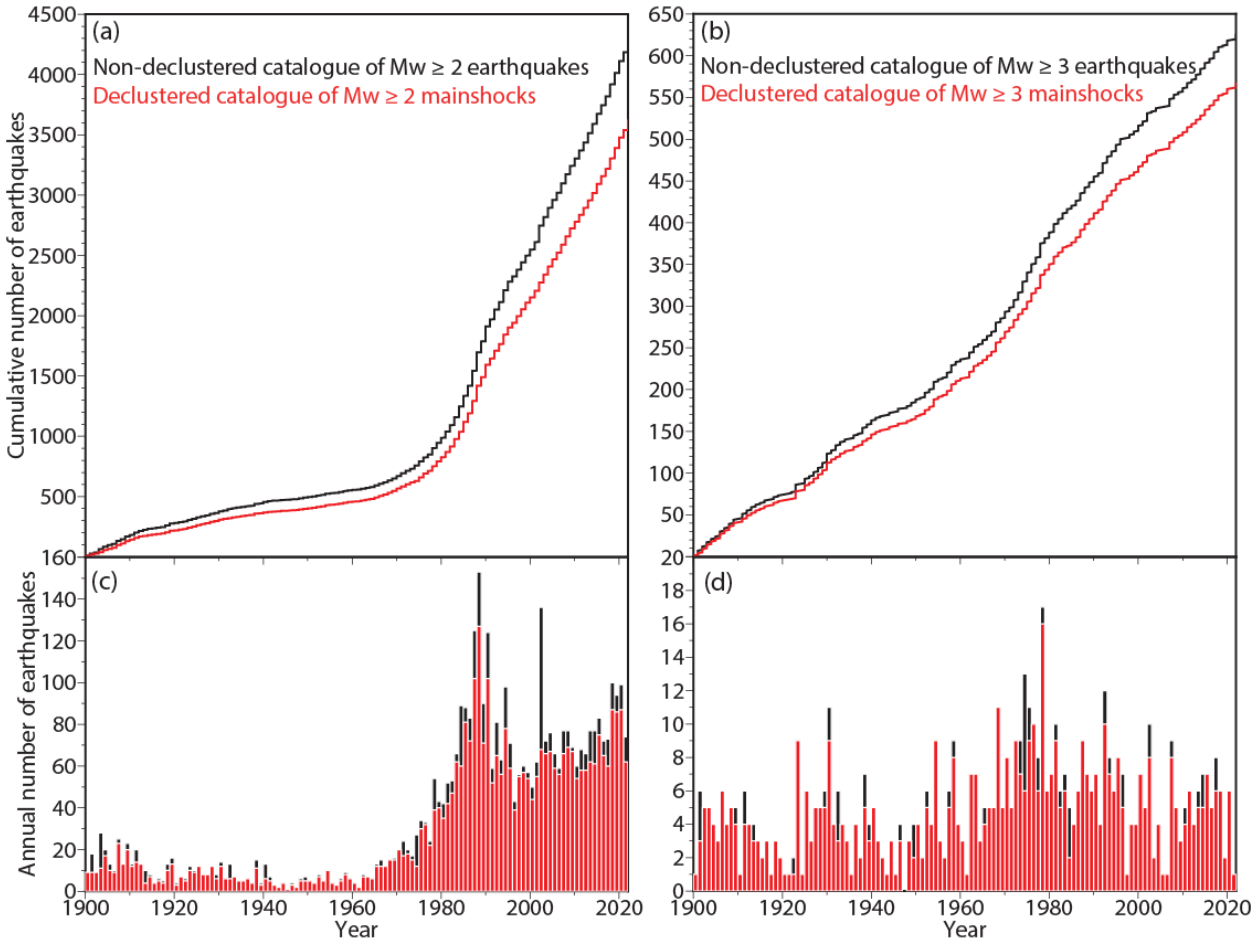

Figure 6: (a) Cumulative number of earthquakes with Mw ≥ 2.0, (b) cumulative number of earthquakes with Mw ≥ 3.0, (c) annual number of earthquakes with Mw ≥ 2.0, (d) annual number of earthquakes with Mw ≥ 3.0 before and after the declustering analysis as a function of time from 1900 to 2022.

3.4 CATALOGUE COMPLETENESS

Earthquake catalogues are incomplete representations of the actual seismicity of a region. Normally, completeness improves with time (i.e. it is generally better nearer the present day) and with magnitude (i.e. it is better for larger earthquakes). The completeness magnitude (Mc) is defined as the lowest magnitude at which (approximately) 100% of the earthquakes in a space-time volume are detected (Rydelek and Sacks, 1989). The Mc value is expected to vary with time and is usually low for recent seismicity, where instrumental recordings are available, and gets progressively higher further back in time.

Since the project catalogue merges local datasets that are very heterogeneous in space and time, we introduce completeness regions to assess the catalogue completeness (Figure 7). The boundaries of these regions are based on the homogeneity of earthquake reporting through time history, i.e. the earthquake reporting rates are assumed to be spatially homogeneous within each of the completeness regions. We assume that the completeness thresholds up to around 70 km distance from the coast are the same as for onshore areas, as long as there are populated areas near the coast (BGS and Arup, 1997).

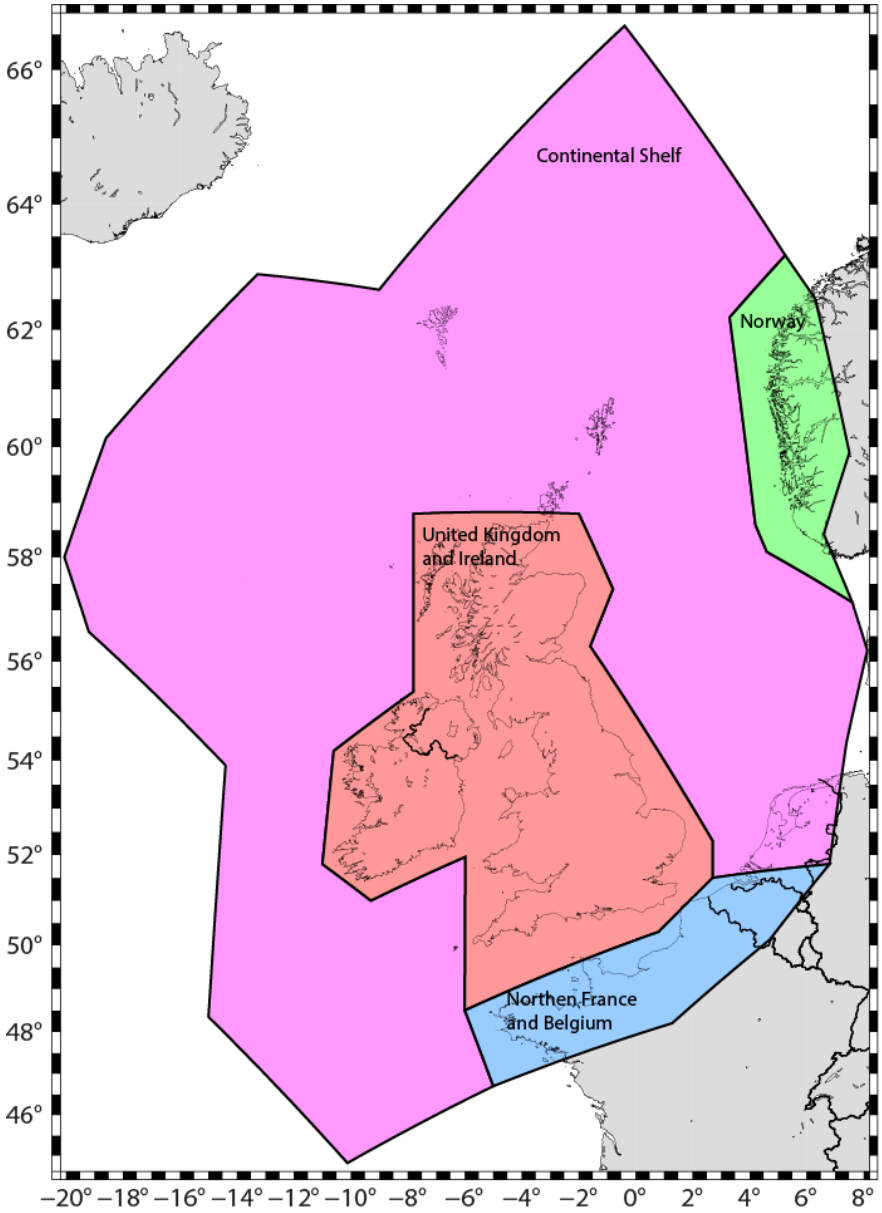

Figure 7: Boundaries and names of the completeness regions.

Several statistical methods are available to assess the completeness of the instrumental (after 1970) earthquake catalogues (e.g., Wiemer and Wyss, 2000; Cao and Gao, 2002). However, Woessner and Wiemer (2005) and Roberts et al. (2015) find that catalogues should contain a minimum of 200 events above the completeness magnitude to apply these methods and produce statistically acceptable results. Since the instrumental part of the catalogue in each region contains less than 150 events within the expected completeness thresholds, we do not apply such statistical methods. Instead, we use the cumulative and annual numbers of earthquakes for specific magnitudes, together with published information on the completeness analysis for the earthquake catalogue of the individual countries and the ESHM20 catalogue. The assumption is that any slope change in the cumulative number of events represents a change in the completeness of the earthquake catalogue.

The results of the completeness analysis for the declustered catalogue are shown in Table 2 for different time windows and the four completeness regions in Figure 7. Figures 8-10 show the cumulative and annual number of mainshocks for selected Mc values.

3.4.1 The United Kingdom and Ireland

For the UK and Ireland region, we use the Mc value of 3.0 Mw for the period after 1975 as used by Mosca et al. (2022). We use a Mc value of 3.5 Mw for the period from 1880 based on the slope change of the cumulative number of earthquakes with ≥ 3.5 Mw as a function of time (Figure 8). For the years 1750,1700 and 1650, we use the same values of Mc in Mosca et al.

(2022), i.e. 4.0, 4.5 and 5.0 Mw, which are based on the studies of UK historical earthquakes by Musson (2007). We use a value of Mc = 6.5 Mw for 1300 based on the work of Johnston et al. (1994). They estimated the global completeness thresholds based on the global instrumental magnitude detection from 1896 to 1994 using information on early seismograph installations from McComb and West (1931) and Ambraseys and Melville (1982) and considering population and seismograph density in specific stable continental regions (SCRs).

EQE02 indicates Mc values of 4.5 Ms (4.8 Mw) and 5.0 Ms (5.2 Mw) from 1800 and 1700, respectively, for the historical catalogue. They agree roughly with the completeness thresholds in this work and Mosca et al. (2022). Also, our estimated completeness thresholds compare relatively well with those for the ESHM20 catalogue for the same regions for Mw ≥ 4.0; whereas there are some clear differences for Mc between 3.5 and 3.7 Mw. For example, the ESHM20 catalogue for the UK, Ireland and surrounding offshore regions is estimated to be complete for ≥ 3.5 Mw from 1839. Although the Mc value of 3.5 Mw from 1850 was indicated in the previous national hazard maps by Musson and Sargeant (2007) and corresponds to the newspaper tax lifting in the UK, we do not think it can be extended to the entire UK, including the most remote regions in Scotland and the surrounding offshore regions.

3.4.2 Northern France and Belgium

For the catalogue in Northern France and Belgium, we use the results of the completeness analysis of Drouet et al. (2020), who developed the national seismic hazard maps in France and included also the seismicity in the bordering regions with France (Table 2). This is based on the detection of any slope change in the cumulative number of events as a function of time, together with the Hakimhashemi and Grünthal (2012) method that tests the standard deviation of the inter-event time. They find that the instrumental earthquake catalogue in metropolitan France is complete for Mw ≥ 2.5 from 1970 and Mw ≥ 3.0 from 1950. Even in seismically active places with a well-developed monitoring network such as California, a Mc value of 2.5 Mw from 1970 seems to be optimistic. For this reason, we do not consider this completeness threshold. Although Mc = 3.5 Mw for 1850 has a clear change in the cumulative number of earthquakes (central plot Figure 9), there is no jump in the cumulative number of mainshocks for the other completeness thresholds.

3.4.3 Norway and Continental Shelf

Figure 10 shows the cumulative and annual number of mainshocks for three Mc values for the Norway region and one Mc value for the Continental Shelf. It is difficult to see any slope change in the cumulative number of events as a function of the year due to the sparse number of events detected here. It is also remarkable that no earthquakes of Mw > 3.4 have occurred in Norway since 2000.

Johnston et al. (1994) find that the catalogue for the Continental Shelf is likely to be complete for 4.6 Mw and above from 1980, and 4.8 Mw from 1964. This estimate corresponds to improvements in the detection capability of global earthquake monitoring after the World-Wide Standard Seismograph Network started to operate in the early 1960s. For Fennoscandia, Johnston et al. (1994) have found the catalogue for Fennoscandia is complete for Mc = 3.7 and 4.0 Mw from 1979 and 1950, respectively.

Bungum et al. (2000) used Mc values of ~4.0-4.3 from the 1960s and ~4.5 from 1880 for the catalogue completeness of the North Sea and Norway. The magnitude scale is not specified. The completeness thresholds for the North Sea region in EQE02 are the same as NORSAR and NGI (1998). Mallard et al. (2003) infer Mc = 5 Ms (5.2 Mw) from 1800 for the historical catalogue in the offshore region based on the material used in site-specific hazard assessments by the Seismic Hazard Working Party. Similarly, they report a completeness threshold of 4.5 Ms (4.8 Mw) from 1980 for the instrumental catalogue in the UK and North Sea. For the North Sea up to Viking Graben, Mosca et al. (2022) use the results of the completeness analysis for Northern Europe undertaken by Woessner et al (2015). According to this, the catalogue in this region can be considered to be complete for 3.7 Mw and above from 1970. In the ESHM20 catalogue, which is an updated version of the catalogue in Woessner et al (2015), the completeness thresholds for Norway and surrounding regions have been revised. In particular, Danciu et al. (2021) find that the catalogue of mainshocks in that region is complete for 3.7 Mw

and above from 1879. This Mc value seems to be unlikely for that region considering the small number of reported events before the instrumental monitoring network started there.

To try to understand the magnitude of offshore earthquakes that might be felt, we used two different intensity prediction equations (IPEs) to estimate earthquake intensities for both a specific event and a grid of possible earthquake locations. Figure 11 shows the expected intensities for the earthquake on 23 March 2022 in the Viking Graben (see Section 4.5 for more information on this event) modelled using the intensity prediction equation of (a) Allen et al. (2012) and (b) Musson (2013). The former shows much higher intensity attenuation, which might be expected for a relationship derived using recordings from active crustal regions. Red squares in Figure 11 show places in the UK where the earthquake was reported as felt. A comparison with the modelled intensities suggests that the Musson (2013) relationship is a better fit of the data. Figure 12 shows the expected magnitude of the earthquakes that might be felt in at least one populated place with an intensity of 3 across the North Sea region. The populated places are marked by red squares and the intensities are modelled using the IPE of Allen et al. (2012) in Figure 12a and Musson (2013) in Figure 12b. These confirm that the magnitude of earthquakes that would be felt increases rapidly with distance offshore. The use of Allen et al. (2012) suggests that for earthquakes in the Central North Sea, only those with a magnitude greater than 6 would be felt, whereas using Musson (2013) suggests that events greater than magnitude 5 would be felt. The different results are explained by the different data used to derive the two intensity models - > 13,000 intensity data from crustal earthquakes worldwide with 5.0-7.9 Mw for Allen et al. (2012) versus 727 intensity data from 326 British earthquakes with 2.0-6.0 Mw for Musson (2013).

Since the Mc values determined by Johnston et al. (1994) for the Continental Shelf and Norway agree well with the results of the test in Figures 11 and 12, here we adopt these completeness thresholds.

United Kingdom and Ireland		*Continental Shelf*		*Norway*		*Northern France and Belgium*	
Mc	*Year*	*Mc*	*Year*	*Mc*	*Year*	*Mc*	*Year*
3.0	1975	4.6	1980	3.7	1979	3.0	1950
3.5	1880	4.8	1964	4.0	1950	3.5	1850
4.0	1750	5.3	1950	4.5	1918	4.5	1700
4.5	1700	5.6	1918	5.0	1860	5.0	1600
5.0	1650	6.0	1899	5.6	1800	5.5	1500
6.5	1300	6.8	1800	6.0	1600		
		7.1	1700	6.5	1350		

Table 2: Completeness magnitudes Mc for the earthquake catalogue of this work using the completeness region in Figure 7.

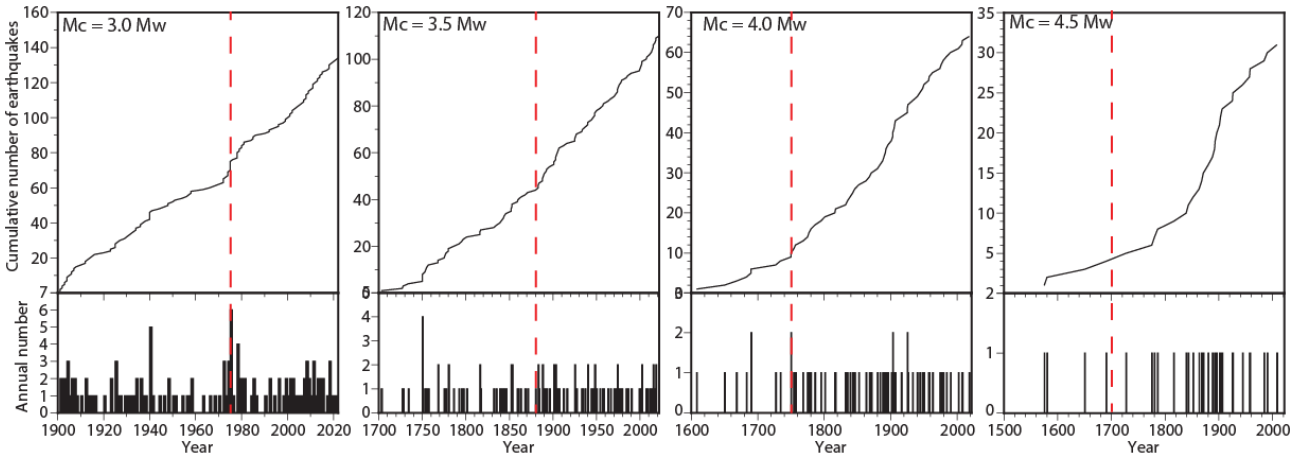

Figure 8: Cumulative number (top panel) and annual number (bottom panel) of mainshocks for selected Mc values for the UK region in Figure 7. The red, dashed lines indicate the completeness threshold.

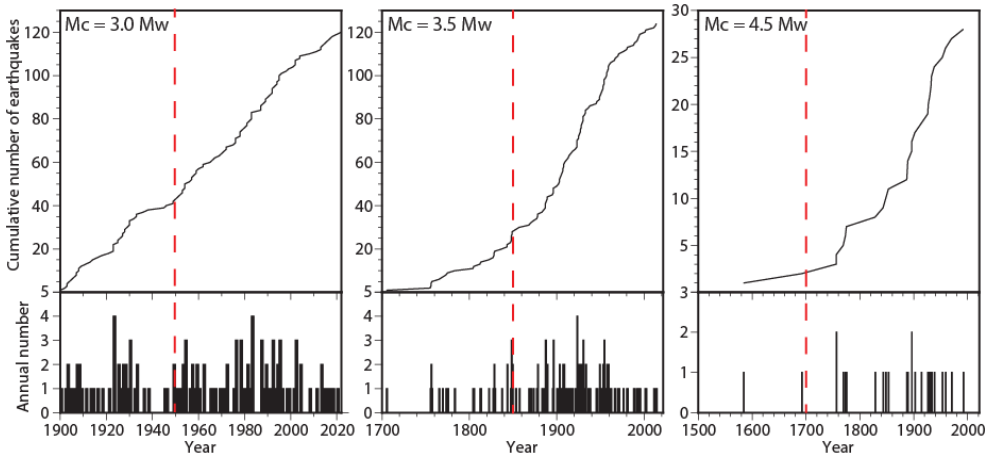

Figure 9: Cumulative number (top panel) and annual number (bottom panel) of mainshocks for selected Mc values for Northern France and surrounding regions in Figure 7. The red, dashed lines indicate the completeness threshold.

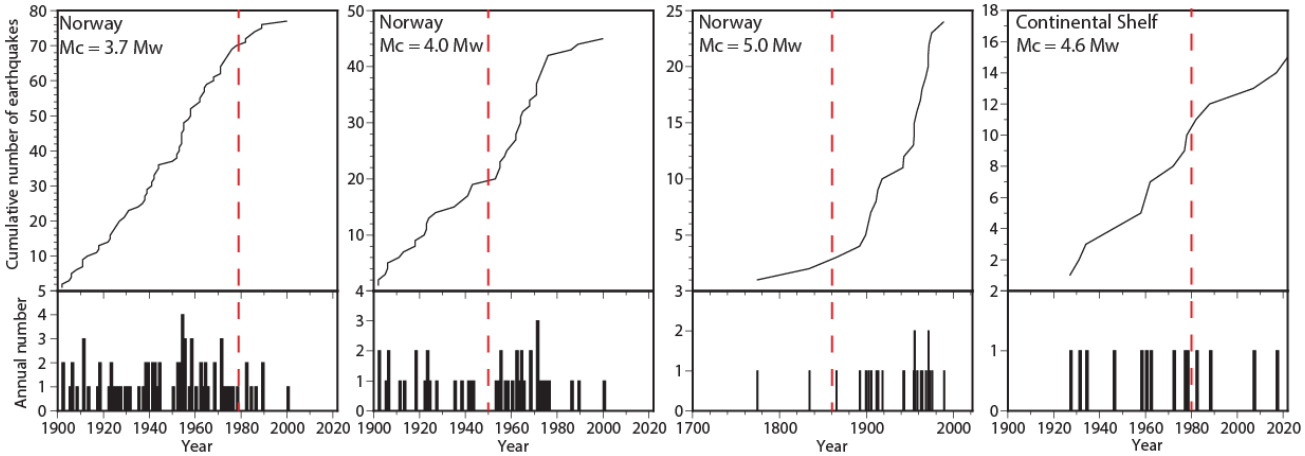

Figure 10: Cumulative number (top panel) and annual number (bottom panel) of mainshocks for selected Mc values for Norway and the Continental Shelf in Figure 7. The red, dashed lines indicate the completeness threshold.

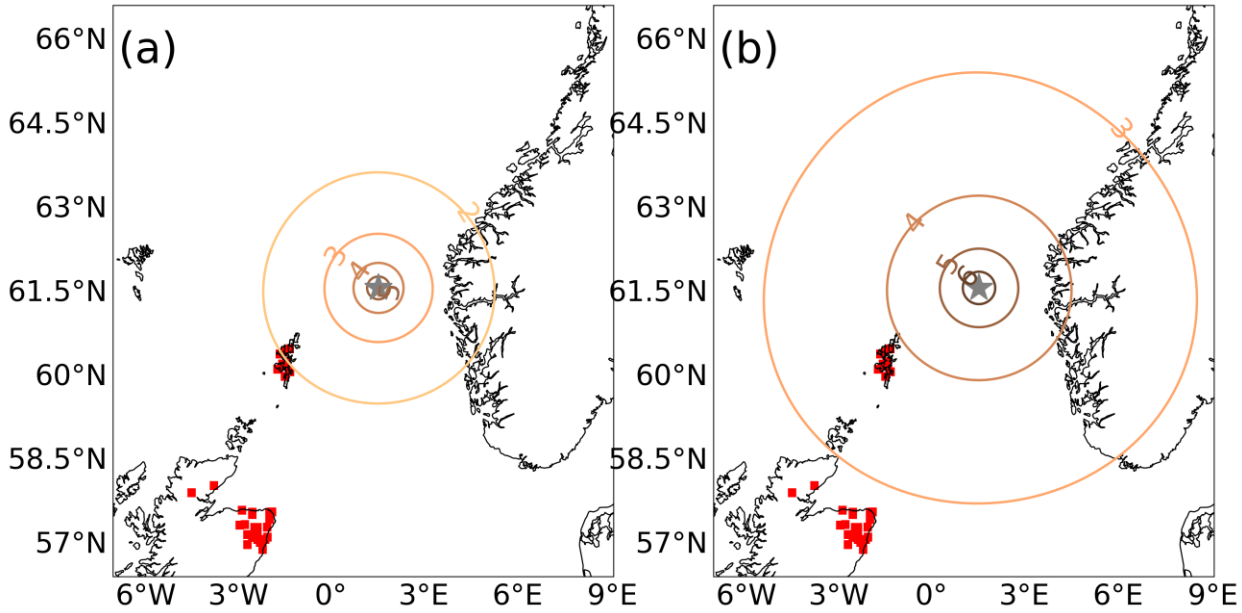

Figure 11: Expected intensities for the earthquake on 23 March 2022 in the Viking Graben modelled using the intensity prediction equation (IPE) of (a) Allen et al (2012) and (b) Musson (2013). Red squares in (a) and (b) show places in the UK where the earthquake was felt. Made with Natural Earth. Free vector and raster map data @ naturalearthdata.com

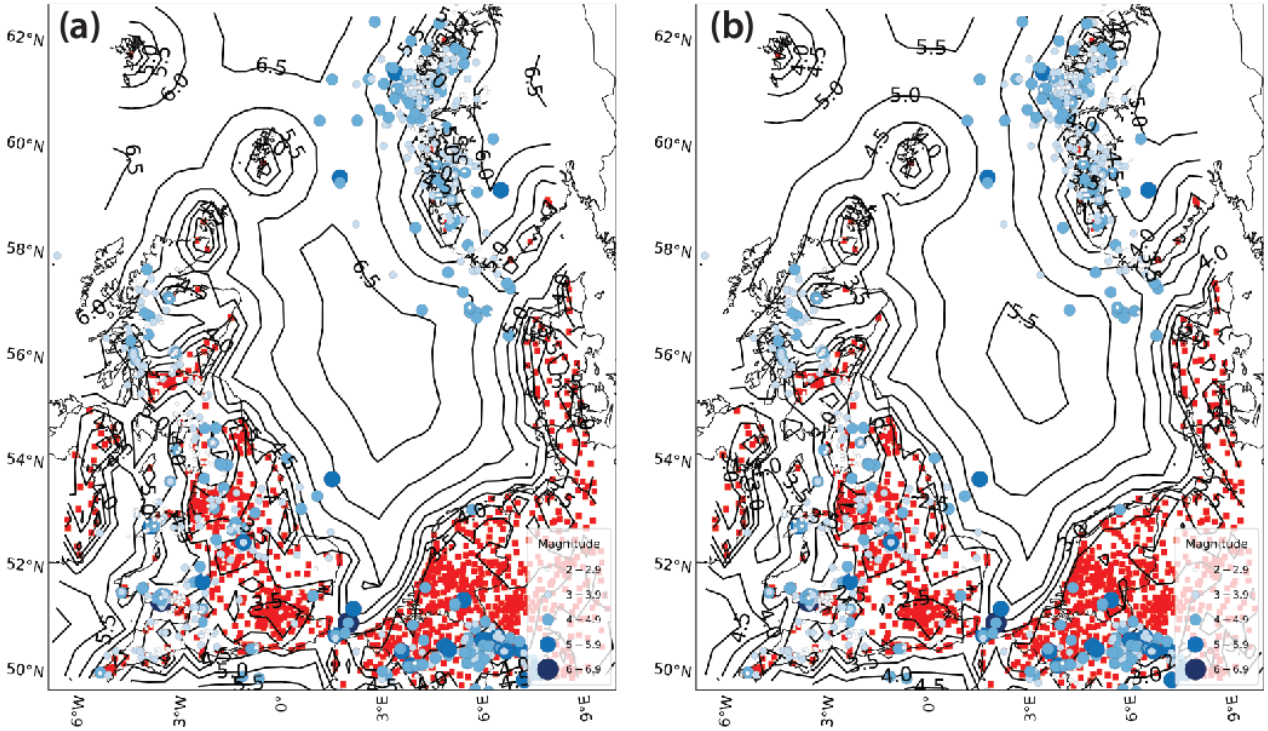

Figure 12: The expected magnitude of the earthquake that would be felt in at least one populated place (red squares) with an intensity of 3 across the North Sea region. Intensities are modelled using the IPE of (c) Allen et al. (2012) and (d) Musson et al. (2013). Blue-shaded circles describe the earthquakes that occurred before 1970 (see Section 3). The figure contains population data © Esri. Made with Natural Earth. Free vector and raster map data @ naturalearthdata.com

4 Seismo-tectonic context

The study area lies in the northwest part of the Eurasian plate at the northeast margin of the North Atlantic Ocean, approximately 1,500 km northeast of the Mid-Atlantic Ridge and around 2,000 km north of the plate boundary between Africa and Eurasia (Figure 13). As a result of this geographic position, distal to active plate boundaries, the UK and North Sea regions are characterised by low levels of earthquake activity (e.g. Musson, 2012c). Evidence for this comes from observations of earthquake activity dating back several hundred years, which suggests that although there are many accounts of earthquakes felt by people, earthquakes causing damage are rare.

The present configuration of the study area resulted from a complex geological history consisting of multiple episodes of deformation (Strachan et al., 2002; Woodcock and Strachan, 2012). This started with a series of tectonic collisions related to the closure of the Iapetus and Rheic oceans, which began in the Ordovician and ended in the earliest Permian with the final assembly of the supercontinent Pangaea (Ziegler, 1992; Woodcock and Strachan, 2012). Two composite orogenic events are recognised: the Caledonian Orogeny (470–390 Ma), which represents the collisions between Baltica, Avalonia and Laurentia and the closure of the Iapetus Ocean; and the Variscan Orogeny (370–290 Ma), which reflects the collisions of a series of other fragments of Gondwana with Laurasia. The basin formation of the North Sea commenced in the Carboniferous to Permian (300-260 Ma). Rifting activity in the North Sea started at the transition from the Permian to the Triassic (260 – 200 Ma), intensified during the Middle Jurassic (175 Ma) to the earliest Cretaceous (140 Ma) times and then gradually abated during the Cretaceous as the focus of crustal extension migrated to the area between Greenland and northern Europe, leading to North Atlantic rifting from the late Cretaceous onwards (Ziegler, 1992). Igneous activity in the North Sea is largely restricted to the Middle Jurassic and was accompanied by the uplift of a broad rift dome, causing a temporary reversal in the subsidence pattern of the Central Graben (Ziegler, 1992). The oil and gas accumulations in the North Sea all originated from shale strata that were deposited from the Late Jurassic to the earliest Cretaceous times (Gautier, 2005). The North Sea Graben Province in the northwest, the Anglo-Dutch Basin Province in the south, and the northwest German Basin Province in the southeast account for the large majority of oil and gas resources in Western Europe (Figure 13). The North Sea Graben Province is distinctly oil-prone, in contrast to the adjacent gas-prone Anglo-Dutch and Northwest German Basin Provinces (Gautier, 2005).

The crustal thickness corresponds to the depth of the crust-mantle boundary, the Mohorovicic (Moho) discontinuity (e.g., Licciardi et al., 2012) and provides an upper bound to the maximum seismogenic depth. Published studies suggest that the Moho is at depths of 29-36 km in Ireland and Great Britain (e.g., Maguire et al., 2011; Davis et al., 2012; Pharaoh, 2018; Licciardi et al., 2020), around 12-22 km in the Atlantic Ocean, west of Ireland (Licciardi et al., 2012), and at depths of 20-25 km under the Viking and Central Grabens (Ziegler, 1992). Licciardi et al. (2012) have found that maximum values of Moho depth are in Wales (36–37 km), southeast England (36–37 km), and near the Faroe Islands (38–40 km), while minimum values of Moho depth (11–12 km) are located offshore southwest Ireland. Sichien et al. (2012) estimated a crustal thickness between 28 and 37 km in Belgium with a value of 31 km beneath the Brabant Massif.

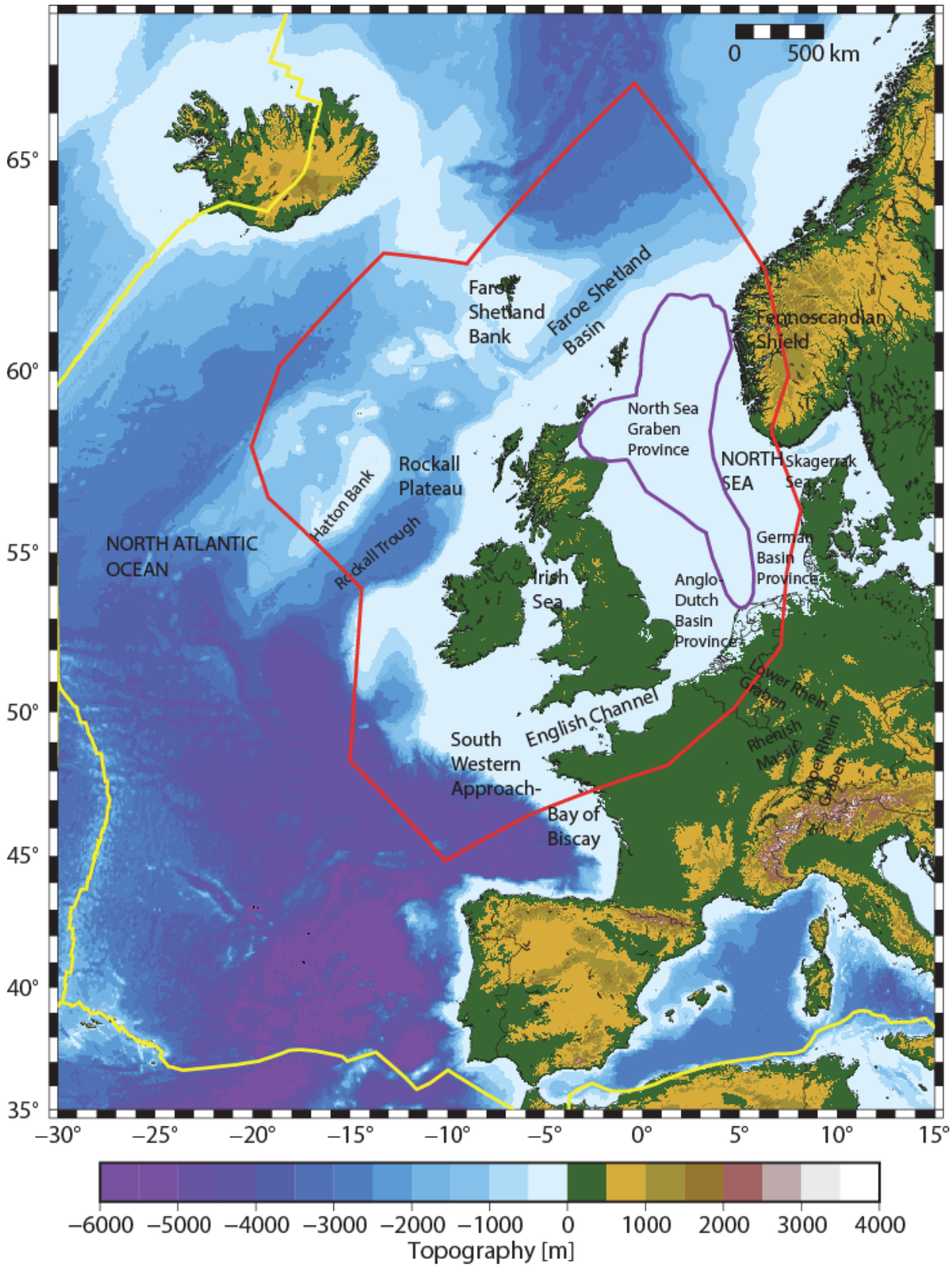

Figure 13: Topographic map of Europe where yellow lines represent the modern plate boundaries (from Bird, 2003) and the red polygon indicates the region being considered in this study. The purple polygon describes the North Sea Graben Province. Topography is from the global model ETOPO1 (Amante and Eakins, 2009).

4.1 TECTONICS OF THE NORTH SEA

The North Sea, which is located in the maritime waters of the United Kingdom, Norway, Denmark, Germany, and the Netherlands, is an intracontinental shallow-marine sedimentary basin with a present-day bathymetry of less than 150 m (Patruno et al., 2022). It is part of the

North Sea Rift System (NSRS), a typical “passive” rift that represents a failed arm of the Arctic-North Atlantic rift system (Figure 13). The NSRS evolved in response to the build-up of regional extensional stress fields during the Triassic-mid-Jurassic break-up of Pangea and the Late Jurassic-Paleogene disintegration of Laurasia (Ziegler, 1992).

Overall, the North Sea region is dominated by grabens and half-grabens: the north-west south-east oriented Lower Rhine Graben under the southern North Sea and the Netherlands, the north–south-oriented North Sea Central Graben that begins north of the Dutch coast and ends in the region east of Scotland, the Viking Graben along the south-east Norwegian coast, the Horn Graben east of the Central Graben and in front of the Danish coast (Figure 14). Generally, the North Sea is characterised by abundant normal faulting in Permian to late Cretaceous times, followed by deposition of late-Cretaceous to Cenozoic sediments with few active faults.

Below we describe the main tectonic structures in the Northern, Central, and Southern North Sea.

4.1.1 Northern North Sea

The northern North Sea includes the North Sea Graben Province of the NSRS, which is a ~150–200 km wide zone of extended crust that separates the East Shetland Platform in the west from the Horda Platform in the east. It is a trilete rift system, which consists of the Moray Firth Basin, the Viking Graben and the Central Graben (Figure 14; Andrews et al., 1990). These structures are characterised by large rotated fault blocks with sedimentary basins in asymmetric half-grabens associated with the extension and thinning of the crust (Fjeldskaar et al, 2004). The Caledonian basement consists of intrusive igneous rocks and low- to high-grade metamorphic rocks, including metasedimentary sequences (Gautier, 2005).

The Moray Firth Basin runs approximately east-west between the northeastern coast of Scotland and the middle of the North Sea. It is separated from the Viking Graben and the Central Graben by the Witch Ground Graben, a NW-SE trending extensional basin (Figure 14). The NE-trending tectonic patterns of the Precambrian basement provided some control over the subsequent development of sedimentary basins (Andrews et al., 1990). The Moray Firth Basin formed during phases of crustal extension in the Late Triassic – Early Cretaceous (213 – 144 Ma). Andrews et al. (1990) subdivide the Moray Firth into its inner and outer basins. The Inner Moray Firth Basin (IMFB) is ~500-1500 m shallower than the Viking and Central Grabens (Argent et al., 2002). This difference is due to a tilt of the whole western area of the North Sea (Underhill 1991; Underhill and Partington, 1993; Japsen, 1999; Argent et al., 2002). Andrews et al. (1990) show that during its formation, the direction of maximum extension in the IMFB was oriented perpendicular to the Great Glen Fault. In the Outer Moray Firth Basin, Andrews et al. (1990) show that faulting occurred without Caledonian control. The rift basin is controlled by major basin-bounding faults, including the Banff Fault to the south, the Helmsdale and Great Glen faults to the northwest and the Wick Fault to the north, that were formed during the late Jurassic (Underhill, 1991; Argent et al., 2002; Tamas et al., 2022). The present understanding of the structure and evolution of the Moray Firth Basin has been considerably advanced by the search for hydrocarbon reserves. The absolute age of faulting and fault reactivation is poorly constrained but the recent work of Tamas et al. (2022) shows that the latest phases of basin-wide fault movement are Early Jurassic–Late Cretaceous, followed by localised Cenozoic reactivation.

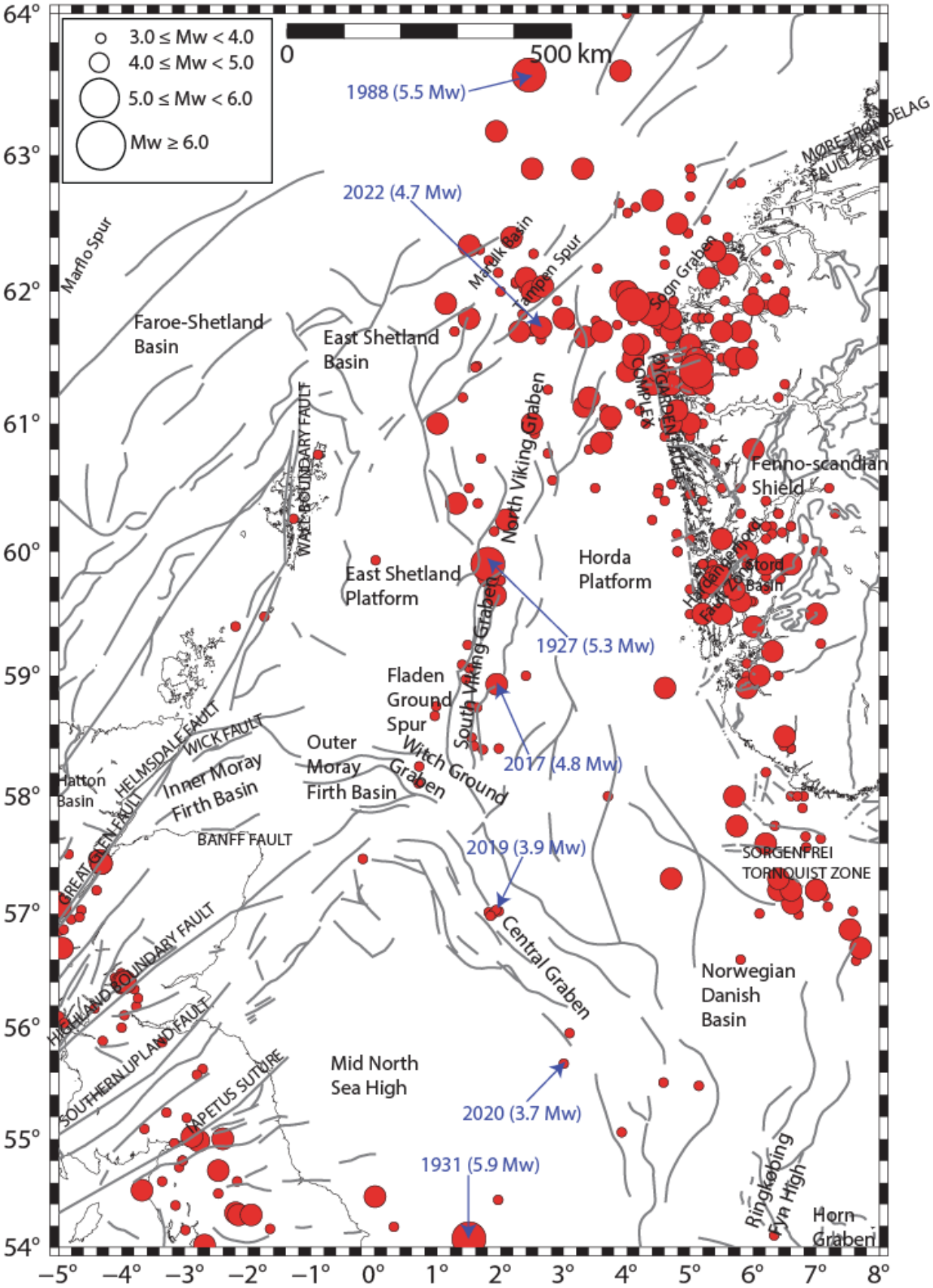

Figure 14: Seismo-tectonic map of the North Sea Region. The faults are from Asch (2003). Red circles show earthquakes and are scaled by magnitude. The earthquake catalogue comes from several sources described in Section 3.

The Viking Graben is a 500-km long, NNE –SSW trending rift system situated in the northernmost part of the NSRS between the East Shetland Platform, the Fladen Ground Spur, the Horda Platform, Fenno-Scandian Shield, and the Norwegian Caledonides (Figure 14). It

terminates to the south at the junction with the Central Graben and the Moray Firth/Witch Ground Graben structures. It is understood to have developed during two phases of extension: the first in the late Permian (*c.* 248 Ma) and the second in the late Jurassic (*c.* 144 Ma; e.g., Christiansson et al., 2000, Odinson et al., 2000). Seismic reflection profiling indicates that the structure is a composite of large rotated fault blocks and basins within asymmetric half-grabens that contain thick sedimentary deposits (Christiansson et al., 2000). The Viking Graben is separated from the Faroe-Shetland Basin below the Atlantic by the Shetland Platform and these two structures join in the area north-east of the Shetland Islands.

The East Shetland Platform is a vast region (c. 62,000 km^2) structural high forming the footwall of the fault-controlled Viking Graben, East Shetland Basin, the Inner and Outer Moray Basins and the Witch Ground Graben (Figure 14). It formed a regional high throughout the Mesozoic and Tertiary with only a thin Triassic to recent succession preserved (Platt and Cartwright, 1998). Limited seismic coverage across the platform and poor seismic imaging beneath the base Mesozoic resulted in a reliance on regional structural studies and gravity data (e.g. Holloway et al. 1991) in understanding the platform structure. The Fladen Ground Spur is the East Shetland Platform's southern extension and occurs west of the Viking Graben.

The East Shetland Basin is located in the northern North Sea, offshore western Norway, on the western margin of the North Viking Graben (Figure 14) and encompasses an area approximately 180 km long and up to 90 km wide. The present geometry of the basin is characterised by large (>25-km length), N-S to NE-SW striking, east-dipping normal fault systems that bound 15- to 25-km-wide half-grabens that developed during protracted, pre-Triassic-to-Late Jurassic rifting (~150 Myr) (e.g., Claringbould et al., 2017; Ravnås et al., 2000).

The Horda Platform comprises a thick sequence of Triassic–Jurassic sediments in a series of large, rotated fault blocks (Platt, 1992), east of the Viking Graben. The rotation of these fault blocks was associated with extensional movement on deep westward-dipping detachment surfaces beneath the Horda Platform. Most movement of the faults in the Horda Platform is thought to be of the Triassic age, although additional fault block rotation occurred during the late Jurassic (Platt, 1992). The Horda Platform is bounded to the east by the Øygarden Fault Complex (Figure 14). This basement-involved structural element marks a major change in crustal thickness in the easternmost part of the northern North Sea. The fault complex strikes approximately north-south, extends well over 100 km and exhibits lateral (along-strike) structural variations from the Horda Platform in the north to the Stord Basin in the south. It marked the eastern extent of major activity in the North Sea during the Permo-Triassic and Jurassic-Cretaceous rift events (Færseth et al., 1995).

The Tampen Spur area is situated in the northern part of the North Sea and is bounded by the Viking Graben to the southeast, the East Shetland Basin to the west, and the Marulk Basin to the northwest (Figure 14). The region comprises major fault blocks tilted in the west direction, the largest being the Snorre fault block, which includes several oil discoveries, e.g., the Snorre, Tordis, and Vigdis fields (Dahl and Sollie, 1993; Jerkins et al, 2023).

4.1.2 Central North Sea

The central North Sea comprised the Central Graben, the Norwegian-Danish Basin, the Mid North Sea High, the Ringkøbing Fyn High, and the Horn Graben.

The Central Graben is a NW–SE–trending fault-bounded trough that runs between 52°N and 58°N (Figure 14). Its formation started during a major rifting period in the late Triassic and continued with crustal extension during the Jurassic (Pekot and Gersib, 1987; Ottemöller et al., 2005). The Central Graben underwent rapid subsidence in the Quaternary mostly due to rapid sedimentary loading. The conclusion of the study on the Earthquake Loading on the Norwegian Continental Shelf by NGI et al. (1988) was that during this period, no other tectonic processes were occurring. Recent (Miocene to present) subsidence can also be attributed to thermal and isostatic crustal adjustment

The Cenozoic Norwegian–Danish Basin is situated east of the Central Graben and south of the Fennoscandian Shield (Figure 14). The basin partly overlies the basement blocks and Palaeozoic half-grabens of the Ringkøbing-Fyn High (e.g. Cartwright 1990; Andresen, 2020). Generally, the Cenozoic evolution of the eastern North Sea was dominated by tectonic

quiescence with thermal subsidence following the Jurassic rifting, local inversion in the Central Graben and halokinesis of mobile Zechstein evaporites deposited in the Northern Permian Basin (e.g., Zanella and Coward 2003; Clausen et al., 2012; Andresen, 2020). This basin includes the Sorgenfrei–Tornquist Zone, which strikes through northern Denmark from the Skagerrak Sea to Bornholm in the SE and is the northwesternmost segment of the Tornquist Zone. This is a fault zone extending from the Black Sea to Skagerrak, which has been active at least since the Late Carboniferous (e.g., Ziegler 1990; Sørensen et al., 2011).

The Horn Graben is a NNE–SSW-trending Late Carboniferous– Late Triassic extensional system formed at the suture between the Avalonia and Baltica tectonic plates, cutting perpendicular to the NNW–SSE-trending Ringkøbing and Schill Grund highs in the present-day offshore areas of Germany and Denmark (Best et al., 1983; Clausen and Korstgård, 1994; Thybo, 1997; Abramovitz and Thybo, 1999; Guterch et al., 2010; Kilhams et al., 2010).

The Mid North Sea High is an E-W trending broad Palaeozoic ridge between the Northumberland coast to the west and the Central Graben to the east (Figure 15). The ridge separates the Forth Approaches Basin to the north from the Southern North Sea Basin to the south. This structure has Devonian and Carboniferous basins at depth, which were controlled by granite-cored blocks (Brackenridge et al., 2020). The structure had a significant control on sedimentation and facies of the region through most of the Mesozoic with significant unconformities during the Permian and Jurassic before regional tilting, subsidence and increased sedimentation during the Cenozoic (Brackenridge et al., 2020).

4.1.3 Southern North Sea

The southern North Sea includes the region from the east coast of England to the Netherlands, Belgium and France and extends from the Dogger Bank in the north to the Dover Strait in the south (Cameron et al., 1992). It comprises Permian-Mesozoic Anglo-Dutch Basins, such as the Sole Pit Basin (or Trough) and Broad Fourteens Basin (Figure 15).

The NW-SE-oriented 150 km-long and 50-km wide Sole Pit Basin, which is located in the western half of the Southern North Sea Basin, is characterised by NW-SE trending, en echelon, inverted basins (Van Hoorn, 1987). It was the principal depocentres during the Jurassic, accumulating up to 1000 m of marine mudstones with subsidiary sandstones and limestones before undergoing erosion at the end of the Jurassic Period, followed by post-Jurassic inversion (Glennie and Boegner, 1981; Van Hoorn, 1987; Cameron et al., 1992). The Sole Pit Basin comprises a complex network of transpressional and transtensional faults at Permian Rotliegend levels, which are thought to represent the upward termination of a series of wrench-induced flower structures with a right-lateral sense of displacement (Van Hoorn, 1987). The NW-SE-striking Dowsing Fault Zone and Swarte Bank Hinge Zone form complementary areas of structural complexity on the southwestern and north-eastern margins of the Sole Pit Basin (Cameron et al., 1992). The Dowsing Fault Zone has been shown to have a complex history of reactivation through the Permian and Mesozoic and probably acted as a syndepositional fault in Carboniferous time (Leeder and Hardman, 1990). Since this fault separates crust of distinctly different seismic reflectivity (Blundell et al., 1991; Klemperer and Hobbs, 1992), it may also represent a major crustal or terrane boundary (Pharaoh et al., 1995). The Vale of Pickering-Flamborough Head Fault Zone was originally thought to be the onshore continuation of the Dowsing-Hewett Fault Zone (Kent, 1974, 1980). However, offshore seismic reflection data suggest these are separate structures, which meet at an acute angle.

The narrow NW –SE trending Broad Fourteens Basin in the southern Dutch North Sea developed in response to multiple Late Palaeozoic and Early Mesozoic rifting events (Ziegler, 1990; De Lugt et al., 2003). This structure is a NW-SE trending Mesozoic basin, approximately 120 km long and 45 km wide. The basin is now inverted and covered unconformably by the Cenozoic sedimentary fill of the Southern North Sea Basin. It rests on the Southern Permian Basin, which in turn unconformably overlies an even older sedimentary basin, the Variscan foreland basin (Verweij and Simmelink, 2002).

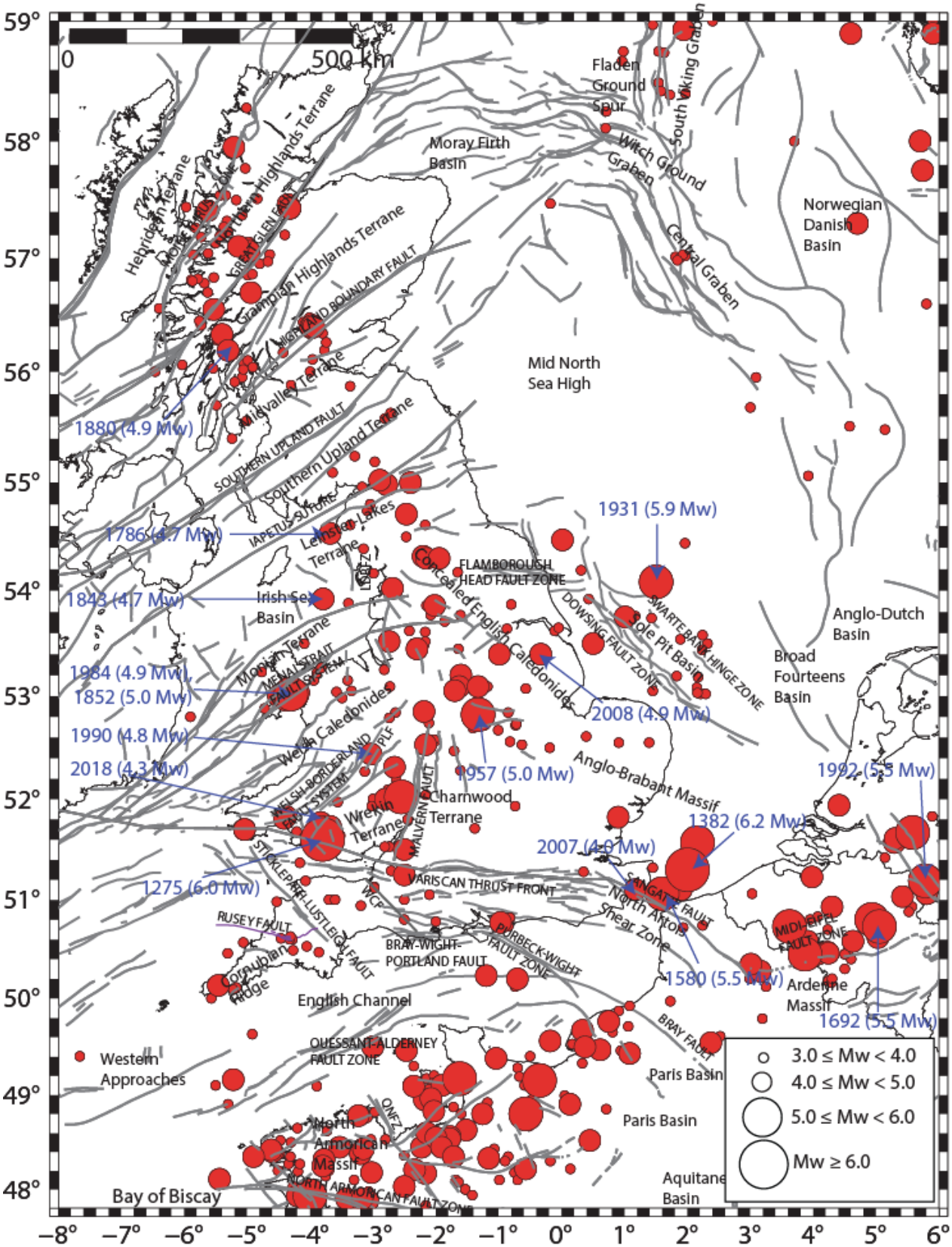

Figure 15: Seismo-tectonic map of the British Isles and the surrounding region. The faults are from Asch (2003). Red circles show earthquakes and are scaled by magnitude. The earthquake catalogue comes from several sources described in Section 3. LDBFZ, Lake District Boundary Fault Zone; PLF, Pontesford-Linley Fault; QNFZ, Quesssoy/Nort-sur-Erdre Fault Zone; WCF, Watchet-Cothelstone Fault.

4.2 TECTONICS OF THE NORTHEAST ATLANTIC

The northeast Atlantic region, which is situated north of Scotland and in the northwest part of the study area, includes the Faroe–Shetland, East Shetland, North Minch Basins, the Rockall Trough, the Faroe-Shetland Trough, and the Faroe-Rockall, Outer Hebrides, and Orkney-Shetland Platforms (Figure 13; Stoker et al., 1993). This region is located in the North Atlantic Ocean on the outer part of the NW European continental margin situated approximately in the central part of the North Atlantic Igneous Province between Iceland and the British Isles (Ólavdóttir et al., 2017).

The 400-km-long and 250-km-wide NE-trending Mesozoic rifting Faroe–Shetland Basin lies between the Faroe Islands and the Shetland Islands (Figure 13) and consists of a complex amalgam of sub-basins generally separated by north- to NE-trending structural highs. The geometry is less clear on the northwestern side of the basin due to the presence of thick Late Paleocene flood basalts (Ritchie et al, 2011).

Rockall Plateau is situated in the NE Atlantic Ocean between 450 and 1000 km west of the Scottish mainland and is separated from the British and Irish continental shelf by the Rockall Trough and the Faroe-Shetland Trough. It comprises the bathymetric features of Rockall Bank, Hatton Bank and the intervening Hatton Basin (Figure 13; Naylor et al., 1999; Hitchen, 2004). Rockall Plateau is underpinned by continental crust, which is thicker beneath the banks and thinner under Hatton Basin. The continent-ocean crustal transition occurs beneath the western flank of Hatton Bank where it is associated with seaward-dipping reflectors resulting from large-scale outpourings of basaltic lava.

4.3 TECTONICS OF THE BRITISH ISLES

A detailed description of the tectonics of the British Isles is given in Chadwick et al. (1996) who subdivide this region into a number of geological provinces or terranes, based upon the crustal, geological and tectonic structures, as well as the geological history of these provinces.

4.3.1 Northern Britain

The region north of the Iapetus Suture (Figure 15) comprises various terranes associated with the margin of Laurentia (Bluck et al., 1992; Woodcock and Strachan, 2012), with crustal formation ages ranging from Archaean (Hebridean and Northern Highlands Terranes) to Palaeoproterozoic (Grampian Terranes), Mesoproterozoic (Midland Valley Terrane) and Ordovician (Southern Uplands Terrane).

The Hebridean Terrane represents the Laurentian foreland of the Caledonian orogen and is bounded by the Outer Hebrides Fault to the northwest and the Moine Thrust Zone to the southeast. The ESE-dipping Outer Hebrides Fault has a long history of reactivation including likely Neoproterozoic and Caledonian thrusting, late Caledonian sinistral strike-slip and later Palaeozoic to Mesozoic normal faulting (Stein, 1988; Imber et al., 2001). It is well-imaged on deep seismic reflection data (e.g. Smythe et al., 1982) and is known to offset the Moho. The ESE-dipping, low-angle Moine Thrust Zone extends for over 200 km from Durness on the north coast to Sleat in Skye. It likely accommodates several hundred kilometres of top-to-the-WNW displacement that occurred during the Silurian Scandian phase of Caledonian shortening (Trewin and Rollin, 2002).

The Northern Highland Terrane is bounded by the Moine Thrust Zone in the northwest and the Great Glen Fault to the southeast. The steeply-dipping strike-slip Great Glen Fault is a regional-scale reactivated fault that cuts across the Ordovician-Silurian Caledonian orogenic belt (Stewart et al., 2001). It has a NE–SW strike and extends to at least 40 km depth suggesting that the structure has some expression in the upper mantle (Hall et al., 1984). The Great Glen Fault extends north-north-eastwards from the north-western coastal region of Ireland, across the Scottish mainland towards the Shetland Islands in the north-east, where it may be kinematically linked with the Walls Boundary Fault, at least since the Silurian.

The Grampian Highlands Terrane is limited by the Great Glen Fault to the northwest and the Highland Boundary Fault to the southeast. The Highland Boundary Fault follows the Caledonian structural trend (NE–SW) and marks the southern boundary of the Laurentian crust. It extends

from Stonehaven on the east coast of Scotland to the Isle of Arran in the west and continues southeast of the Kintyre Peninsula via Fair Head in Northern Ireland to Clew Bay in the Republic of Ireland (Ottemöller and Thomas, 2007). During the formation of the British Isles, this structure behaved as a strike-slip feature associated with a collisional suture (Woodcock and Strachan, 2012; Musson and Sargeant, 2007). Interpretation of deep seismic reflection data suggests that the Highland Boundary Fault dips to the northwest.

The northwest and southeast boundaries of the Midland Valley Terrane are the Highland Boundary Fault and the Southern Upland Fault, respectively, both of which are likely to have experienced Caledonian sinistral strike-slip displacements. The sub-surface geometry of the Southern Upland Fault is steeply inclined to sub-vertical but remains uncertain at depth (e.g. Stone et al., 2012). During the Carboniferous, the Midland Valley was affected by the intense, intra-plate volcanism, associated with the Variscan orogeny in the south of England.

The southernmost terrane in Northern Britain is the Southern Upland Terrane, which is bounded by the Southern Upland Fault to the northwest and by traces of the Iapetus Suture to the southeast. This terrane is viewed as an accretionary wedge, formed during the closure of the Iapetus Ocean. The Iapetus Suture Zone extends into northern Wales and the West Midlands and separates the Caledonian rocks of the Laurentian and Avalonian continents. The Iapetus Suture is not strongly expressed at the surface but it can be recognised in the fossil record and has been imaged on deep profile surveys (Beamish and Smythe, 1986).

4.3.2 Central Britain

Central Britain, south of the Iapetus Suture and north of the Variscan Front (Figure 15) comprises Neoproterozoic and Ordovician crustal terranes accreted to the margin of Gondwana and Avalonia during late Precambrian and Ordovician orogenic episodes and juxtaposed with the Laurentian terranes following the closure of the Iapetus Ocean in Silurian time. The same Caledonian structural trend is also clear throughout the Iapetus Suture Zone, extending into northern Wales and the West Midlands.

The Leinster-Lakes Terrane (or Lake District-Manx Terrane) is bounded by the Iapetus Suture to the north and the Ballycogly Mylonite Zone to the south. This terrane is situated in the northern passive margin of the Avalonia Microcontinent in Cambrian time, bordering on the opening Iapetus Ocean. The latter began to close in early Ordovician time and the margin turned into a destructive one, with the development of a volcanic arc associated with the southward subduction of the Iapetus oceanic lithosphere (Chadwick et al., 1996).

The Monian Terrane in North Wales is separated from the Welsh Caledonides by the Llyn-Menai Strait Shear Zone to the southeast, and from the Lake District-Manx Terrane by the Ballycogly Mylonite Zone to the northeast. It comprises gneisses, intrusions and a younger metasedimentary sequence of the latest Precambrian or early Cambrian age (Chadwick et al., 1996). The Llyn-Menai Strait Shear Zone is interpreted as a major terrane boundary and is dominated by a largely subparallel plexus of north-east to south-west faults, which juxtapose Precambrian and early Palaeozoic rocks as well as late Palaeozoic strata (Howells, 2007).

Eastern England from Pennines to the Thames Estuary comprises the Concealed English Caledonides whose sub-Carboniferous basement is composed of low-grade metasedimentary rocks of Ordovician and Silurian age (Molyneux, 1991) and plutonic and volcanic igneous rocks (Pharaoh et al., 1993). The structural grain of this region is NW-SE reflecting the late Ordovician collision of Avalonia with Baltica (Pharaoh, 2018).

Differently from the Eastern Concealed English Caledonides, the Welsh Caledonides is characterised by a strong NE-SW trending structural grain, resulting from Caledonian deformation of a thick succession of Lower Palaeozoic sediments infilling the Welsh Basin. The Welsh Borderland Fault System marks the southeastern limit of the Welsh Caledonides and separates it from the Wrekin Terrane, which is part of the Welsh Massif.

The Charnwood and Wrekin Terranes form the concealed Midland Microcraton, a wedge-shaped block of Proterozoic crust, and adjacent elements of the Caledonides in southern Britain, forming the core of the Anglo-Brabant Massif in England (Pharaoh, 2018), appear to have been little affected by either Caledonian or Variscan compression or Mesozoic extension.

Pharaoh (2019) suggests that the Malvern Lineament forms the boundary between the Charnwood and Wrekin Terranes.

The Anglo–Brabant Massif (or Platform) is a structural high stretching from the Rhineland in western Germany across northern Belgium (in the province of Brabant) and the North Sea to East Anglia and the middle Thames in southern England. During Devonian and Carboniferous times, the central part of the Larussia paleocontinent formed part of the Anglo-Brabant Massif (Ziegler, 1990) but it was significantly affected by extension at that time. The crust of the Anglo-Brabant Massif is thicker (perhaps up to 38 km) than that of the surrounding regions, typically about 30 km thick (Chadwick and Pharaoh, 1998; Ziegler and Dezes, 2006).

4.3.3 Southern Britain

The region south of the Variscan Front Thrust is part of the Variscan Orogenic Belt and extends from Cornwall to the Ardennes Massif. The south-dipping WNW-trending Variscan Front Thrust is a major structural feature forming the northern edge of the Variscan orogeny, active in Carboniferous to Permian times. This fault is visible on seismic reflections and refraction profiles from southern Ireland to northern France (Figure 15). Much of this front has been buried underneath younger Mesozoic strata, but shear and fault zones still occur at depth, and fault reactivation may have caused faulting in younger and shallower strata. The Variscan Orogenic Belt is cut by both E-W trending thrusts and NW-SE trending transcurrent faults (Stephan et al., 2016). Examples of these include the Watchet-Cothelstone Fault and the dextral strike-slip Sticklepath-Lustleigh Fault.

The Mesozoic-Cenozoic English Channel basin is a ~600 by 200 km ENE-WSW trending basin that lies entirely within the continental crust. The Central English Channel Basin is bounded by the Purbeck-Wight Fault Zone to the north, and the E-W Mid-Channel (or Central Channel) Fault to the south (e.g., Westhead et al., 2018; Figure 15). The Ouessant-Alderney Fault Zone marks the structural boundary between the Palaeozoic Cornubian Ridge on the northern side of the English Channel and the Precambrian Armorican Massif on the southern side of the Channel (Figure 15).

4.3.4 Irish Sea and Ireland

The Irish Sea is surrounded by Ireland, southern Scotland, north-west England and North Wales. The sea has restricted outlets to the Atlantic Ocean through the North Channel to the north, and via the St George's Channel to the south (Jackson et al., 1995). Large sections of the Irish Sea coastline lie close to and run subparallel to, important basin-margin faults or other structural lines. A number of Permo-Triassic and younger basins are located in the East Irish Sea, the largest of which is the East Irish Sea Basin (Figure 15). This basin has been the subject of extensive hydrocarbon exploration and hosts several large hydrocarbon accumulations. It is bounded along its eastern margin by the Lake District Boundary Fault Zone, a network of normal faults, which separates Lower Palaeozoic rocks of the Lake District Block to the east from the younger, Upper Palaeozoic and Mesozoic rocks of the East Irish Sea Basin (Jackson et al., 1995). The East Irish Sea Basin is characterized by a number of half grabens controlled by N-S faults to the south, and by intersecting NE-SW and NW-SE faults to the north.

Ireland and neighbouring Britain share the same tectonic history and the terrane boundaries (e.g. Highland Boundary Fault and Iapetus Suture) described in previous subsections (Figure 15; Lebedev et al., 2023). For example, the Iapetus Suture extends from northeast Highlands into Britain and then across the Irish Midlands to the Shannon Estuary in the west.

4.4 TECTONICS OF THE OVERSEAS REGIONS

The overseas regions include Northern France, Belgium, the Netherlands, and the Western Approaches.

The Brabant Massif, part of the Anglo-Brabant Massif, is a region of shallow basement rocks beneath the central and northern part of Belgium. Outcrops of the Brabant Massif are sparse and are only present in some incised river valleys along the southern rim of the Brabant Massif. The Brabant Massif dips towards the north and is mostly covered by Cretaceous chalk,

Cenozoic sand and clays, and Quaternary loess sediments (Van Noten et al., 2015). The basement of the Ardenne contains Paleozoic sedimentary rocks which were deformed in the Caledonian (only for Cambrian to Silurian) and Variscan orogenies (e.g. Fielitz and Mansy, 1999; Barbarand et al., 2018). This basement belongs to the main Rhenish Massif, which is well-exposed in Germany.

The North Artois Shear Zone, which runs through the Dover Strait from Sangatte in northeast France to Folkestone in southeast England, divides the Paris Basin and Ardenne Massif from the Brabant Massif to the north (Garcia-Moreno et al., 2015; Figure 15). This complex fault-and-fold system defines the eastern part of the Variscan Front Thrust and the Midi–Eifel fault zone. The present-day geometry of this fault zone results from several phases of post-Palaeozoic deformation that have induced different reactivations of structures inherited from the Variscan Orogeny (e.g. Chadwick et al. 1993; Van Vliet-Lanoë et al. 2002; Mansy et al. 2003; Garcia-Moreno et al., 2015). Quaternary activity of the North Artois shear zone is widely debated but no conclusive field evidence of recent tectonic deformation has been associated with any of its fault segments. However, Van Vliet-Lanoë et al. (2000) identify possible extensional faults in the Sangatte cliff, and Colbeaux et al. (1981), Van Vliet-Lanoë et al. (2000), Mansy et al. (2003) show minor right-lateral deformations affecting river development and Quaternary fluvial and aeolian deposits in northeastern France.

The southeastern edge of the study area of this work at the border between the Netherlands, Germany, and Belgium, comprises the Lower Rhine Graben or Roer Valley Rift System, which is the northwestern branch of the Rhine Rift System, part of the European Cenozoic rift system extending from west of the Alps to the North Sea (Figure 13; Ziegler, 1994; Ziegler and Dèzes, 2005; Vanneste et al., 2013). The Lower Rhine Graben is a NW-oriented relay between the N-NE-oriented Upper Rhine Graben and the Anglo-Dutch Basin in the North Sea (van den Berg, 1994). It extends over a distance of ~200 km between the city of Bonn in the southeast and the confluence area of the Rhine and Meuse Rivers in the northwest and consists of a series of grabens and horsts that are separated by NW-SE trending normal faults. The deformation in the Rhine Rift System is the result of the (still ongoing) continent-continent collision from the mid-Cretaceous onset of Alpine orogeny onwards (Sissingh, 2006; Schmid and Kissling, 2000; Grünthal et al. 2017). In the Lower Rhine Graben, the rifting started only in the late Oligocene (Demyttenaere and Laga, 1988; Geluk et al., 1994). This tectonic structure is a reactivated structure that developed over older sedimentary basins of the Carboniferous and Mesozoic age and has gone through a complex evolution involving several phases of extension and inversion (Geluk et al., 1994; Vanneste et al., 2013).

Northwest France is dominated by the Proterozoic Armorican Massif (Perrot et al., 2005), which is bounded by the English Channel Basin to the north, the Paris Basin to the east, and the Aquitaine Basin to the south. The massif is cut in three by the SE-NW striking North and South Armorican Shear Zones (Baize et al., 2012). The Mesozoic-Cenozoic sedimentary Paris Basin lies immediately east of the Armorican Massif and covers much of northern France. A segment of the Bray Fault in Northern France divides the Paris Basin into western and eastern parts. However, the seismogenic potential of this fault has not been demonstrated yet (Wyns, 1977; Larue, 2005; Baize et al., 2012).

The Western Approaches region is a complex, 400 km-long, partly inverted Mesozoic rift in the Western European continental shelf situated at the transition between the Western English Channel and the northern termination of the Bay of Biscay (Figure 13; Ziegler, 1987). It is surrounded by the offshore extension of the Cornubian Ridge to the north and the Armorican Massif to the south. The major element of the Western Approaches is the Western Approaches Basin, containing mainly Permo-Triassic sediments and the Southwest Channel Basin and Brittany Trough, both of which contain thick Jurassic and Early Cretaceous series (Ziegler, 1987; Le Roy et al., 2011).

4.5 SEISMICITY

Seismicity in the study area is concentrated in a north-south band along the length of Britain, mainly along the western flank, Northern France and Belgium, the northern part of the Viking Graben, and along the Norwegian coast. The seismicity levels are higher in the Northern North

Sea and the Norwegian coast than in the British Isles. The northeast of Britain, the northwest Atlantic margin, Ireland, the western North Sea, and the southern North Sea down to the Netherlands all show very little seismicity (Figures 14-15). However, historical accounts of earthquake activity offshore will be limited because of the distance from populated places onshore. The geographical distribution of instrumentally recorded earthquakes from 1970 to the present generally follows the distribution of historical seismicity over the last 300 years but with a generally smaller magnitude. There are a few exceptions to the correlation between instrumental and historical seismicity, such as the historical earthquakes in the Dover Straits, SW Wales and around Inverness in NE Scotland where there has been relatively little instrumentally recorded seismicity. This highlights the fact that instrumentally recorded seismicity is not a reliable indicator of earthquake activity either in the past or in the future.

In common with many regions of diffuse intraplate seismicity, it is difficult to unequivocally associate earthquakes in the entire study area with specific faults for the following reasons. Firstly, no earthquake recorded either historically or instrumentally has produced a surface rupture. Secondly, uncertainties in the epicentral location and depth of the earthquakes are typically several kilometres.

The largest earthquakes in the study area are the ~6.0 Mw 1275 and ~6.2 Mw 1382 events in South Wales and the Dover Strait (Figure 15), respectively, but their magnitude and location estimates are associated with large uncertainties. The largest instrumentally recorded earthquake in the UK catalogue occurred on 7 June 1931 (5.9 Mw) in the Dogger Bank area of the North Sea (Neilson et al., 1984). The epicentre of this event is between 20 and 40 km from the Endurance CCS area.

The hypocentral depth of earthquakes in the study area is often not well-constrained due to the lack of stations close to the epicentre or for historical events it may be completely unknown. Many agencies typically assign a generic value to events with poorly constrained or unknown hypocentral depths. For example, a depth of 10 km is used to indicate that the hypocentre is shallow, while a depth of 33 km is used to indicate that the hypocentre is at the base of a continental seismogenic zone. As a result of this, the uncertainties in the focal depths for instrumentally recorded earthquakes onshore can exceed ±10 km when considering the average spacing between seismic stations in the study area and they are higher in offshore regions, whereas the uncertainties in the depths of historical earthquakes are unknown. The analysis of the depth of earthquakes in the project catalogue shows that the hypocentral depths of the onshore earthquakes within the study area are distributed throughout the upper 35 km of the crust with peaks around 10-12 km for the earthquakes in the British Isles (Figure 16a), Northern France and Belgium (Figure 16b), and the Continental Shelf (Figure 16c). The distribution of hypocentral depths in the offshore regions agrees with the findings of Lindholm et al. (2000) who indicate a focal depth distribution between 5 and 30 km for earthquakes in the northern North Sea region. Earthquakes in Norway are slightly deeper with a modal depth of around 18-20 km (Figure 16d).

In the following sections, we discuss specific regions in more detail with respect to their seismicity.

4.5.1 North Sea

The distribution of seismicity in the central and northern North Sea delineates the trend of the grabens (Figure 14). This is more apparent for the Viking Graben where larger earthquakes have occurred and seismicity rates are higher.

The northern part of the Viking Graben is the most seismically active area in Northern Europe (e.g., Musson, 2007). The largest earthquake for which a magnitude can be estimated reliably is the 5.3 Mw earthquake in 1927 (Figure 14; Bungum et al., 1991). It was felt over most of Scotland and down the east coast of England as far as Norfolk and in western Norway but it caused no damage to buildings (Musson et al., 1986). Earthquakes of magnitude more than 5.0 Mw have occurred in the Northern North Sea and offshore the western coast of Norway in the last 100 years. The largest of these included in our study area is the 5.5 Mw 1988 event (Hansen et al., 1989). Recently, the 4.7 Mw earthquake on 21 March 2022 occurred close to the Snorre oil field in the northern part of the Viking Graben. It was the largest earthquake in the

North Sea in the last 33 years and was felt in Norway, the Shetland Islands and northeast Scotland (Jerkins et al, 2023). This event resulted in a temporary shutdown of the Snorre B oil platform, although no injuries and damage were reported associated with the earthquake. Note that the NNSN database (i.e. Norwegian National Seismic Network) reports a magnitude of 4.7 Mw, whereas the size of this event has been estimated to be 5.1 Mw and 4.9 Mw (5.2 ML) by Jerkins et al. (2023) and the BGS database, respectively.

The Central Graben is much less seismically active than the Viking Graben and it was not clear that it was seismically active at all until monitoring networks improved sufficiently to be able to locate events in this area after 1970. Woo and Muir Wood (1986) describe most of the central North Sea as an aseismic zone but Marrow (1992) was able to show that this is not the case. Recently, two events of magnitude of 3.9 and 3.7 Mw occurred in 2019 and 2020 in the Central North Sea. The 3.9 Mw event occurred in the Shearwater Field approximately 250 km east of Aberdeen and was felt on oil platforms in the nearby Elgin-Franklin fields (Baptie, 2020). It was the largest earthquake in the Central North Sea since a 4.8 Mw event occurred at the southern part of the Viking Graben on 30 June 2017.

Besides the 1931 earthquake in the Dogger Bank, the seismic activity in the southern North Sea is low.

4.5.2 British Isles

Seismicity in and around Scotland is strongly localised to an area bounded approximately by Dunoon and Ullapool (south to north) and Mull to Perth (west to east). There is almost no recorded seismicity anywhere west, north or east of this area until the Viking and Central Grabens to the east. The seismic activity here appears to be associated with steeply dipping fault systems that strike approximately NE-SW or NW-SE (e.g. the Highland Boundary Fault Zone and the Great Glen Fault Zone). These are therefore favourably oriented with respect to the expected stress regime, as confirmed by the focal mechanisms of earthquakes that occurred in Scotland (Baptie, 2010). The largest known Scottish earthquake is the 4.9 Mw Argyll earthquake in 1880 (Figure 15) that was felt along the west coast of Scotland, east as far as Perthshire and throughout the Hebrides.

In Northern Britain, strong earthquake activity is localised along the Pennines, from the Peak District to the Scottish Borders, and in the Lake District. The HyNet site is also relatively close to two earthquakes that occurred in the Irish Sea. The first of these events is the largest earthquake in the Lake District and occurred on 11 August 1786 (4.7 Mw), just off the Cumberland coast near Whitehaven (Musson, 1994). The proximity of the epicentre to the Lake District Boundary Fault has led to the suggestion that the earthquake was caused by movement on this fault (Musson, 1994). However, the large uncertainty in the epicentre and the lack of any information on the mechanism of this event, means that this is highly uncertain (Musson, 1994). The second event is the 4.7 Mw earthquake in 1843 offshore to the west of Barrow-in-Furness (Lancashire). It was felt throughout most of North England, South Scotland, North Wales, along the east coast of Ireland, and on board ships in the Irish Sea but the only damage reported was in the Isle of Man (Musson, 1994).

North Wales is one of the most seismically active areas of mainland Britain, with a relatively high number of earthquakes of Mw ≥ 4.0 having been observed compared to other parts of the UK. Most of these occurred on the Lleyn (or Llŷn) Peninsula, at the northwest edge of Snowdonia, e.g. 1534 (4.2 Mw), 1690 (4.9 Mw), 1852 (5 Mw), 1903 (4.6 Mw) and 1940 (4.4 Mw). The largest (4.9 Mw) onshore earthquake in the UK since 1970 occurred on 19 July 1984 near Yr Eifl on the Lleyn Peninsula in northwest Wales. This area is relatively close to the HyNet CCS site. In particular, the epicentre of the 1984 Lleyn earthquake is 94 km from the HyNet area. South Wales has experienced a number of moderate-magnitude, damaging earthquakes in the last 300 years. Besides the 1275 earthquake of ~6.0 Mw, other examples of large earthquakes in this region occurred in 1727 (4.9 Mw), 1775 (4.8 Mw) and 1906 (4.9 Mw; Musson, 2007). More recently, the 4.3 Mw event occurred close to Swansea on 17 February 2018. Considerable seismicity also appears to be associated with faults within the Welsh Borderland Fault System. For example, the 4.8 Mw Bishop's Castle earthquake on 2 April 1990 is believed to be associated with the Church Stretton Fault (Ritchie et al., 1990), although

uncertainties in both estimated depth and fault geometry make it difficult to assess if the hypocentre lies in the hanging wall or footwall of this fault.

The Midland Microcraton is characterised by relatively low seismicity in the Anglo-Brabant Massif (to the east of the Malvern Fault) and higher levels of seismicity in the Wrekin Terrane to the west of this structure. The largest earthquake in the Anglo-Brabant Massif occurred on 11 February 1957 approximately 10 km southeast of Derby (5.0 Mw). Much of eastern England (south of the Scottish Borders) is characterised by relatively low levels of seismicity. However, here the largest (4.9 Mw) earthquake in the UK since the 1984 Lleyn earthquake occurred on 27 February 2008. Its epicentre was located 4 km north of the town of Market Rasen in Lincolnshire (Ottemöller and Sargeant, 2010; Mosca et al., 2020).

The British region south of the Variscan Front Thrust is characterised by relatively low seismicity with few earthquakes greater than 4.0 Mw. There are considerable variations in seismicity along the Variscal Front Thrust. Significant historical seismicity has occurred close to the Variscan Front Thrust in both south Wales and the Dover Strait, whereas in southern Ireland and central southern England, there is very little recorded activity. Chadwick et al (1996) suggest that areas of seismicity may correspond to intersections between the Variscal Front Thrust and northwest-trending near-vertical transcurrent faults. Seismicity is higher in the southern English Channel, especially close to the Cotentin Peninsula and the Channel Islands, than in the northern English Channel, but it appears to be diffuse.

Ireland is characterised by very low levels of seismic activity in comparison to mainland Britain. Its seismicity is concentrated in Ireland's northernmost part and in the south coast and earthquakes are very rare in onshore Ireland. Lebedev et al. (2023) indicate that the difference in earthquake levels between Ireland and Britain mainland is controlled by the moderate variations in the lithospheric thickness.

4.5.3 Overseas Regions

Seismic activity is higher (up to 5.4 Mw) in the northwest Armorican Massif than in the northeast Armorican Massif, but is diffuse and shows no concentration or alignment along mapped faults. The Paris Basin is characterised by low seismic activity despite a similar basement with the Armorican Massif at depth (Ritz et al., 2021). The recorded (historical and instrumental) seismicity in the Western Approaches is very limited.

Notable historical earthquakes have occurred in the Dover Strait, with a 6.0 Mw earthquake in 1382 and a 5.5 Mw earthquake in 1580, but there is little instrumentally recorded seismicity in the last 50 years. Some authors (e.g., Camelbeeck et al. 2007) have suggested that the magnitude of the 1580 earthquake was as high as 6 Mw. Garcia-Moreno et al. (2015) suggest that the 1580 earthquake occurred on the Sangatte Fault and Camelbeeck et al. (2007) indicate that the 4.0 Mw Folkestone earthquake in 2007 may also have occurred on this fault.

In Belgium, the earthquake activity is moderately high with events up to magnitude 5.5 Mw. The 5.5 Mw 1692 Verviers earthquake occurred in the northern part of the Belgian Ardennes. It caused moderate to severe damages in the Brussels region, 100 km from the epicentre, and further up to the coastal region of Kent, UK, and was felt at least more than 550 km further in Oxford and Bath in the UK (Camelbeeck et al., 2000). Camelbeeck et al. (2000) report a magnitude between 6.0 and 6.5 for this event. The 5.5 Mw 1992 Roermond earthquake occurred in the Roer Valley Graben, which is part of the Lower Rhine Graben and was followed by more than 200 aftershocks (Camelbeeck et al., 1994; Braunmiller et al., 1994).

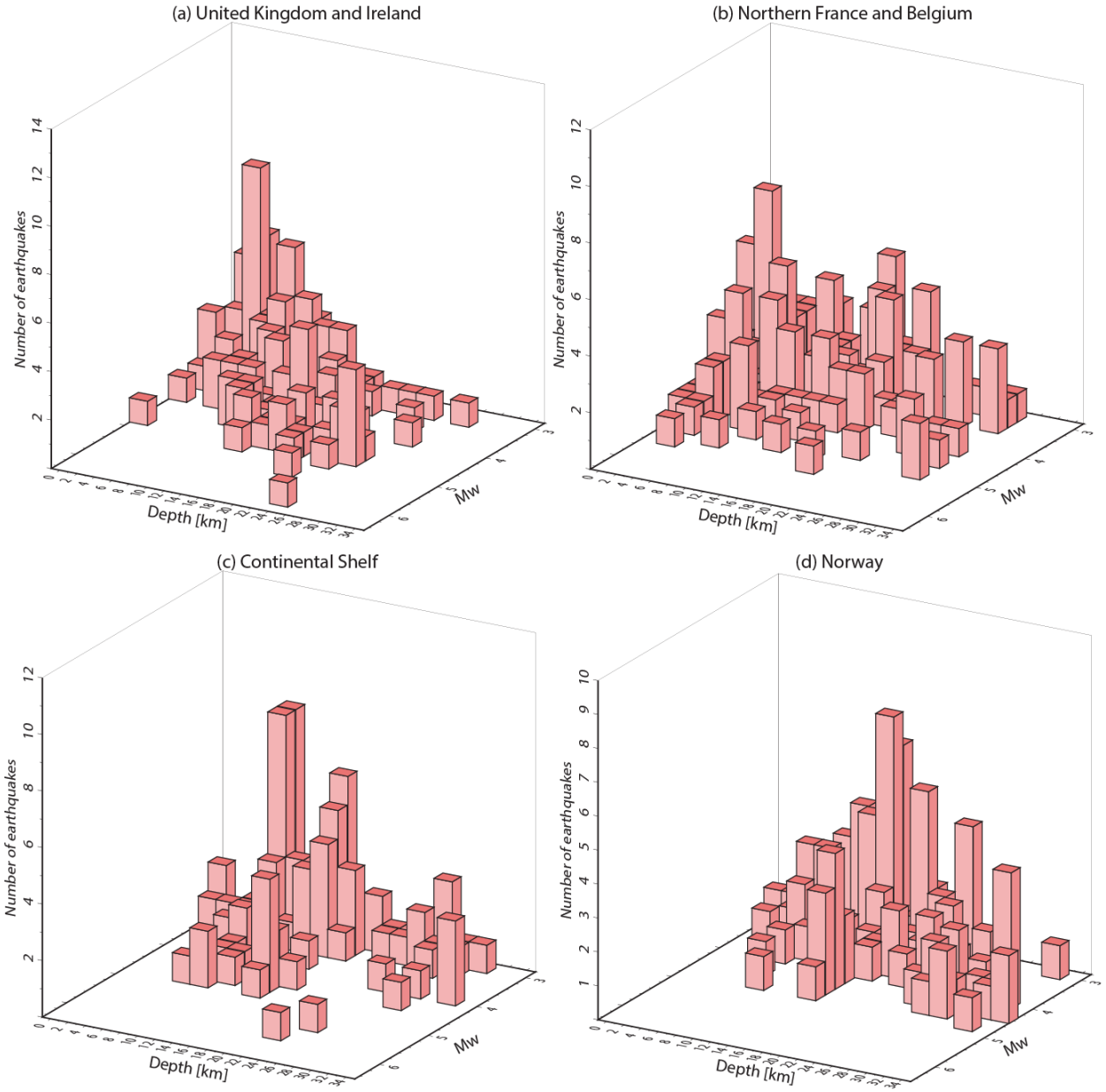

Figure 16: 3D histogram showing the distribution of earthquakes (Mw ≥ 3) with respect to magnitude and depth for (a) the UK and Ireland region, (b) the Northern France and Belgium, (c) the Continental Shelf, and (d) Norway. The earthquake data are from several sources described in Section 3.

4.6 PRESENT DAY DEFORMATION

The observed seismic activity in the region provides evidence of ongoing local crustal deformation. However, the nature of the crustal strain field and its relation to the observed distribution of earthquake activity in the study area is still not clearly understood. This is partly a result of the very low strain rates, requiring a long-term and/or baseline series of geodetic measurements in order to resolve these. Tectonic stresses generated at the Mid-Atlantic Ridge due to forces acting perpendicular to the spreading ridge, as well as strains resulting from the collision of Africa with Europe, are expected to result in a uniform stress field with approximately NW–SE-oriented compression and NE–SW-oriented extension (e.g. Gölke and Coblentz, 1996; Heidbach et al., 2016). This stress field will result in the tectonic loading of existing fault structures.

However, during the Quaternary, the British Isles were affected by repeated glaciations. The last glacial period reached its maximum extent around 29,000-27,000 years ago at the Last Glacial Maximum (LGM) when the British Irish Ice Sheet (BIIS) covered large parts of Britain and all of Ireland. Glacio-Isostatic Adjustment (GIA) of the crust has been ongoing since the

BIIS retreated from its LGM position (e.g. Lambeck, 1993; Shennan et al., 2006). As a result, it has been suggested that GIA may play a significant role in the seismicity of the region. For example, Muir-Wood (2000) suggests that post-glacial rebound is likely to be the dominant influence on current crustal strain rates over much of northern Europe, resulting in a strain field that comprises a radial component of extension over the rebound dome and contraction over the surrounding forebulge. Main et al. (1999) also suggest that the observed neotectonic uplift combined with a direction of maximum (regional) stress deduced from earthquake focal mechanisms supports the theory that deformation is dominated by glacio-isostatic recovery.

Muir-Wood (2000) also argues that the interaction between the GIA strain field, and the pre-existing tectonic strain field, will cause areas of constructive and destructive interference, according to the pre-existing stress state (whether extensional, strike-slip or compressional). In the British Isles, this model predicts that the seismic components of the rebound dome should lie in the northeast and southwest quadrants. The northwest and southeast quadrants of the forebulge should also show seismic activity. However, the model fails to account for the lack of seismicity in the expected forebulge to the northwest. To fully resolve the question of how each of these two strain fields influences modern seismicity and strain accumulation, long-term geodetic observations from permanent GPS stations are required.

Earthquake focal mechanisms provide both fault geometries and principal stress directions that can be used to constrain our understanding of the driving forces of current deformation. In areas of low seismicity and sparse station distribution, determining reliable focal mechanisms can be problematic and the number of available focal mechanisms is limited. Figure 17 shows the focal mechanisms available for 54 earthquakes with ≥ 3.0 Mw in the study area (out of 440 events with ≥ 3.0 Mw since 1970). Note that focal mechanisms of events with 2.5 and 3.0 Mw are available in the UK and northern France but they are not plotted in Figure 17. In Scotland, the strike of left lateral mechanisms is consistent with left-lateral loading of major structures such as the Great Glen Fault or the Highland Boundary Fault that strike NE-SW as a result of north-south compression. In England and Wales, focal mechanisms predominantly show either right-lateral east-west fault planes or left-lateral north-south planes. These orientations appear consistent with tectonic loading from first-order plate motions that result in NW-SE compression and NE-SW tension, or reverse with NW-SE compression, and are supported by other stress data (e.g. Heidbach et al., 2016). Focal mechanisms from Northern France (Mazzotti et al., 2021) are more varied but largely show mechanisms that vary from strike-slip, through oblique normal to normal faulting. There are also a few events with a reverse faulting mechanism, particularly in the Cotentin Peninsula. However, the maximum horizontal compressive stress for most mechanisms is oriented NW-SE to NNW-SSE, which is in good agreement with the regional stress field (Mazzotti et al., 2021) and consistent with the results from mainland Britain. The available focal mechanisms in the North Sea show predominantly thrust to oblique thrust faulting with a compressive stress axis in the W-NW to E-SE direction consistent with the ridge-push forces produced by the mid-Atlantic ridge. Therefore, normal faults in the North Sea from the failed rift can become reactivated as thrust earthquakes when influenced by the forces from the mid-Atlantic ridge over time (e.g., Jerkins et al., 2023). Bungum et al. (2005) and Zarifi et al. (2022) show some deviations from this regional stress pattern suggesting that such secondary effects are caused by isostatic rebound from the past glaciation. Ottemöller et al. (2005) indicate that the NNW-SSE direction of the maximum horizontal stresses in the Central Graben will result in strike-slip or reverse faulting.

Left-lateral strike-slip along a NE–SW trend is consistent with the prevailing N- to NNW-oriented horizontal tectonic stresses of Western Europe (Grünthal and Stromeyer, 1992), and the earlier Palaeocene and Oligocene Alpine-related compression. This trend matches the recent geological history of the large-scale fault structures in the British Isles where Alpine-related compression has driven faulting. While this might suggest that earthquake activity across the region is driven primarily by the reactivation of these favourably oriented fault systems by deformation associated with first-order plate motions, the role of deformation associated with the Glacio-Isostatic Adjustment cannot be ruled out (Baptie, 2010).

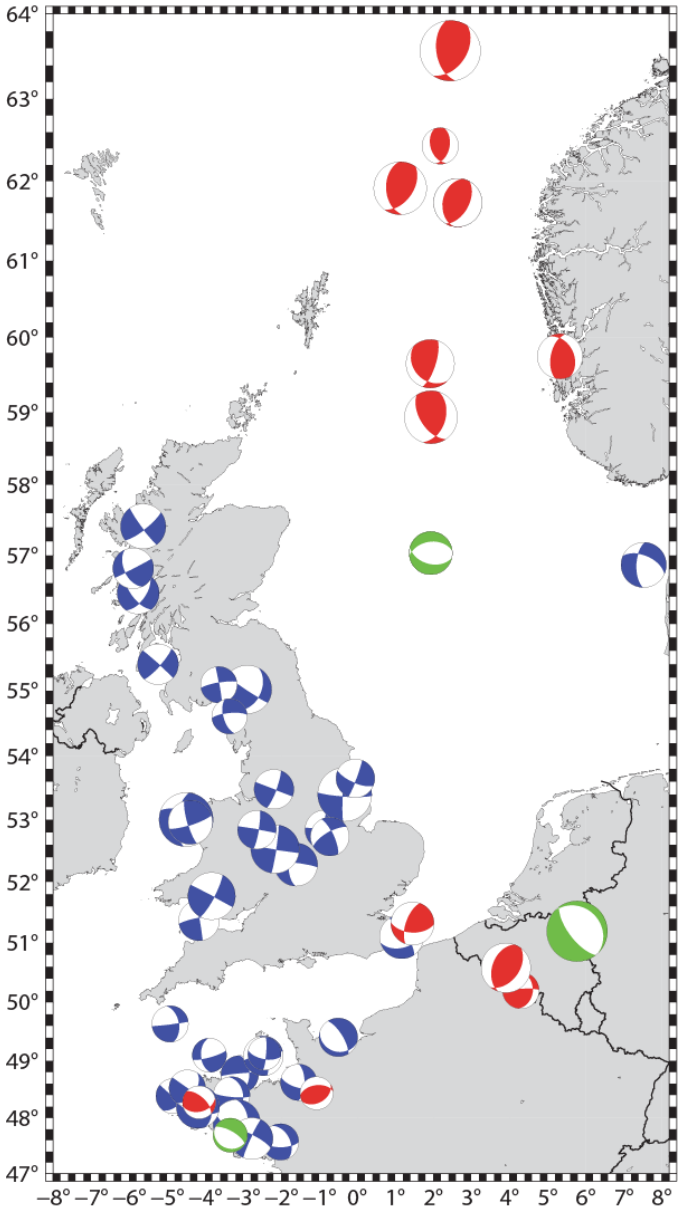

Figure 17: Focal mechanisms available for earthquakes of Mw ≥ 3.0 in the study area. Blue, red, and green beach balls represent strike-slip, reverse, and normal faulting styles, respectively. Focal mechanisms of the British events were published by Trodd et al. (1985), Marrow and Walker (1988), Ritchie et al. (1990), Walker (1991), Sargeant et al. (2008), Ottemöller et al. (2009), Baptie (2010), and the BGS bulletins (e.g. Galloway et al. 2013). BGS © UKRI 2023. The focal mechanisms of the earthquakes in France are from Mazzotti et al. (2021). The focal mechanisms of the earthquakes in the North Sea and Norway are from the ISC Bulletins (ISC, 2021).

5 Seismic source characterisation model

The link between the integrated geological, geophysical, geotechnical, and seismological database, described in Sections 3 and 4, and PSHA is the SSC model (IAEA, 2022), which represents Steps 1 and 2 described schematically in Section 2. The SSC model provides a numerical representation of possible earthquake sources, describing where and how often earthquakes occur in terms of inter-event time and magnitude-frequency in a specific region (e.g. Reiter, 1990). To construct the SSC model, the study area is divided into a series of seismic sources (zones or faults) where the seismic activity within each source is considered to be of homogeneous earthquake potential, and earthquakes have an equal chance of occurring at any point in the source (e.g. Reiter, 1990; Baker et al., 2021).

A general problem that arises in all studies of this kind is whether it is more appropriate to model individual faults as sources or to merge them into zones, which may be considered aggregates of similar faults. Any fault that is a uniquely controlling feature, or is such that the hazard at the site is dependent on the geometry or kinematics of the fault, will generally be treated as an individual source if sufficient information is available to define it. Although some earthquake activity in the UK appears to be spatially associated with large-scale tectonic structures (e.g. Chadwick et al., 1996), it is difficult to conclusively relate specific earthquakes to motion on particular fault structures because of uncertainties in both earthquake locations and the geometry of the faults themselves. Similarly, although faults in the UK are often well-mapped at the surface, there is generally insufficient information to be able to define these as active fault sources due to the lack of supporting geodetic, neotectonic and seismic data. As a result, there is considerable epistemic uncertainty associated with any rupture scenario and we do not include fault sources in the SSC model. This is in keeping with other recent studies in intraplate regions with low levels of seismicity at national (e.g. Drouet et al., 2020; Mosca et al., 2022) and local scales (e.g. Tromans et al., 2019; Villani et al., 2020). In addition, using source zones allows potentially buried, and therefore unknown, fault structures to be accounted for in the SSC model.

Each zone is defined by the following parameters:

a) The geometry of the zone.
b) The Gutenberg-Richter frequency magnitude distribution (FMD).
c) The maximum earthquake magnitude.
d) The expected depth distribution
e) The expected orientations of faulting (which can be random) and the fault types (i.e. thrust, normal, strike-slip, oblique).

Uncertainties in these parameters can be expressed by a range of values with associated weights in a logic tree. The branches for each parameter are randomly sampled in proportion to their weight (see Section 2.1).

The parameters above are used to model each event in a simulated catalogue as a finite fault rupture in a simple way. The software M3C models fault and area sources but not point sources avoiding any simplifications in the fault rupture modelling.

1- For a zone, a synthetic event is generated with a assigned magnitude based on the recurrence parameters of a randomly drawn FMD from the set of 25 pairs of *a* and *b* (Subsection 5.3) and the maximum magnitude sampled from its distribution (Subsection 5.2). The magnitude is equal to or larger than the minimum magnitude for the hazard calculations (Subsection 5.6).
2- The epicentral coordinates of the random event of a specific magnitude are generated at a random location within a source zone. The hypocentral depth, faulting style and orientations are randomly drawn from the possible value in their distribution (Subsections 5.4 and 5.5). For the areal sources, we consider generic values of rake and dip angles for the faulting style, i.e. rake = 0° and dip = 90° for strike-slip faulting; rake = -90° and dip = 50° for normal faulting; rake = 90° and dip = 40° for reverse faulting. For fault sources, rake and dip angles must be provided.
3- The synthetic earthquake is assumed to be located at the centre of a fault rupture. The length of the rupture is then calculated from the event magnitude using Leonard (2014) and its orientation is selected from the logic tree (Subsection 5.5) to determine the coordinates of the two endpoints of the rupture. We assume that the zone boundaries are permeable and therefore the endpoints of the rupture can extend outside the source zone boundaries. Down-dip rupture width is computed by assuming that the fault rupture has an aspect ratio (i.e. the ratio between the length of the rupture along the strike of the fault and the down-dip rupture width) of 1.0.
4- The distance metrics are exactly computed for the synthetic fault rupture with respect to a site to model accurately the ground motion without using conversion relationship.

Ruptures are constrained to stop at 33 km depth, i.e. the generic reference thickness of the seismogenic zone, which corresponds to the depth of the Moho (see Section 4). This seems to agree with the overall distribution of the hypocentral depth of the earthquakes in the project

catalogue (see Subsection 5.4). Hypocentral depths for deeper events, such as the Lleyn Peninsula (1984) and Market Rasen (2008) earthquakes (Turbitt et al., 1985, Ottemöller and Sargeant., 2010), are relatively well-constrained at depths of around 20 km.

5.1 DELINEATION OF THE GEOMETRY

The basic outlines of the delineation of a SSC model reflect geological and geophysical features, which are relevant to controlling the distribution of seismicity, and the seismicity itself in the study area. We use four seismic source zone models (SZM1-SZM4; Figures 18-21) to capture the epistemic uncertainty in the behaviour and location of seismogenic structures and their correlation with seismicity. Figures 18-21 show also which completeness thresholds we apply to the source zones of the four SZMs and the distribution of the mainshocks, which fall within and outside the completeness thresholds in Table 2.

SZM1 is strongly based on the main structural domains and the distribution of seismicity. It corresponds to the SSC model developed for the 2020 national seismic hazard model for the UK (Mosca et al., 2022) and the source model for northern France, Belgium, the North Sea, and the Atlantic Ocean used in the ESHM20 (Danciu et al., 2021). The zone geometry in the UK was developed as the result of our current understanding of the main structural domains and distribution of seismicity. The zonation for SZM1 took the zone boundaries of the 2013 European Seismic Hazard Model (ESHM13) for the SHARE (Seismic Hazard Harmonisation in Europe) project (Woessner et al. 2015) as its starting point but some modifications were made in light of recent developments in the understanding of tectonics in the UK between 2013 and 2020. The ESHM13 model for the UK was heavily influenced by the study of seismo-tectonics in the British Isles by Chadwick et al. (1996). The development of the source model of ESHM20 is an update of the area source model of ESHM13 where the modifications take into account the seismic hazard assessments at a national level that have been conducted across Europe. For example, the SSC model for the British Isles in ESHM20 is that in Mosca et al. (2022). SZM1 consists of 39 zones.

SZM2 is based on geological and structural understanding of the region focusing on zones that are consistent with the known geological structures. This includes rocks of similar type which have been subjected to the same deformation events and therefore have similar structural trends and should behave similarly in a given stress field. Examples of these include the basement terranes of northern Scotland, extensional basins and intervening blocks, such as those in the North Sea and the Irish Sea, and regions underpinned by stable rock mass like granitic intrusions such as Southwest England. In all these regions the geological structure and geology are broadly consistent at the scale of the model. This source model provides a balance against SZM1, which is strongly based on seismicity. SZM2 consists of 35 zones.

Models SZM3-SZM4 are the two seismic source models used in EQE02. They correspond to the source model A and B in EQE02, respectively, which were developed by NORSAR and NGI (1998) as part of the Norwegian seismic hazard study. Bungum et al. (2000) consider only the source model A. The source model for the UK and the harmonisation with the NORSAR zonation are based on expert judgement and the experience gained by the authors of EQE02 in many site-specific seismic hazard studies. SZM3 and SZM4 are the results of the modification of the source models A and B to the study area of the present project. They consist of 41 and 31 zones, respectively, making the latter a coarser model than the former.

Appendix 1 provides a detailed description of the individual zones of SZM1-SZM4.

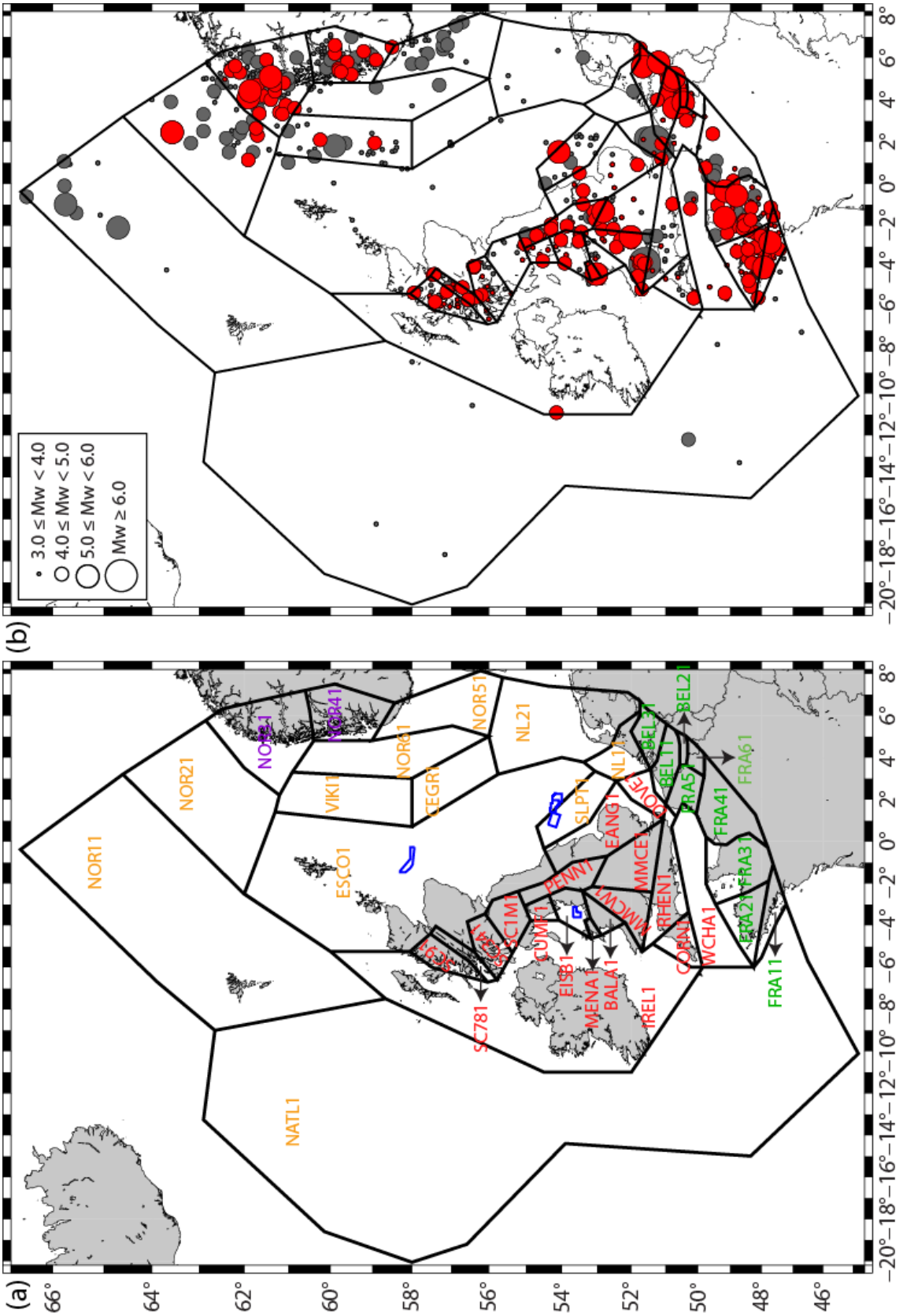

Figure 18: (a) Geometry of the seismic source zone models SZM1. The blue polygons describe the CCS areas selected for the site-specific hazard estimates. The name of the zones is colour-coded based on the completeness region in Figure 7: red for “United Kingdom and Ireland”, orange for “Continental Shelf”, green for “Northern France and Belgium”, and violet for “Norway”. (b) Distribution of the mainshocks of Mw ≥ 3.0 within (red circles) and outside (grey circles) the completeness thresholds in Table 2.

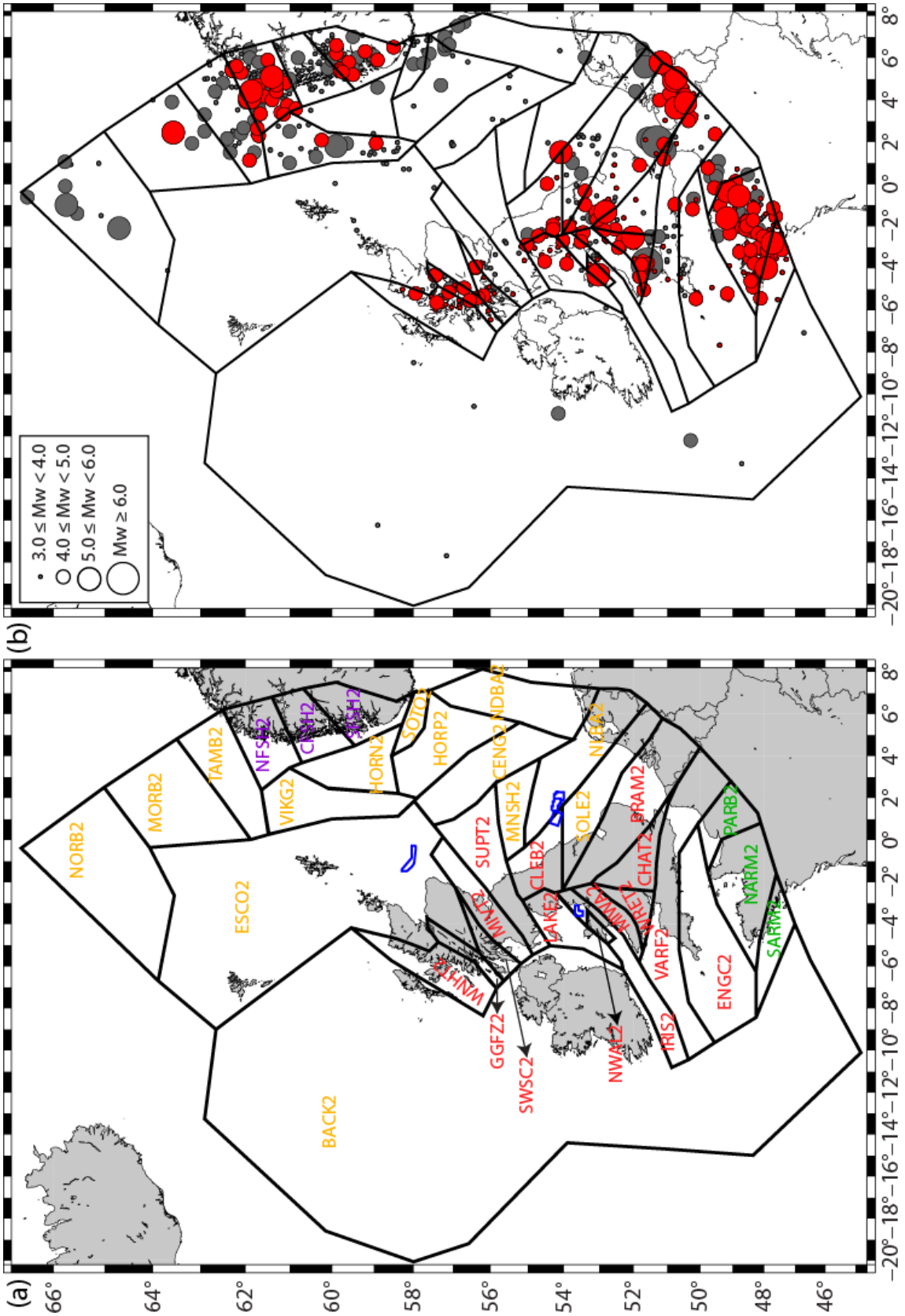

Figure 19: (a) Geometry of the seismic source zone models SZM2. (b) Distribution of the mainshocks of Mw ≥ 3.0 within (red circles) and outside (grey circles) the completeness thresholds in Table 2. The other symbols are described in Figure 18.

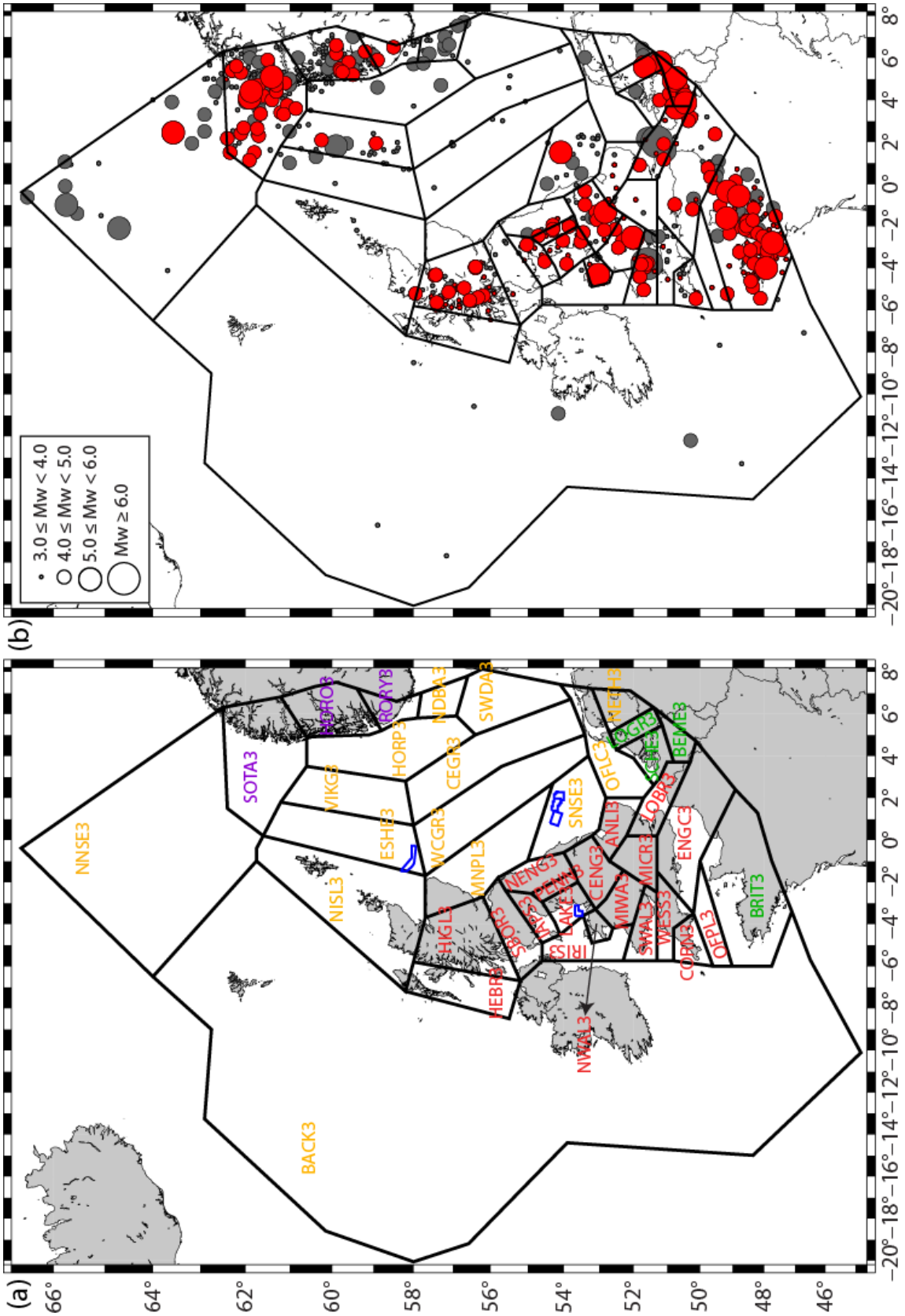

Figure 20: (a) Geometry of the seismic source zone models SZM3. (b) Distribution of the mainshocks of Mw ≥ 3.0 within (red circles) and outside (grey circles) the completeness thresholds in Table 2. The other symbols are described in Figure 18.

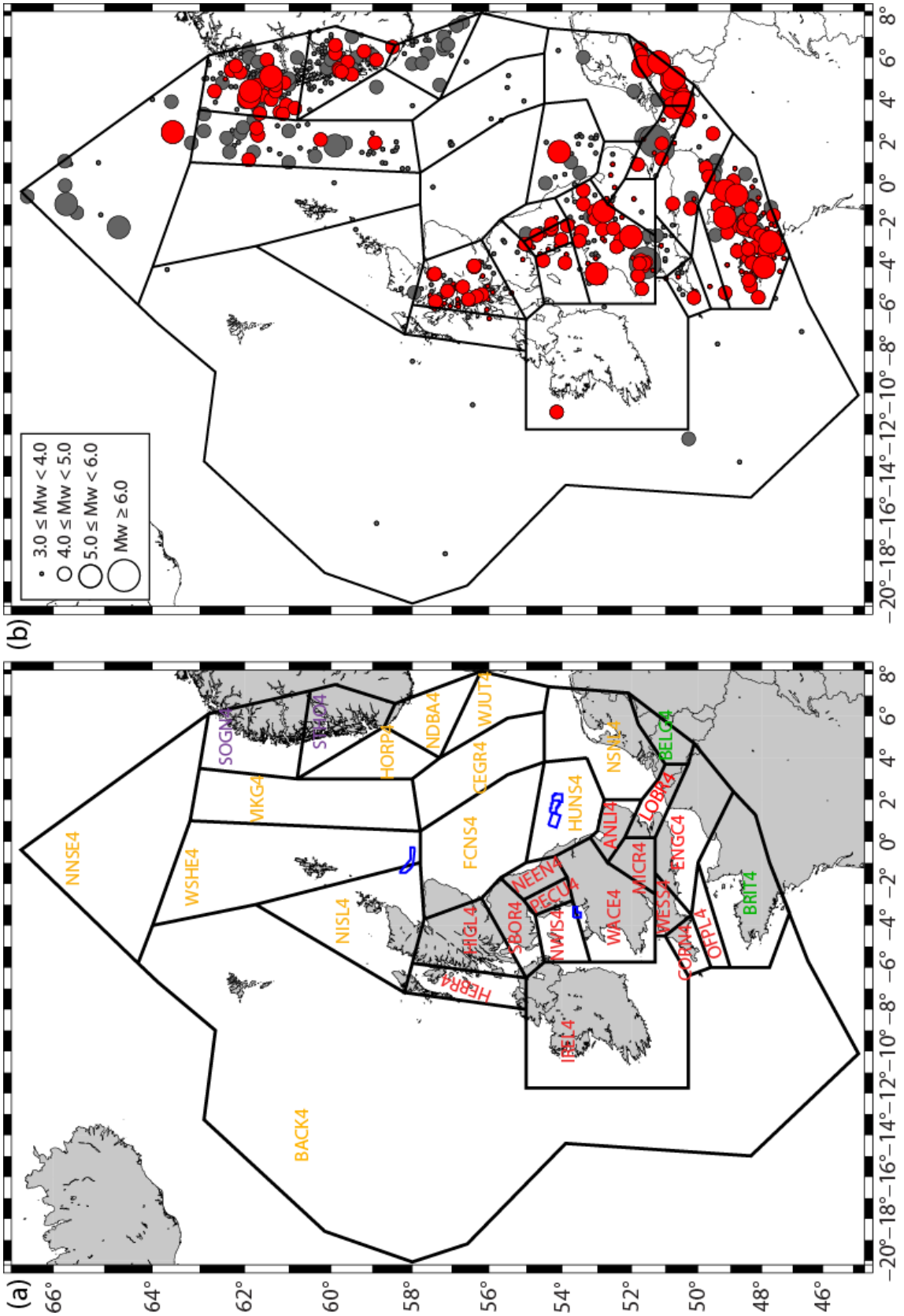

Figure 21: (a) Geometry of the seismic source zone models SZM4. (b) Distribution of the mainshocks of Mw ≥ 3.0 within (red circles) and outside (grey circles) the completeness thresholds in Table 2. The other symbols are described in Figure 18.

The uncertainties in the epicentral location have a strong impact on the delineation of the seismic source zone models. Similar to magnitude uncertainty (see Subsection 3.2), the location uncertainties are not homogeneously assessed across the entire composite catalogue used in this project. For the BGS database, location uncertainty for instrumental earthquakes

has been uniformly estimated in the last three years (Baptie, 2022). For the historical events, they are not quantitatively assessed but they are described by a quality factor in Musson (1994). Historical earthquakes are classified as class A (epicentral uncertainty of less than 5 km), B (epicentral uncertainty between 5 and 15 km), C (epicentral uncertainty between 15 and 35 km), and D (epicentral uncertainty of more than 35 km). Therefore, they can be used to extrapolate a reference value for the location uncertainty for each historical earthquake. The epicentre location of the events from other sources (e.g. FCAT-17 and the catalogue of NNSN) are not associated with uncertainty.

The source models SZM1-SZM4 have been developed to account for the uncertainty in the correlation between seismogenic structures and seismicity and how this may influence the hazard in the UK offshore EEZ. The source model weighting scheme is based on discussions within the project team. SZM1 has the highest weight (0.4) because it has been through high scrutiny, whereas SZM2-SZM4 are assigned the same weight (0.20 each). SZM2 has a lower weight than SZM1 because it is strongly influenced by structural geology and little by seismicity and has not gone through the same level of scrutiny as SZM1. SZM2 is developed with an emphasis on the structural interpretation of the study area to capture the uncertainty in the tectonic structures, which may influence the hazard offshore, and how they correlate to the nearby seismicity. SZM3 and SZM4 also have a lower weight than SZM1 because they were developed more than 20 years ago and did not account for recent developments in understanding tectonics in the UK and the North Sea.

The seismic source models constructed for the SSC model, together with their weights, are given in Table 3.

Source model	*Weight*
SZM1	0.40
SZM2	0.20
SZM3	0.20
SZM4	0.20

Table 3: Weights given to the SZMs in the SSC model developed for this work.

5.2 MAXIMUM MAGNITUDE

Maximum magnitude (Mmax) describes the size of the largest possible earthquake in the region under investigation. This is often highly uncertain, although, in a broad sense the maximum magnitude is theoretically limited by fault length because any large earthquake requires a sufficiently large structure or system of interacting structures to host it. Defining Mmax in intraplate regions is particularly challenging (Holschneider et al., 2011, 2014). This is because the recurrence interval of large earthquakes in such areas is of several hundreds to thousands of years due to the low deformation rate. This greatly exceeds the duration of most earthquake catalogues. As a result, it is quite likely that the largest possible earthquake may not be included in the records.

The historical earthquake catalogue in the study area includes two earthquakes with magnitudes greater than or equal to 6.0 Mw: a 6.2 Mw event in the Dover Strait in 1382 and a 6.0 Mw event in South Wales in 1275. Significant uncertainties are associated with the location and the magnitude of these events (Musson, 2015). The largest earthquake for which a magnitude can be estimated reliably is the Dogger Bank event on 7 June 1931 (5.9 Mw; Neilson et al., 1984). Although no destructive events have been reported in the North Sea, Ghione et al. (2019) suggest that the Øygarden fault in the northern North Sea is capable of producing earthquakes up to 7 Mw. Earthquakes of Mw ≥ 6.0 have occurred in analogous tectonic regions. The largest earthquake, which is known to be observed in northwest Europe, is the 1356 Basel earthquake in Switzerland (6.6 ± 0.5 Mw; Fäh et al. 2011). Other examples of large earthquakes in low seismicity regions are the three principal earthquakes in the 1811-1812 New Madrid sequence in Missouri (6.7 Mw, 6.5 Mw and 6.8 Mw for the 16 December 1811, 23 January

1812, and 7 February 1812 earthquakes, respectively; Hough and Page, 2011) and the 1886 Charleston earthquake in South Carolina (7.3 ± 0.3 Mw; Johnston, 1996).

There is no standard procedure for determining Mmax for a PSHA (for a review, see Wheeler, 2009; and Meletti et al., 2009). In general, Mmax must be at least as large as the largest observed earthquake (e.g. Petersen et al., 2014). EQE02 and NORSAR and NGI (1998) used a Mmax distribution that consisted of three values for all zones in the UK and North Sea: 6.0, 6.5, and 7.0 Mw with weights of 0.4, 0.4, and 0.2. The Mmax distribution in the national seismic hazard models for the UK (Mosca et al., 2022) consists of four values (6.5, 6.7, 6.9, and 7.1 Mw) with weights of 0.5, 0.2, 0.2, and 0.1, respectively. This was determined by Woessner et al. (2015) for the ESHM13 using the statistical approach of Johnston et al. (1994) and EPRI (2012). The Mmax distribution in ESHM20 has been updated and it consists of three values (6.3, 6.6, and 6.9 Mw) with weights of 0.6, 0.2, and 0.2 for the UK, North Sea, Norway, northern France and Belgium (Danciu et al., 2021). The lower bound of Mmax (6.3 Mw) is equal to the highest magnitude observed for the zone plus its standard deviation; the second value (6.6 Mw) is assumed equal to 6.3 Mw plus a magnitude increment of 0.3, and the third value is assumed to be conservatively equal to 6.3 plus a magnitude increment of 0.6. Carlton et al. (2022) use three different Mmax distributions for the UK onshore (5.5 – 6.5 Mw), the UK offshore (6.0 - 6.5 Mw) and Norway offshore (6.0 – 7.0 Mw).

Here we use the Mmax distribution for the national seismic hazard models for the UK (Mosca et al., 2022) for all four SZMs (Table 4) since this was the result of high scrutiny.

Known structures, such as the North Artois shear zone, which has been associated with seismic activity of around 6 Mw, are long enough to accommodate earthquakes of ~7.1 Mw. In the UK, the Great Glen Fault and the Highland Boundary Fault are also long enough to accommodate earthquakes with magnitudes greater than 7.0 Mw, and have associated seismic activity, which is smaller than 5.0 Mw. There are also examples from elsewhere where large earthquakes have resulted from a collection of relatively small ruptures. For example, various faulting scenarios have been posited for the New Madrid earthquakes involving rupture on two fault segments between roughly 30 to 70 km long (Johnston and Schweig, 1996).

Mmax	*Weight*
6.5	0.5
6.7	0.2
6.9	0.2
7.1	0.1

Table 4: Mmax values and assigned weights used in the SSC model.

5.3 RECURRENCE STATISTICS

We use the truncated Gutenberg-Richter frequency-magnitude law (Equation 2) to quantify the predicted FMD. However, the low numbers of events in individual source zones in low seismicity areas, such as the North Sea, means that the uncertainty in the *b*-value may be high. Therefore, it is desirable to maximise the information provided by different time windows of the catalogue with different magnitude completeness thresholds (Weichert, 1980). The penalised maximum likelihood procedure of Johnston et al. (1994) accounts for different time windows of catalogue completeness, the uncertainty in *a* and *b,* the correlation between them, and a weighted prior constraining the *b*-value when there are too few earthquakes in the source zone for a reliable estimate to be made. The prior *b*-value is introduced as a penalty function for which the weight can be specified. The weight and the deviation of estimated *b* from a prior *b*-value are then factored into the likelihood function to produce the penalised likelihood function. The estimated *b*-value is conditioned by the prior *b*-value as the weight increases and the number of events in the zones decreases. The results from the penalised maximum likelihood procedure are expressed by a 5×5 matrix of possible values for *a* and *b* (i.e., median value, median value ± one standard deviation, and median value ± two standard deviations) determining 25 triplets of

activity rate, *b*-value and their weight. The weights are computed from a normal probability distribution of the recurrence parameters derived from the penalised maximum likelihood procedure. As explained in Subsection 3.2, in the calculation of the activity rate, we do not consider the magnitude uncertainty in the recurrence statistics to avoid over- and under-estimation of the activity rate.

To estimate the regional *b*-value, we apply the penalised maximum likelihood procedure to the study area excluding the offshore regions (Figure 22a) using only the portion of the instrumental catalogue complete for Mc =3.0 since 1975 (Table 2). We excluded the offshore regions due to the limited completeness of the catalogue there. For the recurrence calculations, we use a minimum magnitude of 3.0 Mw and a maximum magnitude (Mmax in Equation 2) of 7.1 Mw. This is the largest value in the Mmax distribution in the SSC model used for the hazard calculations (Table 4). However, the choice for this is not critical for the results because Mmax has little influence on the estimation of the activity rates and *b*-values of the source models (Musson, 2012b). We do not specify a prior *b*-value. The results of the recurrence statistics are shown in Figure 22b where the length of the error bars is inversely proportional to the number of observations above a certain magnitude in the catalogue for that zone. This gives a general indication of the uncertainties in the estimate of the long-term recurrence rate for that magnitude. The 25 recurrence parameters in the probability distribution of the FMD are described by the grey lines in Figure 22b, whereas the black lines are the FMD from the weighted mean of the 25 recurrence parameters. The regional estimates of the recurrence parameters are $b = 0.950 \pm 0.082$ and (N ≥ 3.0 Mw) /yr = 2.69 ± 0.23. This is equivalent to about 2-3 earthquakes of 3.0 Mw and above per year somewhere in the red polygon in Figure 22a.

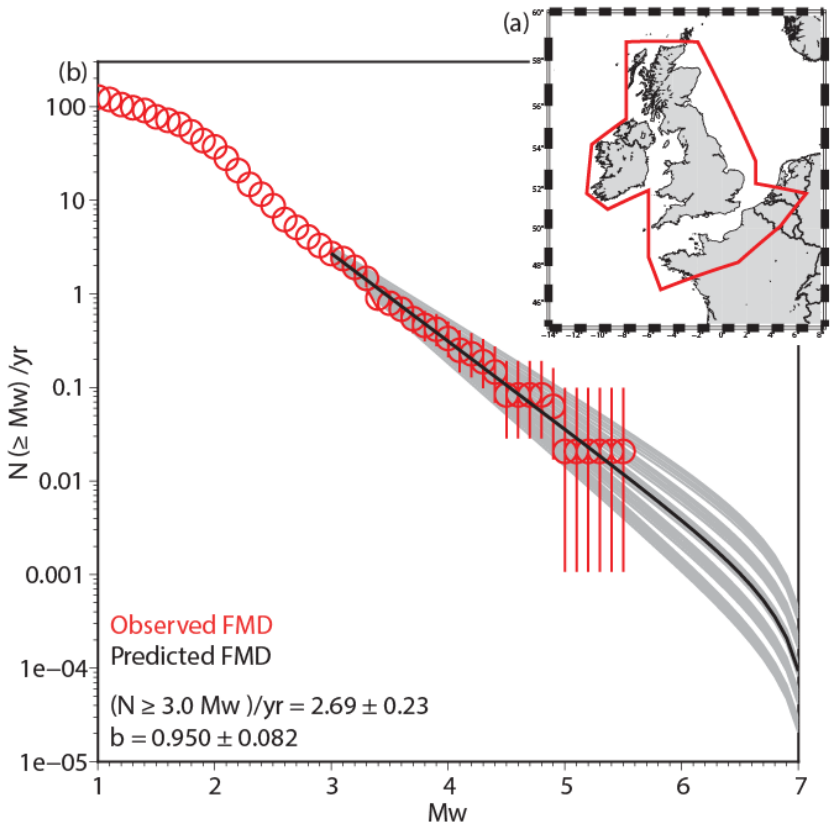

Figure 22: Statistical distribution of seismicity. (a) The red polygon indicates the region selected to determine the regional estimate for the *b*-value. (b) Frequency-magnitude distribution (FMD) calculated for the polygon described in (a) using Mc = 3.0 Mw since 1975 (see Table 2). The red circles show the observed FMD and the black line shows the best-fitting model estimated using the penalised maximum likelihood method. The values of *N (≥3.0 Mw)/yr* and *b* are shown with their standard deviation. The grey lines describe the 25 recurrence parameters in the probability distribution of the FMD computed using the penalised maximum likelihood procedure.

We apply the penalised maximum likelihood procedure to each zone in the four seismic source models using the results of the completeness analysis for the regions in Table 2 and the regional *b*-value as the prior. The results for the four seismic source models are given in Figures 23-26 and Appendix 1. For zones, which contain no earthquakes within the completeness thresholds, the *b*-value is fixed to be the chosen prior of 1.0 ± 0.1 (it is rounded to one decimal place) and (N ≥ Mw) /yr depends on the area of the zone and the average rate of seismicity for the completeness regions in Figure 7. This is applied to zones ESCO1, CEGR1, NOR11, NOR51, NOR61, NL11, NL21 NATL1, ESCO2, NORB2, CFSH2, SOTO2, HORP2, NDBA2, CEGR2, MNSH2, HORN2, NLBA2, BACK2, NISL3, MNPL3, IRIS3, OFLC3, NETH3, ESHE3, WCGR3, CEGR3, HORP3, SWBA3, NDBA3, BACK3, NISL4, FCN4, NSNL4, WSHE4, CEGR4, HORP4, NDBA4, WJUT4, and BACK4. Note that including the southern North Sea and the northeast Atlantic in the same completeness region may result in a slight increase in the activity rate of NATL1, BACK2, BACK3, and BACK4 (i.e. the zones located in the northeast Atlantic). However, this issue is mitigated by including realistic uncertainty in the *a* and *b* parameters for those zones. If there are few earthquakes in the zone, a 100% weight for the prior *b*-value indicates that the *b*-value is forced to be the prior *b*-value; otherwise, the estimated *b*-value is slightly adjusted to the events in the zone.

We compare the recurrence statistics between the source model in Mosca et al. (2022) and SZM1. The comparison is done for the 20 source zones that are in common with the two studies. We have found that the mean activity rate and *b*-value are almost identical for all the zones in the UK mainland except for BALA1 and MENA1 (Figure 27). In the 2020 national seismic hazard model of Mosca et al. (2022), BALA did not have any events within the completeness thresholds; whereas in the present work, BALA1 contains one event due to the addition of the completeness threshold of Mc = 3.5 from 1880. In 2020, the recurrence parameters for MENA were estimated using seven events within the completeness thresholds, whereas now *a* and *b* for MENA1 were computed from six events. The extra event is the 1 September 1990 earthquake, which was assigned previously a ML value of 3.2 (3.0 Mw) and recently has been re-estimated to be 3.0 ML (2.8 Mw) (see Subsection 3.2). The difference in the recurrence parameters between the two source models is significant for SLPT1, ESCO1, and VIKI1 because the completeness thresholds for the North Sea region have been revised in the last three years. In particular, the results of the completeness analysis in Table 2 produce a higher predicted seismicity for these zones.

The seismicity in South and North Wales shows a “hump”, or departure from a straight line, around 4.5 Mw with more earthquakes of Mw ≥ 4.5 than those predicted by the Gutenberg–Richter FMD between 3.0 and 5.0 Mw (see Figures 23-25). We follow the same approach as in Tromans et al. (2019), Villani et al. (2020), and Mosca et al. (2022) to apply a ‘bipartite FMD’ as shown in Figures 23-25 (see Musson, 2015). This means that the seismicity of MMCW1, MENA1, NWAL2, NWAL3, and SWAL3 are modelled as two populations of earthquakes with distinct FMDs. The first is a population of “normal” earthquakes represented by the levels of seismicity in the magnitude range between 3.0 and 4.4 Mw. The second population consists of earthquakes in the magnitude range of 4.5–7.1 Mw. The *b*-value is very similar for the two populations of earthquakes identified in each zone. Any attempt to model the seismicity by a single FMD was found inevitably to underestimate the number of earthquakes around 4.5 – 5.0 Mw, a hazard-critical range for the UK (see Figure 7 in Mosca et al., 2022). Although this behaviour may be because the earthquake catalogue is not long enough to adequately reflect the long-term hazard in the region, the use of a bipartite FMD is a pragmatic decision to fit the data in these five zones and reduces the possibility of underestimating the number of earthquakes of Mw ≥ 4.5 in North and South Wales.

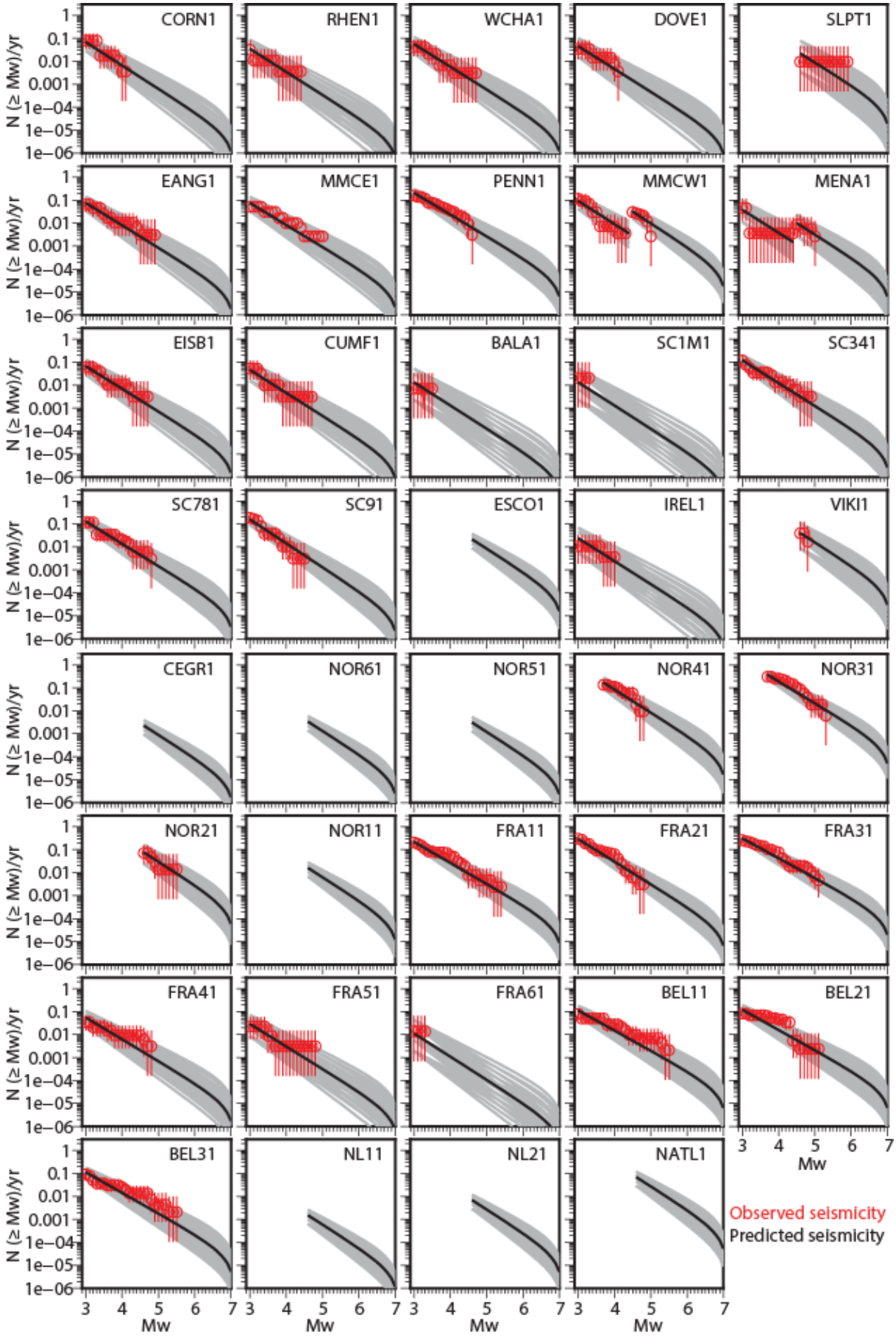

Figure 23: FMD for each of the zones in the source zone model SZM1 in Figure 18. The other symbols are described in Figure 22.

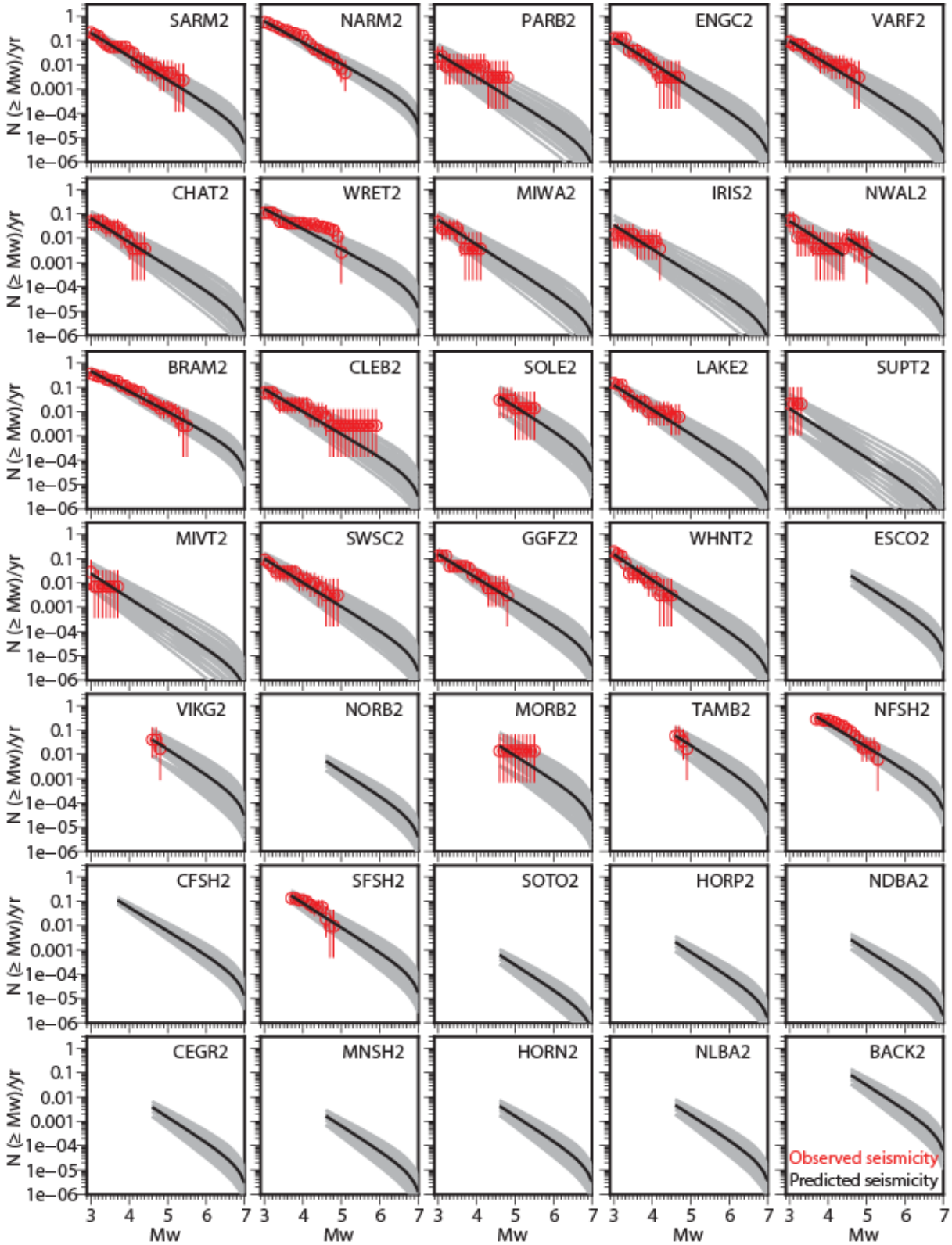

Figure 24: FMD for each of the zones in the source zone model SZM2 in Figure 19. The other symbols are described in Figure 22.

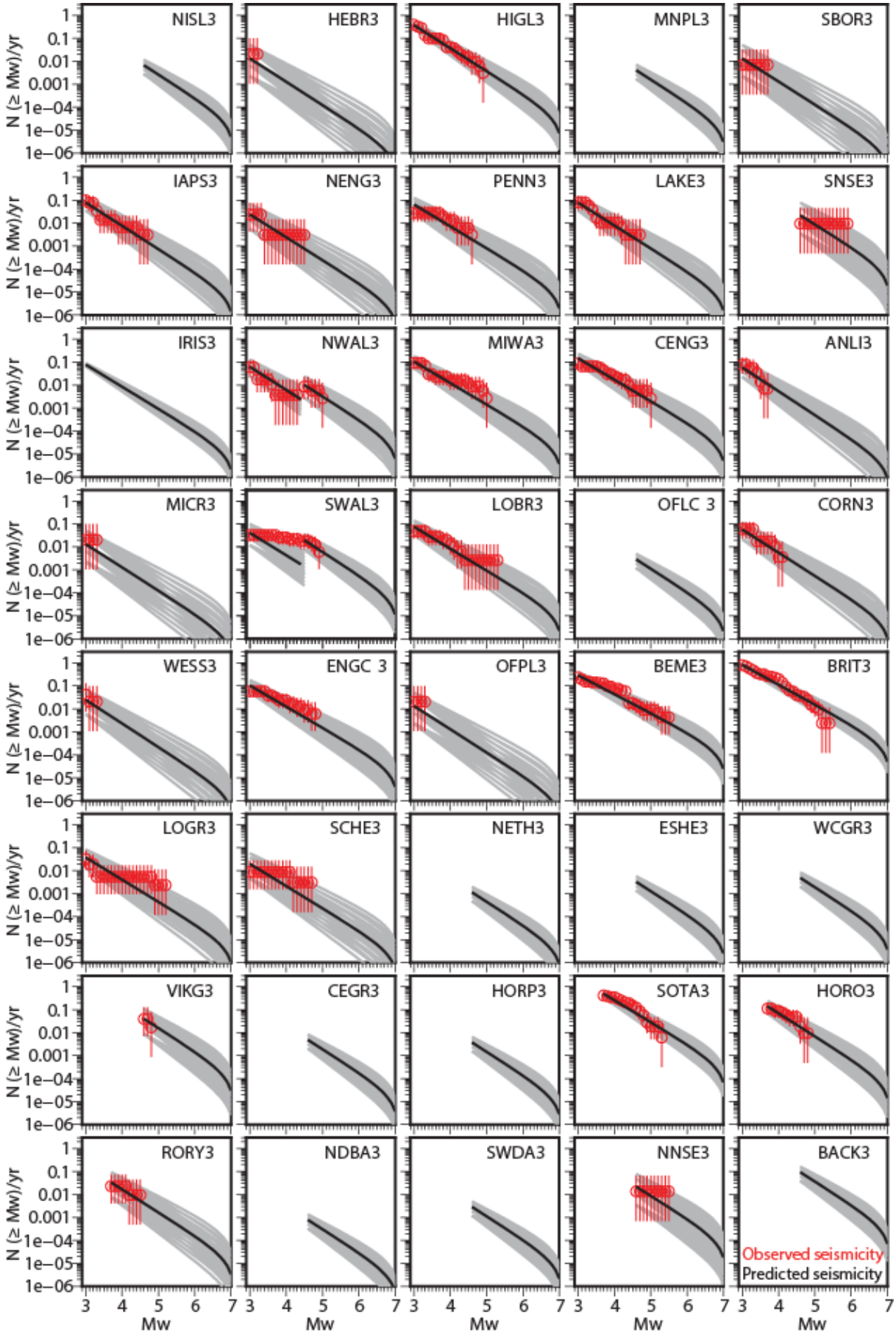

Figure 25: FMD for each of the zones in the source zone model SZM3 in Figure 20. The other symbols are described in Figure 22.

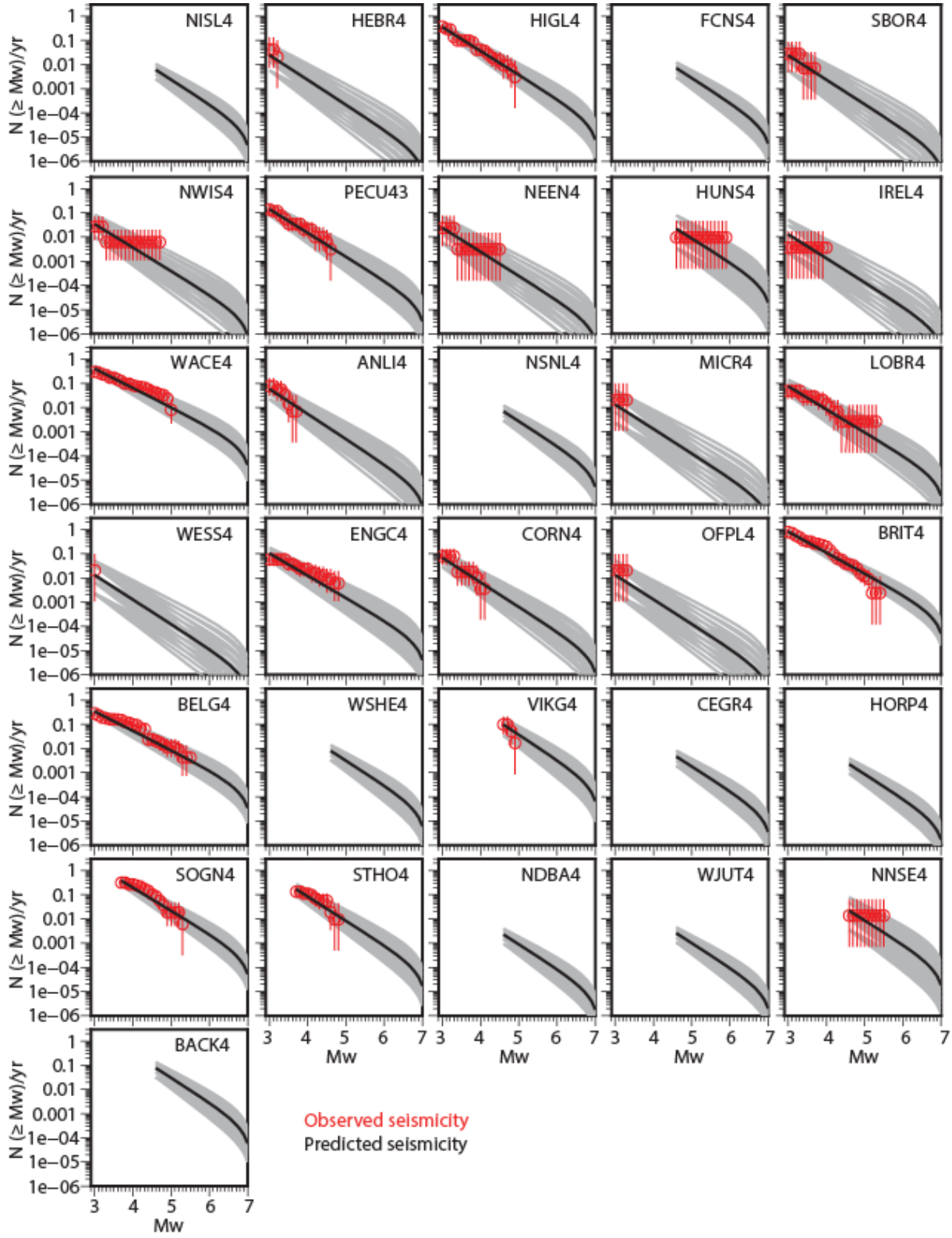

Figure 26: FMD for each of the zones in the source zone model SZM4 in Figure 21. The other symbols are described in Figure 22.

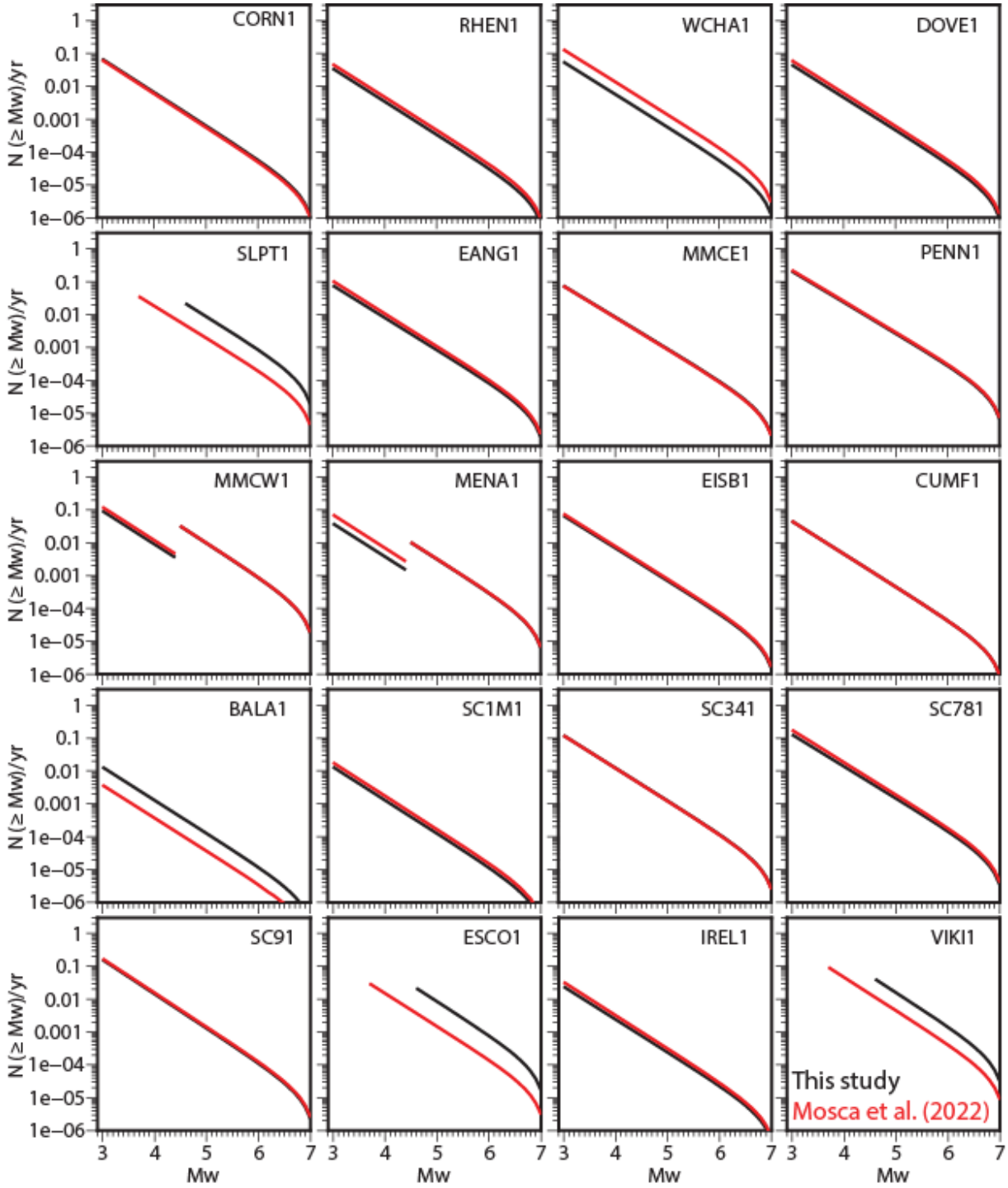

Figure 27: FMDs for 20 zones in the source zone model SZM1 in Figure 18 and the seismic source model in Mosca et al. (2022).

5.4 DEPTH DISTRIBUTION

In general, the hypocentral depths of the earthquakes in the study area are distributed throughout the upper 25 km of the crust with more earthquakes of shallow (< 15 km) depth (see Section 4.5). The distribution of hypocentral depths of earthquakes along Norwegian coast area appear to be slightly deeper than that in the UK and northern France. The depth distribution for the SSC model in Table 5 captures this and accounts for the depth uncertainty in the logic tree (see Section 4.5).

Depth (km) for the UK and Ireland	Weight	Depth (km) for the Continental Shelf and Norway	Weight	Depth (km) for Northern France and Belgium	Weight
5	0.25	5	0.20	5	0.30
10	0.35	10	0.25	10	0.30
15	0.20	15	0.25	15	0.15
20	0.15	20	0.20	20	0.15
25	0.05	25	0.10	25	0.10

Table 5: Depth distribution used in the SSC model.

5.5 FAULTING

Each zone in the SSC model has a weighted distribution of possible faulting styles and orientations of faulting associated with it. This describes the faulting of synthetic ruptures for future, potential earthquakes and it is based on the focal mechanisms of past earthquakes. Given the stress conditions in the study area, it is assumed here that future significant earthquakes in the UK are most likely to be strike-slip faulting events with N–S to NW-SE compression and E–W to NE-SW tension for the zones in the British Isles. This is consistent with the tectonic structures and what has been observed predominantly for events in the last 30 years of seismicity in the study area (e.g., Baptie, 2010; Figure 17). In the South Armorican Massif, based on the focal mechanisms in Figure 17, we expect 70% strike-slip earthquakes and 30% normal faulting earthquakes, whereas the proportion of strike-slip and normal faulting events is 80% and 20% in the North Armorican Massif. The earthquakes that occur in the North Sea and Norway are expected to be either strike-slip or reverse faulting with equally weighted N-S or NW-SE orientations (Lindholm et al., 2000; Ottemöller et al., 2005; see also Figure 17). In the northeast Atlantic region, we assume that future earthquakes are most likely to be strike-slip events with unknown fault orientation due to the limited information on faulting in that region.

The orientation of the synthetic faults for the zones in the study area is derived from the faulting maps in Figures 14-15. If the orientation of faults is unknown, random orientations are considered (Musson, 2009).

5.6 MINIMUM MAGNITUDE

The minimum magnitude in a hazard calculation is defined as the threshold for potentially damaging earthquakes (e.g. Bommer and Crowley, 2017). This parameter is usually defined between 4 - 5 Mw for engineered structures. In this work, we consider the minimum magnitude to be 4.0 Mw to include the probability that the impulsive nature of small earthquakes and their high-frequency content could potentially cause damage at the site. This is consistent with the PSHA for the national seismic hazard model for the UK (Mosca et al., 2022).

6 Ground motion characterisation model

The GMC model (Step 3 in Section 2) describes the distribution (i.e. median prediction and variability) of the ground motion parameter of interest at the site from all possible earthquake scenarios. Its choice is one of the most challenging aspects of seismic hazard studies because the hazard estimates are strongly affected by the GMC model, both in terms of estimated median prediction and the aleatory variability.

In PSHA, earthquake ground motions are commonly modelled using empirical GMPEs (also called ground motion model – GMM) that are derived from large datasets of strong-motion

recordings. The development of empirical GMPEs for low seismicity regions, such as the UK, is difficult due to the limited amount of strong-motion recordings available from large earthquakes and at near-source distances. Although there are a few empirical GMPEs derived using UK strong motion recordings (e.g. PML, 1985, 1988, and Free, 1996), they do not meet the requirements for current practice for PSHA (Lubkowski et al., 2004; Bommer et al, 2011). Stochastic ground motion models developed for the UK (Winter, 1995; Rietbrock et al., 2013; Rietbrock and Edwards, 2019) have been published. They are derived from stochastic simulations calibrated using source, path and site parameters estimated from weak-motion data recorded in the UK. Recently, Brooks et al. (2020) and Brooks (2021) investigated which ground-motion model from more than a dozen recent models is the most appropriate for the North Sea based on a residual analysis of ground-motion data from onshore seismic stations surrounding the North Sea. They also applied adjustments to the model with the best performance (i.e. Akkar et al., 2014a) to make the model more site- and path-specific thereby allowing a smaller aleatory variability to be used within a probabilistic seismic hazard assessment.

The most common practice in the GMC model for low seismicity regions is to import a suite of GMPEs derived for other regions that can be considered appropriate for the tectonic setting of the target region, i.e. the study area. The procedure to select this suite of GMPEs consists of three steps (Cotton et al., 2006; Delavaud et al., 2012):

1) Select candidate GMPEs using the exclusion criteria of Cotton et al. (2006) and Bommer et al. (2010). For example, these criteria suggest excluding GMPEs that are not relevant to the tectonic regime of the study area, are not published in peer-reviewed journals, do not cover the entire magnitude-distance range, and do not include the non-linear magnitude scaling, magnitude-dependent decay with distance and soil non-linearity.
2) Compare these GMPEs with the regional strong-motion recordings using quantitative tests.
3) Adjust the selected GMPEs to change parameter compatibility from the host region for which the GMPEs were derived to the target region where the hazard is being estimated.

The use of multiple GMPEs in a logic tree, referred to as the “multi-GMPE approach”, is intended to capture the centre, body, and range of technically defensible interpretations of the GMC model (Budnitz et al., 1997; Atkinson et al., 2014). The variability in the ground motion is captured by including alternative models and parameters in the logic tree where weights are assigned to each branch using expert judgement and/or data-driven approaches to reflect the relative confidence in the models and parameters (Coppersmith and Bommer, 2012). This often introduces a certain degree of judgement making the process to define the logic tree weighting scheme opaque. Moreover, Bommer and Scherbaum (2008) argue that because the alternative models selected to populate the ground motion logic tree are often derived from the same dataset, they do not fully capture the epistemic uncertainty in the median prediction of the ground motion model.

The backbone approach has emerged as an alternative way to capture the epistemic uncertainties in the median prediction of the ground motion model (e.g. Atkinson et al., 2014; Bommer and Stafford, 2020). It is based on the selection of one, or more, GMPEs, which is referred to as the ‘backbone model’. The median predictions of the backbone model are then scaled (or adjusted) up and down to describe the range of epistemic uncertainties in the median ground motion (e.g. Atkinson et al., 2014; Douglas, 2018). The scaling factors can be considered as HTTAs to adapt the source, path, and site components of the backbone model that was derived for a host region to the target region (e.g. Stafford et al., 2022). The backbone approach has been successfully applied at a regional scale (e.g. Goulet et al.; 2017; Akkar et al., 2021; Weatherill et al.; 2020, Stafford, 2022) and a local scale (e.g. Coppersmith et al., 2014; Bommer et al., 2015; Kowsari and Ghasemi, 2021; Boore et al., 2022). The backbone model for the UK of Douglas et al. (2024) has been recently published and was not available when we started to test the existing GMPEs against the UK strong motion data in 2023. For this reason, here we prefer to use the multi-GMPE approach that has been used for the recent PSHA works for the nuclear sites in the UK (Tromans et al., 2019; Villani et al., 2020; Aldama-Bustos et al., 2022), and the national seismic hazard maps (Mosca et al., 2022).

We apply the exclusion criteria of Cotton et al. (2006) and Bommer et al. (2010) to select eight candidate GMPEs that are valid for active shallow crustal regions (ASCRs) and four candidate GMPEs for stable continental regions (SCRs) that are all published before 2021 (e.g. Douglas, 2021). Note that the difference in the number of models between the two tectonic regimes is because the number of available GMPEs for SCRs is significantly less than those for ASCRs. Table 6 summarises the main features of the 12 GMPEs, together with their range of applicability.

Pezeshk et al. (2018) develop two models using two different approaches for scaling at large magnitudes using: (1) the hybrid-empirical method (HEM) of Campbell (2003) to model magnitude scaling over the entire magnitude range; and (2) the HEM to model magnitude scaling for events of Mw ≤ 6.0 and the magnitude scaling predicted by the GMPEs from the Next Generation Attenuation (NGA) – West 2 (NGA-West2) project (Bozorgnia et al., 2014) for larger events. Here we use the model based on the second approach that is preferred by Pezeshk et al. (2018) because it eliminates or significantly reduces oversaturation of ground motion predictions at large magnitudes, short distances, and short periods. The GMPEs of Yenier and Atkinson (2015) and Pezeshk et al. (2018) were among the 20 ground motion models for Central and Eastern North America (CENA), which were derived from a uniformly processed database of empirical ground motion recordings and simulations within the Next Generation Attenuation (NGA)-East project (Goulet et al., 2014; Rezaeian et al., 2021). Since most of these models are presented only in non-parametric form (i.e. tabular values for given magnitudes, distances, and spectral periods), we exclude them because we prefer a parametric form (i.e. equation) that can be extrapolated more readily than non-parametric forms.

Rietbrock and Edwards (2019), who updated the UK stochastic earthquake ground motion model derived by Rietbrock et al. (2013), developed different models for three stress drop values, i.e. 5, 10, and 20 MPa.

The GMPE of Kotha et al. (2020) is a regionally-adjustable ground motion model, which was developed following the backbone approach, for the ESHM20 (Weatherill et al., 2020). Here, we test this model without the regional adjustment term since this term was derived without strong motion data in the UK and the North Sea. This “default” (without regional adjustment) model consists of nine branches to account for the epistemic uncertainty in the attenuation and source terms.

We exclude the GMPE of Brooks et al. (2020) following the exclusion criteria of Cotton et al. (2006) and Bommer et al. (2010) because it was derived using a limited amount of strong motion data, which do not cover the entire range of magnitudes and source-to-site distances. We also did not consider GMPEs developed for France or Fennoscandia (e.g. Fülöp et al., 2020) because these regions are at the edge of the study area and only a small part of France and Fennoscandia is included in the study area.

6.1 SOIL CONDITIONS

To estimate site response (and instead of a site-specific site response study) one can use either a site classification in terms of broad categories of stiffness such as the National Earthquake Hazards Reduction Program (NEHRP; Building Seismic Safety Council, 2009) site classes or a measured Vs30 value (time-averaged shear wave velocity for the top 30 m).

In this project, we assume a generic bedrock condition with a Vs30 value of 800 m/s. This value marks the transition from subsoil class A (rock, Vs >800 m/s) to class B (very dense soil, gravel, or very stiff clay, 350 m/s < Vs30 < 800 m/s) in Eurocode 8 (BS NA EN 1998-1, 2008). Since the UK and surrounding regions are very variable in terms of shear wave velocity (Vs) profile, using Vs30 = 800 m/s is for engineering bedrock levels. This can be converted to the hazard values for the appropriate soil conditions at a specific site using conversion factors reported in international guidelines for recommended practice for offshore structures (e.g. ISO 19901-2, 2022; DNV 2021) and building codes (BS NA EN 1998-1, 2008). However, we highlight that the amplification factors in NEHRP and Eurocode 8 are different, with Eurocode 8 being unconservative (McCully et al., 2014).

GMPE	Code	Tectonic region/ Type	Region of the ground motion data	Max Period [s]	Definition of ground motion	Magnitude range [Mw]	Distance type	Distance range [km]
Abrahamson et al. (2014)	ASK14	ASCR, Empirical	Worldwide	10.0	RotD050	3.0-8.5	Rrup, Rjb	0-300
Boore et al. (2014)	BSSA14	ASCR, Empirical	Worldwide	10.0	RotD050	3.0-8.5	Rjb	0-400
Campbell and Bozorgnia (2014)	CB14	ASCR, Empirical	Worldwide	10.0	RotD050	3.3-8.5	Rrup, Rjb	0-300
Chiou and Youngs (2014)	CY14	ASCR, Empirical	Worldwide	10.0	RotD050	3.5-8.5	Rrup, Rjb	0-300
Akkar et al. (2014a)	AKK14	ASCR, Empirical	Europe, Middle East	4.0	GM	4.0-7.6	Rjb	0-200
Bindi et al. (2014)	BIN14	ASCR, Empirical	Europe, Middle East	3.0	GM	4.0-7.6	Rjb	0-300
Cauzzi et al. (2015)	CAU15	ASCR, Empirical	Japan, worldwide	10.0	GM	4.5-7.9	Rrup	0-150
Yenier and Atkinson (2015)	YEN15	SCR, Stochastic	CENA	10.0	RotD050	3.0–8.2	Rrup	1–600
Pezeshk et al. (2018)	PEZ18	SCR, Stochastic	CENA	10.0	GM	4.0–8.0	Rrup	1–1000
Rietbrock and Edwards (2019)	RE19	SCR, Stochastic	UK	5.0	GM	3.0-7.0	Rjb	0-300
Kotha et al. (2020)	KOT20	ASCR, Backbone	Europe, Middle East	8.0	RotD050	3.0-7.4	Rrup, Rjb	0-545
Weatherill and Cotton (2020)	WC20	SCR, Backbone	Northeast Europe	10.0	RotD050	3.0–7.4	Rrup	0–600

Table 6: Main features of the candidate GMPEs. ASCR = Active Stable Continental Region. SCR = Stable Continental Region. CENA = Central and Eastern North America. GM = geometric mean of two horizontal components. RotD050 = 50th percentile of the response spectra over all non-redundant rotation angles. Rjb = Joyner-Boore distance. Rrup = Rupture distance.

6.2 COMPARISON BETWEEN PREDICTED AND OBSERVED GROUND MOTION

To select the suite of GMPEs for the GMC model, we compare the modelled ground motion from the 12 GMPEs in Table 6 with a relatively large dataset of homogeneously processed ground motion recordings that consist of PGA and also spectral acceleration at 0.2 s ($SA_{0.2\ s}$) and 1.0 s ($SA_{1.0\ s}$). These data were derived from raw ground motions using the workflow described in Mosca et al. (2023a), and contain only those observations that have a signal-to-noise ratio (i.e., the ratio between the smoothed Fourier amplitude spectrum of the signal and the noise) higher than 4 for the three-component acceleration time series. The assembled UK ground motion dataset consists of 466 observations for PGA, $SA_{0.2\ s}$, and $SA_{1.0\ s}$ for source-to-site distances smaller than 400 km from 46 small-to-moderate ($3.3 \leq Mw < 5.0$) earthquakes that occurred in the UK and North Sea between February 1984 and 2022. The recording stations, which are all located in the UK, are uncharacterised in terms of local site conditions and often little information is available on the geological conditions where the stations are located (Mosca et al., 2023b). For this reason, we use a constant Vs30 value of 800 m/s to compute the ground motion predictions and compare them with UK ground motion observations. The data of events before 2002 were recorded on short-period seismometers, whereas afterwards earthquakes in the UK were recorded by a broadband seismic network across the UK (Hawthorn et al., 2023).

Figure 28a shows the location of the 46 earthquakes and recording stations and Figure 28b shows the distribution of the strong motion data as a function of epicentral distances (up to 400 km) and moment magnitude. The majority of the data are weak motion recordings for earthquakes of magnitude lower than 4 Mw and distances larger than 50 km and do not cover the range of magnitudes and distances that are relevant to seismic design in the UK (i.e., 5 - 6 Mw and < 50 km; Villani et al., 2019). The largest earthquake, for which strong motion records are available, is the 4.9 Mw Market Rasen earthquake on 27 February 2008. The green circles in Figure 28b show recordings from earthquakes that occurred in the North Sea. This subset of 51 recordings from 13 earthquakes of 3.3 to 4.7 Mw is too small to be used for any statistical analysis.

Although a portion of recordings from this dataset falls outside the range of applicability of many GMPEs in terms of magnitude and distance (see Table 6), we do not exclude these GMPEs because PSHA studies often have to extrapolate GMPEs outside of their range of applicability (Kale and Akkar, 2013).

We show the visual comparison of ground motion predictions for PGA and observed ground motions for four earthquakes and five of the candidate GMPEs (Figure 29): the 4.9 Mw Market Rasen earthquake on 27 February 2008; the 3.9 Mw Central North Sea earthquake on 24 September 2019; the 4.3 Mw Cwmllynfell earthquake on 17 February 2018; the 3.5 Mw Wem earthquake on 30 May 2022 (see Figure 28a for the location of these events). The ground motion predictions are computed for Vs30 = 800 m/s and a strike-slip faulting mechanism. The predictions have not been corrected for the HTTA (see Section 6.4). In general, the agreement between predictions calculated from CAU15, YEN15, and RE19 and observations seems to be relatively good within one standard deviation; whereas, GMPEs of ASK14 and BIN14 appear to underestimate the UK data.

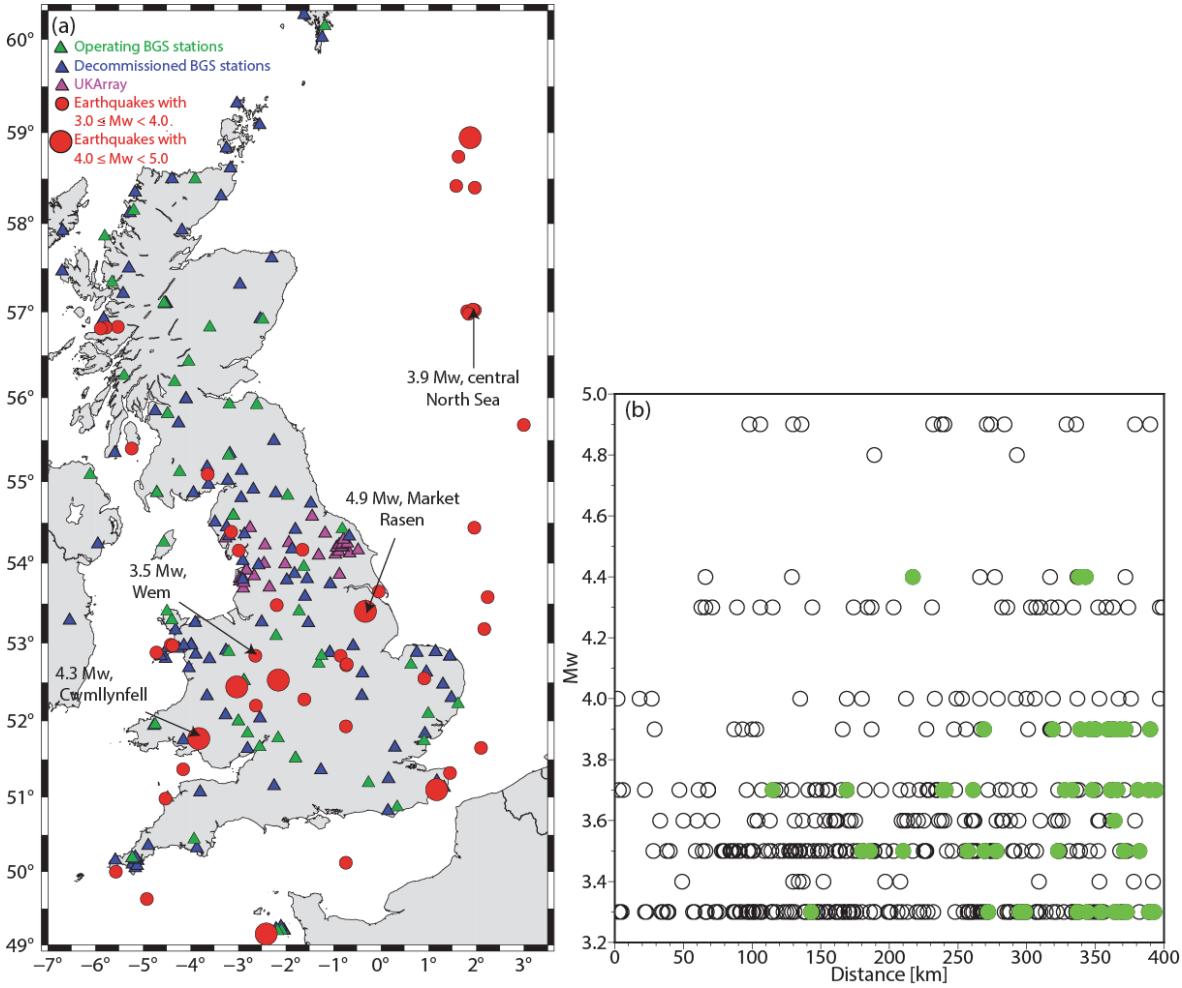

Figure 28: (a) Location of the earthquakes (red circles) and stations (triangles) for which the strong motion observations are used in this project. (b) Distribution of the UK ground motion data in terms of magnitude and distance (for distances up to 400 km) where green circles indicate recordings from earthquakes that occurred in the North Sea.

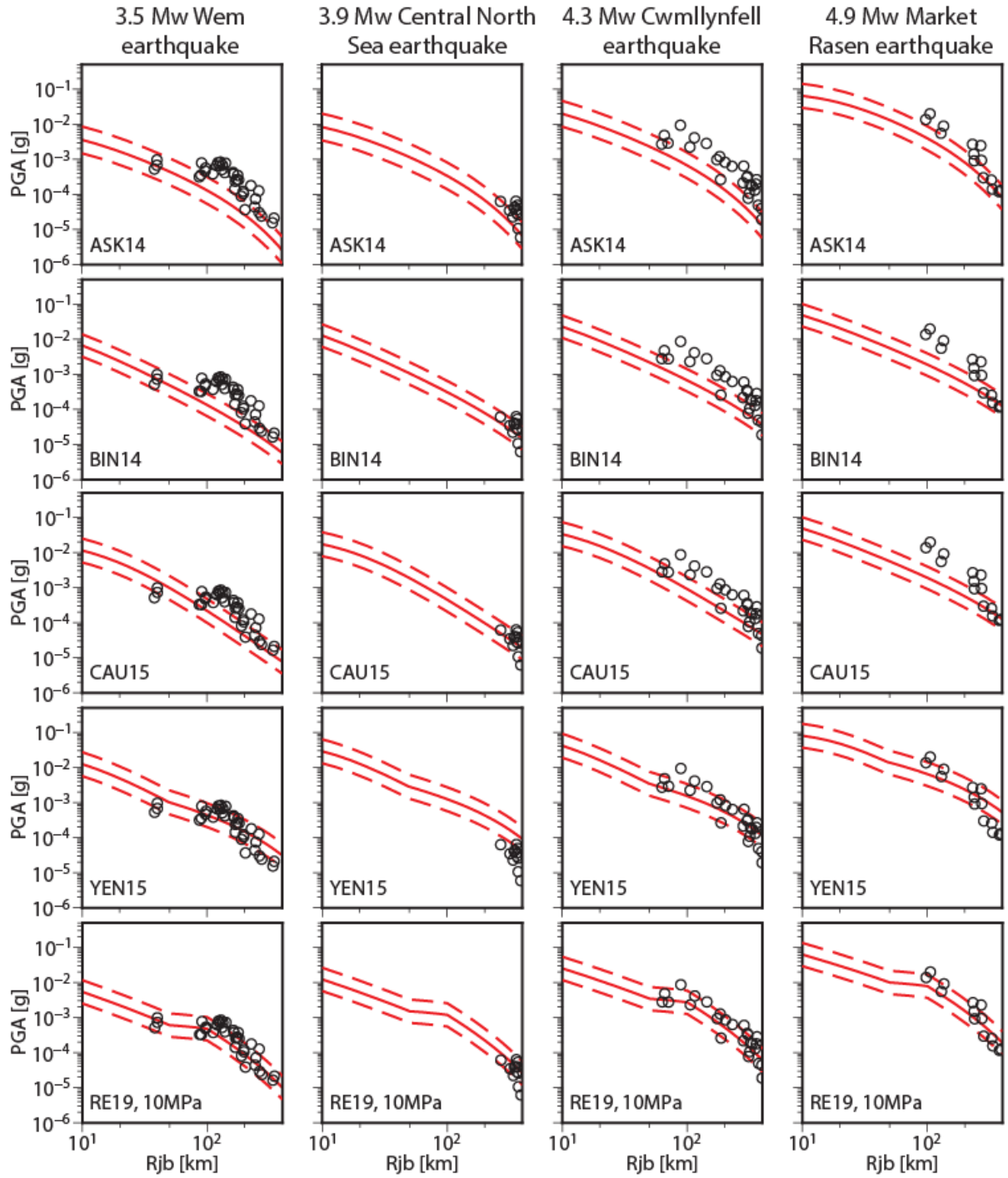

Figure 29: Comparison of the ground motion predictions using a set of the candidate GMPEs in Table 6 with PGA observations for four UK earthquakes. The solid and dashed lines describe the median prediction, and the median prediction ± one sigma, respectively. See Table 6 for the acronyms of the GMPEs. See Figure 28a for the location of the earthquakes.

To quantify the comparison between predicted and observed ground motions, we use three statistical methods, i.e. residual analysis, the log-likelihood method of Scherbaum et al. (2009), and the Euclidian Distance-based Ranking method of Kale and Akkar (2013), to overcome the limitations of the individual statistical methods. In this analysis, we use a Vs30 value of 800 m/s and the standard deviation of the individual GMPEs and not the sigma model introduced in Section 6.5. Note that for the GMPE of KOT20, we apply the statistical methods to all the nine branches of the model but here we show the results only for the central branch in the interests of brevity.

6.2.1 Residual analysis

The normalised residual is defined as the difference between observed ground motions and predictions by a GMPE on a logarithmic scale (Al Atik et al. 2010):

$$\Delta_{ij} = \frac{\left[\ln\left(GM_{ij}^{obs}\right) - \ln\left(GM_{ij}^{th}\right)\right]}{\sigma} \quad (7)$$

where $\ln\left(GM_{ij}^{obs}\right)$ and $\ln\left(GM_{ij}^{th}\right)$ are the log of the observed and predicted ground, respectively, σ is the total standard deviation, and Δ_{ij} is the normalised residual for the i-th earthquake and at the j-th station. Ideally, the residual should be zero indicating that the observed and predicted ground motions match exactly. If the residual is positive, the GMPE under-predicts the ground motion; whereas if the residual is negative, the GMPE is over-predicting ground motion.

Figure 30 shows the normalised residuals for PGA as a function of distance for the candidate GMPEs. The black stars show the average values for distance intervals of 50 km to help identify any clear trend. The residuals for the GMPEs for ASCRs are mainly positive for distances larger than 20 km suggesting that these GMPEs tend to underpredict the UK data. The residuals for RE19 are well-centred around zero and the mean residuals are close to zero. This is unsurprising since this GMPE was derived using almost the same dataset of UK recordings. Furthermore, the GMPEs of ASK14, BSSA14, CB14, and KOT20 do not have any trend in the mean residuals for distances larger than 100 km, whereas the model of CY14 seems to have a positive trend, and all the other ground motion models have a negative trend suggesting a dependency on regional attenuation. The mean residuals for distances smaller than 100 km seem to have a negative trend but this may be an artefact due to the small number of recordings for short distances. The plots in Figure 30 highlights also the residuals for recordings from events in the North Sea (green circles in Figure 30) and the recordings from earthquakes that occurred between 1984 and 2002 (blue circles in Figure 30). These events were recorded by short-period seismometers, whereas afterwards earthquakes in the UK were recorded by a broadband seismic network (see Hawthorn et al., 2023). The residuals of blue circles are mainly negative for all the GMPEs at near-source (< 10km) distances suggesting some kind of limitations in the observations recorded from short-period instruments. Figure 31 shows the normalised residuals for PGA as a function of magnitude for the 12 candidate GMPEs. The mean residuals, which are computed for magnitude intervals of 0.3 Mw, do not show any trend and their fluctuations are due to the small number of recordings available for some magnitude bins (e.g. 4.5-4.8 Mw). Appendix 2 shows the residual plots for $SA_{0.2\ s}$ and $SA_{1.0\ s}$.

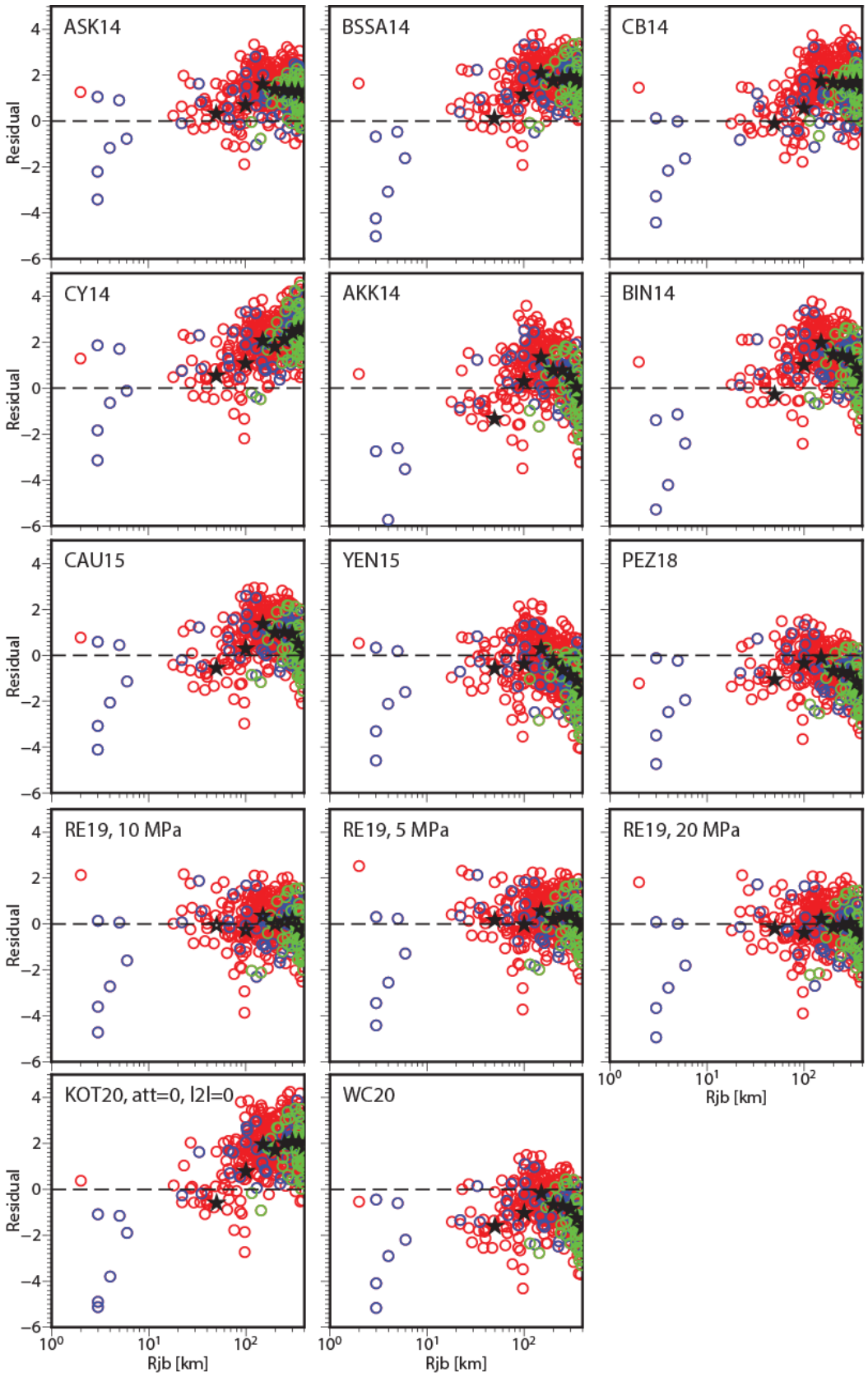

Figure 30: Normalised residuals between the UK strong motion data and the predictions for the 12 candidate GMPEs for PGA as a function of distance. The green circles describe recordings from earthquakes that occurred in the North Sea, whereas recordings from earthquakes that occurred between 1984 and 2002 are given in blue. The black stars represent the average residuals for distance bins of 50 km. The black dashed line describes the ideal case, i.e. when the residuals are zero.

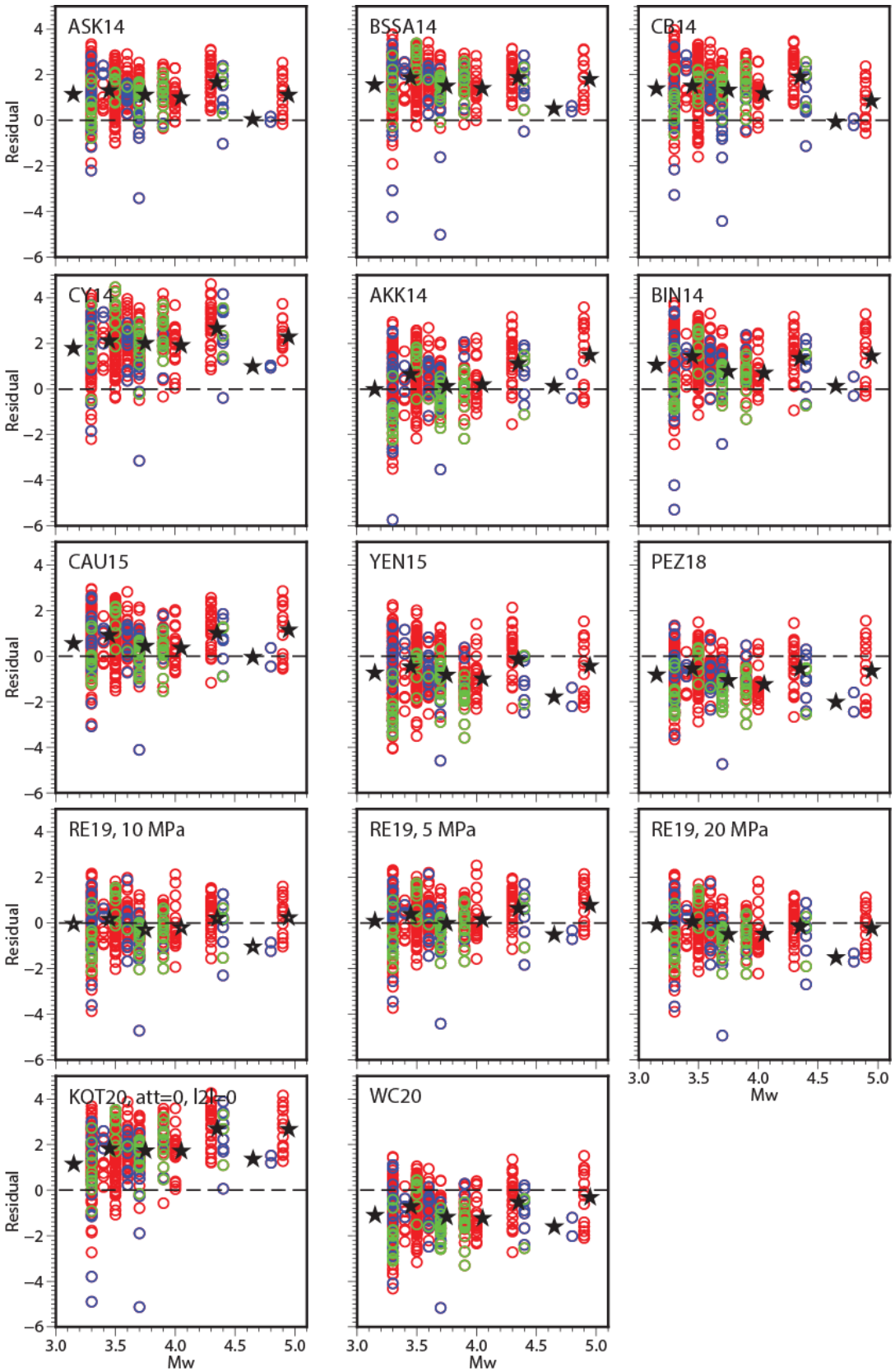

Figure 31: Normalised residuals between the UK strong motion data and the predictions for the 12 candidate GMPEs for PGA as a function of moment magnitude. The black stars represent the average residuals for magnitude bins of 0.3 Mw. The other symbols are described in Figure 30.

Following Rodriguez-Marek et al. (2014), the difference between recorded ground motions and the values predicted by a GMPE can be separated into a between-event (also called inter-event) term, δB_e, and a within-event (also called intra-event) term, δW_{es},

$$\Delta_{es} = \delta B_e + \delta W_{es}. \quad (8)$$

The between-event residual describes the earthquake-to-earthquake variability and depends on source parameters that are not accounted for by the GMPEs; and the within-event residual describes the station-to-station variability and depends on site and path factors that are not captured in the GMPEs (for background, see Al Atik et al., 2010). The standard deviations of δB_e and δW_{es} are τ and φ, respectively, which are uncorrelated and therefore the total standard deviation is:

$$\sigma = \sqrt{\tau^2 + \varphi^2}. \tag{9}$$

To estimate these residuals for the selected GMPEs and the strong-motion observations in the UK, we use the equations of Abrahamson and Youngs (1992):

$$\delta B_e = \frac{\tau^2[\sum_{n_e} \ln(GM_{es}^{obs}) - \ln(GM_{es}^{th})]}{n_e\tau^2 + \varphi^2} \tag{10a}$$

$$\delta W_{es} = \frac{\ln(GM_{es}^{obs}) - \ln(GM_{es}^{th}) - \delta B_e\tau}{\varphi^2} \tag{10b}$$

with n_e, the number of recordings for the earthquake e.

Figure 32 shows the between-event residuals for PGA as a function of magnitude, together with the mean residuals. The largest range is for the GMPE of CB14 and the smallest range is for RE19. The δB_e values for the GMPEs for SCRs are mostly negative, whereas they are positive for the models for ASCRs. This may suggest that the source component for the empirical models is not well calibrated for the source parameters of British earthquakes; whereas, the source parameters used in the stochastic model of RE19 are based on almost the same UK strong motion dataset used here. The within-event residuals as a function of distance have values between -8 and 6 and the mean residuals are closer to -2 and 2 (Figure 33). The largest range is for the GMPE of RE19, whereas the smaller range of the within-event residuals is for the model of KOT20 and WC20.

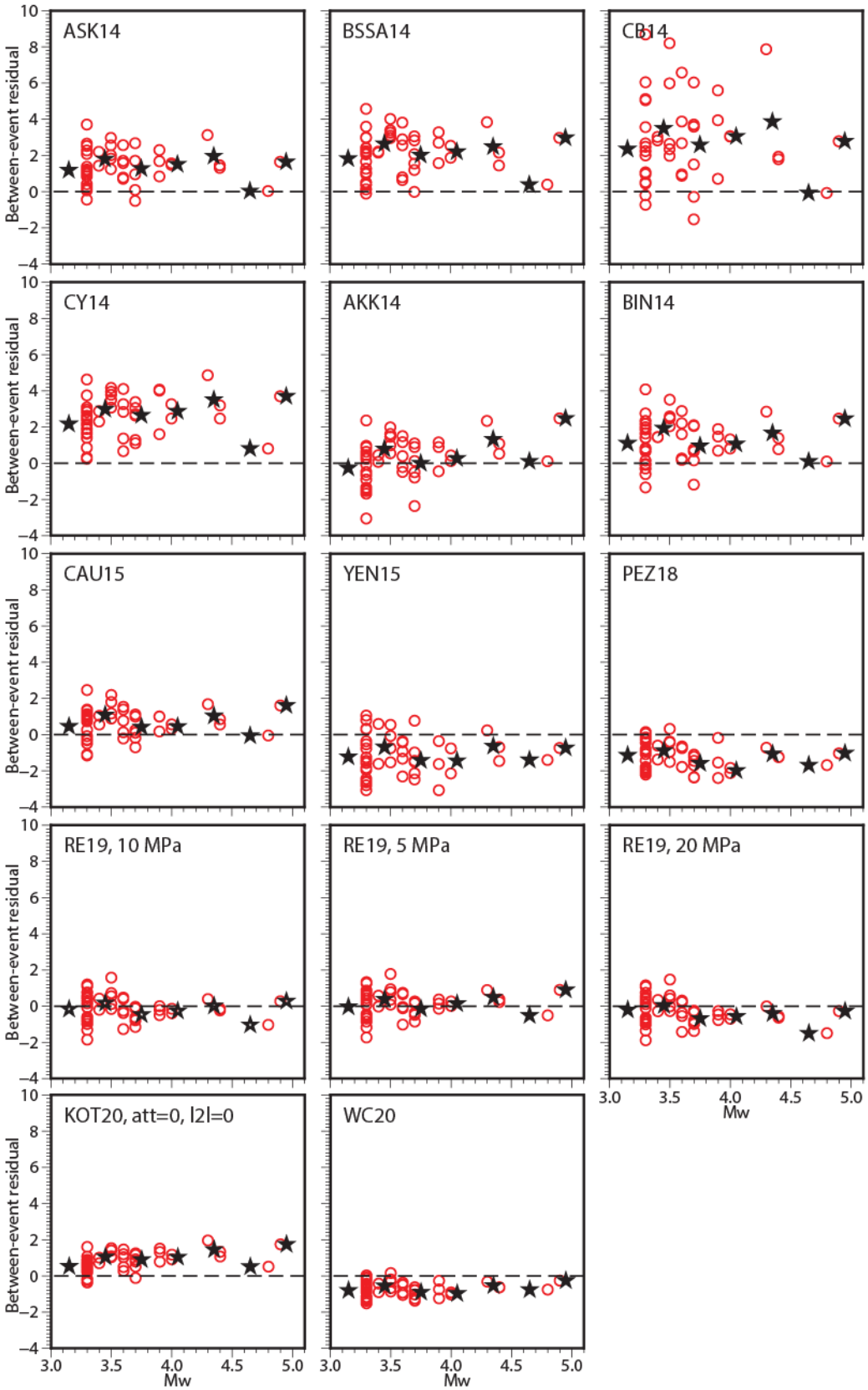

Figure 32: Normalised between-event residuals between the UK strong motion data and the predictions for 12 candidate GMPEs for PGA. The black stars represent the average residuals for magnitude bins of 0.3 Mw. The black dashed line describes the ideal case, i.e. when the residuals are zero.

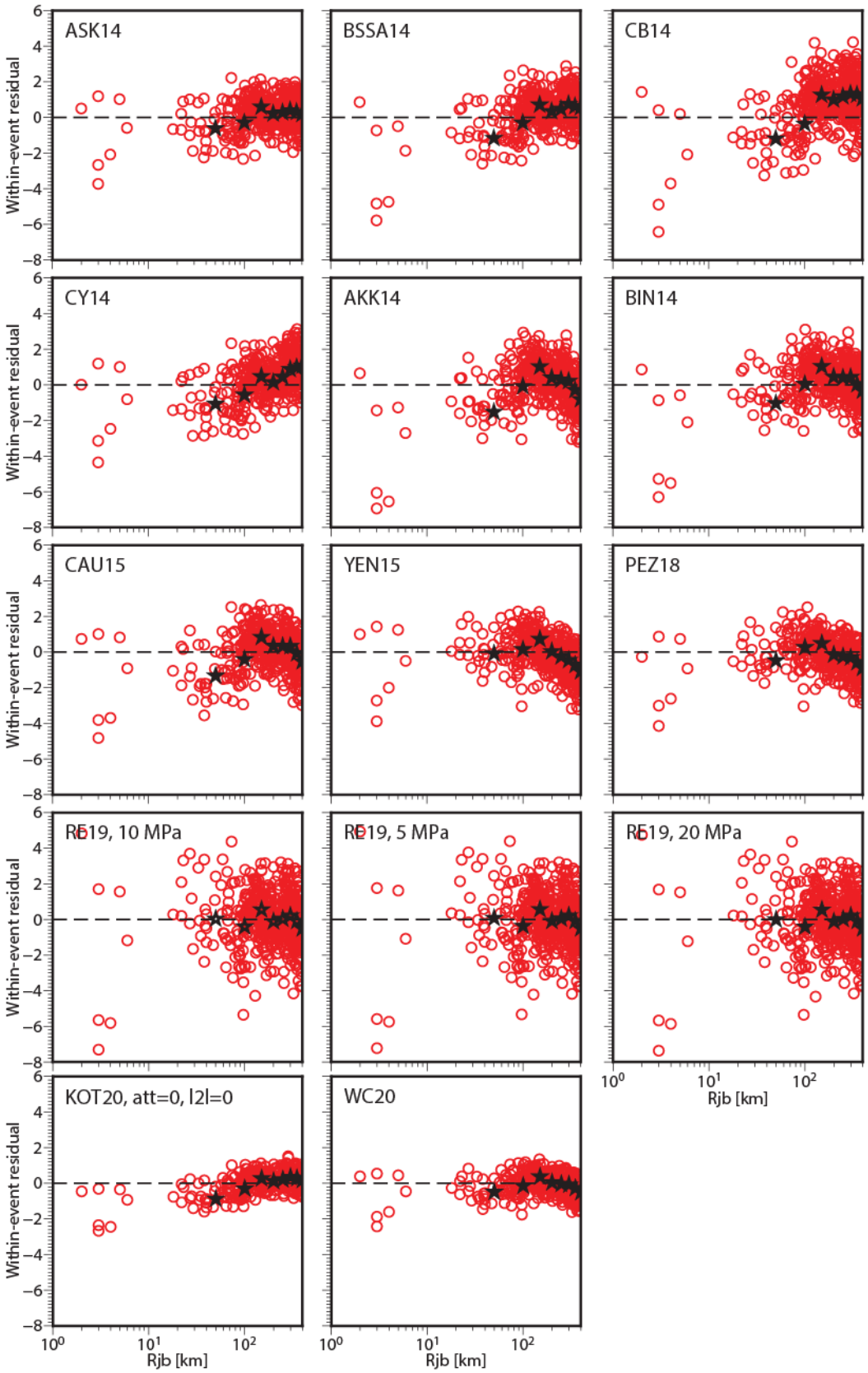

Figure 33: Normalised within-event residuals between the UK strong motion data and the predictions for 12 candidate GMPEs for PGA. The black stars represent the average residuals for distance bins of 50 km. The black dashed line describes the ideal case, i.e. when the residuals are zero.

6.2.2 Statistical tests

The log-likelihood (LLH) method of Scherbaum et al. (2009) evaluates the performance of the GMPE for a particular ground motion dataset:

$$LLH(g,x) = -\frac{1}{N}\sum_{i=1}^{N}\log_2\big(g(x_i)\big) \quad (11)$$

where x_i is the i^{th} empirical datum, $g(x_i)$ is the probability density function from a specific GMPE to predict the observation x_i. The smaller the LLH, the better the performance of the GMPE for a particular ground motion dataset. Kale and Akkar (2013) argue that the LLH approach of Scherbaum et al. (2009) may favour GMPEs with large aleatory uncertainty and therefore the hazard estimates may be over-conservative for low annual frequencies of exceedance (Restrepo-Velez and Bommer, 2003). To overcome this, Kale and Akkar (2013) propose an approach based on the Euclidian distance. The main outcomes of this approach are the parameters MDE (Modified Euclidian distance), $k^{0.5}$, and EDR (Euclidian distance-based ranking). The first evaluates the effect of the standard deviation of the GMPE with the observed ground motion dataset. The parameter $k^{0.5}$ evaluates the median prediction of the GMPE for the observed dataset. The overall effect of these two parameters is given by EDR. Similar to LLH score, lower values of MDE, $k^{0.5}$, and EDR indicate a better performance of a model for the ground motion dataset.

Figure 34 displays the results of the LLH score and the EDR method for PGA, $SA_{0.2\ s}$, $SA_{1.0\ s}$, and their average for the GMPEs in Table 6. Table 7 presents the average LLH values, MDE, $k^{0.5}$, and EDR values over three spectral periods for each GMPE. We can make the following observations from Figure 34 and Table 7:

- All the GMPEs developed for the NGA – West 2 project by the Pacific Earthquake Engineering Research Center (Bozorgnia et a., 2014) have similar performance, although the model of ASK14 seems to perform slightly better than the others (BSSA14; CB14; CY14). These were all derived using a similar dataset of recordings.
- The GMPEs of AKK14 and BIN14 were derived using recordings from earthquakes in Europe and the Middle East included in the RESORCE European strong-motion database (Akkar et al., 2014b). The statistical results indicate that the former predicts the UK strong motion data better than the latter.
- The GMPE of CAU15 performs also relatively well against strong motion data even if this GMPE was derived using recordings worldwide with a large majority of data from Japan.
- The models of YEN15 and PEZ18, which were derived from a uniformly processed database of empirical ground motion recordings and simulations under the NGA-East project (Goulet et al., 2014; PEER, 2015; Rezaeian et al., 2021), have a similar performance.
- The three stochastic models of RE19 perform very well against the UK data. This is not surprising since they were derived using partially the same UK strong-motion dataset.
- The KOT20 model was derived using the European Strong Motion Database, an update of the RESORCE database (Lanzano et al., 2019). It has a slightly worse performance than BIN14 in terms of EDR score but it has the lowest LLH score among all the candidate models.
- The WC20 GMPE seems to perform worse in terms of EDR but better in terms of LLH than the models of YEN15 and PEZ18. This GMPE combines the range of median ground motions developed by the NGA-East ground motion models with the scaled backbone ground motion approach of WC20 developed for the ASCRs in Europe to better capture the ground motion characteristics of stable cratonic environments in northeast Europe.

Since the ground motion dataset in the UK is relatively small, does not contain recordings from large earthquakes, and has too few recordings for near source-to-site distances, the statistical methods used here provide a qualitative indication of the predictive model performance of the selected GMPEs for the ground motion dataset in the UK.

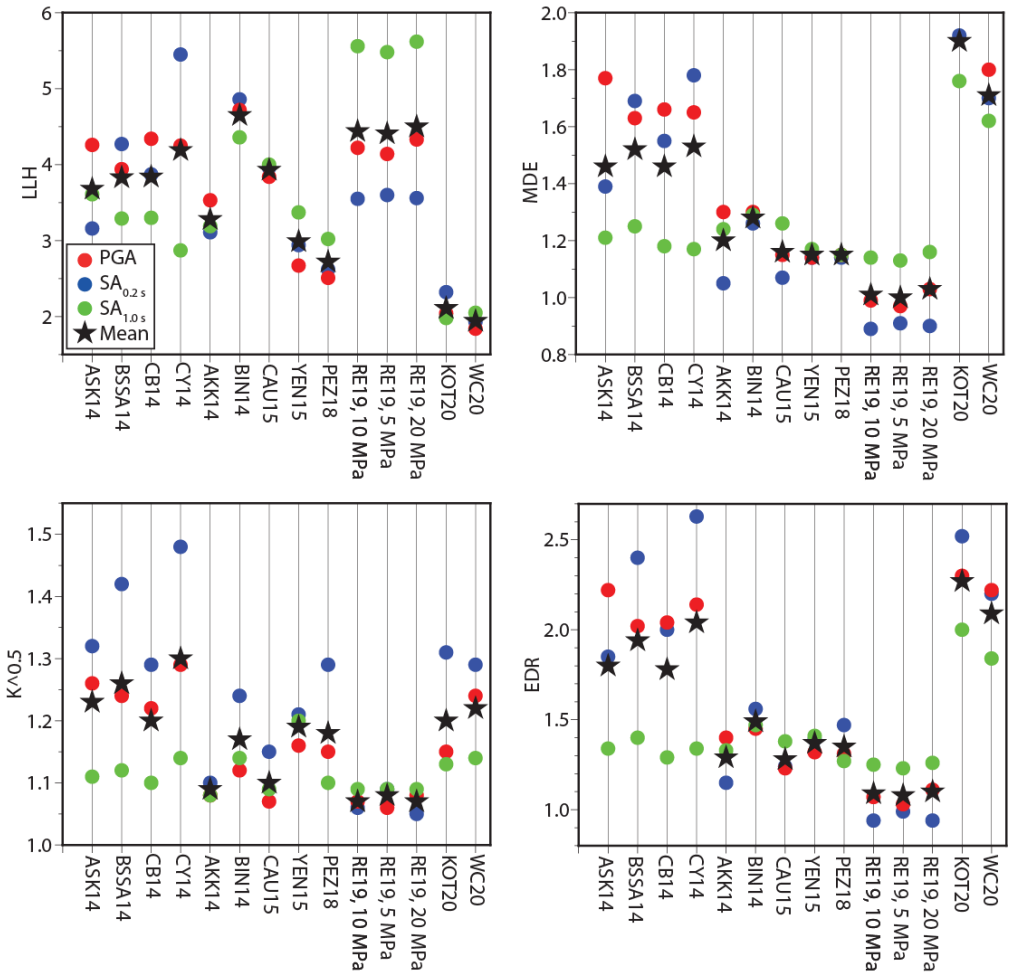

Figure 34: LLH, MDE, $k^{0.5}$, and EDR values as a function of 12 candidate GMPEs for PGA (red circles), $SA_{0.2\ s}$ (blue circles), $SA_{1.0\ s}$ (green circles), and the average over these three (black stars).

GMPE	*LLH*	*MDE*	*$K^{0.5}$*	*EDR*
ASK14	3.68	1.46	1.23	1.80
BSSA14	3.83	1.52	1.26	1.94
CB14	3.84	1.46	1.20	1.78
CY14	4.19	1.53	1.30	2.04
AKK14	3.28	1.20	1.09	1.29
BIN14	4.65	1.28	1.17	1.49
CAU15	3.93	1.16	1.10	1.28
YEN15	2.99	1.15	1.19	1.37
PEZ18	2.72	1.15	1.18	1.35
RE19, 10MPa	4.44	1.01	1.07	1.09
RE19, 5MPa	4.41	1.00	1.08	1.08
RE19, 20MPa	4.50	1.03	1.07	1.10
KOT20	2.11	1.90	1.20	2.27
WC20	1.94	1.71	1.22	2.09

Table 7: Results of the performance of the candidate GMPEs against the UK ground motion dataset.

6.3 SELECTION OF THE GMPES IN THE LOGIC TREE

Since the majority of the data are weak motion recordings for earthquakes of magnitude lower than 4 Mw and distances larger than 50 km and do not cover the range of magnitudes and distances that are relevant to seismic design in the UK (i.e., 5-6 Mw and < 50 km; Villani et al., 2019), the selection of the suite of the GMPEs for the GMC model, together with the assignment of their weights, combines the LLH and EDR results and discussion within the project team.

We select ASK14 among the NGA-West 2 models because it performs slightly better against the UK data than the other NGA-West 2 models. From the ASCR models for Europe and the Middle East (AKK14; BIN14; and KOT20), we select the model of BIN14. Although the AKK14 GMPE has a slightly better performance against the UK data, the differences in terms of LLH and EDR are small and the model of BIN14 has been used in the recent PSHA for nuclear sites in the UK (Tromans et al., 2019; Villani et al., 2020; Aldama-Bustos et al., 2022). We exclude the GMPE of KOT20 because the use of individual branches in the backbone logic tree has not been subject to extensive testing yet. We select the model of RE19 for the stress drop of 10 MPa. This is in agreement with Villani et al. (2019) who compare spectral accelerations obtained from available instrumental ground-motion data in the UK with the predictions from various GMPEs including RE19 and suggest that the model for 10 MPa fits the observations best. From the three models for SCRs, we select the YEN15 GMPE, which has the best performance. To complete the suite of GMPEs for this work, we select also the GMPE of CAU15, which performs relatively well against the UK ground motion data and was derived using a different dataset from the other candidate GMPEs.

We assign the highest weight (0.30) to YEN15 because of their good performance in the statistical tests. The GMPEs of ASK14, BIN14, and CAU15 are given the same weight of 0.20 because they perform very similar to each other but less well than the YEN15 GMPE. The lowest weight is assigned to RE19 despite its good performance against the UK data because this model is poorly constrained at short distances and for long periods. The GMPEs selected for the GMC model, together with their weights, are given in Table 8. They imply that the ground motion models for ASCRs (i.e., ASK14, BIN14, and CAU15) are two times more likely than a GMPE for SCRs (i.e., YEN15). This is because the seismological properties of the UK, such as the anelastic attenuation model and κ_0, are more similar to those for active crustal regions, such as California, than CENA (Sargeant and Ottemöller, 2009; Ottemöller and Sargeant, 2013).

GMPE	*Weight*
ASK14	0.2
BIN14	0.2
CAU15	0.2
YEN15	0.3
RE19	0.1

Table 8: Logic tree for the median prediction of the GMC model developed for this work.

This suite of GMPEs is an update of the ground motion logic tree used in the national PSHA for the UK (Mosca et al., 2022) where the model of Rietbrock et al. (2013) and Atkinson and Boore (2006) have been superseded by their more recent updates (i.e. RE19; YEN15). Furthermore, we have used a larger dataset of high-quality recordings for PGA, $SA_{0.2\ s}$, $SA_{1.0\ s}$ than in Villani et al. (2019) and Mosca et al. (2022) for our evaluation of the candidate GMPEs. The suite of GMPEs in Table 8 is very similar to the ground motion logic tree for the site-specific PSHA in Aldama-Bustos et al. (2022). The main difference is that Aldama-Bustos et al. (2022) selected the model of CY14 and RE19 for a 5 MPa stress drop, rather than ASK14 and RE19 for a 10 MPa. In both cases, our selection is driven by the results from the statistical analysis in Section 6.2. The GMPE of CY14 has been identified as a highly adaptable ground motion model for regions with crustal earthquakes since it has a functional form that closely mimics the theoretical scaling implicit in stochastic simulations and includes terms that can be individually adjusted for host-to-target region differences in source, path, and site characteristics (Bommer and Stafford, 2020; Stafford et al., 2022). However, since in this project, we will adjust the

GMPEs only for the site characteristics, we have selected the GMPEs that fit better the UK observations.

The selected GMPEs in Table 8 agree well with the set of GMPEs of Carlton et al. (2022). However, they selected models that were derived using the same recording datasets, such as AKK14 and BIN14. Standard practice for PSHA recommends selecting GMPEs, which are derived from different recording datasets to fully capture the epistemic uncertainty in the median prediction of the GMC model (Bommer and Scherbaum, 2008). Moreover, the model of Atkinson and Boore (2011) has been superseded by YEN15. Finally, the model of Akkar and Cağnan (2010) was derived using the Turkish strong-motion database. The databases of Akkar et al. (2014b) and Lanzano et al. (2019) include also recordings from Turkey and therefore considering this specific ground motion model in the GMC model would be a redundancy.

6.4 HOST-TO-TARGET ADJUSTMENTS

GMPEs used for estimating earthquake ground motions are usually based on empirical data from regions where there are large numbers of recordings. Such GMPEs reflect the site conditions of the region for which they were derived, usually referred to as the host region. Before using the GMPEs in PSHA, they should be adjusted for the region under investigation, usually referred to as the target region. Here, we apply the HTTAs to account for differences in site conditions between the host and the target (e.g. Douglas and Edwards 2016). This process accounts for both the effects of elastic amplification due to shear wave velocity structure and near-surface attenuation at a site. The near-surface site-specific attenuation is described by the parameter κ_0, which represents the attenuation of shear waves at a given site as a result of the physical properties of the near-surface rocks and soils.

We follow the approach of Al Atik et al. (2014) that is also used to determine HTTAs for the recent PSHA works for the nuclear sites in the UK (Tromans et al., 2019; Villani et al., 2020; Aldama-Bustos et al., 2022), and the national seismic hazard maps (Mosca et al., 2022). The reader can refer to Mosca et al. (2020) for an extensive description of the procedure.

6.4.1 Input parameters

The input parameters required for the HTTAs are the Vs profile and the near-surface site-specific attenuation parameter (κ_0) for the target site and the host region for the selected GMPEs.

We use the generic Vs profile given for the target Vs30 of 800 m/s across the entire UK offshore EEZ (see Figure 35a). This profile is derived using the approach outlined by Cotton et al. (2006), which provides a smooth velocity profile, where the velocities at specific depths are interpolated from the generic models of Boore and Joyner (1997). Between these depths, the velocities are represented by a power-law model. The target κ_0 value is computed for the target Vs30 = 800 m/s using the empirical relationship between Vs30 and κ_0 of Van Houtte et al. (2011), which was derived from a large number of measurements worldwide. We estimate a value for κ_0 of 0.027 s for Vs30 = 800 m/s. We use the standard deviation of 0.55 in $ln(\kappa_0)$ (Van Houtte et al., 2011) to estimate lower and upper bounds for κ_0 of 0.016 and 0.047 s, respectively. This allows us to account for epistemic uncertainty in κ_0. The three values of κ_0 (0.016, 0.027, and 0.047 s) are assigned weights of 0.2, 0.6, and 0.2 following a three-point approximation to a normal distribution (Miller and Rice, 1983).

We use the Vs profile of Cotton et al. (2006) for 800 m/s for the GMPEs of BIN14 and CAU15; whereas the host 760 m/s Vs profile for the model of ASK14 is given in Al Atik and Abrahamson (2021). The Vs profile for the GMPE of RE19 is the generic Vs profile for the UK given by Booth et al. (2001) that was derived for Central Scotland using data from the lithospheric seismic profile in Britain. YEN15 uses the amplification factors of Atkinson and Boore (2006) who do not provide the Vs profile. We apply the Quarter Wavelength method (Boore, 2003) to estimate frequency-dependent site amplification factors for the target and host velocity profiles. Figure 35 shows the Vs profile and site amplification factors for the target site and the host GMPEs, together with the host-to-target amplification ratios used for correcting the FAS.

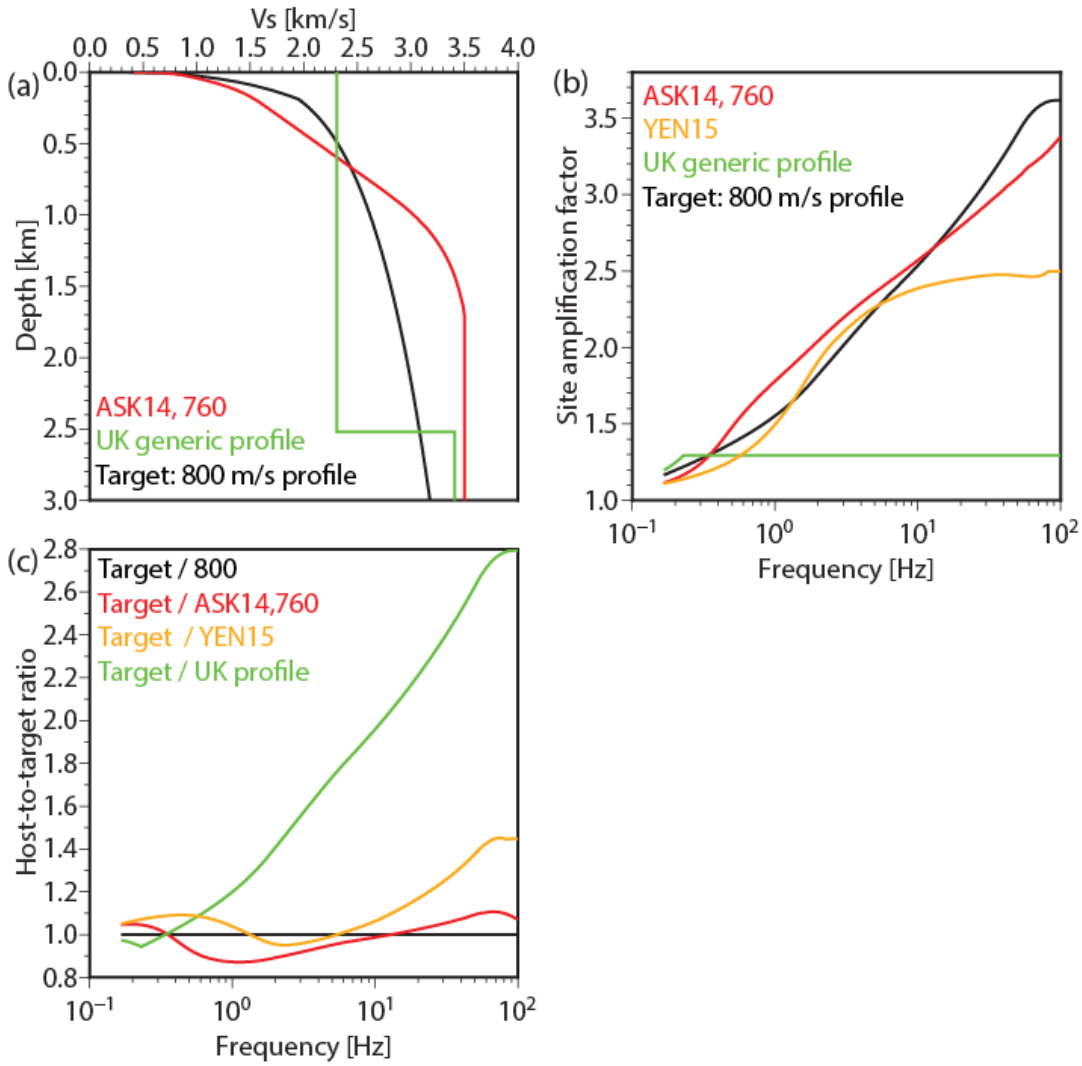

Figure 35: (a) Target and host Vs profiles used for the five GMPEs in Table 8. (b) Target and host site amplification factors used for the FAS of each GMPE. (c) Host-to-target amplification ratios.

6.4.2 Results

Figure 36 shows how we implement the HTTA procedure to scale the GMPE of ASK14 to a target κ_0 of 0.027 s, Vs30 = 800 m/s, and the Vs profile of Cotton et al. (2006) for the scenario of a 5.0 Mw earthquake at a Joyner-Boore distance (Rjb) of 5.0 km. The approach consists of the following steps:

1) Compute the response spectra from the GMPE for the selected earthquake scenario and Vs30 = 800 m/s.

2) Convert the response spectra into Fourier amplitude spectra using the Inverse Random Vibration Theory.

3) Host κ_0 is computed from the slope in the high-frequency part of the corrected FAS spectra by fitting the Anderson and Hough (1984) κ function in a given frequency range. The lower and upper limits of this frequency range, f_1 and f_2 (green line in Figure 36), are picked by visual inspection to ensure that the natural logarithm of the FAS as a function of the frequency is linear within this frequency range. Al Atik et al. (2014) suggest that f_2 should be smaller than 35 Hz, i.e. the frequency limit for the Brune (1970) single-corner-frequency point-source model developed for the western United States. PNNL (2014) suggest that f_2 should not exceed 20 Hz for the western United States. Here, we use f_2 = 20 Hz, while f_1 equals the frequency for the maximum value of the FAS plus 2 Hz. These frequency limits generally allow us to consider the largest acceptable portion of the

corrected FAS to estimate the host κ_0 value. The κ_0 value is the average of the first derivatives of $ln[a(f)]$ between f_1 and f_2 and divided by $-\pi$.

4) If $\kappa_{0,host}$ is greater than $\kappa_{0,target}$ and the frequency is higher than f_1, the FAS is replaced by a straight line fit to the FAS slope between f_1 and f_2 (black dashed line in Figure 36). This step avoids having an increase in the FAS at high frequencies when the kappa corrections are applied. If $\kappa_{0,host} < \kappa_{0,target}$, the FAS remains unchanged.

5) The FAS is multiplied by $exp[-\pi f (\kappa_{0,target} - \kappa_{0,host})]$ where f is the frequency (red line in Figure 36) to obtain the κ_0 – adjusted FAS.

6) To adjust the FAS to the target Vs profile, the FAS is multiplied by the ratio between the target-to-host site amplification factors computed using the Quarter Wavelength method (cyan solid line in Figure 36).

7) The Vs – κ_0 scaled FAS is converted into response spectra using the Random Vibration Theory (orange line in Figure 36).

8) The HTTA factors are computed by dividing the Vs – κ_0 scaled FAS by the initial GMPE response spectra.

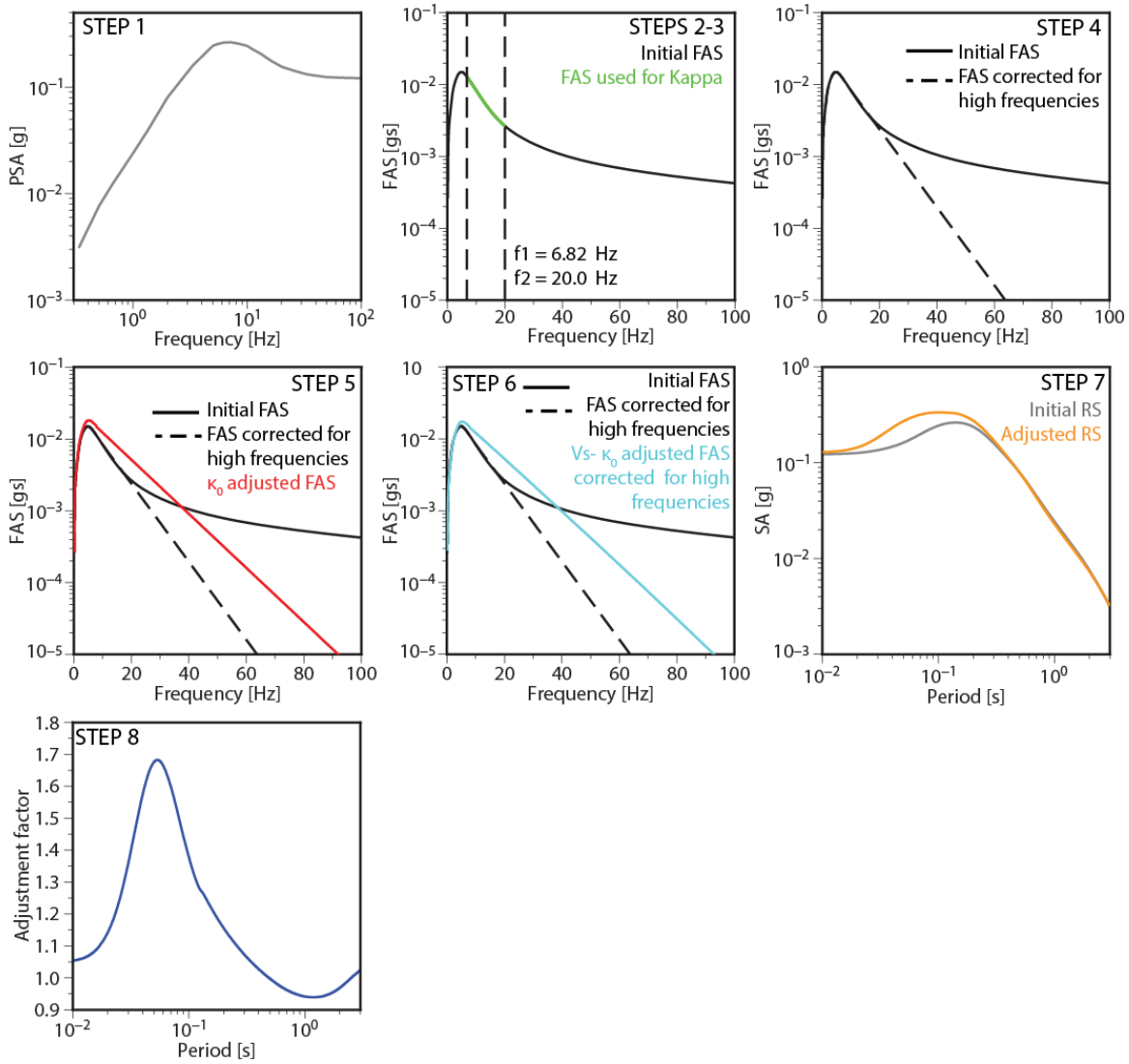

Figure 36: Example of the Inverse Random Vibration Theory for the GMPE of ASK14. The case study is for the earthquake scenario of 5.0 Mw, Rjb of 5.0 km, 15 km focal depth, strike-slip faulting, Vs30 = 800 m/s, and the Vs profile of Cotton et al. (2006). After Al Atik et al. (2014).

Response spectra are calculated using each GMPE for different earthquake scenarios with different magnitude and distance combinations. Since the HTTA factors are larger at short distances (≤ 20 km) and high frequencies (> 10 Hz; Al Atik et al., 2014), we select nine earthquake scenarios based on the disaggregation analysis in the high-frequency range in Mosca et al. (2022): Mw = 4.0, 5.0, and 6.0, and Rjb = 5, 15, and 25 km. The final HTTA curve for the GMPE is the average from all nine scenarios. This selection is in agreement with the disaggregation analysis for PGA and $SA_{0.2\ s}$ in Section 7.1, except for the Acorn site where far-distance earthquakes dominate the hazard at short periods. Since HTTAs are insensitive to far distances, we did not consider this earthquake scenario here.

Figure 37 shows the calculated HTTA factors as a function of the period for each of the five GMPEs in Table 9 using the Vs profile of Cotton et al. (2006). These are the average values of all nine scenarios. Calculated adjustments for both the median value and the upper and lower limits in our target κ_0 are shown. The average $\kappa_{0,host}$ values calculated using the Inverse Random Vibration Theory for the five GMPEs are shown in Table 9. For the three empirical GMPEs (i.e., ASK14; BIN14; and CAU15), the average $\kappa_{0,host}$ values are larger than the median target κ_0 value of 0.027 s, whereas for the models of YEN15 and RE19 these are smaller than $\kappa_{0,target}$.

GMPE	$\kappa_{0,host}$ *[s]*
ASK14	0.0392 ± 0.0021
BIN14	0.0375 ± 0.0057
CAU15	0.0347 ± 0.0035
RE19	0.0162 ± 0.0038
YEN15	0.0163 ± 0.0020

Table 9: Average $\kappa_{0,host}$ values of the GMPEs in the GMC model. These are the average values of the nine scenarios.

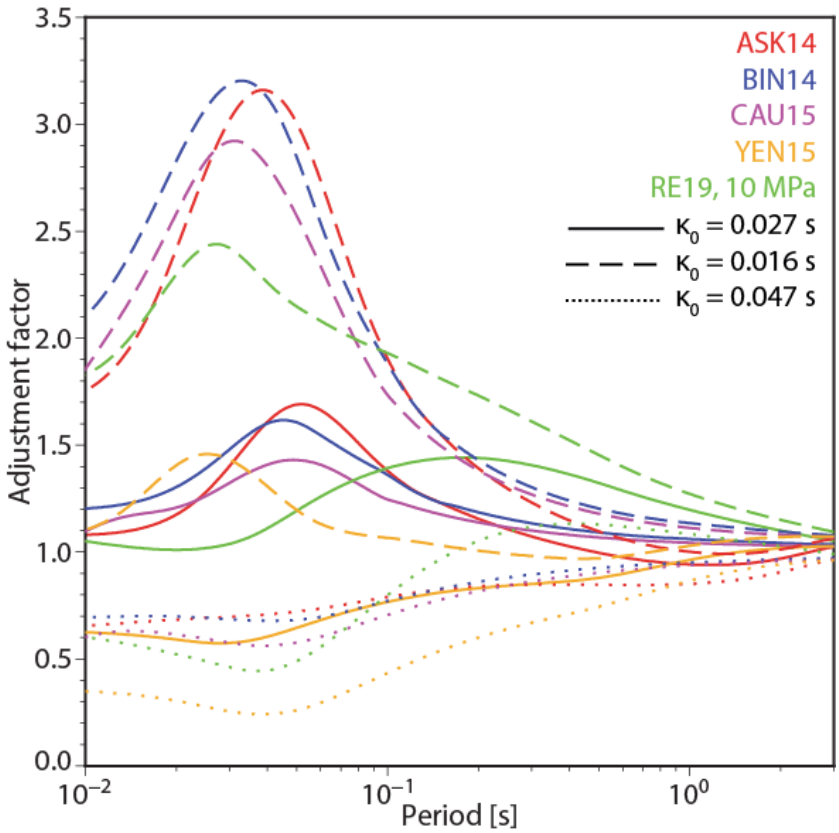

Figure 37: HTTA factors for the five GMPEs Table 8 using the Vs profile of Cotton et al. (2006).

Overall, the calculated adjustment factors for PGA and the GMPEs vary between approximately 0.6 and 1.7 for κ_0 = 0.027 s (Figure 37). The adjustments for the three empirical GMPEs have a similar form, with a peak at 0.03-0.05 s and values that decrease at longer periods. These results are consistent with the calculated values for the host κ_0 for the GMPEs, which are all larger than those for the target (Table 8). This suggests that the differences in the site conditions from host to target are due to the near-surface attenuation rather than elastic amplification since the host and target Vs profiles are the same. We observe notable differences in the period-dependent adjustments for the stochastic GMPEs (YEN15; RE19). This may be a result of differences in both elastic amplification and κ_0 for the host and target site. Specifically, the adjustment factors for YEN15 are between 0.5 and 0.7 at periods of less than 0.1 s and increase up to ~1.0 at long periods. The adjustment factors for RE19 have a peak of 1.4 at 0.2 s and then decrease to 1 for longer periods.

The calculated adjustments for upper and lower target κ_0 allow us, to some extent, to assess the effect of epistemic uncertainty in target κ_0 on the results. The adjustments for the lower $\kappa_{0,target}$ value of 0.016 s are consistently larger than those for the $\kappa_{0,target}$ value of 0.027 s, and are greater than 1.0 for all GMPEs at most periods. Conversely, adjustments for the upper $\kappa_{0,target}$ value of 0.047 s are less than 1.0 for all the GMPEs.

6.5 GLOBAL ERGODIC SIGMA MODEL

Recordings of strong ground motions are rarely available for a specific site, so PSHA generally invokes the ergodic assumption (Anderson and Brune, 1999), which states that variability over space can be used as a substitute for variation over time. However, for a specific site of interest, repeatable contributions to the seismic motion (i.e., the site term) can be modelled by an appropriate adjustment to the median ground-motion predictions. In this case, the aleatory variability in the GMPEs (sigma) can be reduced by an amount that reflects the variability in the site term. This concept is referred to as nonergodic sigma (Anderson and Brune, 1999) and the resulting value of sigma is referred to as single-station sigma (Atkinson, 2006).

Following Rodriguez-Marek et al. (2014), the within-event residual in Equation (8) can be further separated into two terms:

$$\delta W_{es} = \delta S2S_s + \delta WS_{es} \tag{12}$$

where $\delta S2S_s$ represents the systematic deviation of the observed ground motion at site *s* from the median event-corrected ground motion predicted by the GMPE, and δWS_{es} is the site- and event-corrected residual. The standard deviations of δB_e (the between-event residuals in Equation 8), $\delta S2S_s$ and δWS_{es} are τ, φ_{S2S} and φ_{SS}, respectively. Under the ergodic assumption, the residuals are considered as part of the aleatory variability so that

$$\sigma_{ergodic} = \sqrt{\tau^2 + \varphi_{SS}^2 + \varphi_{S2S}^2} \tag{13}$$

In the partially nonergodic approach, the site term, $\delta S2S_s$, is assumed to be known, so φ_{S2S} can be excluded from Equation (13) and the single-station sigma is given by

$$\sigma_{SS} = \sqrt{\tau^2 + \varphi_{SS}^2} \tag{14}$$

While the net effect on the mean hazard is expected to be close to zero because the increased epistemic uncertainty is balanced by the decreased aleatory variability, the application of single-station sigma results in a clearer separation between aleatory and epistemic uncertainties. It also avoids any double-counting of uncertainty that might result if the site-to-site variability is included in the total sigma and assigned an epistemic uncertainty in the logic tree of the HTTAs.

The single-station sigma approach can only be applied if the following three requirements are satisfied (Rodriguez-Marek et al., 2014):

- The site term is known with accuracy.
- The epistemic uncertainty in the site term is taken into account.
- The epistemic uncertainty in the site term is incorporated into the PSHA.

Although these conditions are partially satisfied by the use of the HTTA procedure, we do not include uncertainty in the Vs shear profile and therefore the epistemic uncertainty in the site term is not fully incorporated. For this reason, here we use the ergodic sigma model in Equation 13.

Al Atik (2015) develop a global ergodic $\sigma_{ergodic}$ model using the four GMPEs of the NGA-West 2 project, ASK14, BSSA14, CB14, and CY14. These models were chosen because they were derived from a large uniformly processed global dataset and are applicable to a large range of magnitudes (from 3.0 to 8.0 or 8.5 Mw). The global magnitude-dependent $\sigma_{ergodic}$ model results from the global τ, φ_{ss}, and φ_{S2S} model and has the following form:

$$\sigma_{ergodic} = \begin{cases} \sigma_1 & for\ M \leq 4.5 \\ \sigma_1 + \frac{(Mw-4.5)(\sigma_2-\sigma_1)}{0.5} & for\ M \leq 5.0 \\ \sigma_2 + \frac{(Mw-5.0)(\sigma_3-\sigma_2)}{0.5} & for\ M \leq 5.5 \\ \sigma_3 + \frac{(Mw-5.5)(\sigma_4-\sigma_3)}{1.0} & for\ M \leq 6.5 \\ \sigma_4 & for\ M > 6.5 \end{cases} \quad (15)$$

where $\sigma_1, \sigma_2, \sigma_3, \sigma_4$ are the model coefficients from the magnitude breaks of the τ model at 4.5, 5.0, 5.5, and 6.5 Mw, respectively.

In the present work, we adopt this global ergodic sigma model, together with the standard deviation from Al Atik (2015). We did not use the sigma model from the individual GMPEs in the ground motion logic tree because the sigma model for the stochastic models is not considered to be as reliable as empirically derived sigma models. Figure 38 shows the comparison of the global τ, φ_{ss}, $\sigma_{ergodic}$ models, together with the standard error, and the between-event, within–event and total sigma of each of the three empirical GMPEs in Table 9. The global between-event sigma model of Al Atik (2015) is period-independent but magnitude-dependent which are physically justified features. Furthermore, it includes the tau model of the empirical GMPEs within one standard deviation (Figure 38a). The τ model of Cauzzi et al. (2015) is larger than the others due to the Pan-European event terms associated with reverse faults, especially those of the 2012 Emilia (Northern Italy) sequence (Cauzzi and Faccioli, 2018). The global within-event model of Al Atik (2015) seems to be underestimated compared to the φ model of the empirical GMPEs (Figure 38c); whereas the total ergodic sigma model includes well the σ models of the empirical GMPEs within one standard deviation except that for Cauzzi et al. (2015).

Al Atik (2015) assign weights of 0.63, 0.185 and 0.185 for the three branches of the global $\sigma_{ergodic}$ model following a continuous scaled χ-square distribution.

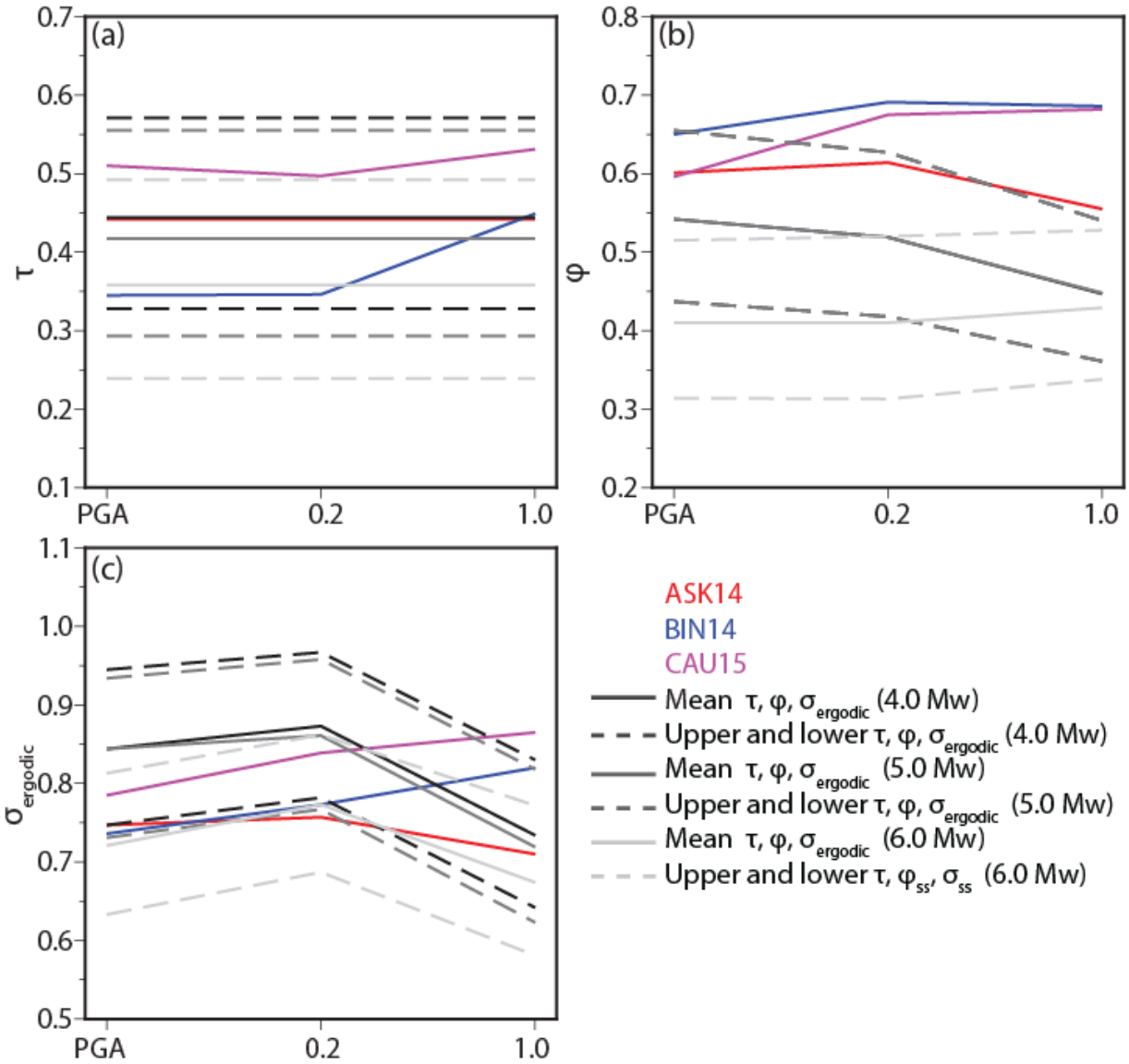

Figure 38: Comparison of (a) the global between-event sigma (τ), (b) single-station within-event sigma (φ), and (c) total ergodic sigma ($\sigma_{ergodic}$) models, together with their standard error, and the between-event, within-event and total sigma from the individual three empirical GMPEs in Table 9. They are given for PGA, 0.2 s and 1.0 s. The sigma values are expressed in a natural logarithmic scale.

7 Hazard calculations

The logic tree for the SSC and GMC models used in the hazard computation is shown in Figure 39. However, we did not include some of the branches of the SSC model (e.g. faulting style) to simplify the figure. The reader can refer to Section 5 for a full description of the SSC model.

We used the Monte Carlo-based approach for PSHA where the branches in the SSC and GMC logic tree are sampled at random based on their weights (see Section 2.1). Using the SSC model (top panel in Figure 39 and Section 5), we generate 100,000 synthetic earthquake catalogues, each 100 years long. This gives a total of 10,000,000 years of simulated data, which is sufficient to resolve the hazard accurately for return periods up to 10,000 years (Musson 2000). The ground motion for each earthquake in the simulated catalogues is computed using the ground motion logic tree at the bottom panel of Figure 39 (see Section 6). The sigma model used in the hazard calculations is described in Subsection 6.5. We did not truncate the ground motion distribution above and below the median predictions. Strasser et al. (2009) show that although there must be a physical limit, a purely statistical truncation is not

justified with current strong motion datasets. We did not consider the correlation between inter-event and within-event residuals.

Sorting the ground motion results in order of decreasing severity allows us to identify ground motions associated with different frequencies of exceedance (Musson 2000).

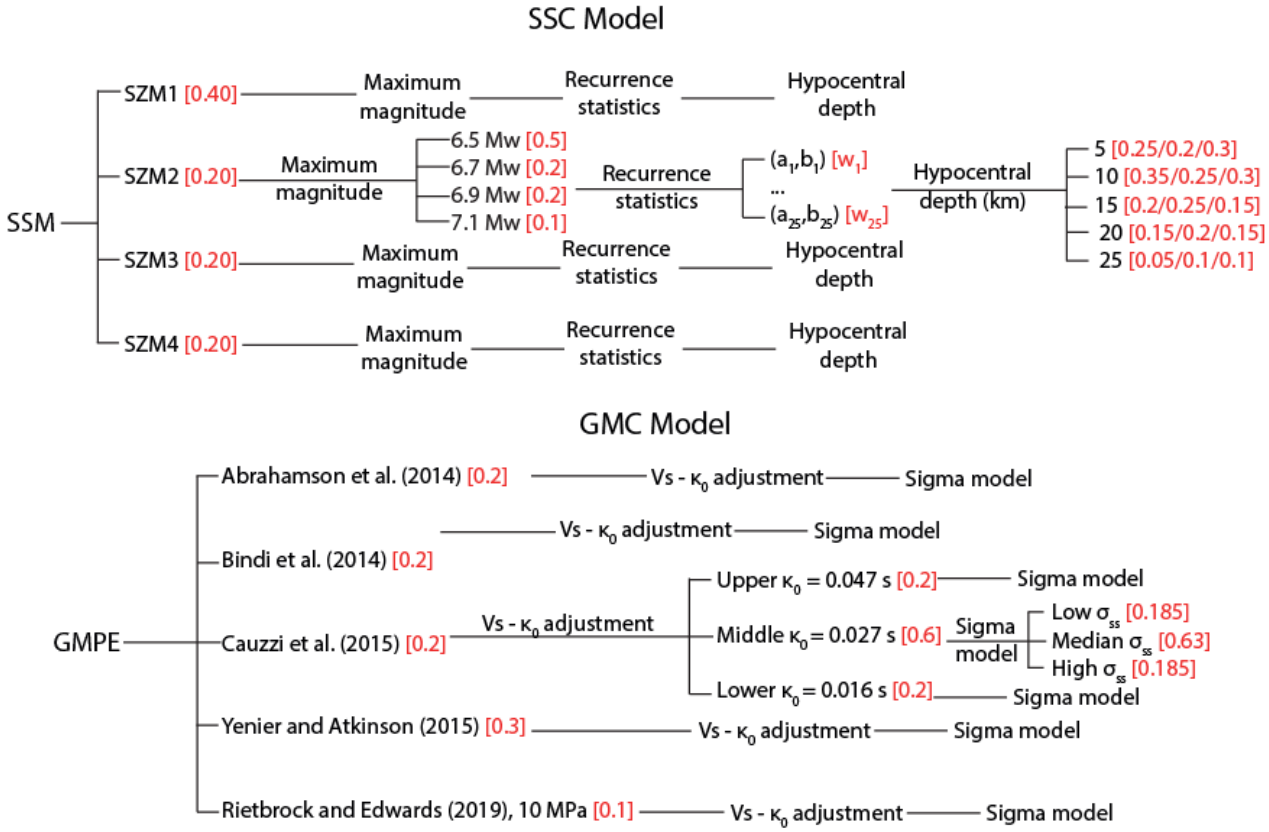

Figure 39: Summary of the SSC and GMC logic tree for this work. The three weights for the depth distribution are for the UK and Ireland, the North Sea and Northern France and Belgium.

The hazard maps cover the UK offshore EEZ and the hazard has been calculated for a grid of 4585 points that are spaced 0.125° in latitude and 0.25° in longitude (this is the same grid spacing used by Mosca et al., 2022). We have estimated the hazard for PGA, $SA_{0.2\,s}$, and $SA_{1.0\,s}$ for 5% damping on rock conditions (Vs30 = 800 m/s) and for return periods of 475 years (Figure 40) and 2475 years (Figure 41). The seismic hazard maps for return periods of 95, 1100, and 5000 years are shown in Appendix 3. Note that we use the same colour scale as Mosca et al. (2022) to facilitate the comparison between the two studies. Also, the hazard maps in Figures 40-41 and Appendix 3 do not show the hazard of UK onshore, which is described in Mosca et al. (2020, 2022).

For 475 years, PGA is less than 0.02 g for most of the UK offshore EEZ, except for the northern North Sea east of Shetland, around the western isles of Scotland, in the Irish Sea, particularly close to North Wales, and the southern North Sea immediately offshore Lincolnshire and East Anglia, where the hazard reaches around 0.07 g, 0.03 g, 0.05 g, and 0.05 g, respectively (left panel of Figure 40). The hazard values are higher at 0.2 s reaching 0.16 g, 0.05 g, 0.11 g, and 0.10 g in the same locations (central panel of Figure 40). At 1.0 s, accelerations are smaller than 0.02 g everywhere (right panel of Figure 40).

Figure 41 shows hazard maps for a return period of 2475 years. The hazard values in the northern North Sea, the Irish Sea close to North Wales, and the southern North Sea increase to 0.19 g, 0.18 g, and 0.13 g for PGA, and 0.39 g, 0.35 g, and 0.27 g for $SA_{0.2\,s}$, respectively. Hazard values for $SA_{1.0\,s}$ do not exceed 0.06 g even in the areas of highest hazard.

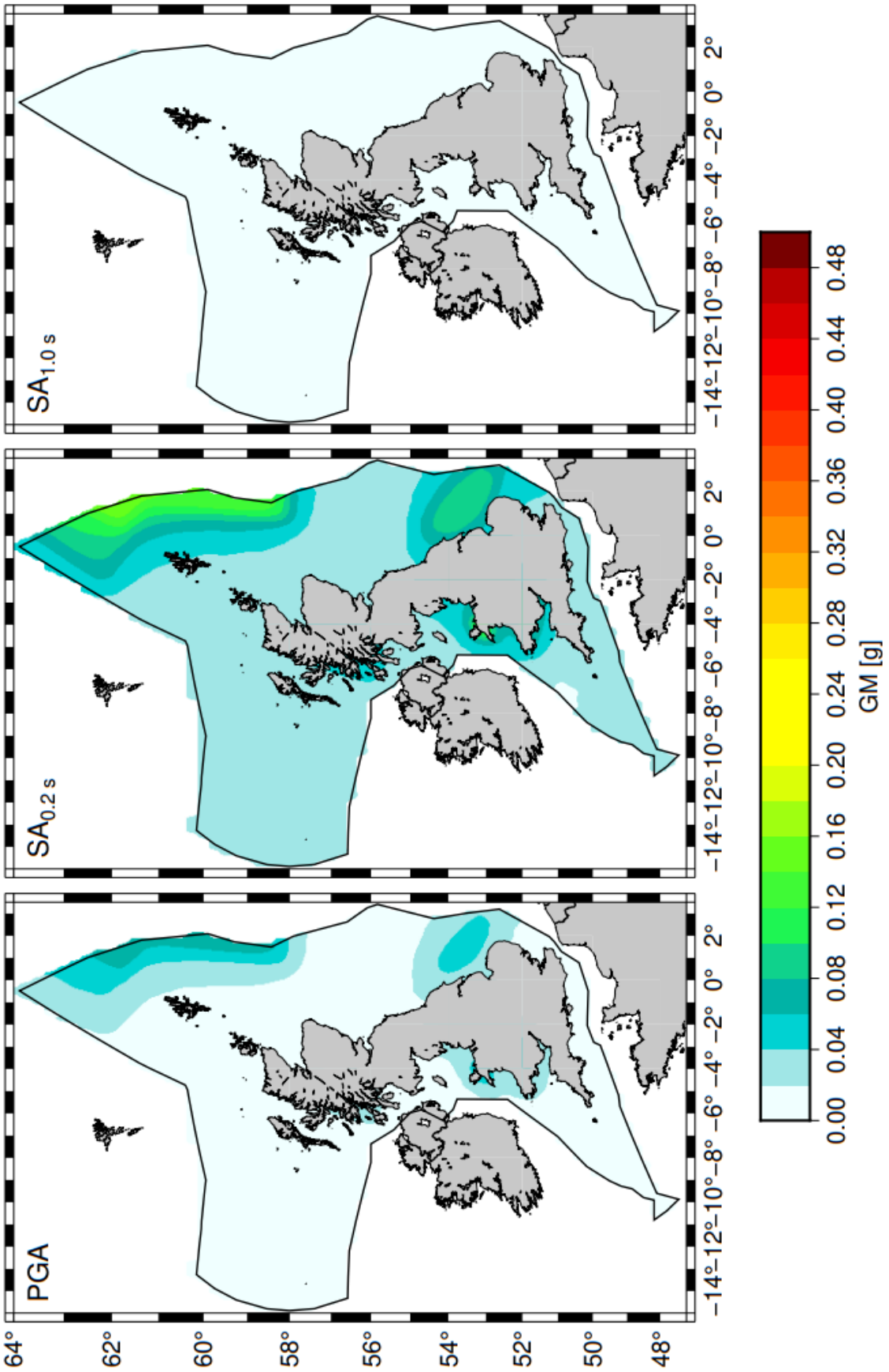

Figure 40: Hazard map for PGA, $SA_{0.2\ s}$, and $SA_{1.0\ s}$ at the 475-year return period. The black polygon describes the UK offshore EEZ.

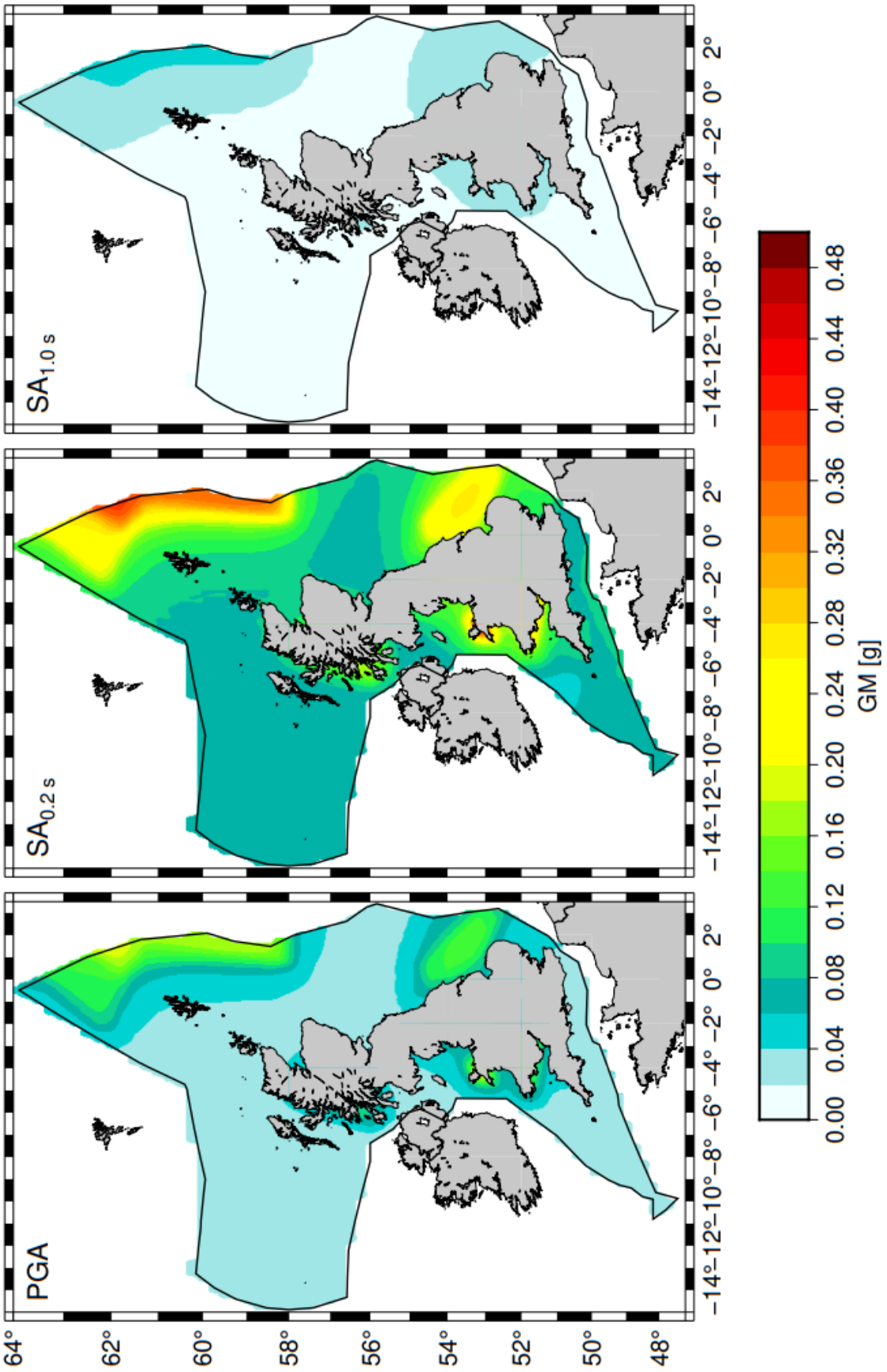

Figure 41: Hazard map for PGA, $SA_{0.2\ s}$, and $SA_{1.0\ s}$ at the 2475-year return period. The black polygon describes the UK offshore EEZ.

7.1 RESULTS FOR EXAMPLE SITES

We have also computed the hazard for three selected CCS license areas: Acorn (58.10°N, 0.60°W) in the Moray Firth Basin, Endurance (54.23°N, 1.00°E) in the Sole Pit Basin, and the HyNet North West storage area (53.60°N, 3.5°W) in the southeast Irish Sea (see bottom right-hand side plot in Figure 42). Note that for the Endurance area, we selected the site which produces the highest hazard, which is indicated as Endurance 1 in Appendix 4. The hazard curves for PGA, $SA_{0.2\,s}$, and $SA_{1.0\,s}$ are shown in Figure 42. Table 10 gives the PGA, $SA_{0.2\,s,}$ and $SA_{1.0\,s}$ for the three sites and two return periods (475 years and 2475 years). The uniform hazard spectra for 475 years and 2475 years are shown in Figure 43. These show the hazard values for different periods of ground motion with an equal probability of exceedance and demonstrate that the hazard values peak between periods of 0.1 to 0.4 s. These results should not be considered as a substitute for site-specific assessments of the hazard in these locations and are only intended to provide a regional indication of the seismic hazard in UK waters.

Site	*Return period [yr]*	*PGA [g]*	*$SA_{0.2\,s}$ [g]*	*$SA_{1.0\,s}$ [g]*
Acorn	475	0.016	0.037	0.008
Acorn	2475	0.041	0.098	0019
Endurance	475	0.040	0.085	0.011
Endurance	2475	0.113	0.234	0.031
HyNet North West	475	0.026	0.059	0.010
HyNet North West	2475	0.071	0.160	0.027

Table 10: PGA, $SA_{0.2\,s}$, and $SA_{1.0\,s}$ for the Acorn, Endurance, and HyNet and two return periods.

We disaggregate the results for these sites by magnitude, distance, and epsilon ε (the number of standard deviations above or below the median ground motion prediction), and by zone. Note that ε was computed from the ergodic sigma model. The disaggregation analysis aims to identify the earthquakes that control the hazard for the key return periods and can either be done analytically (McGuire, 1995) or empirically (Musson, 1999). The latter is straightforward using the Monte Carlo approach and follows on from the simulations used to compute the hazard. We do this by searching the synthetic catalogues to find those events that resulted in the design acceleration (plus or minus a small tolerance factor, we use 0.001 g here) and then compare their distribution in terms of magnitude, distance, and epsilon. We can also disaggregate the results by zone. The design accelerations are the values listed in Table 10 for the three CCS sites and the return periods of 475 and 2475 years.

The results in Figures 44-49 show the contribution to the hazard (in %) for PGA, $SA_{0.2\,s}$, and $SA_{1.0\,s}$ in terms of Mw, Joyner-Boore distance (Rjb), and ε. The analysis selects magnitude bins of 0.2 units and distance bins of 10 km. Disaggregating by zone for the Acorn site shows that the hazard is dominated by the zones VIKI1 and VIKG4 in the Viking Graben in the North Sea for 475 and 2475 years (10 - 18% for PGA, $SA_{0.2\,s}$, and $SA_{1.0\,s}$) and the ESCO1 zone, which comprises Eastern Scotland and the Moray Firth Basin (18% for PGA and $SA_{0.2\,s}$ and 475 years; 22-25% for PGA and $SA_{0.2\,s}$ and 2475 years; 10-13% for $SA_{1.0\,s}$ and the two return periods). The southern North Sea zones control the hazard at the Endurance site. The largest contribution to PGA is from the SLPT1 zone that includes the Sole Pit Basin in SZM1 (49-54% for PGA; 45-50% for $SA_{0.2\,s}$; and 30-39% for $SA_{1.0\,s}$) for 475 and 2475 years. For the HyNet North West site, the largest contributions to PGA are from the MENA1 zone that includes the Menai Straits fault system (16-19% for PGA and $SA_{0.2\,s}$; 11-15% for $SA_{1.0\,s}$), the EISB1 zone that includes the East Irish Sea Basin (11-19% for PGA; 10-15% for $SA_{0.2\,s}$; 5-9% for $SA_{1.0\,s}$), and the WACE4 zone that includes Wales and Central England (9-12% for PGA and $SA_{0.2\,s}$; 10-13% for $SA_{1.0\,s}$). The other zones contribute less than 5% to the hazard at the three sites. Table 11 shows an overview of the disaggregation results in terms of the zone indicating only the zones that contribute more than 5% to the hazard to avoid a lengthy table.

Contribution to hazard [%] for Acorn						
	PGA		$SA_{0.2\ s}$		$SA_{1.0\ s}$	
Zone	*475 yr*	*2475 yr*	*475 yr*	*2475 yr*	*475 yr*	*2475 yr*
ESCO1	18.8	25.9	17.5	22.2	9.5	12.6
VIKI1	17.7	11.4	18.3	13.9	14.1	16.4
ESCO2	8.4	12.4	7.7	10.4	4.0	5.6
VIKG2	5.1	3.4	5.9	4.3	5.1	5.3
ESHE3	4.8	8.9	4.1	7.1	1.7	2.5
VIKG3	9.0	6.4	9.4	8.0	7.5	8.5
WSHE4	4.6	8.0	3.8	6.9	1.8	2.5
VIKG4	17.8	13.9	17.8	16.5	13.2	14.9
Other zones	< 5.0	< 5.0	< 5.0	< 5.0	< 5.0	< 5.0
Contribution to hazard [%] for Endurance						
	PGA		$SA_{0.2\ s}$		$SA_{1.0\ s}$	
Zone	*475 yr*	*2475 yr*	*475 yr*	*2475 yr*	*475 yr*	*2475 yr*
SLPT1	49.0	54.3	45.2	50.4	30.2	38.8
SOLE2	8.7	4.1	9.7	5.1	9.7	10.3
SNSE3	18.1	18.7	18.7	18.8	13.3	15.6
HUNS4	16.0	17.5	16.0	18.4	12.0	14.6
Other zones	< 5.0	< 5.0	< 5.0	< 5.0	< 5.0	< 5.0
Contribution to hazard [%] for HyNet						
	PGA		$SA_{1.0\ s}$		$SA_{1.0\ s}$	
Zone	*475 yr*	*2475 yr*	*475 yr*	*2475 yr*	*475 yr*	*2475 yr*
MMCW21	8.3	4.7	9.7	6.8	11.5	11.5
MENA21	17.2	18.5	16.7	16.1	11.3	14.7
EISB1	11.8	19.1	9.9	15.2	5.1	8.6
NWAL22	7.3	8.2	7.0	7.6	5.2	6.2
LAKE2	5.3	8.6	5.0	5.9	2.5	3.9
NWAL13	7.9	3.7	7.0	7.4	3.7	0.0
NWAL23	7.9	7.0	7.4	7.5	5.5	6.8
WACE4	9.7	11.3	9.7	12.0	10.2	12.7

Table 11: Disaggregation results (by zone) for the three CCS sites and for PGA, $SA_{0.2\ s}$, and $SA_{1.0\ s}$ at 475 and 2475 years. Only zones that contribute more than 5% to the hazard are reported here.

Disaggregating the hazard by magnitude, distance and ε for the Acorn site (Figures 44-45), we observe that for 475, the greatest contribution to PGA and $SA_{0.2\ s}$ comes from relatively moderate earthquakes (4.0-4.5 Mw for PGA and $SA_{0.2\ s}$) at short (< 25 km) distances; whereas earthquakes of 5.7-5.9 Mw at large distances (195-205 km) contribute to $SA_{1.0\ s}$ (Figure 44). For 2475 years, moderate earthquakes dominate PGA and $SA_{0.2\ s}$ at short (< 20 km) distances; a broader range of earthquakes contributes to the $SA_{1.0\ s}$ hazard (distances of 80 -220 km and magnitudes of 5.3-6.5 Mw; Figure 45). For the Endurance site, the hazard for PGA, $SA_{0.2\ s}$, and

$SA_{1.0\ s}$ is dominated by moderate (4.3-5.0 Mw) earthquakes at close distances (< 20 km) for 475 years (Figure 46). For 2475 years, the hazard at Endurance is dominated by large (5.0-6.0 Mw) earthquakes at distances of 25-45 km (Figure 47). For the HyNet site, the hazard for PGA and $SA_{0.2\ s}$ is dominated by moderate (4.5-4.7 Mw) earthquakes at close (35-45 km) distances for 475 years (Figure 48); whereas for $SA_{1.0\ s}$, the magnitude of the contributing earthquakes slightly increases up to 5.5-5.7 Mw at distances of 45-55 km for 475 years (Figure 48). For 2475 years, the hazard is dominated by large earthquakes (5.3-6.1 Mw) at relatively small (25-45 km) distances Figure 49).

7.2 SENSITIVITY ANALYSIS

We have carried out a sensitivity analysis to investigate the impact of different decisions taken to develop the seismic hazard model on the seismic hazard for the three CCS sites in the North Sea. We tested the following features:

- Using each individual SZM in the SSC model rather than a combination of the four SZMs.
- The maximum magnitude distribution used for northern Europe in ESHM20, i.e. 6.3, 6.6, and 6.9 Mw with weights of 0.5, 0.4, and 0.1.
- Using a minimum magnitude of 4.5 and 5.0 Mw (rather than 4.0 Mw).
- Using each individual GMPE in the GMC model rather than a combination of the five GMPEs.
- Excluding the Vs-κ_0 adjustments from the GMC logic tree.

The results are expressed in terms of the percentage difference between the values of PGA, $SA_{0.2\ s}$, and $SA_{1.0\ s}$ for the individual tests and the values in Figure 42 for return periods of 475 years (Figure 50) and 2475 years (Figure 51). A percentage difference of less than ± 5% corresponds to a hazard variation between − 0.001 and 0.001 g; whereas a percentage difference < ± 20% results in a variation in the hazard between −0.02 and 0.02 g.

When each source model is used with a weight of one in the SSC model, for the Acorn site, the variation of the hazard is between -20% and 22% with the largest increase for SZM4 and the largest reduction for SZM2 (Figures 50-51). For 475 years and 2475 years, the hazard changes very little (< 5%) when only SZM1 or SZM3 is used. For the Endurance site and the two return periods, using only SZM1 results in an increase in the hazard (< 25% for the two return periods); whereas the hazard decreased down to -40% if only SZM2 is used in the SSC model. If the source model consists only of SZM3 or SZM4, the reduction in the hazard is down to less than 20%. For the HyNet North West site, the variation in hazard is less than 20% if the individual source models are used (Figures 50-51).

Using the Mmax distribution of ESHM20 for Central and North Europe results in an overall decrease in the hazard at all the sites. This reduction is more pronounced for $SA_{1.0\ s}$ because large earthquakes dominate the hazard for long periods. Using 4.5 Mw or 5.0 Mw as a minimum magnitude reduces the hazard for all the sites. This reduction is less pronounced for $SA_{1.0\ s}$ because large earthquakes dominate the hazard for long periods.

When we use the individual GMPEs in the GMC model, the variation of the hazard is between -61% and 100% for 475 and 2475 years with the largest variation associated with Rietbrock and Edwards (2019), which however has the lowest weight in the GMC model (see Section 6). Finally, if exclude the HTTAs for the GMPEs in the GMC model, it results in a reduction of the hazard (by -23%) for all the sites.

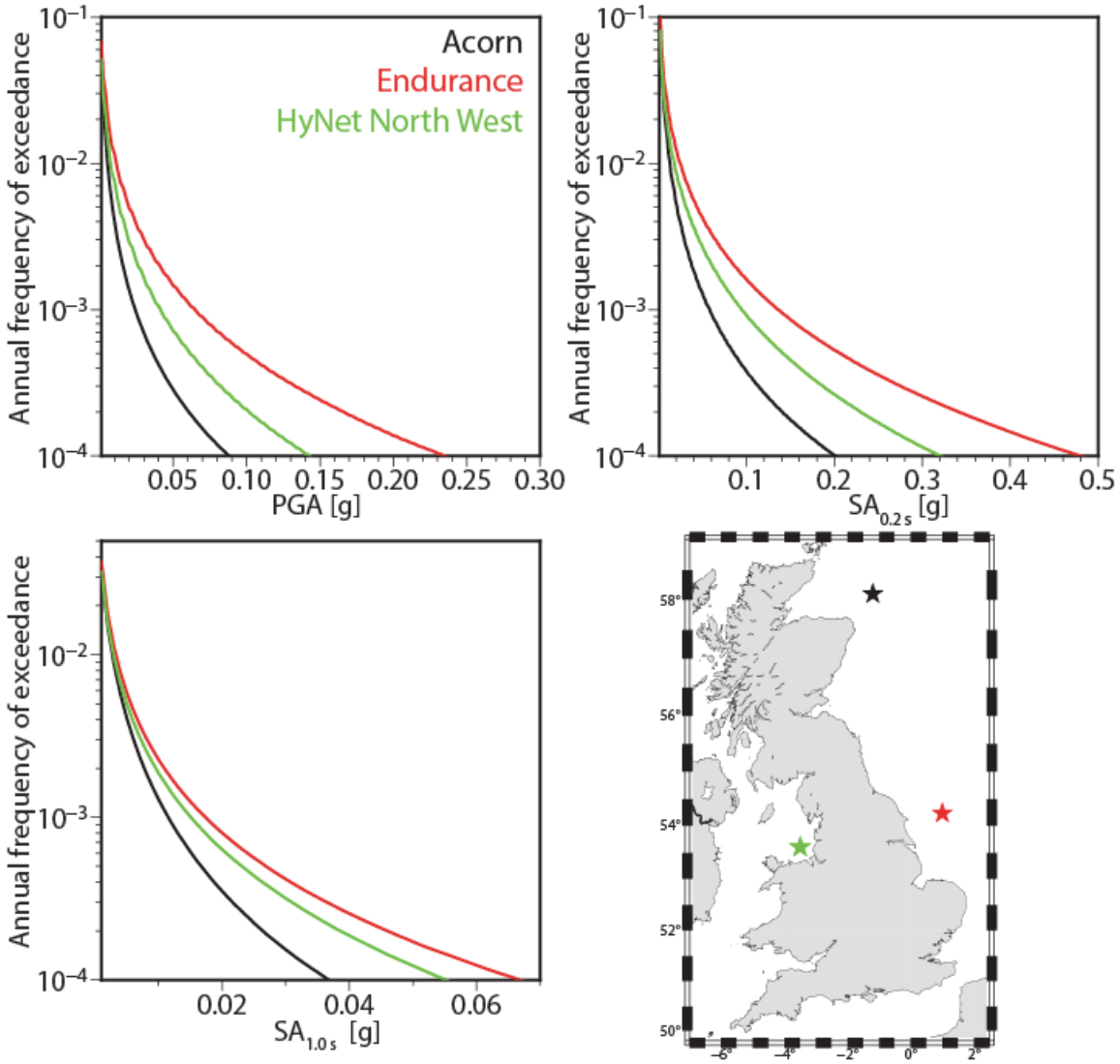

Figure 42: PGA, $SA_{0.2\,s}$, and $SA_{1.0\,s}$ hazard curves for sites in Acorn (black star), Endurance (green star), and the HyNet North West (red star).

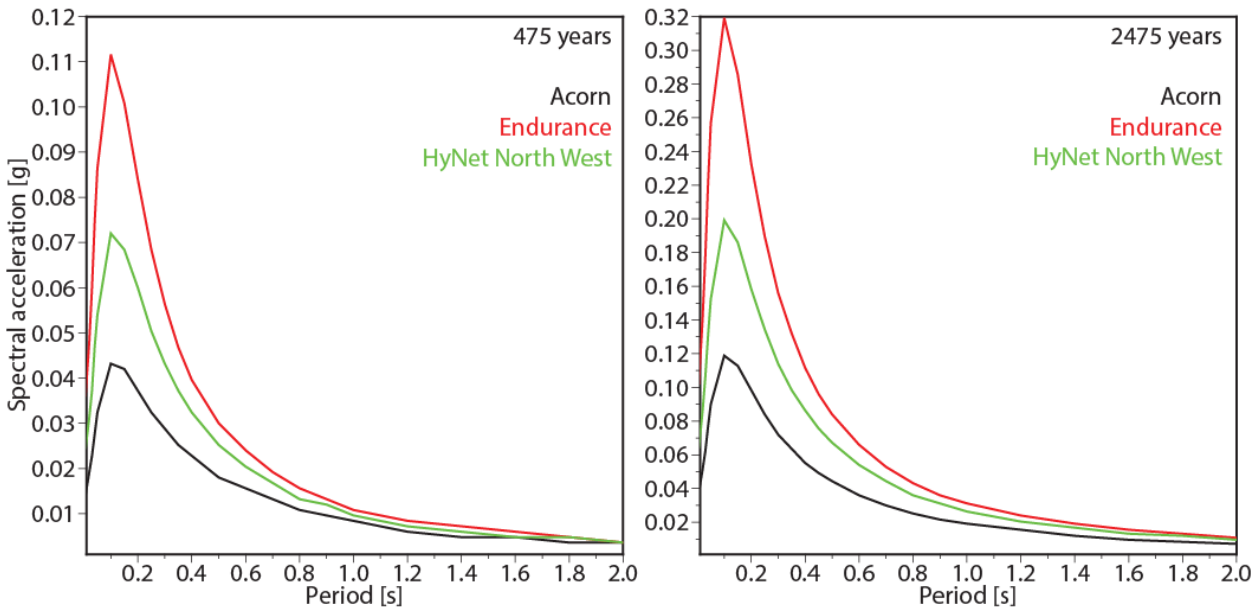

Figure 43: UHS for return periods of 475 years and 2475 years for the sites shown in Figure 42.

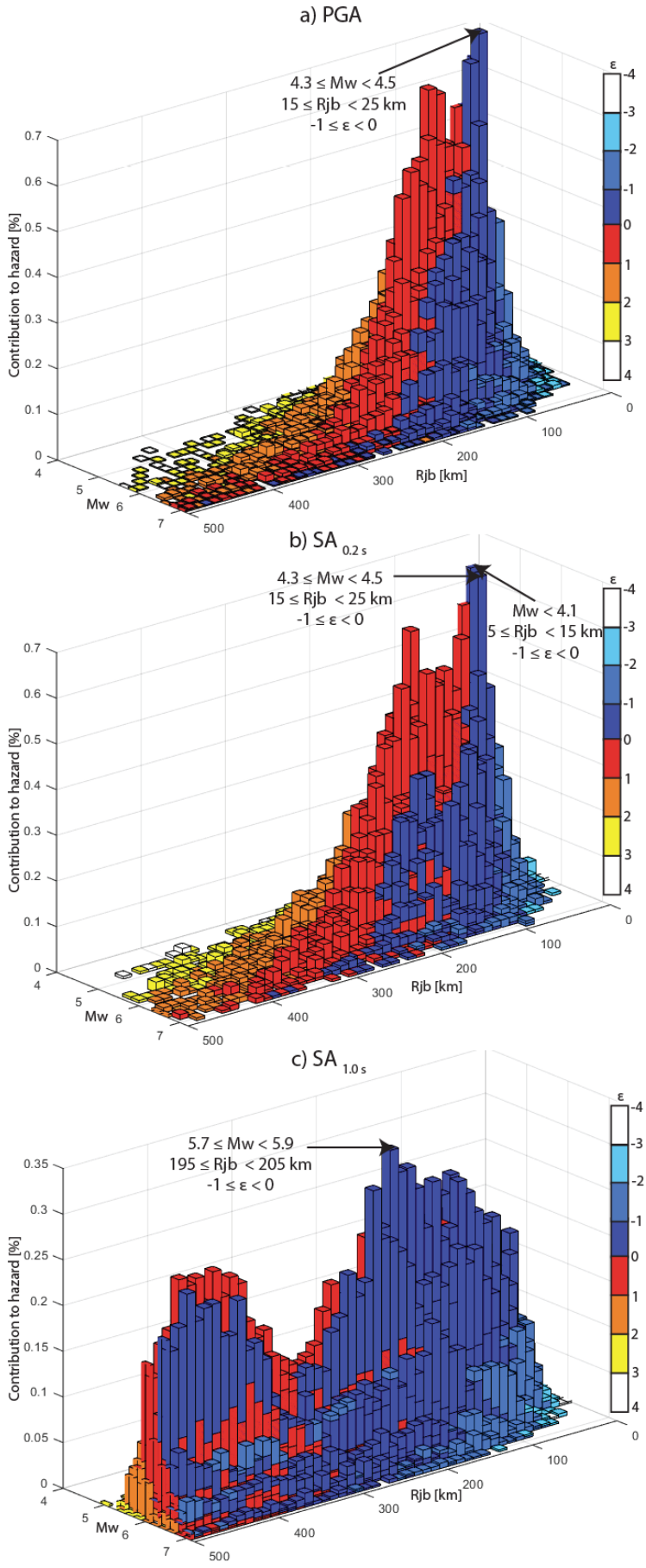

Figure 44: Disaggregation of the hazard for the Acorn site and 475-year return period by magnitude (Mw), Joyner-Boore distance (Rjb) and epsilon (ε) for (a) PGA, (b) $SA_{0.2\ s}$, and (c) $SA_{1.0\ s}$.

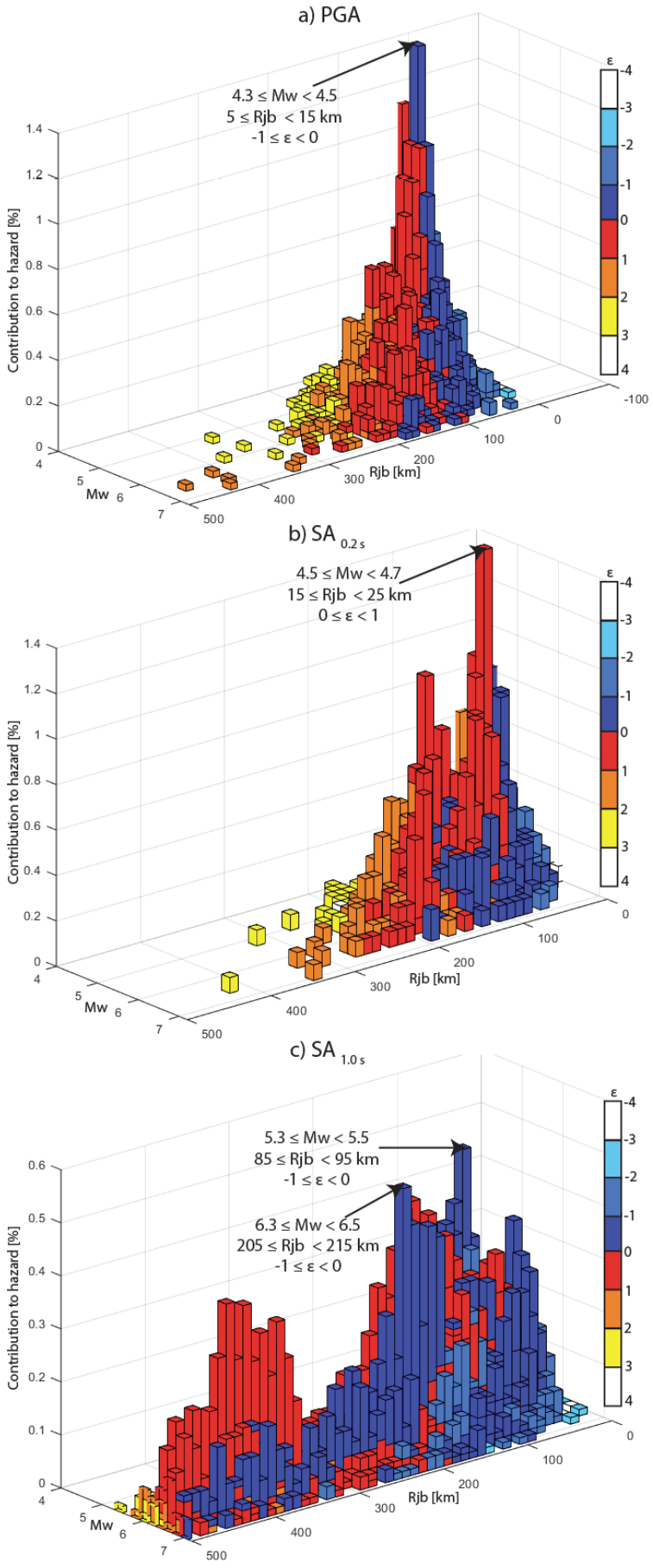

Figure 45: Disaggregation of the hazard for the Acorn site and 2475-year return period by magnitude (Mw), Joyner-Boore distance (Rjb) and epsilon (ε) for (a) PGA, (b) $SA_{0.2\ s}$, and (c) $SA_{1.0\ s}$.

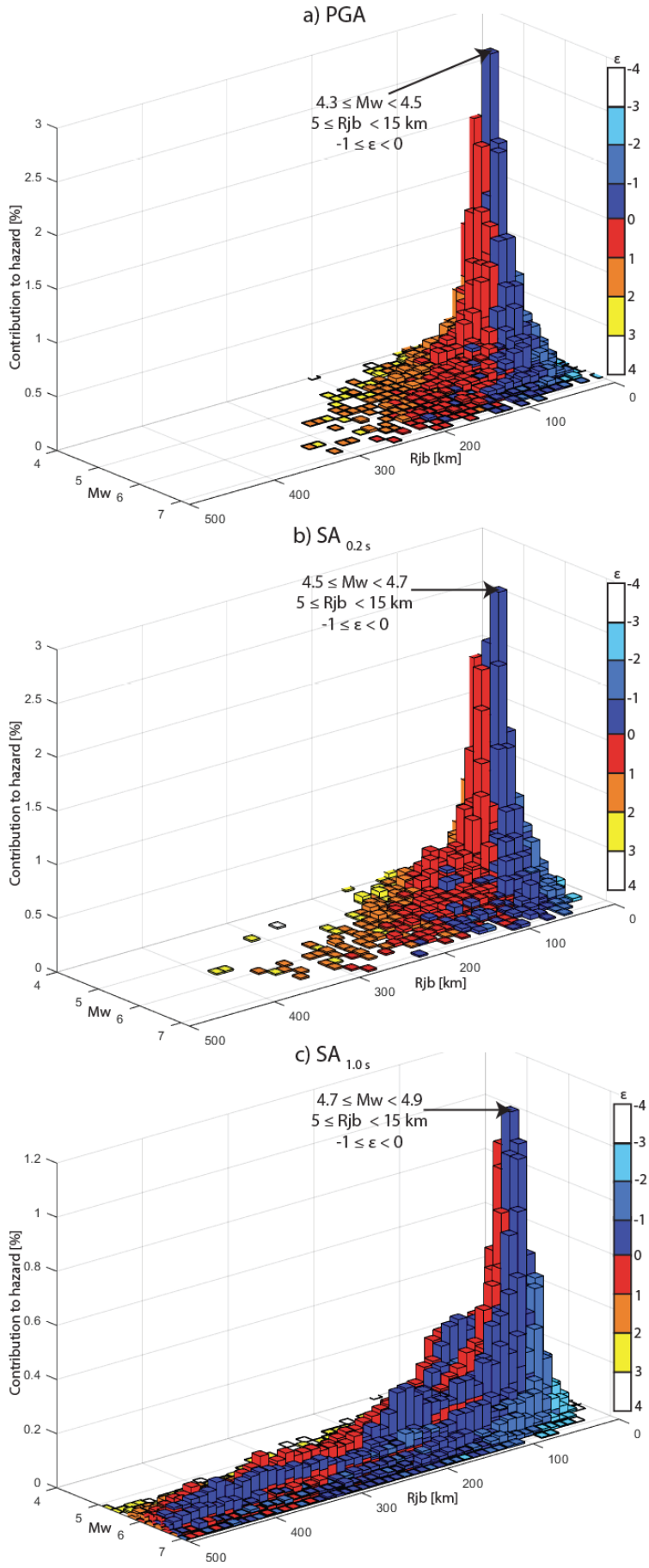

Figure 46: Disaggregation of the hazard for the Endurance site and 475-year return period by magnitude (Mw), Joyner-Boore distance (Rjb) and epsilon (ε) for (a) PGA, (b) $SA_{0.2\ s}$, and (c) $SA_{1.0\ s}$.

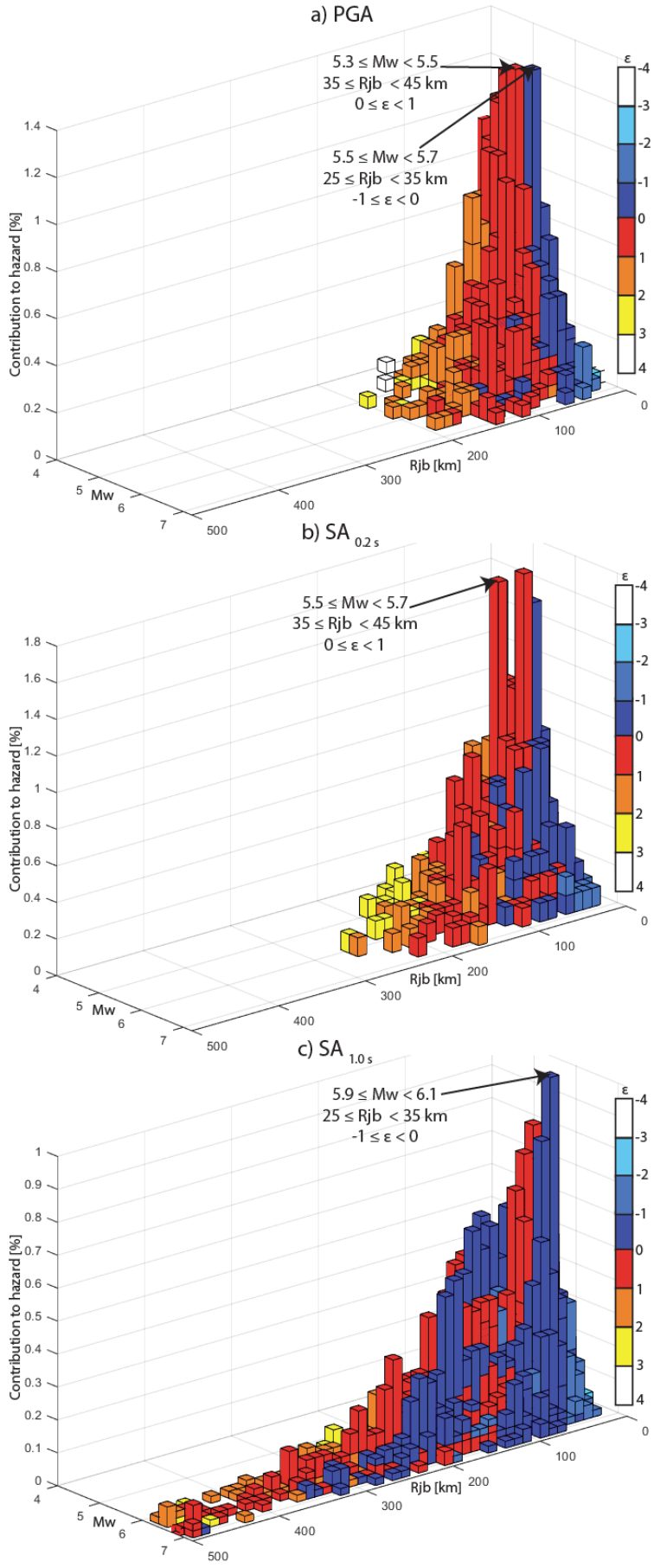

Figure 47: Disaggregation of the hazard for the Endurance site and 2475-year return period by magnitude (Mw), Joyner-Boore distance (Rjb) and epsilon (ε) for (a) PGA, (b) $SA_{0.2\ s}$, and (c) $SA_{1.0\ s}$.

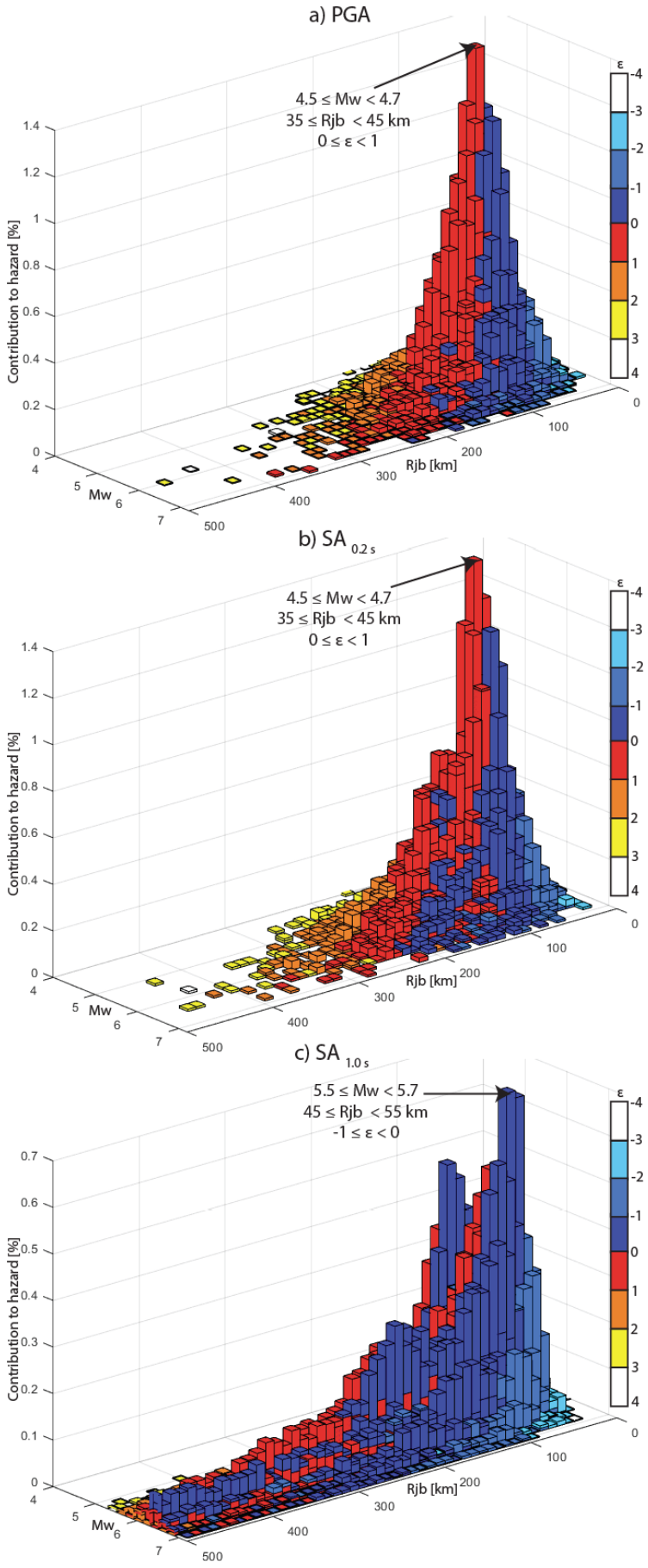

Figure 48: Disaggregation of the hazard for the HyNet site and 475-year return period by magnitude (Mw), Joyner-Boore distance (Rjb) and epsilon (ε) for (a) PGA, (b) $SA_{0.2\ s}$, and (c) $SA_{1.0\ s}$.

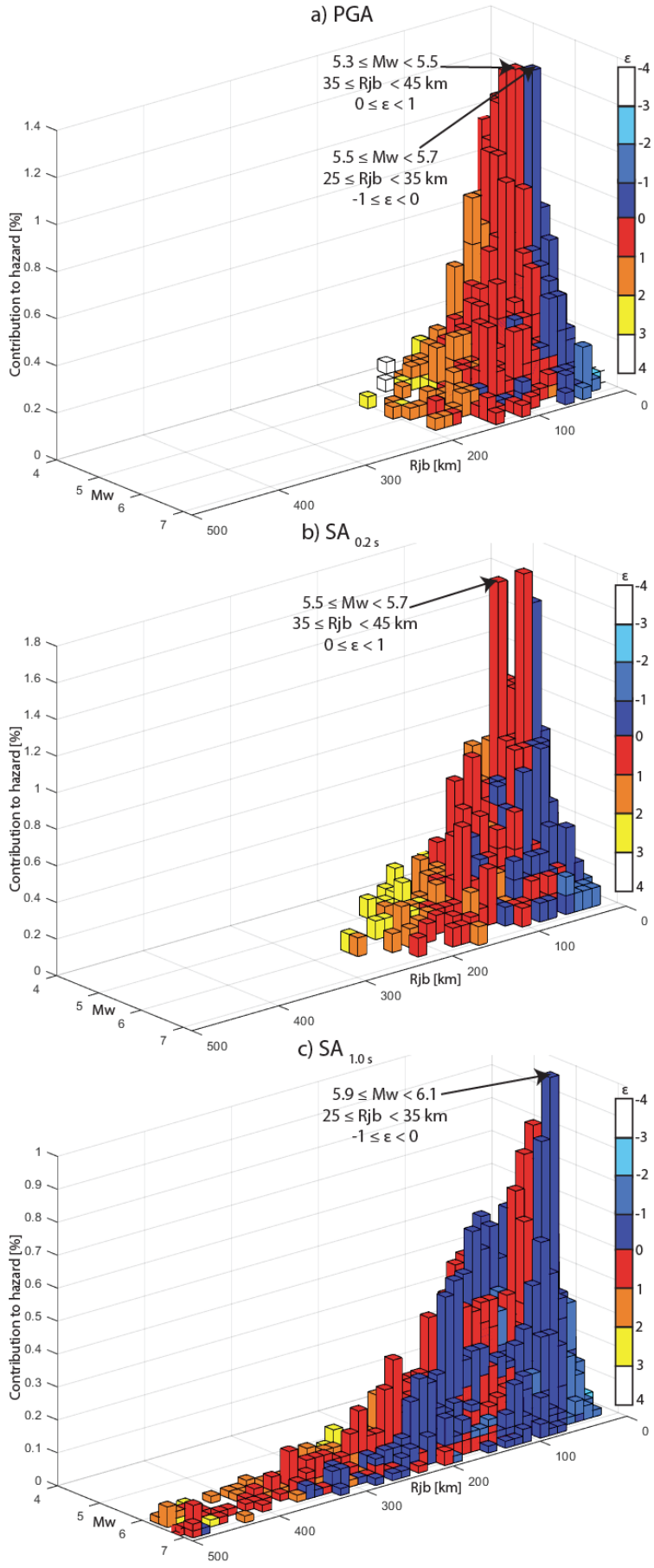

Figure 49: Disaggregation of the hazard for the HyNet site and 2475-year return period by magnitude (Mw), Joyner-Boore distance (Rjb) and epsilon (ε) for (a) PGA, (b) $SA_{0.2\ s}$, and (c) $SA_{1.0\ s}$.

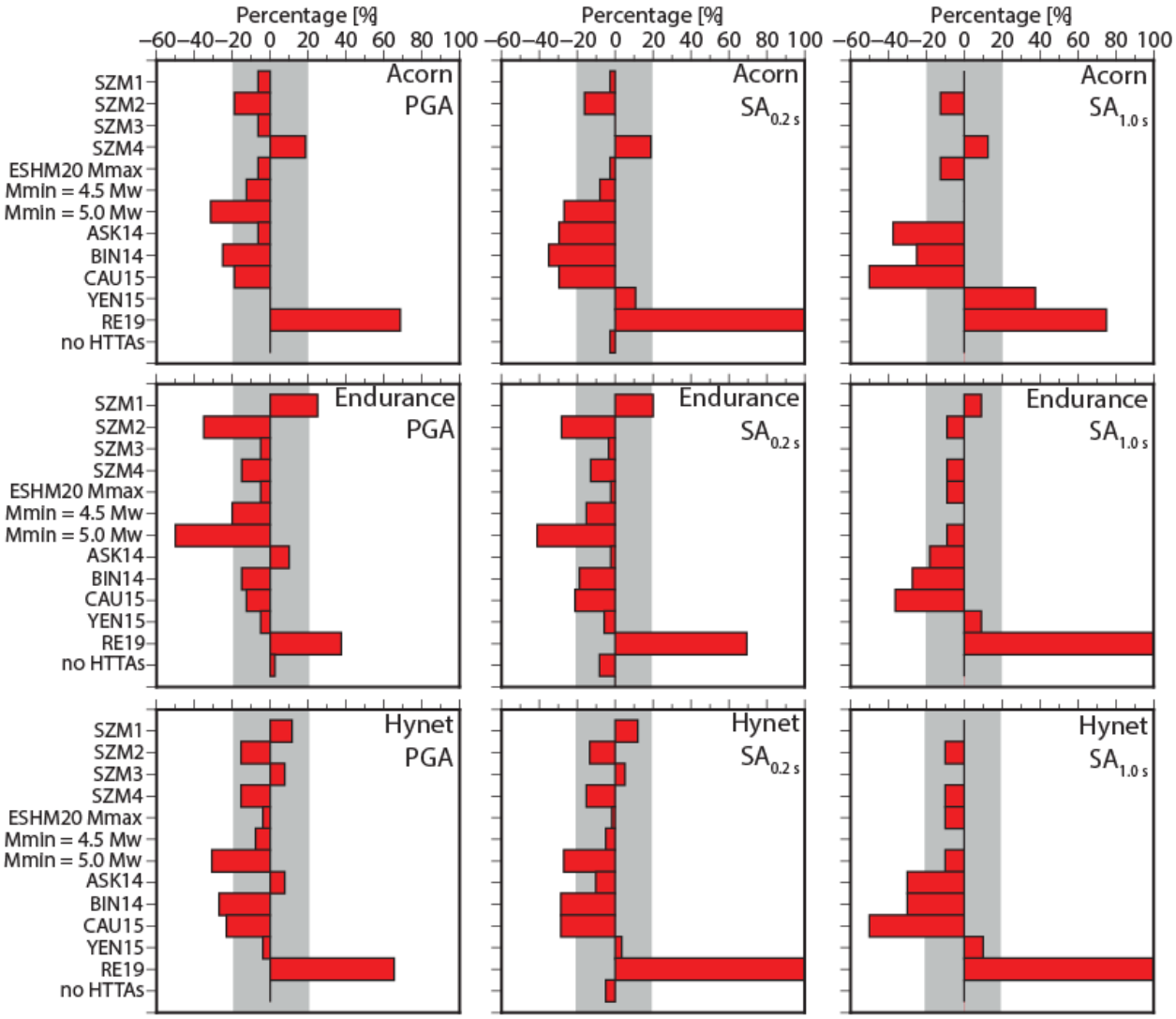

Figure 50: Results of the sensitivity analysis for three CCS sites expressed as the percentage difference between the results computed using the 2024 seismic hazard model and the modified model used for each test. Results are for a 475-year return period and three ground motion measures: PGA (left), $SA_{0.2\ s}$ (centre) and $SA_{1.0\ s}$ (right). The grey area describes the variation in hazard of less than ±20%.

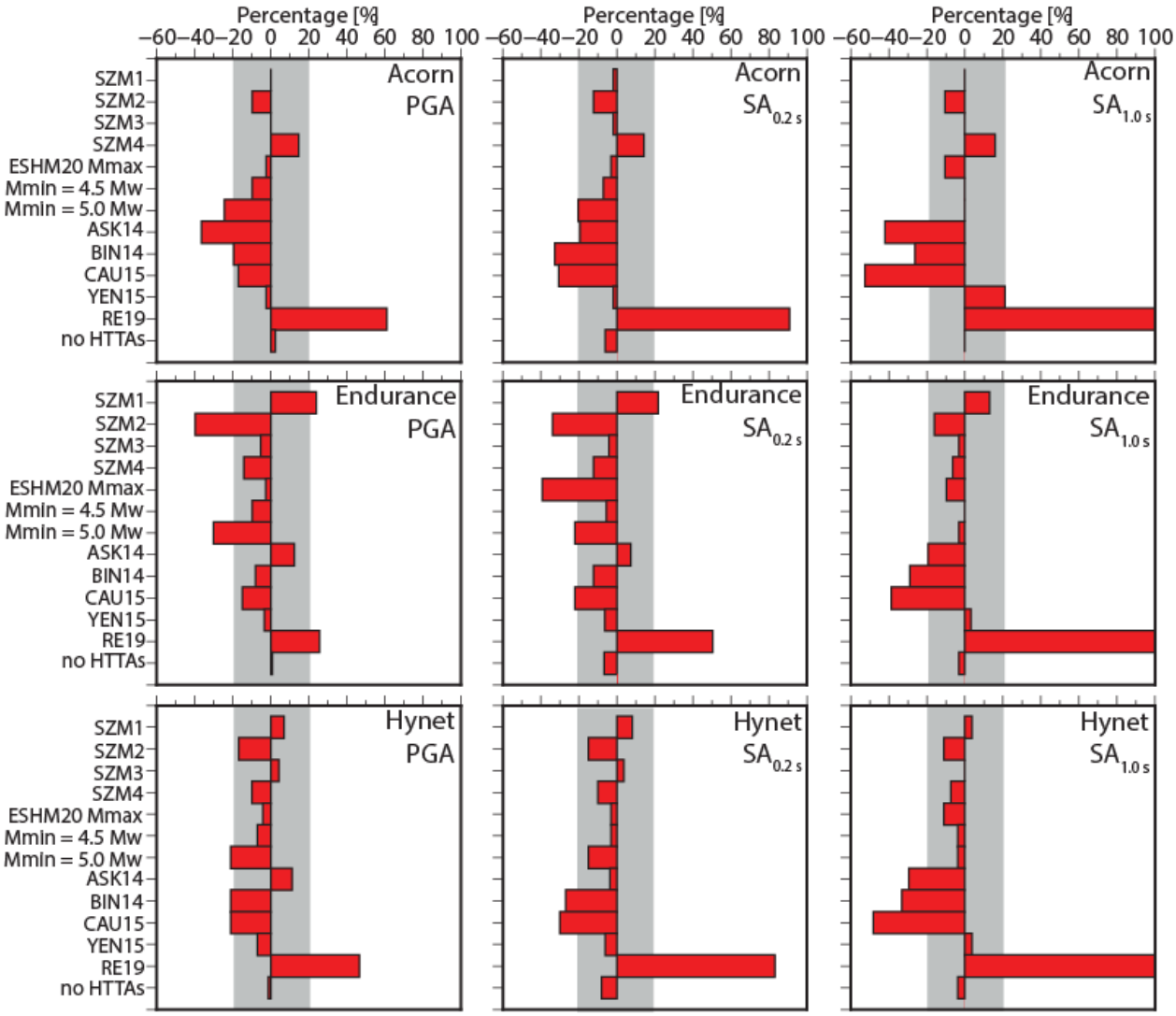

Figure 51: Results of the sensitivity analysis for three CCS sites expressed as the percentage difference between the results computed using the 2024 seismic hazard model and the modified model used for each test. Results are for a 2475-year return period and three ground motion measures: PGA (left), $SA_{0.2\,s}$ (centre) and $SA_{1.0\,s}$ (right). The grey area describes the variation in hazard of less than ±20%.

7.3 COMPARISON WITH PREVIOUS STUDIES

We further evaluate our results by comparing the hazard maps produced in this study with the latest national seismic hazard maps for the UK onshore (Mosca et al., 2022), the offshore seismic hazard maps for the North Sea in EQE02, and the recent hazard assessment for the Sophia offshore wind farm in the southern North Sea by Carlton et al. (2022). Table 12 shows a summary of the PGA, $SA_{0.2\,s}$, and $SA_{1.0\,s}$ values used to compare these studies.

Comparing the hazard values close to the coast of Wales with those around Snowdonia from Mosca et al. (2022) for 475 and 2475-year return periods shows that both models give similar results. For example, for the hazard model developed here, hazard values for the return periods of 475 and 2475 years offshore North Wales are 0.05 g and 0.18 g for PGA, 0.11 g and 0.35 g for $SA_{0.2\,s}$, and 0.01 g and 0.04 g for $SA_{1.0\,s}$. The corresponding values in Mosca et al. (2022) for Snowdonia and the same return periods are 0.09 g and 0.25 g for PGA, 0.16 g and 0.47 g for $SA_{0.2\,s}$, and 0.02 g and 0.06 g for $SA_{1.0\,s}$.

The highest PGA values for the return period of 475 years in our study are 0.07 g, 0.05 g, and 0.06 g in the northern North Sea, the southern North Sea, and offshore Wales, respectively. EQE02 estimate values of around 0.08 g, 0.06 g, and 0.05 g in the same areas for the same

return period resulting in a good agreement. The differences between our work and EQE02 can all be explained by differences in the two models, including the earthquake catalogue, the completeness thresholds of the catalogue, and the GMC model. We note that EQE02 show contour values, so local maxima and minima in the hazard values may be hidden.

We also compare our results with those of Carlton et al. (2022) for the Sophia offshore wind farm. Our results from the present study show that the PGA values at that site are 0.02 g and 0.04 g for 475 years and 2475 years. Carlton et al. (2022) estimated a PGA value of 0.03 g and 0.05 g for the same return periods showing a good agreement with ours.

	Return period [yr]	*PGA [g]*	*$SA_{0.2\ s}$ [g]*	*$SA_{1.0\ s}$ [g]*
		This work		
Northern North Sea	475	0.07	0.16	0.02
Northern North Sea	2475	0.19	0.39	0.05
Southern North Sea	475	0.05	0.10	0.01
Southern North Sea	2475	0.13	0.27	0.04
Offshore North Wales	475	0.05	0.11	0.01
Offshore North Wales	2475	0.18	0.35	0.04
Sophia wind farm	475	0.02	-	-
Sophia wind farm	2474	0.04	-	-
		Mosca et al. (2022)		
Snowdonia	475	0.09	0.16	0.02
Snowdonia	2475	0.25	0.47	0.06
		EQE02		
Northern North Sea	475	0.08	-	-
Southern North Sea	475	0.06	-	-
Offshore North Wales	475	0.05	-	-
		Carlton et al. (2022)		
Sophia wind farm	475	0.03	-	-
Sophia wind farm	2475	0.05	-	-

Table 12: Summary of PGA, $SA_{0.2\ s}$, and $SA_{1.0\ s}$ for 475 and 2475 years return period from this study, Mosca et al. (2022), EQE02, and Carlton et al. (2022).

8 Discussion and conclusions

We have developed a seismic hazard model for the UK offshore EEZ with accompanying hazard maps for PGA and spectral acceleration at different return periods using a Monte Carlo approach for PSHA. The hazard model incorporates updated datasets and some of the advances made in PSHA and ground motion modelling since 2002, such as the use of the HTTA in the GMC model. For the first time, the offshore maps have been computed for $SA_{0.2\ s}$ and $SA_{1.0\ s}$, which is particularly relevant for offshore structures.

The 2024 offshore hazard maps confirm that seismic hazard in UK waters is generally low with PGA hazard values of less than 0.03 g at a return period of 475 years for much of the UK offshore EEZ. Hazard is higher off the coast of North Wales and in the northern North Sea as a result of higher observed seismic activity in those regions. In the Irish Sea close to North Wales,

the PGA hazard for 475 years is 0.05 g. In the northern North Sea, it is 0.07 g for the same return period. The hazard maps for spectral accelerations at short ($SA_{0.2\ s}$) and long ($SA_{1.0\ s}$) periods show a similar spatial pattern to the PGA hazard values, although the $SA_{0.2\ s}$ values are up to twice the PGA values in the areas of highest hazard. The $SA_{1.0\ s}$ are lower than the PGA values. This may reflect the contribution of small to moderate earthquakes at relatively small distances to the overall hazard. Another region of high hazard is the southern North Sea and the Dogger Bank where the largest instrumentally recorded earthquakes (5.9 Mw) in the region occurred in 1932. Here, for 475 and 2475-year return periods, the hazard values are 0.05 g and 0.13 g for PGA, 0.10 g and 0.27 g for $SA_{0.2\ s}$ and 0.01 g and 0.04 g for $SA_{1.0\ s}$.

In general, our estimates agree well with EQE02 for a 475-year return period and with the study for the Sophia offshore wind farm by Carlton et al. (2022) despite the three works having developed different seismic hazard models.

In this project, we have attempted to improve some of the limitations of the 2020 national seismic hazard model for the UK (Mosca et al., 2022), for example, by including magnitude uncertainties from the BGS earthquake catalogue (see Subsection 3.2). However, we find that magnitude uncertainty appears to be either estimated differently by other agencies or is not available at all. As a result, we do not use magnitude uncertainties to avoid any bias in the estimate of the seismicity rates using data from different catalogues. Alternatively, we could have given a constant uncertainty for all events (e.g. the standard deviation from the conversion equations) but this would introduce some degree of subjectivity.

Another limitation is that completeness thresholds are based on published information for each of the earthquake catalogues used rather than from statistical methods, as the low seismicity rates in the region mean that there are too few events to robustly apply the latter. The cumulative and annual numbers of earthquakes for specific magnitudes are of limited use in regions with a few earthquakes in the last hundreds of years. Developing a uniform procedure to assess the completeness of the composite catalogue has been unfeasible for this project's relatively short time period. This problem is significant for the northeast Atlantic portion included in the study area which contains no events within any realistic magnitude thresholds. Using the same completeness region for this area and the North Sea may result in a slight increase in the completeness and activity rate of the zones located in the northeast Atlantic. However, the occurrence of low (< 4 Mw) instrumentally recorded seismicity, which falls outside the completeness thresholds, suggests that the lack of historically observed seismicity may be a consequence of the large distance from coastal populated areas.

A limitation of the 2020 national hazard model was the use of a single source model. Here, the SSC model consists of four different source zone models to account for different interpretations of the mapped tectonic structures, large-scale deformation, regional stress field, and observed seismicity in the UK and surrounding regions. We recognise that we have not included any zoneless models as an alternative branch in the source model logic tree. This has been done by other regional (ESHM20), national (Wiemer et al. 2016; Grünthal et al. 2018; Drouet et al. 2020), and site-specific (Carlton et al., 2022) studies. However, the zoneless approach requires robust estimates of the uncertainties in earthquake locations and magnitudes for all earthquakes, which are not uniformly assessed or not available in a composite catalogue such as the present. The use of a zoneless source model would mean some degree of subjectivity to assess the magnitude and location uncertainties for the entire catalogue.

We also use a large (for an intraplate region with low levels of seismicity) dataset of homogeneously processed high-quality ground motion recordings PGA, $SA_{0.2\ s}$ and $SA_{1.0\ s}$ to help select and weight the GMPEs used in the GMC model. This is the first time that such a dataset has been compiled for this region. However, we recognise that the inherent limitations of the dataset (e.g. lack of recordings at near-source distances and for large earthquakes) still make the selection of the GMPEs for the GMC model challenging. Recordings for slightly larger earthquakes are available from NORSAR and France strong motion database, but we did not include these in our analysis. The inclusion of these data may have slightly changed the results of the analysis in Section 6.2, but we believe this is unlikely to have significantly influenced the selection of the GMPEs for the GMC model in Section 6.3. The development of new backbone models for the UK may provide a better way to model the ground motion, together with its

uncertainty, generated by potential, future earthquakes in the UK and to track the epistemic uncertainty of the ground motion into the hazard estimates.

In this project, we used a single generic shear wave velocity profile and a uniform Vs30 of 800 m/s across the entire study area. However, multiple profiles could produce the same Vs30 of 800 m/s leading to different amplification functions. These two parameters (Vs profile and Vs30) vary significantly in the North Sea as shown by Figure 52, which displays the thickness of Quaternary deposits across the UK Continental Shelf. This significant variation may have an impact on offshore infrastructure deployment. Quaternary thickness can be considered a proxy for the bedrock level and suggests that in most offshore locations the Vs30 may be lower than 800 m/s. This is also confirmed by the analysis of boreholes at the CCS sites selected for this work. A detailed soil description for these boreholes is in Appendix 4.

The use of uniform Vs30 for the entire offshore region describes well why regional hazard maps are only a first-order approximation of seismic hazard for engineering structure and help to identify regions of high seismic hazard to inform the need for site-specific risk assessments. The decisions to construct the seismic hazard model are not driven by a specific site of interest as in a site-specific PSHA but are taken uniformly across the region (e.g. Musson and Sargeant 2007; Gerstenberger et al. 2020). A site-specific assessment might be required if the hazard exceeds some given threshold at the site after the appropriate site conditions for the site are taken into account. This should also consider a "capable fault assessment (e.g., IAEA, 2022) of the faults identified close to the site to understand when these faults were last active.

All anthropogenic events were removed from the earthquake catalogue so that they did not bias estimates of activity rates for tectonic earthquakes. However, we note that anthropogenic events, such as those related to carbon capture and storage, could contribute to the overall seismic hazard of proposed CCS sites. The magnitude for most such events in and around the North Sea region is less than the minimum magnitude used for the hazard calculations in this study. Further work is needed to assess this hazard.

The products of this project will be accessible to the public through a dedicated webpage (https://earthquakes.bgs.ac.uk/hazard/hazard_offshore.html) and an interactive mapping tool to ensure the transparency of the hazard model. The website allows users to download all elements of the hazard model and the output files in text format. The mapping tool Geoindex (offshore) allows users to view the hazard maps interactively, navigate to a specific area of interest, query the maps, and download the hazard values at a specific location or area of interest. The computer code can be made available on request to ukeqs@bgs.ac.uk.

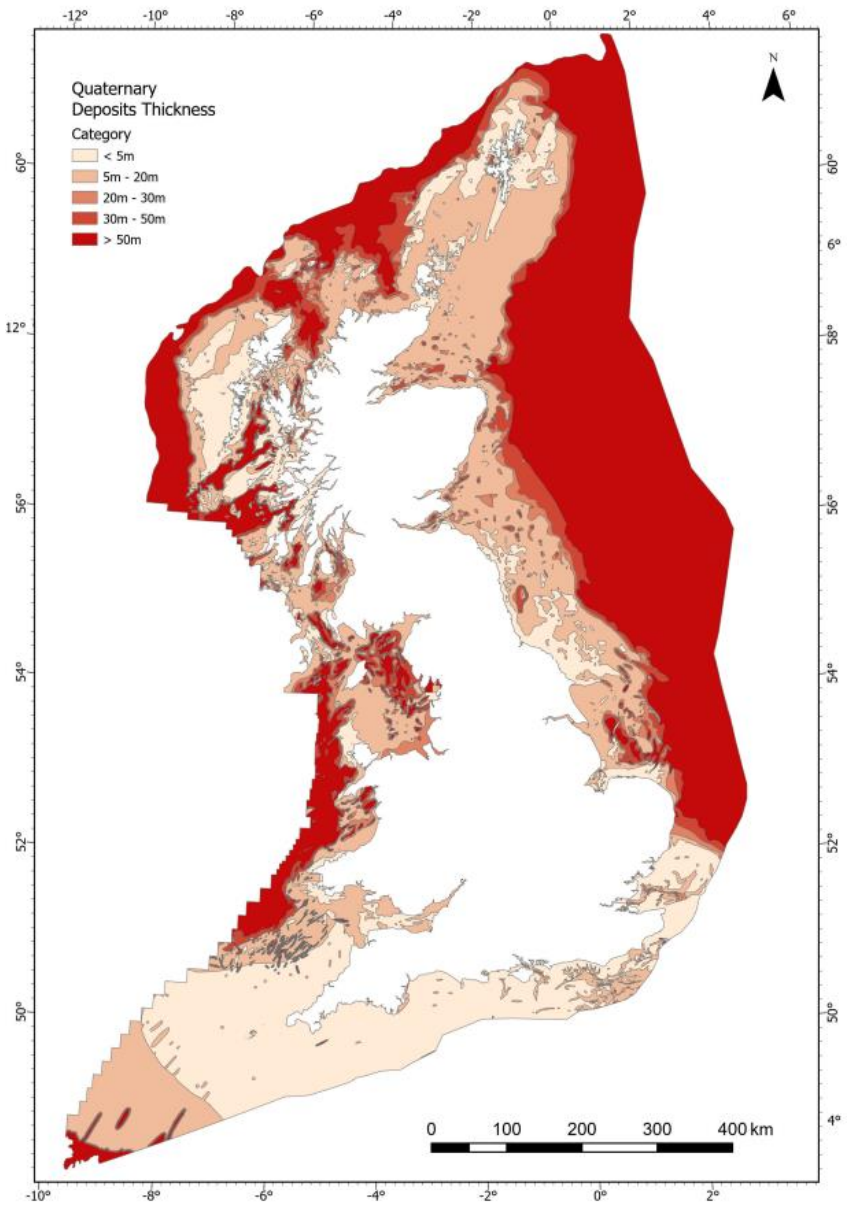

Figure 52: The Quaternary deposits thickness across the bulk of the Continental Shelf for the UK. The map is derived from (unpublished) BGS 1:1000000 scale Quaternary digital geological mapping. The map was produced in 2015 in collaboration with, and co-funded by, The Crown Estate as part of a wider commissioned project to assess seabed geological constraints on engineering infrastructure across the Continental Shelf for the UK.

Appendix 1

Below we provide a detailed description of the individual zones in the source models SZM1-SZM4 (see Figures 18-21) and an overview of their recurrence statistics. Figure 53 shows the geometry of the source zones for the four models superimposed with the regional faulting map to fully understand the source delineation.

The labels of the zones are based on the main tectonic structures in the zone or the region encompassing the zone (e.g. ENGC and NARM stand for English Channel and North Armorican Massif, respectively), followed by the number of the model (i.e. 1 for SZM1, 2 for SZM2, etc). Note that the largest magnitudes mentioned below are those observed in each zone and therefore they are not the largest possible magnitude discussed in Subsection 5.2.

It is a basic assumption in PSHA that an earthquake has an equal probability of occurring anywhere within a source zone, i.e. events are not clustered. Here, this is tested using nearest

neighbour analysis. This method computes the average nearest neighbour ratio as the observed average distance $\bar{D}$ divided by the expected average distance between events if they are randomly distributed in a source zone:

$$Ratio = \frac{\bar{D}}{0.5\sqrt{A/n}} \quad (15)$$

where A is the area of the source zone and n is the number of events in the zone.

Overall, if the average nearest neighbour ratio is less than 1, the seismicity in a source zone exhibits clustering; if the index is greater than 1, the seismicity is towards dispersion (uniform or random distribution; Davis, 1986). We will apply the nearest neighbour analysis to each zone of the SZMs below. Note that we are only considering the clustering of epicentres rather than the clustering of hypocentres due to the large epistemic uncertainties on the depth estimates for earthquakes in the catalogue.

SZM1

CORN1 - This low (≤ 4.1 Mw) seismicity zone corresponds to the Cornubian Ridge. The predominant faulting trend in this zone is E-W.

RHEN1 - The region south of the Variscan Front is modelled as a single zone because there is insufficient evidence (geological, tectonic, earthquake activity) for dividing it into smaller source zones. The northern boundary of this zone is represented by the Variscan Thrust Front. RHEN1 has low (Mw < 4.5) levels of seismicity with the largest (4.4 Mw) earthquake occurring here in 1963. The general structural trends are mainly E–W.

WCHA1 - The English Channel is included in a single zone. The northern boundary runs along the south coast of England, whereas the southern boundary corresponds to the Ouessant-Alderney Fault Zone and the edge of the Cotentin Peninsula. The largest earthquake in this zone is of magnitude 4.7 Mw and occurred in 1925. Structural trends are NE–SW, NW–SE, and E-W.

DOVE1 – The Dover Strait is an area where large earthquakes are known to have occurred in the last 1000 years, although many of these events are outside the completeness thresholds of the catalogue. The southern boundary corresponds to the North Artois Shear Zone, whereas the northern and eastern boundaries have been drawn to include the revised location of the 1382 and 2007 earthquakes.

SLPT1 – This zone includes the Sole Pit Basin. The northern boundary of SLPT1 is marked by the Flamborough Head Fault Zone, a major structure in this area. This zone experienced the largest instrumental recorded earthquake in the UK, i.e. the 5.9 Mw 1931 earthquake in Dogger Bank. The predominant trends of the faults here are NW-SE, NE-SW, and E-W.

EANG1 – This zone comprises the southeastern part of England with E-W and NW-SE-trending faults and is characterised by low levels of seismicity, except for the 4.9 Mw 2008 Market Rasen event being the largest in this zone. Similarly to SLPT1, the northern boundary of the zone EANG1 corresponds to the Flamborough Head Fault Zone.

MMCE1 - This low seismicity zone corresponds to the Anglo-Brabant Massif where the largest earthquake was the 5.0 Mw Derby earthquake on 11 February 1957. The western boundary of this zone is the Malvern Fault, which divides the highly seismic Welsh Massif (MMCW1) and the Anglo-Brabant Massif and reflects the discussions in Pharaoh (2018). Faults in this zone are NW–SE and N-S-trending.

PENN1 – The Pennines are included in PENN1 whose boundaries follow the topography of this region. The predominant trend of the faults here is NW–SE and N-S and the largest earthquake has magnitudes 4.6 Mw and occurred in 1871.

MMCW1 – This zone, which includes Mid and South Wales, corresponds to the Welsh Massif. Faults in this zone are predominantly NE–SW-trending. The largest earthquake that occurred here within the completeness thresholds is the 5.0 Mw 1896 Hereford earthquake.

MENA1 – This zone, which includes the NE-SW-trending Menai Strait fault system and the region around Snowdonia, is characterised by the highest levels of seismicity in the UK producing some of the largest onshore events that occurred in the country. The largest events here within the completeness thresholds are the 5.0 Mw 1852 and 4.9 Mw 1984 earthquakes.

EISB1 - The East Irish Sea Basin is included in the zone EISB1, which has experienced moderate earthquakes with the 4.7 Mw event in 1843 being the largest here. The general structural trends are mainly NW-SE and N–S.

CUMF1 - This zone comprises the Lake District Dome, which has moderate earthquake activity (< 4.8 Mw). The main faulting trend here is NE-SW and E-W.

BALA1 – This zone of low seismicity comprises the Bala region and includes NW-SE and N-S trending faults.

SC1M1 - The Southern Uplands of Scotland, which is included in SC1M1, is an area of generally low seismicity (Mw < 4.0). Faults in this zone are predominantly NE–SW-trending.

SC341 - Southwest Scotland is included in the zone SC341, which comprises the Highland Boundary Fault and the Grampian Highlands Terrane. These areas are included in a single zone because the seismicity appears to be homogeneous here and there is no strong evidence for a structural boundary to divide them into two zones. The predominant trend of the faults in this zone is NE–SW. The largest earthquake in SC341 is the 4.9 Mw Argyll earthquake in 1880, the largest known earthquake in Scotland.

SC781 - This zone corresponds to the NE–SW-trending Great Glen Fault, which acts as a zone of weakness, promoting seismicity. Observed earthquake activity with Mw ≤ 5.0 is relatively high in this zone with the largest (4.8 and 4.7 Mw) earthquakes occurring in 1816 and 1901 in Inverness.

SC91 – This source with moderate seismicity levels includes the Northern Highland Terrane that is located NW of the Great Glen Fault. Structural trends within this zone are both NE–SW and NW–SE. The largest earthquake in this zone was the 4.5 Mw Invergarry earthquake in 1888.

ESCO1 - This low seismicity source zone includes Eastern Scotland and the offshore area in the North Sea east of Scotland. Structural trends are NE–SW and E-W.

IREL1 - This is also a low seismicity source zone that includes Ireland, the Irish Sea, and the Celtic Sea. Faults here are NE–SW and NW–SE-trending.

VIKI1 - This zone corresponds to the Viking Graben. Here it is assumed that the seismicity at the triple graben junction and around the southern tip of the Fladen Ground Spur is related to the Viking Graben, leading to a zone that is angled slightly to the SSW. Structural trends within this zone are predominantly N–S with E–W-trending faults in the southern part of VIKI1. This zone has high levels of seismicity but many events are outside the completeness thresholds of the catalogue.

CEGR1 - The Central Graben is included in the zone CEGR1 with a simplified geometry. The predominant trend of the faults in this zone is N–S. The seismic activity in this zone is characterised by low magnitudes (< 4.0 Mw).

NO61 - This source zone includes the Horda Platform where the structural trends are predominantly N–S. It is characterised by low levels of seismicity.

NO51, NO41, NO31, NO21, and NO11 – These zones include the Norwegian coast and the Norwegian part of the North Sea and are characterised by intense earthquake activity with the largest events there being of magnitude 4.6-5.5 Mw. Structural trends are NE–SW, NW–SE, and N-S.

FRA11 – This zone comprises the South Armorican Massif and is divided by the North Armorican Massif through the North Armorican Shear Zone. The largest (5.4 Mw) earthquake in this zone occurred in 1959 and the faults have predominantly NE-SW and NW-SE trending.

FRA21 – The North Armorican Massif is included in FRA21 and is bounded by the North Armorican Shear Zone to the west and the Quesssoy/Nort-sur-Erdre fault zone to the east. The

seismic activity in this zone is intense with a 4.8 Mw earthquake in 1888 being the largest event here. The predominant trends of the faults here are NW-SE and N-S.

FRA31 – This highly seismic zone comprises the Channel Islands, the Cotentin Peninsula, and Normandy. The eastern boundary of FRA31 divides the region and the Mesozoic Paris Basin. The largest (5.1 Mw) earthquakes in this zone occurred in 1775, 1926 and 1927 and the predominant fault trends are E-W and NE-SW.

FRA41 – This zone includes the western Paris Basin in the study area. The Bray Fault, which divides the western and eastern Paris basin, describes the eastern boundary of FRA41. The largest (4.8 Mw) earthquake in this zone occurred in 1769 along the coast. Structural trends within this zone are both N–S and NW–SE.

FRA51 - The zone FRA51 covers the Belgium-Pas de Calais region and the eastern Paris Basin. The largest earthquake (4.8 Mw) here occurred in 1896 and the faults have predominantly NE-SW trending.

FRA61 – This zone of low seismicity is at the border between France and Belgium and at the edge of the study area. The predominant fault trends here are NE-SW and E-W.

BEL11, BEL21, and BEL31 – Belgium is included in these zones where the levels of seismicity are relatively high (up to 5.5 Mw). Structural trends in these zones are NE–SW, NW–SE, and E-W.

NL11, NL21 – These low seismicity zones include the Netherlands and the Dutch sector of the North Sea. The faults here are predominantly N-S and NNW-SSE.

NATL1 – The portion of the Atlantic in the study area, together with the West Approaches and the Faroes Islands, is included in the zone NATL1. This zone has little seismicity.

The results of the nearest neighbour analysis on the individual zones of SZM1 show that the seismicity in these zones is dispersed.

SZM2

SARM2 – The Proterozoic South Armorican Massif is included in SARM2. It is bounded by the SE-NW striking North Armorican Shear Zones to the east. The largest (5.4 Mw) earthquake in this zone occurred in 1959 and the faults have predominantly NE-SW and NW-SE trending.

NARM2 - This zone comprises the North Armorican Massif, the Channel Islands, and the Cotentin Peninsula. The western boundary of NARM2 is the North Armorican Shear Zones; the northern boundary is marked by the Ouessant-Alderney Fault Zone and the southern margin of the Western Approaches Basin; whereas the eastern boundary of NARM2 divides the Variscan North Armorican Massif and the Mesozoic Paris Basin. The largest (5.1 Mw) earthquakes in this zone occurred in 1775 and 1926 and the structural trends are NE–SW, NW–SE, and E-W.

PARB2 – This zone includes the western Paris Basin. The Bray Fault, which divides the western and eastern Paris basin, describes the eastern boundary of PARB2. The largest (4.8 Mw) earthquake in this zone occurred in 1769 along the coast and structural trends within this zone are both N–S and NW–SE.

ENGC2 - This zone comprises the Cornubian Batholith, Western Approaches Basin, and the English Channel. The northern and eastern boundary is marked by the Bray-Wight-Portland fault, the northern margin of the Cornubian Granites and the Rusey Fault Zone. The largest earthquake in this zone is of magnitude 4.7 Mw and occurred in 1925. Structural trends are NE–SW, NW–SE, and E-W.

VARF2 – This zone includes the inverted Variscan basins of southern England. It is bounded by the Variscan Front Thrust to the north, the Bray-Wight-Portland-Rusey Fault and the northern boundary of the Cornubian granites to the southeast. The main trend of the faults here is E-W and the largest earthquake that occurred in this zone was the 4.8 Mw event in 1896.

CHAT2 – This zone with moderate levels of seismicity includes the Charnwood Terrane, which is part of the Anglo-Brabant Massif. The western and southern boundaries are given by the

Malvern Fault and the Variscan Front Thrust, respectively. CHAT2 has low levels of seismicity with the 4.4 Mw 2002 event being the largest here and the faults are NW–SE and N-S-trending.

WRET2 – The Wrekin terrane is included in this zone. WRET2 is bounded by the Pontesford-Linley Fault to the west, the Malvern Fault to the east, and the Variscan Front Thrust to the south. Faults in this zone are predominantly NE–SW-trending. The largest earthquake that occurred here within the completeness thresholds is the 5.0 Mw 1896 Hereford earthquake.

MIWA2 – This zone, which includes Mid-Wales, has low (< 4.2 Mw) levels of seismicity and the predominant fault trend is NE-SW. The Pontesford-Linley Fault separates MIWA2 from WRET2.

IRIS2 – The IRIS2 zone follows the offshore extent of the North Celtic Sea Basin which is bounded to the NW and SE by fault systems. Onshore the SE extent is marked by the Bala Lineament through Wales and then margining with the southern boundary to the Ribblesdale Fold Belt. The NW extent continues through Anglesey, North Wales, and projects northwards to the northern margin of the Ribblesdale Fold Belt. Onshore this zone broadly matches the Môn–Deemster Fold–Thrust Belt (Pharaoh et al., 2020). This zone is characterised by low (≤ 4.2 Mw) earthquake activity and the predominant fault trend is NE-SW.

NWAL2 – The seismically active Northern Wales is included in this zone. It is characterised by the highest levels of seismicity in the UK producing some of the largest onshore events that occurred in the UK, including the 5.0 Mw 1852 and 4.9 Mw 1984 earthquakes within the Mc values. Faults here have predominantly NE-SW trending.

BRAM2 – This zone comprises the Fenlands Terraine, with the Wash Granite, of the Anglo-Brabant Massif which itself is inferred to extend south-eastwards into Belgium. The northwestern boundary is marked by the Pennine Axis while the northeastern boundary is marked by the Broadlands Thrust, the northeast extent of the Wash Granite, and the Sothern Craven-Morley-Campsall-Askern-Spital Fault. The southwestern boundary is located along the concealed boundary of the Midlands-Microcraton and the Nieuwpoort-Asquempont Fault in Belgium. The largest earthquake that occurred in this zone is the 5.5 Mw event in 1692 in Belgium and the faults are NW-SE and E-W-trending. The completeness thresholds for the UK onshore are applied to BRAM2 because the offshore part in this zone corresponds to the Dover Strait (DOVE1 in SZM1), to which the UK completeness analysis is applied on the basis that the completeness thresholds for land can extend some distance offshore if a coastal urban area is present (BGS and Arup, 1997).

CLEB2 – The Cleveland and Northumberland Basins are included in CLEB2 whose eastern boundary is defined by the boundary with the Anglo-Dutch Basin and Mid-North Sea High. The northern boundary is along the Southern Upland Fault and the southern boundary is along the Flamborough Head Fault Zone. The western boundary is along the Dent and Pennine Faults. The zone is consistent with the block and basin model of Carboniferous geology in the UK with the Northumberland and Stainmore Trough and the Alston and Askrigg Blocksgrav. This zone experienced the largest instrumental recorded earthquake in the UK, i.e. the 5.9 Mw 1931 earthquake in Dogger Bank. The predominant trends of the faults here are N-S and E-W.

SOLE2 – This zone includes the Sole Pit Basin, Broad Fourteens Basin, and West Netherlands Basins which extend southwards into the Roer Valley Graben. Its northeast boundary follows the Indefatigable fault zone, IJmuiden High, and Mass-Bommel High. The southwest boundary is marked by the Broadlands Thrust, the northeast extent of the Wash Granite, and the Sothern Craven-Morley-Campsall-Askern-Spital Fault. The northern boundary is marked by the east-west striking Flamborough Head Fault Zone. The predominant trends of the faults here are NW-SE and N-S and the largest earthquake that occurred in this zone is the 5.5 Mw event in 1992 in Belgium. We applied the completeness analysis for the North Sea to this zone since it includes a small part of East England. Most of SOLE2 either is offshore or comprises the Netherlands which is assigned the completeness analysis for the North Sea (see Figure 7).

LAKE2 – This zone includes the Lake District and the boundaries are defined by changes in structural trends and seismicity. This zone is characterised by moderate levels of seismicity with the 4.7 Mw events in 1786 and 1843 being the largest here. The faults here have N-S and NE-SW trends.

SUPT2 – This zone of low (< 4.0 Mw) seismic activity includes the Southern Upland Terrane, which formed as an accretionary thrust complex above the northward-dipping subduction zone of the Iapetus Ocean crust beneath present-day Scotland (Stone et al. 2012). It is bounded to the south by the North Solway, Gilnockie and Featherwood faults which mark the northern margin of the Northumberland Trough and to the north by the Southern Uplands Fault which marks the southern boundary of the Midland Valley of Scotland. The eastern boundary is marked by the western edge of the Central North Sea Graben while the western boundary is marked by the North Channel Basin Bounding fault (West). The predominant trend for faults here is NE-SW.

MIVT2 – The MIVT2 is composed of the Midland Valley Terrane of Scotland, which comprises the relatively low-lying central part of Scotland lying between the Grampian Highlands to the north and the Southern Uplands to the south (Cameron et al., 1985). It is defined geologically to the north by the Highland Boundary Fault and south by the Southern Upland Fault. The terrane consists of Devonian to Carboniferous rift basin. This zone has low (< 4.0 Mw) earthquake activities and includes predominantly NE-SW-trending faults.

SWSC2 – South-west Scotland is included in this zone whose boundaries are based on seismicity. The predominant trend of the faults in this zone is NE–SW. The largest earthquake in SWSC2 is the 4.9 Mw Argyll earthquake in 1880, the largest known earthquake in Scotland.

GGFZ2- This zone is associated with the NE–SW-trending strike-slip Great Glen Fault. Although this fault may be linked to the Walls Boundary Fault offshore in the North Sea and extends in Northern Ireland, we did not include these segments because the seismicity dies out abruptly. The eastern boundary of this zone corresponds to the continuation of the Loch Shin Line in the north and the Deeside lineament in the south; whereas the western boundary marks the transition between onshore and offshore areas. Observed earthquake activity with Mw ≤ 5.0 is relatively high in this zone with the largest (4.8 and 4.7 Mw) earthquakes occurring in 1816 and 1901 in Inverness.

WNHT2 - The Western Northern Highland Terrane and Hebridean Terranes are included in a WNHT2 as a single zone. WNHT2 is bounded by the Outer Hebrides Fault to the north, the Great Glen Fault to the south, and the continuation of the Gairloch Shear Zone and the northern section of the Moine Thrust to the east. This zone is characterized by intense activity of moderate (< 4.5 Mw) seismicity and includes NE-SW trending faults.

ESCO2 – Eastern Scotland, the Eastern Northern Highland Terrane, the Shetland Platform and Moray Firth Basin are included in this zone. This zone comprises a large region of New Caledonian Granite intrusions including the Cairngorm Granites. The northwestern boundary runs along the Shetland Spine Fault before merging into the Moin Thrust. The southern boundary runs along the Highland Boundary fault and the Peterhead Ridge. The eastern boundary is marked by the western margin of the Viking Graben and East Shetland Basin. It includes little seismicity. Structural trends are NE–SW, NW–SE, and E-W.

VIKG2 – This zone includes the Viking Graben and its boundaries are drawn on the geological lines of this structure. Structural trends within this zone are predominantly N–S. This zone has high levels of seismicity but many events are outside the completeness thresholds of the catalogue.

TAMB2, MORB2, NORB2 – These three zones comprise basins in the Northern North Sea and are marked by the geological lines of these tectonic structures. TAMB2 and MORB2 have high levels of seismicity with the 4.9 Mw 1977 and 5.5 Mw 1988 earthquakes being the largest in these zones, respectively. The zone NORB2 is characterised by low (< 4.0 Mw) seismic activity. Structural trends are NE–SW and N-S.

SFSH2, CFSH2, NFSH2 – These zones comprise the Fennoscandian Shield and are divided into three zones by major faults and basins. The NFSH2 zone consists of the Western Gneiss Terrane (Precambrian basement) is bound to the north by the Møre-Trøndelag Fault Zone and south by the northern limits of the Caledonian rocks which compose the CFSH2 zone (Ebbing et al., 2012). The Caledonian rocks are located in the Faltungsgraben (Stratford et al., 2009) and are bounded to the south by the Hardangerfjord Fault Zone (Ebbing et al., 2012). The SFSH2 zone is marked again by Precambrian crystalline rocks and is bound to the south by the

Western extent of the Skagerrak and Oslo grabens (Ebbing et al., 2012). The zone CFSH2 has the lowest (< 4.0 Mw) levels of seismicity among these three zones. Structural trends in these zones are NE–SW, NW–SE, and N-S.

SOTO2 – This zone includes the Sorgenfrei-Tornquist Zone, a continental suture zone separating the younger Western Europe from the older Eastern Europe. SOTO2 has low (< 4.0 Mw) levels of seismicity and the faults here are N-S and NW-SE trends.

HORP2 – This includes the Horda Platform and the boundaries are marked by the geological lines of this tectonic structure. This zone is characterized by low earthquake activity and includes faults with N-S and NW-SE trends.

CEGR2 – This zone includes the Central Graben. The boundaries of CENG are drawn on the geological lines of this structure. The predominant trend of the faults in this zone is N–S and NW-SE. The seismic activity in this zone is characterised by low magnitudes (< 4.0 Mw).

NLBA2, NDBA2 – These zones include the Carboniferous basins that are marked by faults. These two zones have experienced earthquakes of magnitude smaller than 4.0 Mw and include predominantly N-S and NNW-SSE-trending faults.

MNSH2 – This low (< 4.0 Mw) seismicity zone includes the Mid-North Sea High with E-W, NW-SE, and NE-Sw trending faults.

HORN2 – This zone is associated with the Horn Graben system of faults. The largest earthquake that occurred here is the 4.6 Mw event in 1958 and the fault trends are N-S, NW-SE, and E-W.

BACK2 – This zone comprises Ireland and the eastern Atlantic Ocean included in the study area. It has little seismicity.

The results of the nearest neighbour analysis on the individual zones of SZM2 show that the seismicity in the zones is dispersed.

SZM3

The seismic source zone model SZM3 corresponds to the source model A in EQE02, which was developed by NORSAR and NGI (1998) as part of the Norwegian seismic hazard study and was used also in Bungum et al. (2000). The source model for the UK and the harmonisation with the NORSAR zonation are based on expert judgement and the experience gained by the authors of EQE02 in many site-specific seismic hazard studies. SZM3 consists of 41 zones, which are the results of the modification of the source model A of EQE02 to the study area of the present project.

NISL3 – This zone comprises the west Shetland Platform and the Shetland Islands and is characterised by low (< 4.0 Mw) levels of seismicity. Faults here have predominantly N-S and NE-SW trends.

HEBR3 – The Hebridean region, which includes part of the Outer Isles Thrust, forms the low seismic zone HEBR3. It is characterised by low (< 4.0 Mw) seismic levels and the predominant structural trend in this zone is NE-SW.

HIGL3 – This zone includes the Scottish Highlands and the seismic activity between Dunoon and Ullapool (south to north) and Mull to Perth (west to east). It has high levels of moderate (Mw < 5.0) seismicity and the largest earthquake here is the 4.9 Mw Argyll earthquake in 1880. Faults in HIGL3 are predominantly NE-SW.

MNPL3 – This low (< 4.0 Mw) seismicity zone covers the Mid-North Sea Highs and the Grampian region in Northeast Scotland. The predominant structural trend in this zone is NW–SE, E-W, and NE-SW-trending.

SBOR3 – SBOR3 includes the Southern Uplands of Scotland and is an area of generally low seismicity (Mw < 4.0). Faults in this zone are predominantly NE–SW-trending.

IAPS3 – The Iapetus Suture, which may be a region of seismic reactivation, is included in this zone. The largest earthquake that occurred here is the 4.7 Mw event in 1786. The predominant trend of the faults here is NW-SE.

NENG3 – This zone comprises northeast England, including the Northumberland, Staimore Troughs and the Alston Block. The largest earthquake in this zone is of magnitude 4.5 Mw and occurred in 1780. Structural trends are NE–SW, NW–SE, and E-W.

PENN3 – The Pennines region is included in PENN3 whose northern boundary follows the Iapetus Suture zone. This zone has a high concentration of seismicity of magnitude less than 4.6 Mw and includes NW–SE-trending faults.

LAKE3 – This zone, which is bounded by the Iapetus Suture zone to the north, includes the East Irish Sea Basin, the southern Lake District High, and the active Lake District Boundary Fault Zone. The structural trend of faults here is predominantly N-S and NE-SW.

SNSE3 – This seismically active zone includes the Sole Pit Basin and in general the southern North Sea included in UK waters. The largest earthquake that occurred in this zone is the largest (5.9 Mw) instrumentally recorded 1931 event in Dogger Bank in the region. Faults here are predominantly NW-SE and E-S-trending.

IRIS3 – This zone includes both the northwestern and south Irish Sea, which were modelled into two separate zones in EQE02. We merged them into a single zone because their levels of seismicity are low and there are no earthquakes within the completeness thresholds. IRIS3 includes NE-SW-trending faults.

NWAL3 – This zone corresponds to North Wales and includes the Menai Strait group faults. It has the highest levels of seismicity in the UK producing some of the largest onshore events that occurred in the UK. The largest events here within the completeness thresholds are the 5.0 Mw 1852 and 4.9 Mw 1984 earthquakes and faults have NE-SW trend.

MIWA3 - This zone, which includes Mid Wales, corresponds to the Welsh Massif. Faults in this zone are predominantly NE–SW-trending. The largest earthquake that occurred here within the completeness thresholds is the 5.0 Mw 1896 Hereford earthquake.200seismic

CENG3 - This active zone includes South Yorkshire and Lancashire, Derbyshire and Nottinghamshire, which constitute a major seismic belt in north-central England. The largest event in this zone was the 5.0 Mw 1957 Derby earthquake and the predominant fault trends are NW-SE, NE-SW, and N-S.

ANLI3 – East Anglia and Lincolnshire are included in ANLI3, which comprises part of the Anglo-Bramant Platform. This zone is characterised by low (< 4.0 Mw) levels of seismicity and includes E-W and NW-SE-trending faults.

MICR3 – This zone corresponds to the Midland Microcraton, which has low (< 4.0 Mw) seismic activity. Structural trends are NE–SW, NW–SE, and E-W.

SWAL3 – South Wales is included in SWAL3, which experienced several moderately damaging earthquakes, the largest of which were of magnitude 4.9 Mw in 1727 and 1906. Faults in this zone are NE-SW and E-W-trending.

LOBR3 – This zone, which comprises the London-Brabant Massif, extends from Belgium across the Channel through into East Anglia and includes the Dover Strait, the North Artois Shear Zone, and the Belgium-Pas de Calais region. It has experienced some of the largest regional historical earthquakes, although many of these events are outside the completeness thresholds of the catalogue. The largest event in this zone was the 5.3 Mw 1938 earthquake and the predominant fault trends are NW-SE.

OFLC3 - This area comprises the southern part of the North Sea bordering Belgium and the Netherlands and has very low seismic activity. Faults here are NW-SE and N-S-trending.

CORN3 - This low (≤ 4.1 Mw) seismicity zone corresponds to a part of the Cornubian Ridge. The predominant trends of the faults in this zone are NE-SW and E-W.

WESS3 – The region to the south of the Bristol Channel is included in WESS3 and lies on the foreland below the Variscan Front. It is characterized by low (< 4.0 Mw) levels of seismicity and includes E-W-trending faults.

ENGC3 - This zone is underlain by Variscan south-dipping low-angle overthrusts and is a moderately active region with events of < 5.0 Mw with the largest earthquake being of 4.8 Mw in 1896. The structural trends are predominantly E-W and NW-SE.

OFPL3 – This zone covers the Mid-Channel Suture and has low (< 4.0 Mw) earthquake activity. Faults have NW-Se and E-W trends.

BEME3 – The Belgian earthquake zone is an important lateral branch of the Rhenish earthquake zone and is characterised by high levels of seismicity with a 5.5 Mw earthquake in 1692 being the largest event here. Structural trends in BEME3 are E-W.

BRIT3 - This seismically active zone, which includes the Channel Islands, the Cotentin Peninsula, and Normandy, comprises Late-Variscan NW-SE wrench faults, bordered to the north by the Ouessant-Alderney Fault. The largest earthquake that occurred in this zone is the 5.4 Mw event in 1959. This zone includes NW-SE, E-W, and NE-SW-trending faults.

LOGR3 – The lower Graben, which is the northern part of the Rhenish earthquake zone, is included in LOGR3. This has high earthquake activity with the 5.2 Mw 1932 event being the largest earthquake in LOGR3 and includes predominantly NW-SE and N-S-trending faults.

SCHE3 -This zone includes the Schelde Estuary at the border between Belgium and the Netherlands. The largest earthquake in this zone is of magnitude 4.7 Mw and occurred in 1848 and the faults are predominantly N-S and NNW-SSE.

NETH3 – The Northern Netherlands is included in NETH3 as a single zone of low (< 4.0 Mw) levels of seismicity. The structural trend is N-S and NNW-SSE.

ESHE3 – This zone includes the East Shetland Platform and borders the more active Viking Graben on its western edge. It is characterized by low (< 4.0 Mw) earthquake activity and includes E-W, NW-SE, and N-S-trending faults.

WCGR3 – This zone includes the area of the North Sea bordering the Central Graben and has low seismicity levels. Faults here are predominantly N-S, NW-SE-trending faults.

VIKG3 - This zone includes the Viking Graben with N–S–trending faults. The largest earthquake that occurred in this zone is the 5.3 Mw 1927 event, which is outside the completeness thresholds of the catalogue.

CEGR3 - This zone broadly encompasses the Central Graben with predominantly N–S–trending faults. The seismic activity in this zone is characterised by low magnitudes (< 4.0 Mw).

HORP3 - This source with very low seismicity levels includes the Horda Platform. Structural trends within this zone are predominantly N–S.

SOTA3 – The Sogn-Tampen region is included in SOTA3, which has intense seismic activity. The largest earthquake in this zone is the 5.3 Mw 1989 event. The predominant trends of the faults here are NE-SW, E-W and N-S.

HORO3 – This zone includes the Hordaland – Rogaland region and the offshore θygarden Fault zone, which is the most easterly coast-parallel N-S fault of the northern North Sea. The largest (4.8 Mw) earthquake in this zone occurred in 1962.

RORY3 – This zone comprises the Rogaland and Ryfylke area and is characterised by low-to-moderate seismicity with a 4.5 Mw 1943 event being the largest here. Faults here are predominantly N-S, NE-SW-trending.

NDBA3 - This zone includes the seismically active Sorgenfrei–Tornquist Zone. The largest earthquake here was the 4.6 Mw earthquake in 1958 and the faults have E-W and N-S trends.

SWDA3 - This zone, which includes part of the Rinkrbing-Fyn High, has low seismicity. The predominant structural trend is N-S.

NNSE3 – This zone, which comprises the northern part of the North Sea included in the study area, was not part of model A in EQE02. Due to high (< 5.5 Mw) levels of seismicity compared to the neighbouring areas, we model this region as an individual zone. Structural trends in this zone are predominantly NE–SW and N-S.

BACK3 – This background zone includes the Faroes Islands, Ireland, the eastern part of the Atlantic Ocean, and Western Approaches. It contains very little seismicity.

The results of the nearest neighbour analysis on the individual zones of SZM3 show that the seismicity in these zones is dispersed, except for NENG3 which the nearest neighbour ratio is 0.5. The zones LOGR3 and SCHE3 show a slightly clustered seismicity with a nearest neighbour ratio of 0.8-0.9. However, we did not modify these zones because we used this source model as proposed in EQE02.

SZM4

NISL4 – This zone of low earthquake activity comprises the west Shetland Platform but excludes the Shetland Islands. Faults here have predominantly N-S and NE-SW trends.

HEBR4 – Similar to HERB3, this zone includes the Hebridean region. It is characterised by low (< 4.0 Mw) seismic levels and the predominant structural trend in this zone is NE-SW.

FCNS4 – This low (< 4.0 Mw) seismicity zone covers the Mid-North Sea Platform, the Grampian region in Northeast Scotland, and the Forth Basin. The structural trends are predominantly NE-SW and E-W.

SBOR4 – SBOR4 includes the Southern Uplands and the Midland Valley in Scotland and is an area of generally low seismicity (Mw < 4.0). Faults in this zone are predominantly NE–SW-trending.

NWIS4 – The north Irish Sea is an area of low seismic activity, except for the eastern side where moderate (4.7 Mw) earthquakes occurred in 1786 and 1843. The structural trend of faults here is predominantly N-S and NE-SW.

PECU4 – This zone comprises the Pennines and Cumbria regions with moderate (up to 4.5 Mw) seismic activity. The predominant faulting trend in this zone is N-S.

NEEN4 – This zone includes northeastern England with E-W and NW-Se-trending faults and is characterised by low levels of seismicity, except for the 4.5 Mw 1780 event.

HUSN4 – This seismically active zone includes the Humber region, the Sole Pit Basin and in general the southern North Sea in the UK sector of the North Sea. The largest earthquake that occurred in this zone is the largest instrumentally recorded 1931 Dogger Bank event. Faults here are predominantly NW-SE and E-S-trending.

IREL4 – Ireland and the western Irish coast are included in a single zone of low (< 4.1 Mw) seismicity. Faults here are NE–SW and NW–SE-trending.

WACE4 – This zone includes the entire Wales and central England. Faults here are predominantly NE–SW, N-S, and NW-SE-trending. The largest (5.0 Mw) earthquakes that occurred in WACE4 within the completeness thresholds in Table 2 occurred in 1852, 1896, and 1957.

NSNL4 – The Netherlands and the offshore area of the south North Sea bordering this country are included in NSNL4, which has very low seismic activity. The faults here have predominantly N-S and NNW-SSE.

WESS4 – The region to the south of the Bristol Channel is included in WESS4 and lies on the foreland below the Variscan Front. It is characterized by low (< 4.0 Mw) levels of seismicity and includes E-W-trending faults.

CORN4 - This low seismicity zone corresponds to a part of the Cornubian Ridge. The predominant trends of the faults in this zone are NE-SW and E-W.

BELG4 – Central Belgium is included in a single zone, which is characterised by high levels of seismicity with 5.5 Mw earthquakes in 1692 and 1992 being the largest events here. Faults here are predominantly NE-SW and NW-SE.

WSHE4 – This low seismicity zone includes parts of the West and East Shetland Platform and borders the more active Viking Graben on its western edge. The predominant faulting trend is E-W, N-S and NE-SW.

VIKG4 - This zone includes the most active area in the North Sea, i.e. the Viking Graben, with N-S and NE-SW-trending faults. The largest earthquake that occurred in this zone is the 5.3 Mw 1927 event which is outside the completeness thresholds of the catalogue.

CEGR4 - This zone broadly encompasses the Central Graben with predominantly N–S–trending faults. The seismic activity in this zone is characterised by low magnitudes (< 4.0 Mw).

HORP4 - This source with very low seismicity levels includes the Horda Platform. Structural trends within this zone are predominantly N–S.

SOGN4 – The Sogn region, which is included in SOGN4, has intense seismic activity with a 5.3 Mw 1989 event being the largest in this zone. Faults have N-S and NE-SW trends.

STHO4 – This zone comprises the Stord - Hordaland area with N-S and NE-SW-trending faults and is characterised by low-to-moderate seismicity with a 4.9 Mw 1865 event being the largest here.

NDBA4 - This zone includes the seismically active Sorgenfrei–Tornquist Zone. The largest earthquake here was the 4.6 Mw earthquake in 1958 and faults are E-W and N-S trends.

WJUT4 - This zone, which includes part of the Rinkrbing-Fyn High, has low seismicity and NE-SW and N-S-trending faults.

NNSE4 – This zone, which comprises the northern part of the North Sea included in the study area, was not part of model B in EQE02. Due to high (< 5.5 Mw) levels of seismicity compared to the neighbouring areas, we model this region as an individual zone. Structural trends in this zone are predominantly NE–SW and N-S.

BACK4 – This background zone includes the Faroes Islands, the eastern part of the Atlantic Ocean, and West Approaches. It contains very little seismicity.

HIGL4, ANLI4, MICR4, LOBR4, OFPL4, BRIT4, and ENGC4 – These zones are the same as HIGL4, ANLI4, MICR4, LOBR4, OFPL4, BRIT4, and ENGC4.

The results of the nearest neighbour analysis on the individual zones of SZM4 show that the seismicity in the zones is dispersed, except for NEEN4 for which the seismicity is clustered (the nearest neighbour ratio is 0.6). As explained for SZM3, we did not modify these zones because we used this source model as proposed in EQE02.

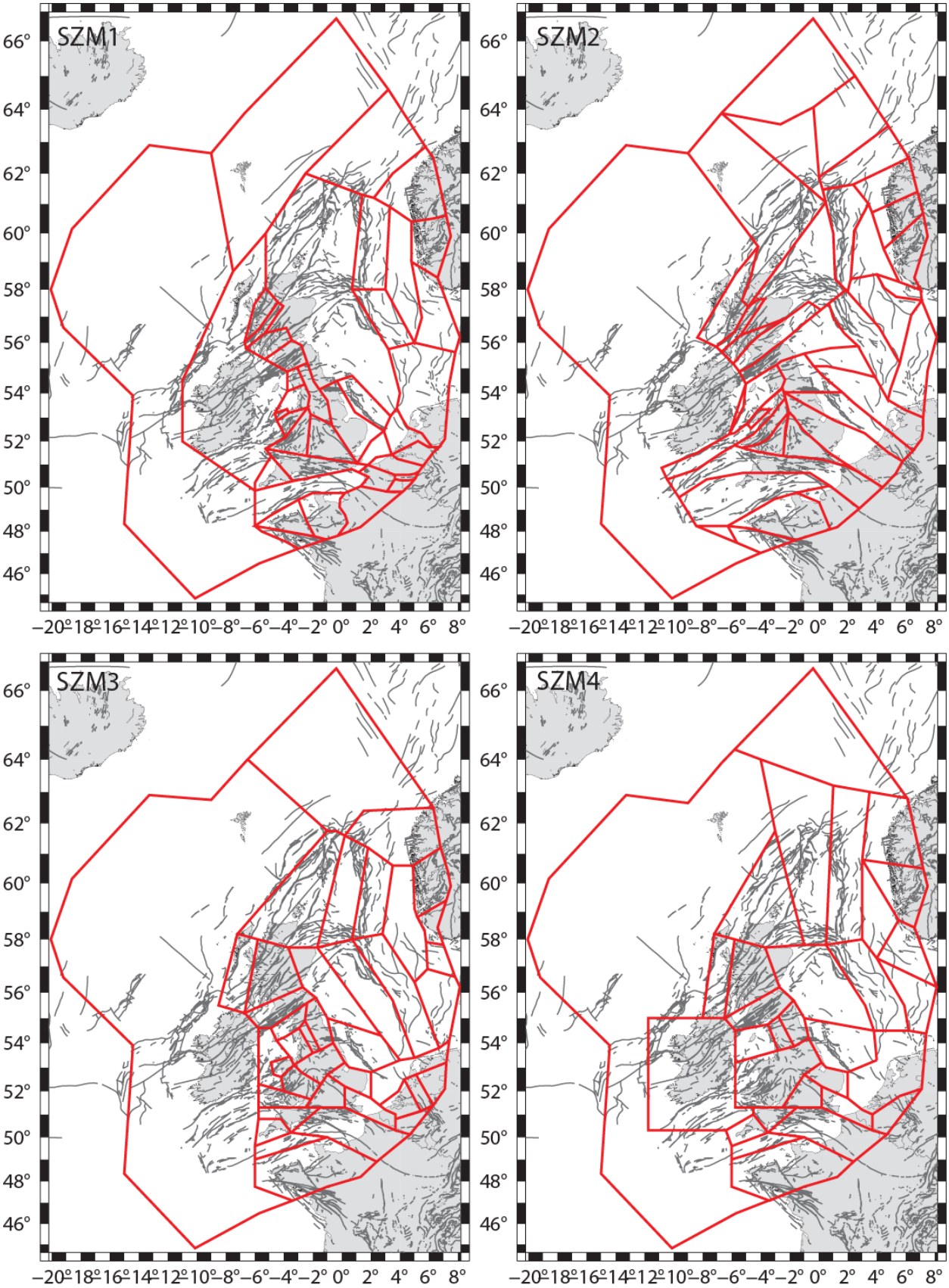

Figure 53: Simplified tectonic map of the study area and geometry of the seismic source zone models SZM1-SZM4. The faults are from Asch (2003) and the British Geological Survey DigMapGB series.

Overview of the recurrence statistics

Tables 13-16 show an overview of the recurrence statistics determined for each of the zones in the source models SZM1-SZM4. For each zone (first column), the tables present the number of

earthquakes in the zone within the completeness periods in Table 2 (second column), the maximum observed magnitude (Mmax [obs] in the third column), the mean magnitude (Mw [mean] in the fourth column), the recurrence parameters (fifth and sixth columns), and the area of the zone (seventh column).

Zone	*N*	*Mmax[obs]*	*Mw [mean]*	*(N≥ 3.0 Mw)/yr*	*b-value*	*Area (km^2)*
CORN1	6	4.1	3.6	0.068 ± 0.027	1.016 ± 0.094	15493
RHEN1	3	4.4	3.7	0.035 ± 0.019	1.004 ± 0.097	35039
WCHA1	5	4.7	3.8	0.056 ± 0.024	0.990 ± 0.095	59072
DOVE1	4	4.1	3.8	0.045 ± 0.022	0.993 ± 0.096	12349
SLPT1	1	5.9	5.9	0.82 ± 0.87	0.983 ± 0.098	25088
EANG1	7	4.9	3.9	0.077 ± 0.028	0.977 ±0.093	43681
MMCE1	7	5.0	4.1	0.075 ± 0.028	0.957 ± 0.093	29881
PENN1	20	4.6	3.9	0.208 ± 0.046	0.946 ± 0.085	16512
MMCW1	7	4.3	3.5	0.093 ± 0.034	1.011 ± 0.096	20060
MMCW2	10	5.0	4.8	1.10 ± 0.51	1.024 ± 0.098	20060
MENA11	3	4.4	3.5	0.038 ± 0.021	1.004 ± 0.098	1680
MENA21	3	5.0	4.8	0.33 ± 0.22	1.005 ± 0.098	1680
EISB1	6	4.7	3.9	0.067 ± 0.026	0.987 ± 0.094	12124
CUMF1	4	4.7	3.8	0.046 ± 0.022	1.000 ± 0.096	5388
BALA1	1	3.5	3.5	0.013 ± 0.012	1.007 ± 0.098	7452
SC1M1	1	3.3	3.3	0.013 ± 0.012	1.011 ± 0.098	14056
SC341	11	4.9	3.8	0.120 ± 0.036	0.994 ± 0.091	13742
SC781	12	4.8	3.9	0.129 ± 0.036	0.970 ± 0.090	6497
SC91	14	4.5	3.6	0.158 ± 0.041	1.043 ± 0.089	11861
ESCO1	-	-	-	0.89 ± 0.48	1.012 ± 0.095	297205
IREL1	2	4.0	3.8	0.024 ± 0.016	1.000 ± 0.097	293742
VIKI1	2	4.8	4.8	1.71 ± 1.40	1.017 ± 0.098	42056
CEGR1	-	-	-	0.094 ± 0.051	1.012 ± 0.095	31187
NOR61	-	-	-	0.139 ± 0.076	1.012 ± 0.095	46302
NOR51	-	-	-	0.128 ± 0.69	1.012 ± 0.095	42556
NOR41	11	4.8	4.3	0.84 ± 0.29	1.001± 0.090	26958
NOR31	25	5.3	4.5	1.69 ± 0.43	0.953 ± 0.079	42273
NOR21	4	5.5	5.0	3.20 ± 2.05	1.014 ± 0.097	77667
NOR11	-	-	-	0.67 ± 0.36	1.012 ± 0.095	223086
FRA11	25	5.4	3.8	0.217 ± 0.043	0.913 ± 0.080	15409
FRA21	32	4.8	3.7	0.289 ± 0.050	0.985 ± 0.079	26028
FRA31	37	5.1	3.9	0.311 ± 0.051	0.862 ± 0.073	41881
FRA41	6	4.8	4.0	0.055 ± 0.022	0.950 ± 0.094	38517

FRA51	3	4.8	3.9	0.029 ± 0.016	0.981 ± 0.096	14038
FRA61	1	3.3	3.3	0.011 ± 0.010	1.008 ± 0.098	5219
BEL11	13	5.5	4.2	0.111 ± 0.030	0.876 ± 0.087	15443
BEL21	14	5.1	4.1	0.120 ± 0.032	0.883 ± 0.086	2806
BEL31	13	5.5	4.1	0.113 ± 0.031	0.897 ± 0.087	13638
NL11	-	-	-	0.063 ± 0.034	1.012 ± 0.095	21008
NL21	-	-	-	0.29 ± 0.16	1.012 ± 0.095	95216
NATL1	-	-	-	2.89 ± 1.57	1.012 ± 0.095	961124

Table 13: Recurrence statistics for each zone of SZM1.

Zone	*N*	*Mmax[obs]*	*Mw [mean]*	*(N≥ 3.0 Mw)/yr*	*b-value*	*Area (km^2)*
SARM2	23	5.4	3.7	0.206 ± 0.042	0.963 ± 0.083	24336
NARM2	73	5.1	3.8	0.613 ± 0.071	0.869 ± 0.061	71058
PARB2	3	4.8	4.0	0.029 ± 0.016	0.974 ± 0.096	29120
ENGC2	11	4.7	3.7	0.121 ± 0.036	1.003 ± 0.091	113852
VARF2	9	4.8	3.9	0.097 ± 0.032	0.975 ± 0.092	105678
CHAT2	6	4.4	3.8	0.067 ± 0.026	0.989 ±0.094	27524
WRET2	17	5.0	4.3	0.160 ± 0.038	0.825 ± 0.084	14450
MIWA2	5	4.1	3.5	0.058 ± 0.025	1.022 ± 0.095	15506
IRIS2	3	4.2	3.9	0.035 ± 0.019	0.988 ± 0.097	37665
NWAL12	4	4.4	3.6	0.050 ± 0.024	1.003 ± 0.098	3566
NWAL22	3	5.0	4.8	0.33 ± 0.22	1.005 ± 0.098	3566
BRAM2	49	5.5	4.0	0.457 ± 0.066	0.830 ± 0.069	82983
CLEB2	8	5.9	4.2	0.083 ± 0.029	0.923 ± 0.092	28262
SOLE2	2	5.5	4.2	1.58 ± 1.29	0.997 ± 0.098	53170
LAKE2	11	4.7	3.7	0.122 ± 0.036	1.007 ± 0.091	28507
SUPT2	1	3.3	3.3	0.013 ± 0.012	1.011 ± 0.098	48599
MIVT2	2	3.7	3.3	0.024 ± 0.016	1.019 ± 0.097	29227
SWSC2	9	4.9	3.9	0.098 ± 0.032	0.979 ± 0.092	11489
GGFZ2	14	4.8	3.9	0.150 ± 0.039	0.970 ± 0.089	8897
WNHT2	13	4.5	3.5	0.148 ± 0.040	1.056 ± 0.090	35385
ESCO2	-	-	-	0.81 ± 0.44	1.012 ± 0.095	271827
VIKG2	2	4.8	4.8	1.71 ± 1.40	1.017 ± 0.098	36137
NORB2	-	-	-	0.22 ± 0.12	1.012 ± 0.095	71564
MORB2	1	5.5	5.5	0.85 ± 0.90	0.992 ± 0.098	48527
TAMB2	3	4.9	4.8	2.53 ± 1.78	1.022 ± 0.097	31087

NFSH2	24	5.3	4.5	1.59 ± 0.41	0.945 ± 0.080	24860
CFSH2	-	-	-	0.52 ± 0.12	0.969± 0.075	21138
SFSH2	11	4.8	4.3	0.84 ± 0.29	1.001 ± 0.090	26884
SOTO2	-	-	-	0.026 ± 0.014	1.012 ± 0.095	8785
HORP2	-	-	-	0.087 ± 0.047	1.012 ± 0.095	28991
NDBA2	-	-	-	0.109 ± 0.059	1.012 ± 0.095	46215
CEGR2	-	-	-	0.157 ± 0.085	1.012 ± 0.095	52173
MNSH2	-	-	-	0.069 ± 0.037	1.012 ± 0.095	22888
HORN2	-	-	-	0.175 ± 0.095	1.012 ± 0.095	58094
NLBA2	-	-	-	0.19 ± 0.10	1.012 ± 0.095	63472
BACK2	-	-	-	3.33 ± 1.81	1.012 ± 0.095	1107715

Table 14: Recurrence statistics for each zone of SZM2.

Zone	*N*	*Mmax[obs]*	*Mw [mean]*	*(N≥ 3.0 Mw)/yr*	*b-value*	*Area (km^2)*
NISL3	-	-	-	0.28 ± 0.15	1.012 ± 0.095	92844
HEBR3	1	3.2	3.2	0.013 ± 0.012	1.014 ± 0.098	31971
HIGL3	34	4.9	3.7	0.367 ± 0.063	0.999 ± 0.079	44748
MNPL3	-	-	-	0.170 ± 0.092	1.012 ± 0.095	56313
SBOR3	1	3.7	3.7	0.013 ± 0.012	1.002 ± 0.098	24689
IAPS3	7	4.7	3.7	0.079 ± 0.029	1.012 ±0.094	11674
NENG3	2	4.5	3.9	0.024 ± 0.016	0.994 ± 0.097	16773
PENN3	6	4.6	4.1	0.065 ± 0.026	0.952 ± 0.094	5057
LAKE3	7	4.7	3.8	0.078 ± 0.029	0.995 ± 0.094	13672
SNSE3	1	5.9	5.9	0.82 ± 0.87	0.983 ± 0.098	44771
IRIS3	-	-	-	0.0772 ± 0.0066	0.962 ± 0.064	24699
NWAL13	5	4.4	3.5	0.062 ± 0.027	1.005 ± 0.097	6156
NWAL23	3	5.0	4.8	0.33 ± 0.22	1.005 ± 0.098	6156
MIWA3	10	5.0	4.1	0.104 ± 0.032	0.934 ± 0.091	17162
CENG3	14	5.0	4.0	0.145 ± 0.038	0.933 ± 0.088	21867
ANLI3	5	3.7	3.4	0.058 ± 0.025	1.036 ± 0.095	17852
MICR3	1	3.3	3.3	0.013 ± 0.012	1.011 ± 0.098	18619
SWAL13	3	4.3	4.0	0.041 ± 0.023	0.973 ± 0.098	18387
SWAL23	6	4.9	4.8	0.66 ± 0.35	1.016 ± 0.096	18387
LOBR3	7	5.3	4.1	0.075 ± 0.028	0.951 ± 0.093	22454
OFLC3	-	-	-	0.120 ± 0.065	1.012 ± 0.095	39698
CORN3	5	4.1	3.7	0.057 ± 0.024	1.007 ± 0.095	14914

WESS3	2	3.3	3.2	0.025 ± 0.016	1.027 ± 0.097	19083
ENGC3	10	4.8	4.2	0.103 ± 0.032	0.920 ± 0.091	74917
OFPL3	1	3.3	3.3	0.013 ± 0.012	1.011 ± 0.098	19425
BEME3	35	5.5	4.0	0.286 ± 0.048	0.823 ± 0.072	10605
BRIT3	98	5.4	3.8	0.821 ± 0.083	0.866 ± 0.055	121815
LOGR3	4	5.2	4.1	0.038 ± 0.018	0.965 ± 0.095	10385
SCHE3	2	4.7	4.4	0.020 ± 0.013	0.967 ± 0.097	17135
NETH3	-	-	-	0.047 ± 0.026	1.012 ± 0.095	15665
ESHE3	-	-	-	0.137 ± 0.074	1.012 ± 0.095	45558
WCGR3	-	-	-	0.20 ± 0.11	1.012 ± 0.096	67211
VIKG3	2	4.8	4.8	1.71 ± 1.40	1.017 ± 0.098	34825
CEGR3	-	-	-	0.20 ± 0.11	1.012 ± 0.095	66570
HORP3	-	-	-	0.155 ± 0.084	1.012 ± 0.095	51491
SOTA3	34	5.3	4.4	2.29 ± 0.52	0.953 ± 0.075	53137
HORO3	9	4.8	4.3	0.69 ± 0.26	1.000 ± 0.091	26483
RORY3	2	4.5	4.3	0.17 ± 0.12	1.003 ± 0.097	10336
NDBA3	-	-	-	0.033 ± 0.18	1.012 ± 0.095	10846
SWDA3	-	-	-	0120 ± 0.065	1.012 ± 0.095	39727
NNSE3	1	5.5	5.5	0.85 ± 0.90	0.992 ± 0.098	172194
BACK3	-	-	-	3.88 ± 2.10	1.012 ± 0.095	1288600

Table 15: Recurrence statistics for each zone of SZM3.

Zone	*N*	*Mmax[obs]*	*Mw [mean]*	*(N≥ 3.0 Mw)/yr*	*b-value*	*Area (km^2)*
NISL4	-	-	-	0.25 ± 0.14	1.012 ± 0.095	83458
HEBR4	2	3.2	3.2	0.025 ± 0.016	1.027 ± 0.097	31336
HIGL4	33	4.9	3.7	0.354 ± 0.062	0.990 ± 0.079	45672
FCNS4	-	-	-	0.29 ± 0.16	1.012 ± 0.095	97395
SBOR4	2	3.7	3.5	0.024 ± 0.016	1.012 ± 0.097	27848
NWIS4	3	4.7	4.2	0.034 ± 0.019	0.971 ±0.097	23165
PECU4	13	4.6	3.8	0.140 ± 0.038	0.982 ± 0.089	9004
NEEN4	2	4.5	4.9	0.024 ± 0.016	0.994 ± 0.097	14905
HUNS4	1	5.9	5.9	0.82 ± 0.88	0.983 ± 0.098	55150
IREL4	1	4.0	4.0	0.013 ± 0.012	0.996 ± 0.098	215346
WACE4	44	5.0	4.1	0.399 ± 0.061	0.799 ± 0.070	82178
ANLI4	5	3.7	3.4	0.058 ± 0.025	1.036 ± 0.095	17852
NSNL4	-	-	-	0.29 ± 0.15	1.012 ± 0.095	94887

MICR4	1	3.3	3.3	0.013 ± 0.012	1.011 ± 0.098	18619
LOBR4	7	5.3	4.1	0.075 ± 0.028	0.951 ± 0.093	22454
WESS4	1	3.0	3.0	0.013 ± 0.012	1.017 ± 0.098	13987
ENGC4	10	4.8	4.2	0.103 ± 0.032	0.920 ± 0.091	74917
CORN4	6	4.1	3.6	0.068 ± 0.027	1.016 ± 0.094	16669
OFPL4	1	3.3	3.3	0.013 ± 0.012	1.011 ± 0.098	19425
BRIT4	98	5.4	3.8	0.821 ± 0.083	0.866 ± 0.055	121815
BELG4	42	5.5	4.0	0.338 ± 0.052	0.803 ± 0.068	20871
WSHE4	-	-	-	0.33 ± 0.18	1.012 ± 0.095	109942
VIKG4	5	4.9	4.8	4.36 ± 2.59	1.038 ± 0.096	75388
CEGR4	-	-	-	0.19 ± 0.10	1.012 ± 0.095	63799
HORP4	-	-	-	0.092 ± 0.050	1.012 ± 0.095	30565
SOGN4	26	5.3	4.5	1.76 ± 0.44	0.954 ± 0.079	44579
STHO4	11	4.8	4.3	0.84 ± 0.29	1.001 ± 0.090	35670
NDBA4	-	-	-	0.094 ± 0.051	1.012 ± 0.095	31300
WJUT4	-	-	-	0.107 ± 0.058	1.012 ± 0.095	35444
NNSE4	1	5.5	5.5	0.85 ± 0.90	0.992 ± 0.098	107847
BACK4	-	-	-	3.19 ± 1.73	1.012 ± 0.095	1059685

Table 16: Recurrence statistics for each zone of SZM4.

Appendix 2

The results of the residual analysis (Equation 8) are shown in Figures 54-55 for $SA_{0.2\ s}$ and Figures 56-57 for $SA_{1.0\ s}$. The black stars in the figures show the average values for distance intervals to highlight if a clear trend exists. As observed for PGA in Figure 30, the residuals of the empirical GMPEs for ASCRs are positive and therefore they tend to underestimate the UK data, whereas the residuals for the models for SCRs are mainly negative. The mean residuals for all the GMPEs seem to have a negative trend for distances smaller than 100 km but this may be an artefact due to the small number of recordings. The model of CY14 seems to have a positive trend, whereas all the other ground motion models, except for the GMPEs of ASK14, BSSA14, CB14, KOT20, and the three models of RE19, have a negative trend suggesting a dependency on regional attenuation. The mean residuals as a function of magnitude seem not to show any trend (Figure 55 and Figure 57).

The between-event and within-event residuals for $SA_{0.2\ s}$ and $SA_{1.0\ s}$ are displayed in Figures 58-59 and Figures 60-61, respectively. The largest range is for the GMPE of CB14 and the smallest range is for KOT20 and WC20. Note that the range of δB_e for RE19 increases as the period of the spectral acceleration increases. The δB_e values for the GMPEs for SCRs are mostly negative, whereas they are positive for the models for ASCRs. The within-event residuals as a function of distance have values between -8 and 6 and the mean residuals are closer to -2 and 2 (Figure 59 and Figure 61). The largest range is for the GMPE of RE19, whereas the smaller range for the within-event residuals is for the model of KOT20 and WC20.

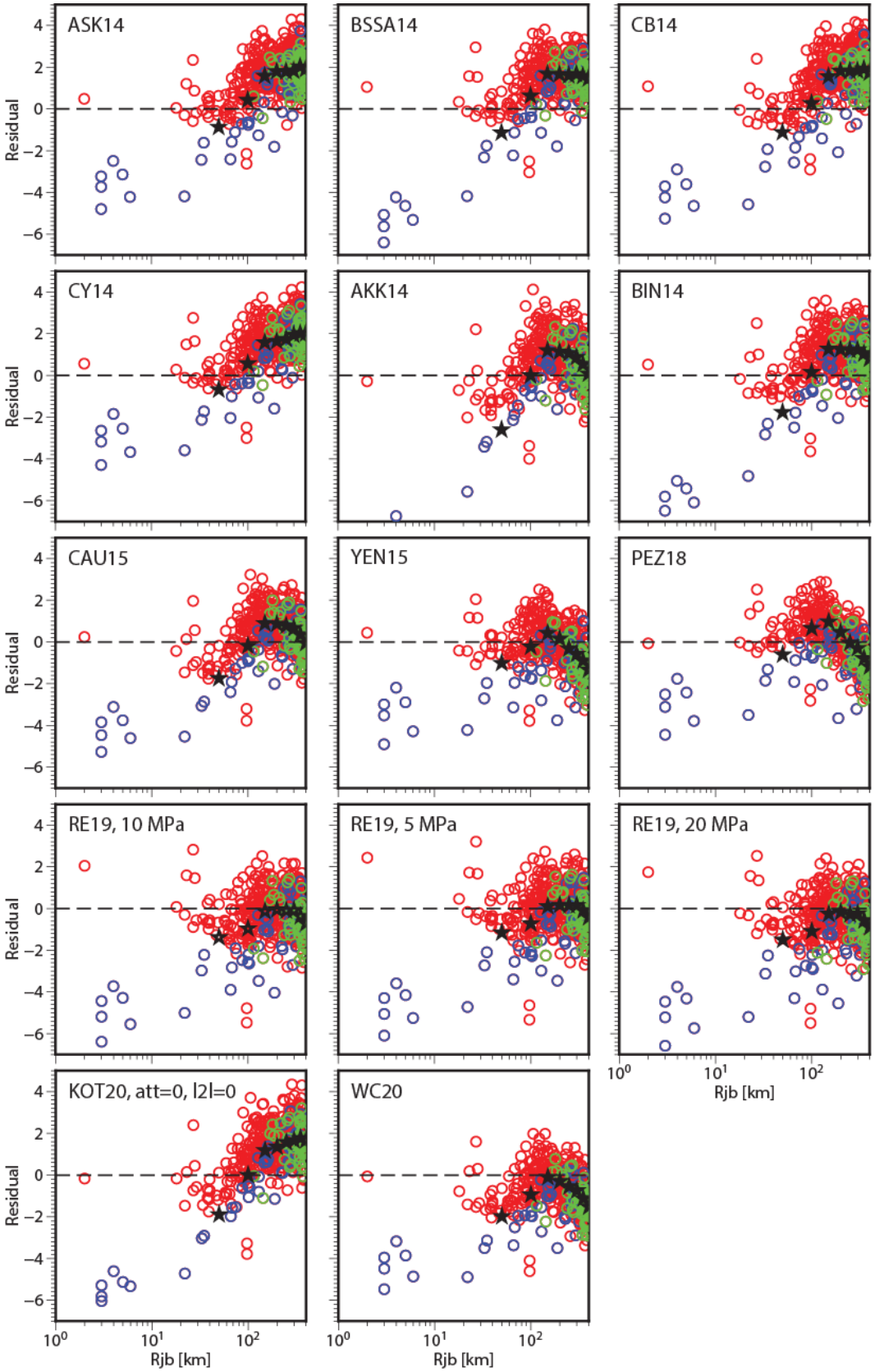

Figure 54: Normalised residuals between the UK strong motion data and the predictions for the 12 candidate GMPEs for $SA_{0.2\,s}$ as a function of distance. The black stars represent the average residuals for distance bins of 50 km. The other symbols are described in Figure 30.

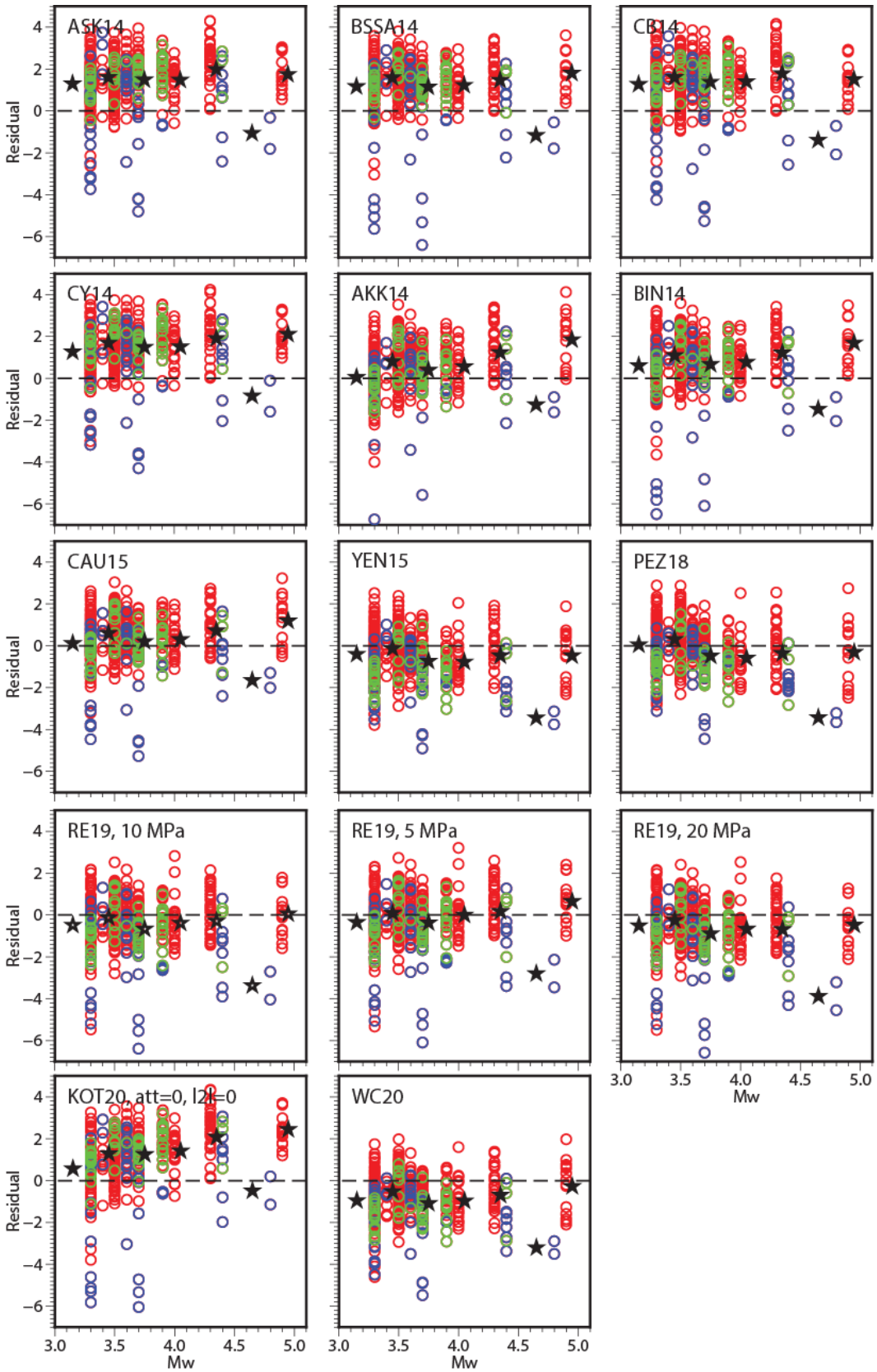

Figure 55: Normalised residuals between the UK strong motion data and the predictions for the 12 candidate GMPEs for $SA_{0.2\ s}$ as a function of moment magnitude. The black stars represent the average residuals for magnitude bins of 0.3 Mw. The other symbols are described in Figure 30.

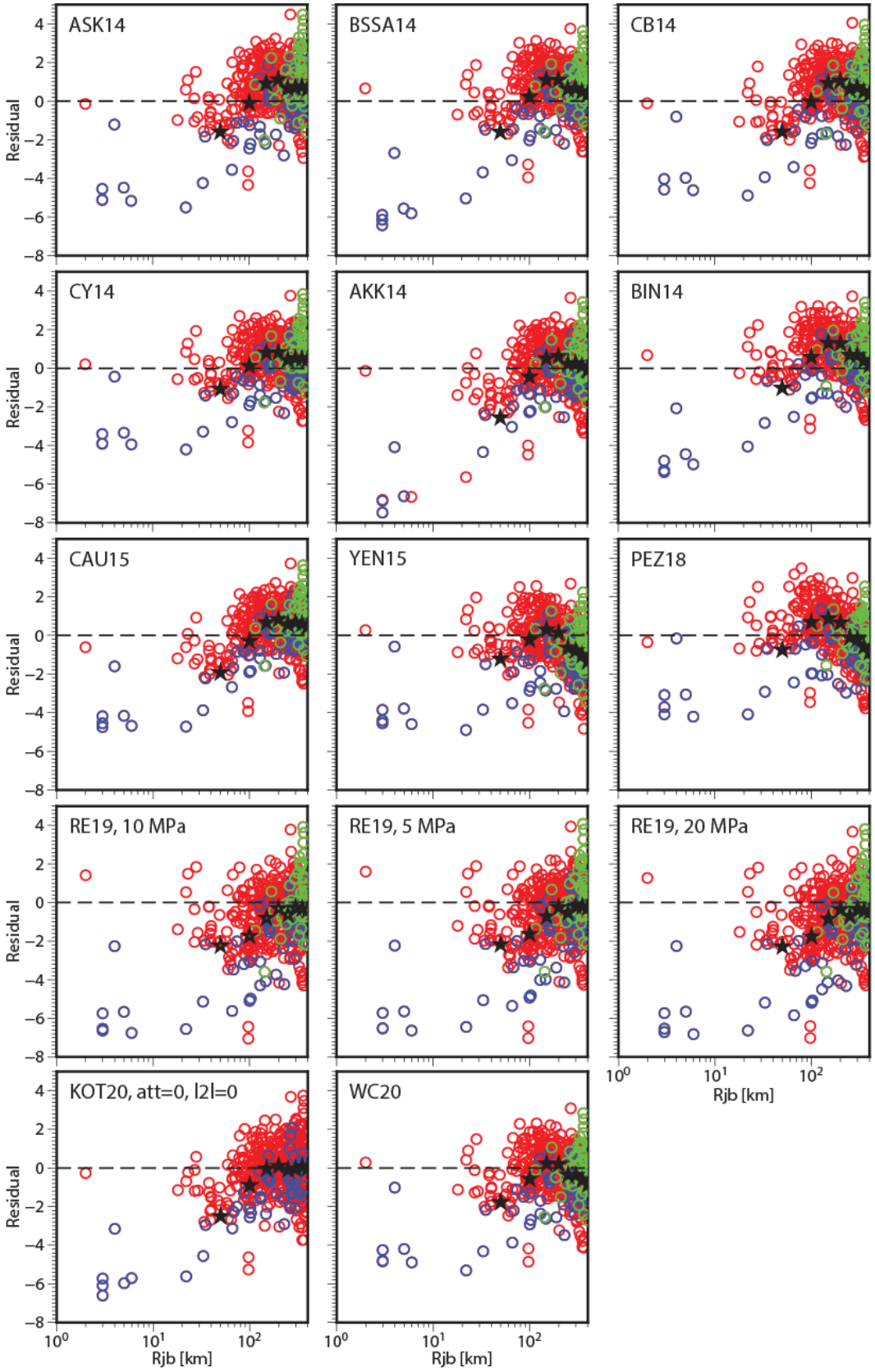

Figure 56: Normalised residuals between the UK strong motion data and the predictions for the 12 candidate GMPEs for $SA_{1.0\,s}$ as a function of distance. The black stars represent the average residuals for distance bins of 50 km. The other symbols are described in Figure 30.

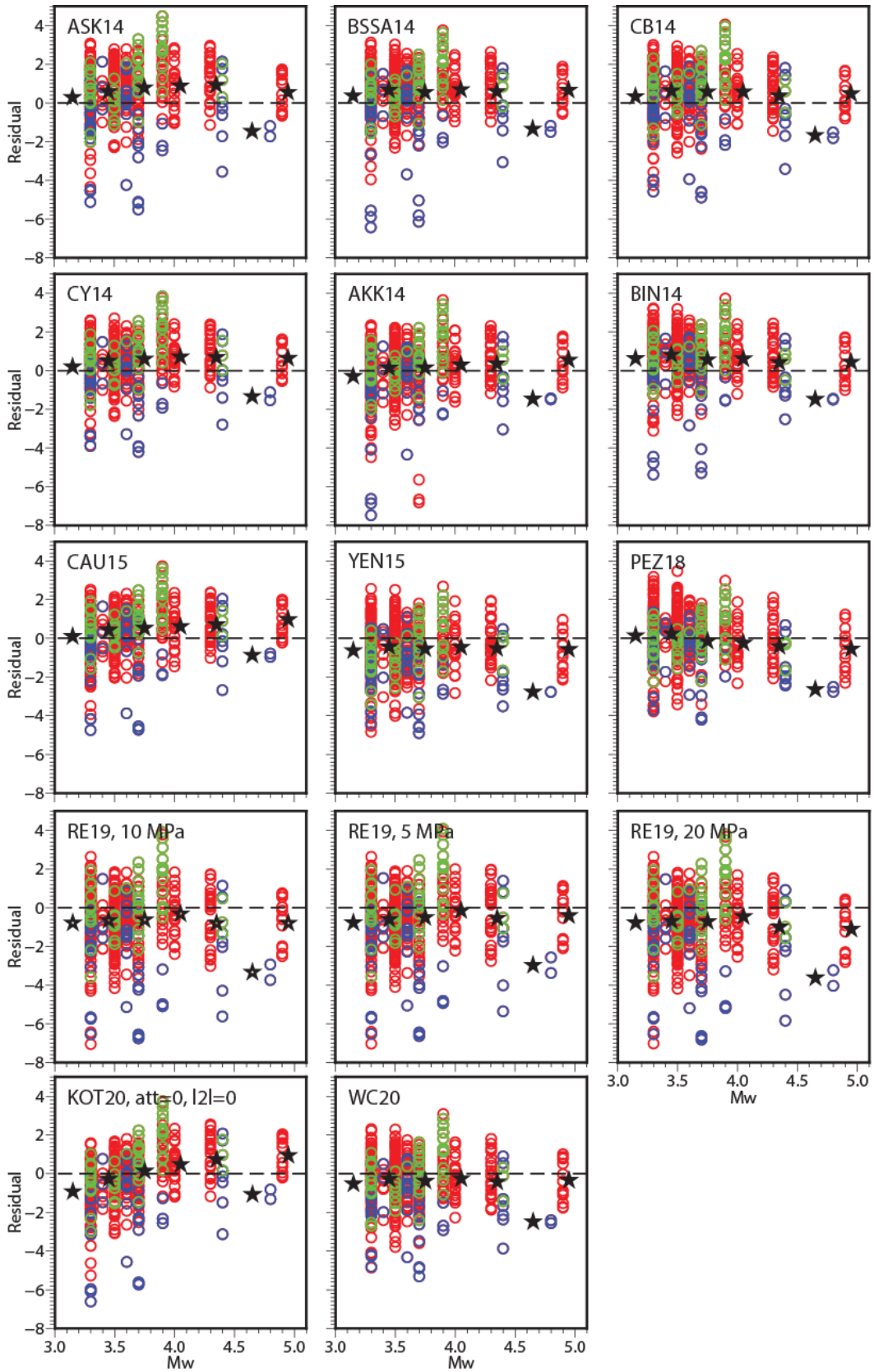

Figure 57: Normalised residuals between the UK strong motion data and the predictions for the 12 candidate GMPEs for $SA_{1.0\ s}$ as a function of moment magnitude. The black stars represent the average residuals for magnitude bins of 0.3 Mw. The other symbols are described in Figure 30.

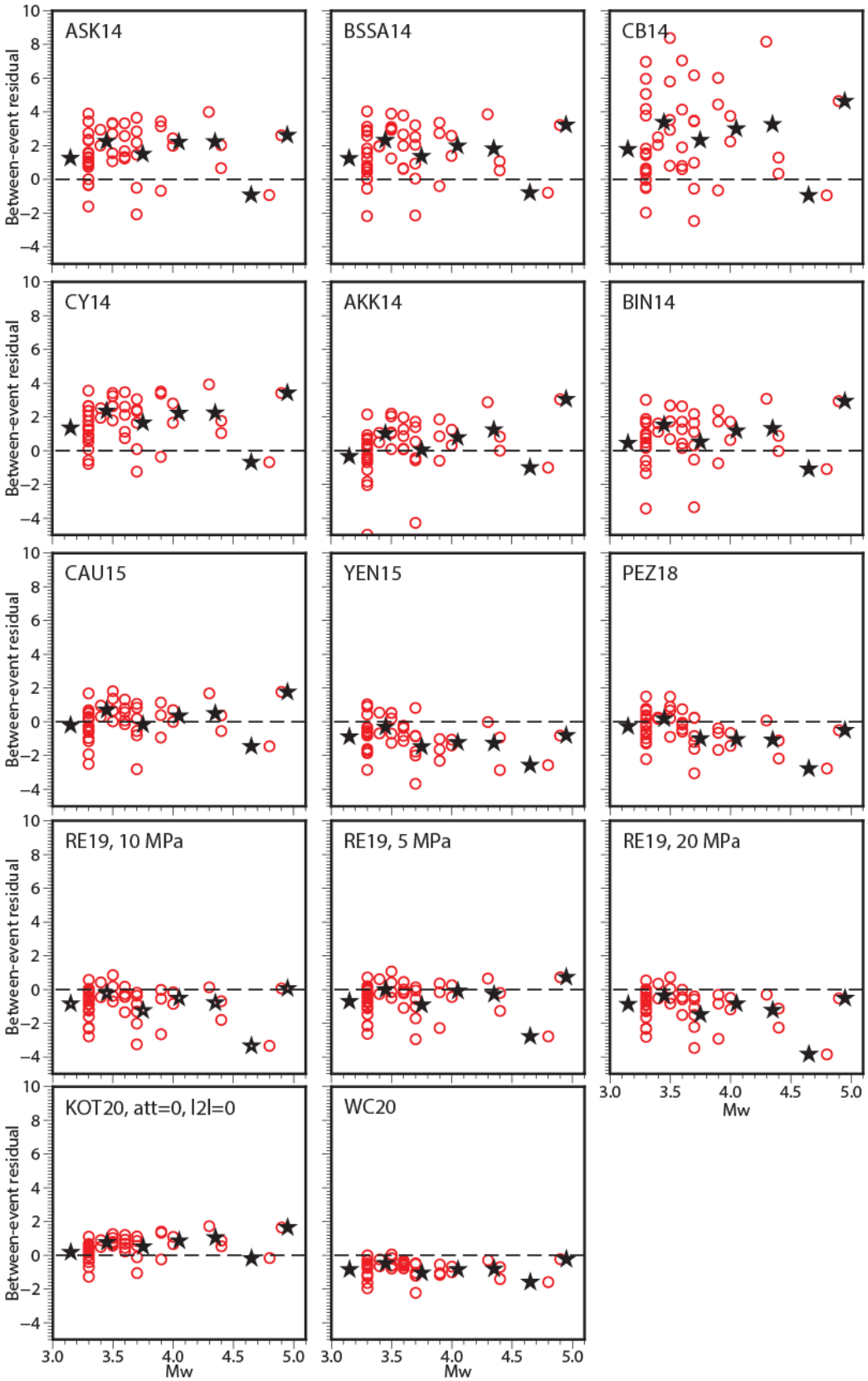

Figure 58: Normalised between-event residuals between the UK strong motion data and the predictions for 12 candidate GMPEs for $SA_{0.2\ s}$. The black stars represent the average residuals for magnitude bins of 0.3 Mw. The black dashed line describes the ideal case, i.e. when the residuals are zero.

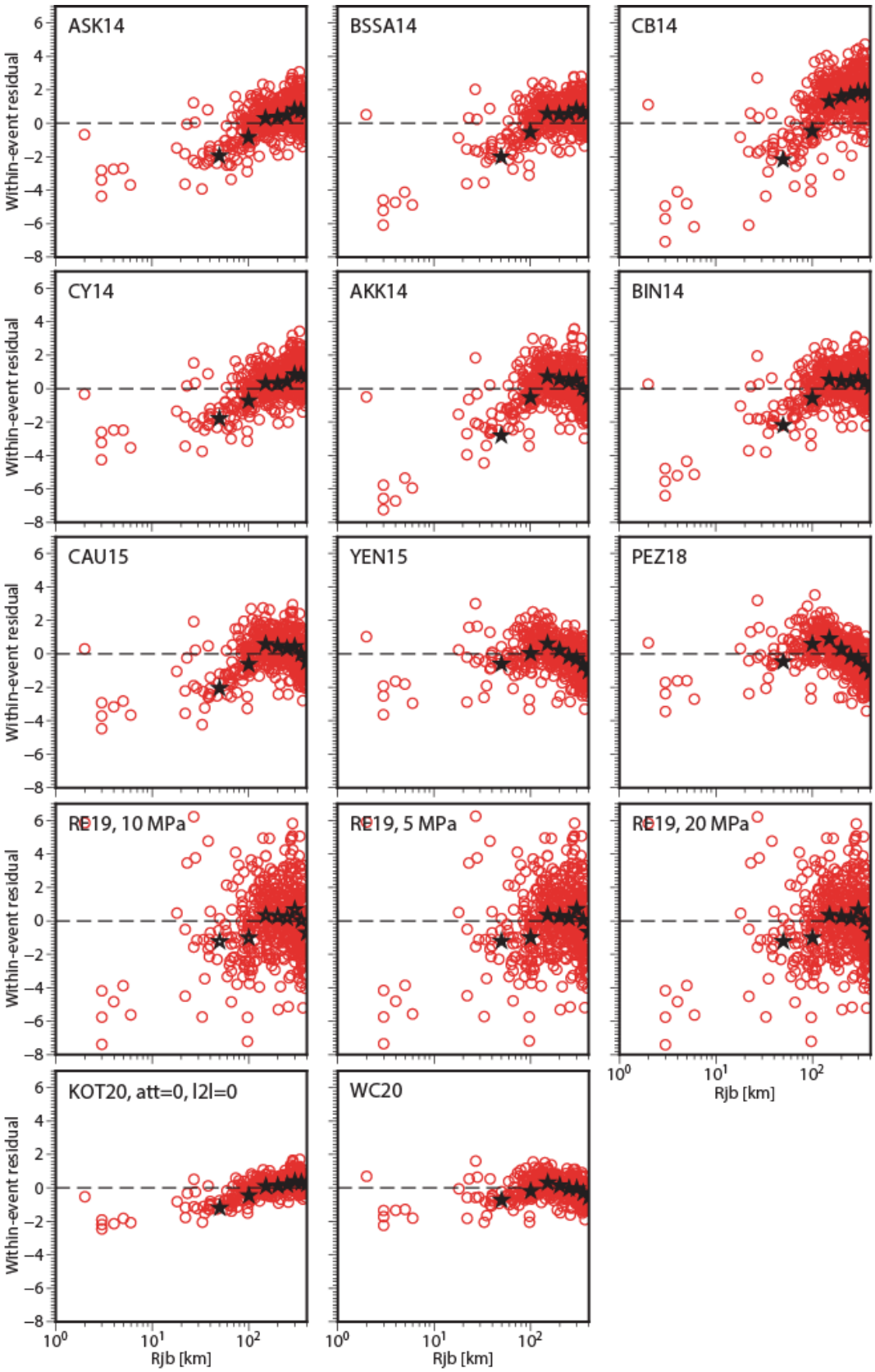

Figure 59: Normalised within-event residuals between the UK strong motion data and the predictions for 12 candidate GMPEs for $SA_{0.2\,s}$. The black stars represent the average residuals for distance bins of 50 km. The black dashed line describes the ideal case, i.e. when the residuals are zero.

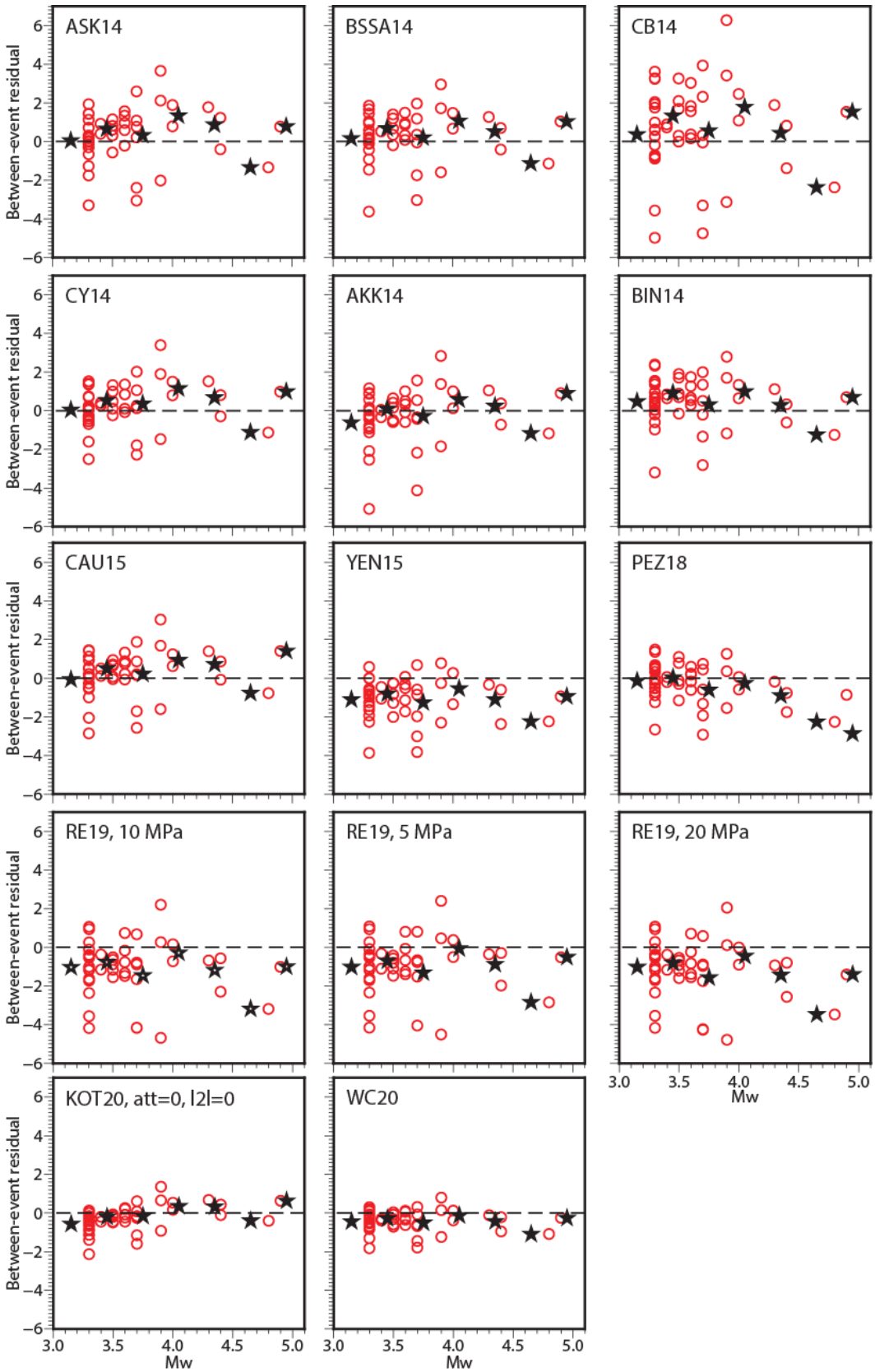

Figure 60: Normalised between-event residuals between the UK strong motion data and the predictions for 12 candidate GMPEs for $SA_{1.0\ s}$. The black stars represent the average residuals for magnitude bins of 0.3 Mw. The black dashed line describes the ideal case, i.e. when the residuals are zero.

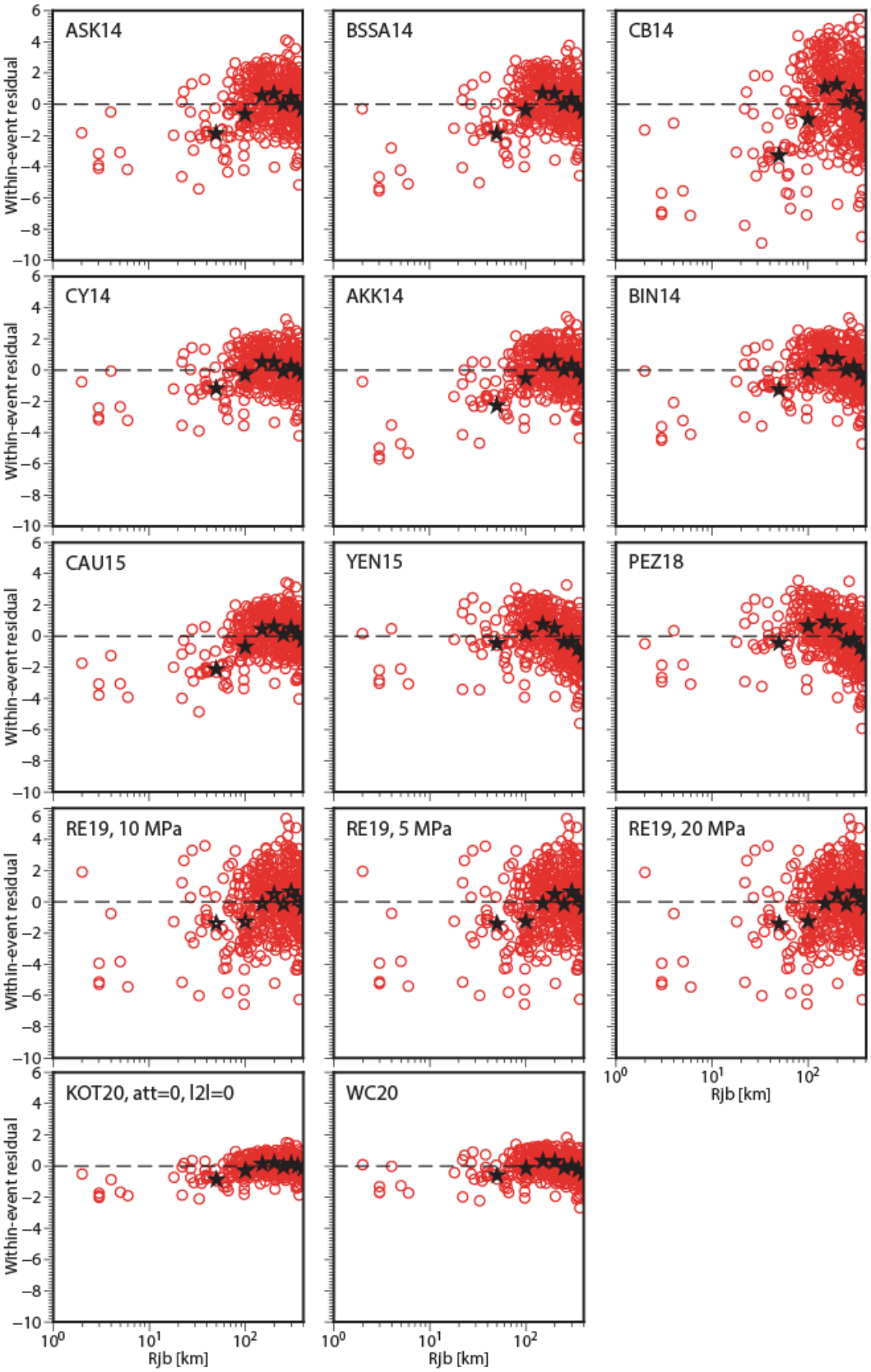

Figure 61: Normalised within-event residuals between the UK strong motion data and the predictions for 12 candidate GMPEs for $SA_{1.0\ s}$. The black stars represent the average residuals for distance bins of 50 km. The black dashed line describes the ideal case, i.e. when the residuals are zero.

Appendix 3

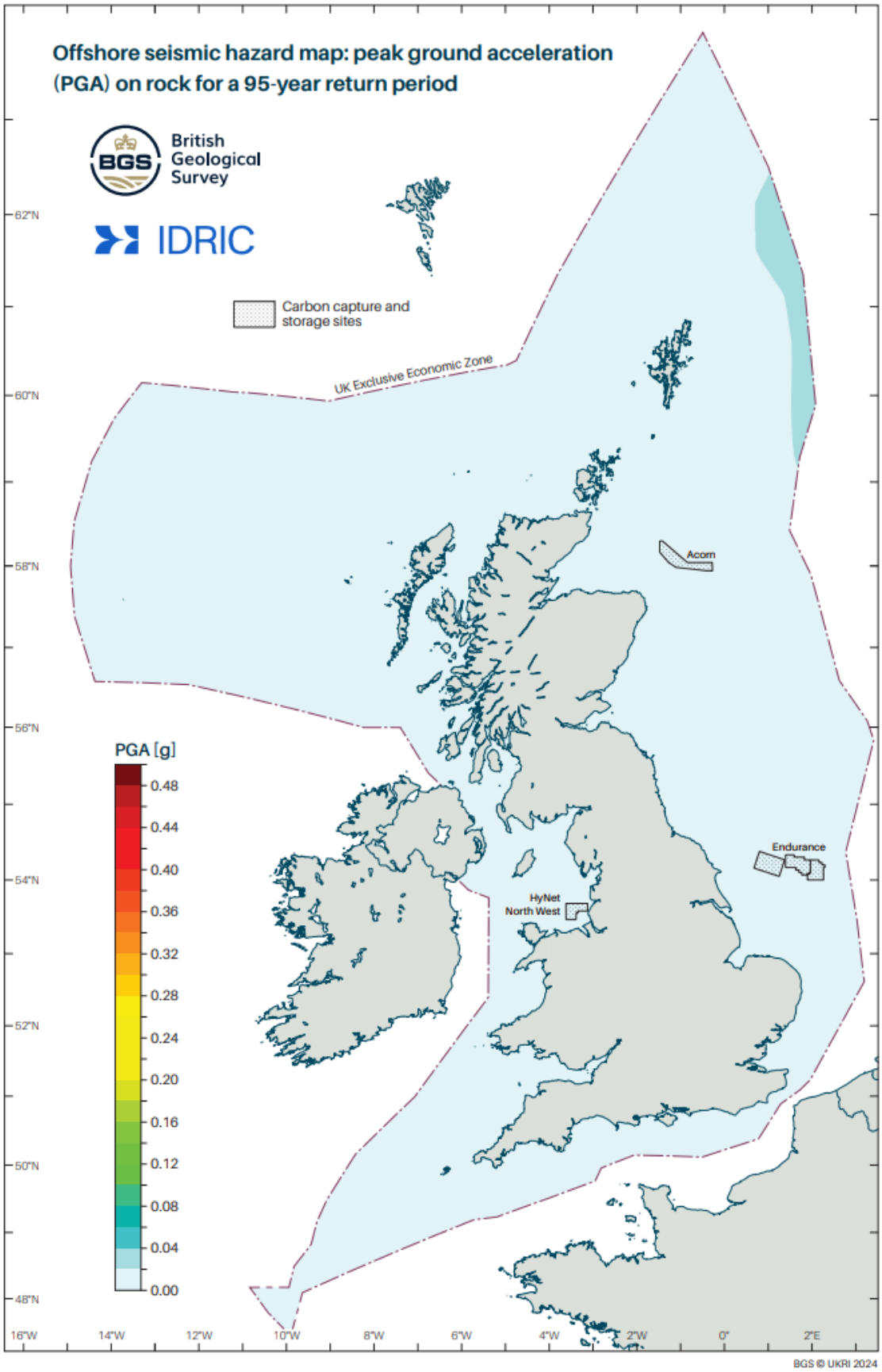

Figure 62: Hazard map for PGA for a 95-year return period. The black polygon describes the UK offshore EEZ. Contains OS data © Crown copyright and database right 2024.

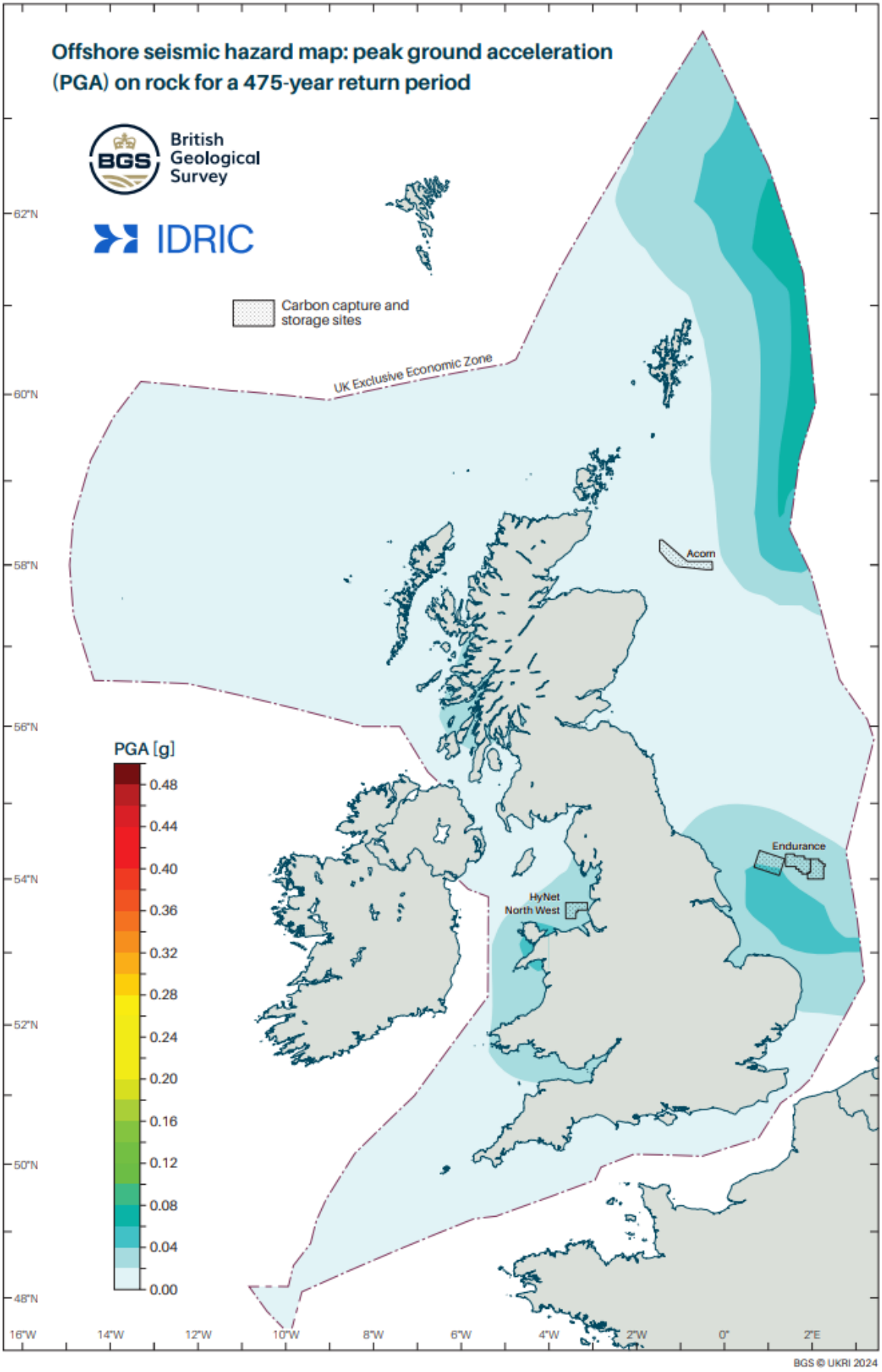

Figure 63: Hazard map for PGA for a 475-year return period. The black polygon describes the UK offshore EEZ. Contains OS data © Crown copyright and database right 2024.

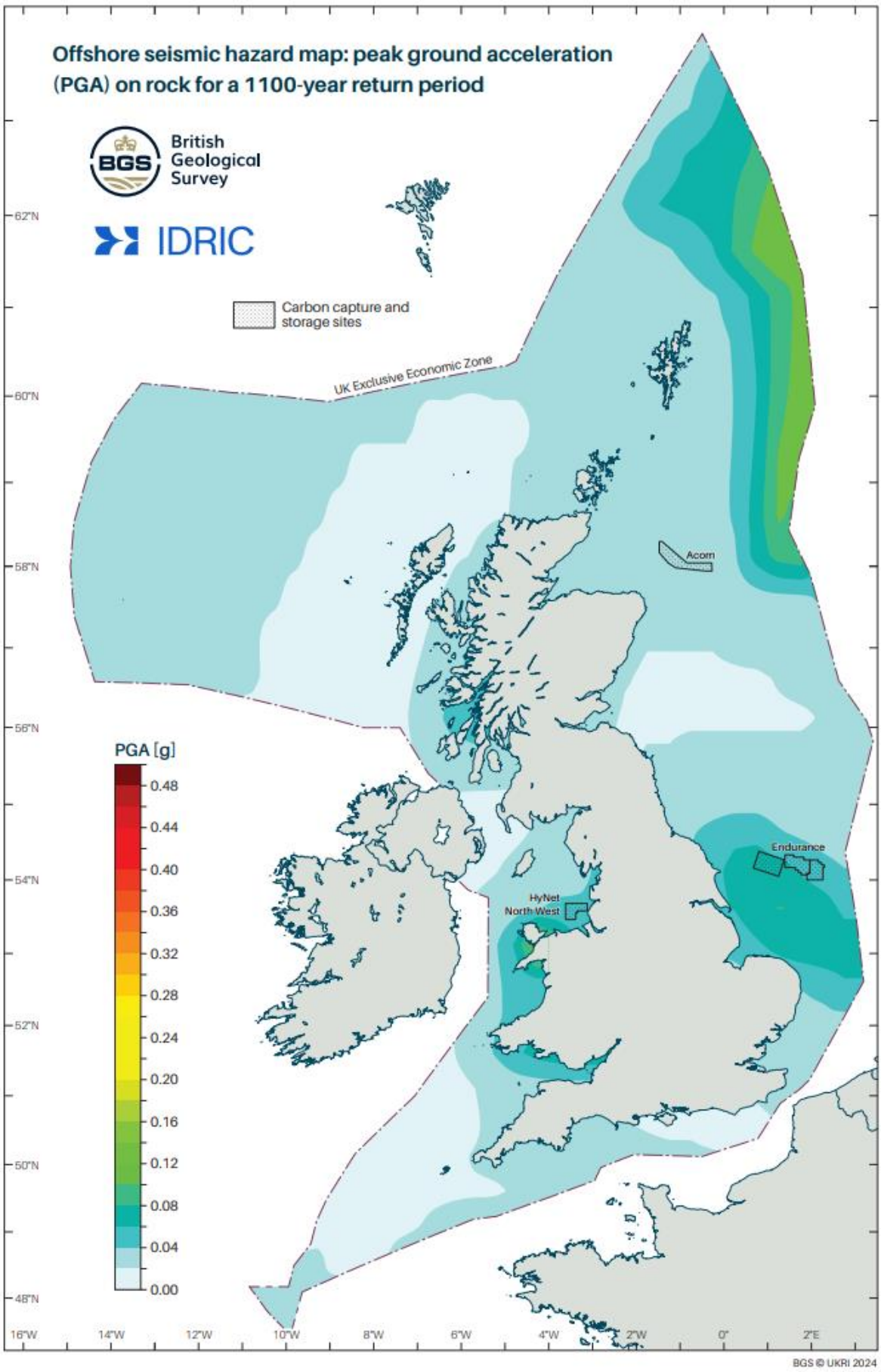

Figure 64: Hazard map for PGA for a 1100-year return period. The black polygon describes the UK offshore EEZ. Contains OS data © Crown copyright and database right 2024.

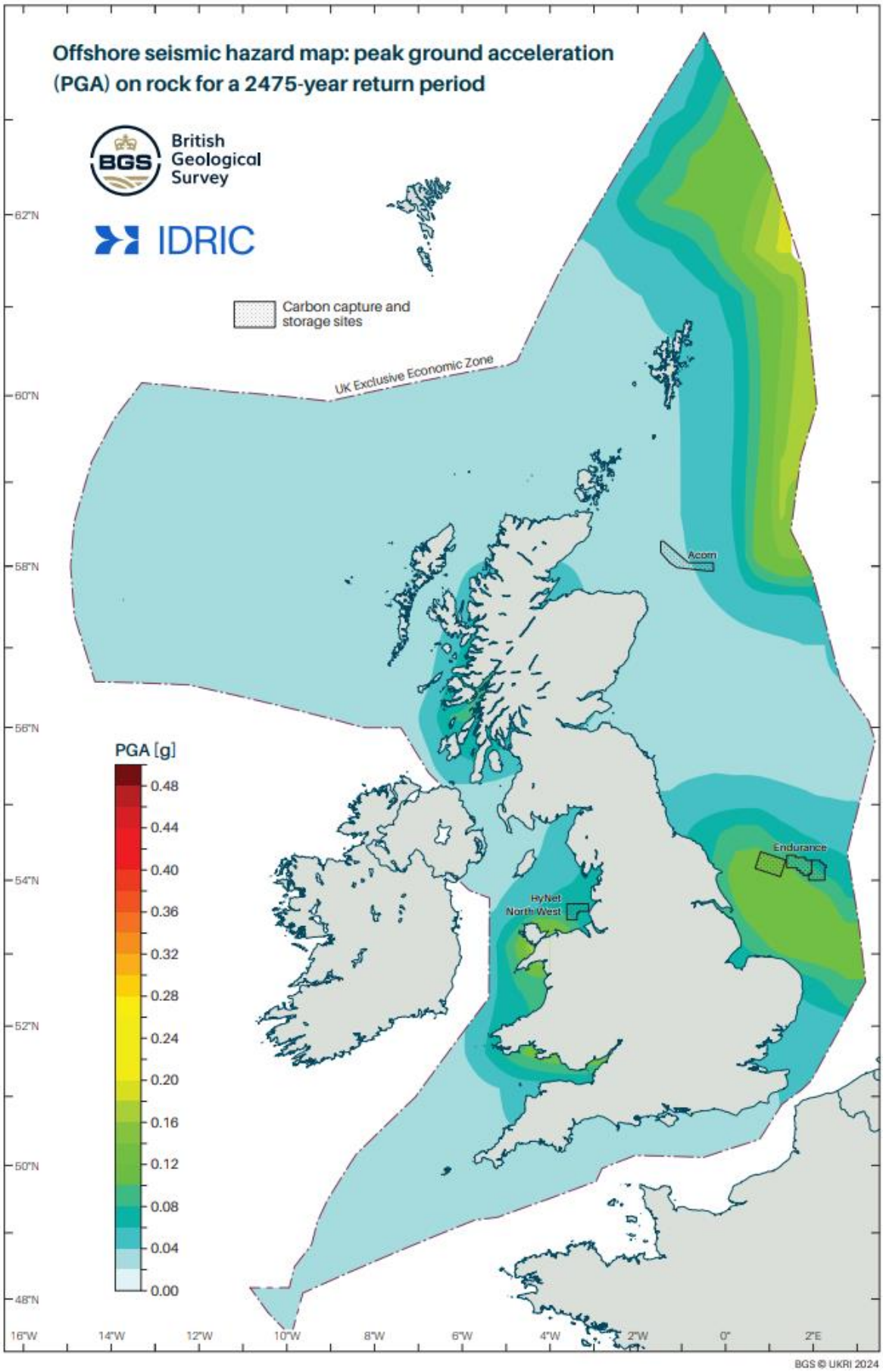

Figure 65: Hazard map for PGA for a 2475-year return period. The black polygon describes the UK offshore EEZ. Contains OS data © Crown copyright and database right 2024.

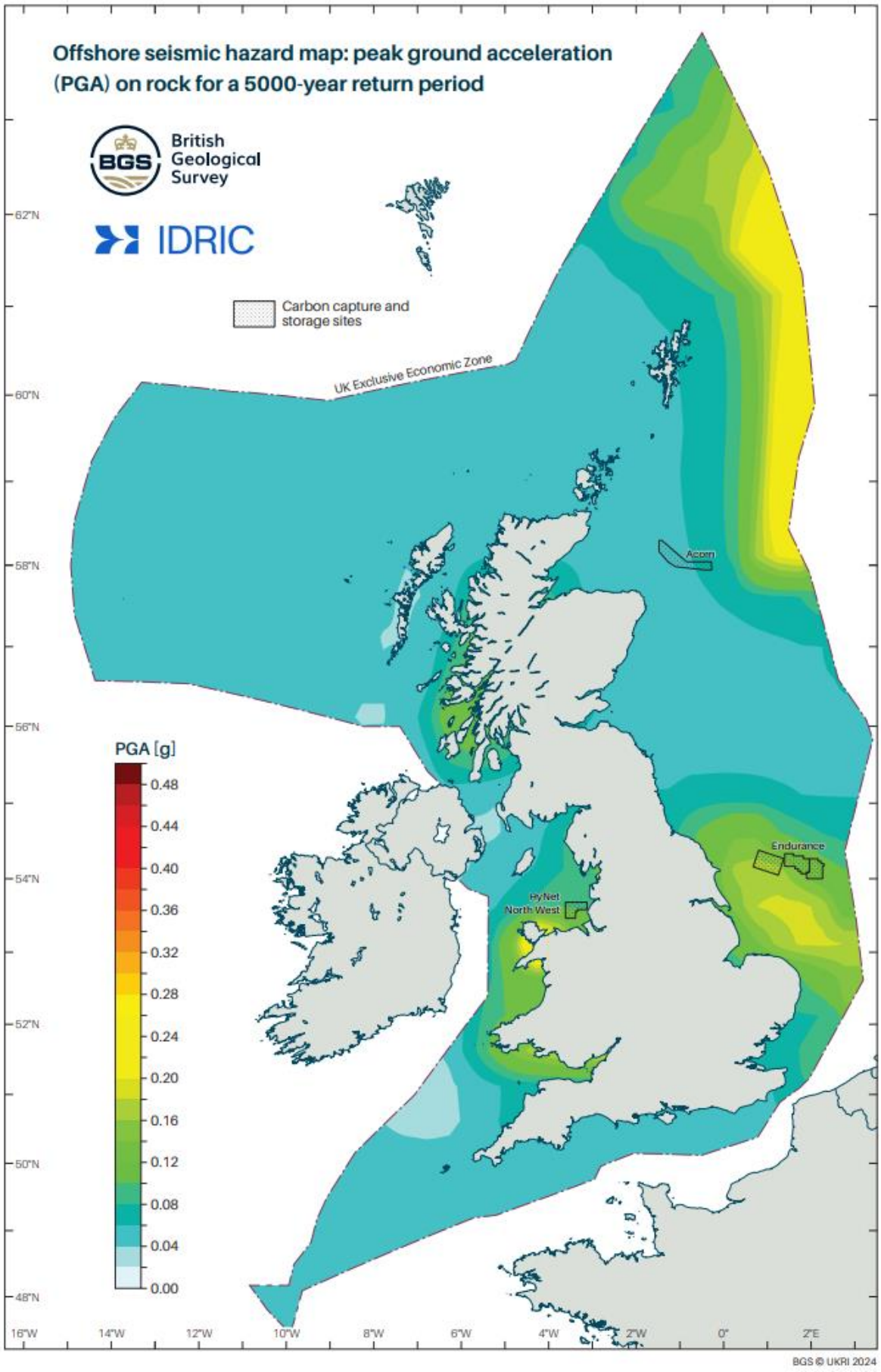

Figure 66: Hazard map for PGA for a 5,000-year return period. The black polygon describes the UK offshore EEZ. Contains OS data © Crown copyright and database right 2024.

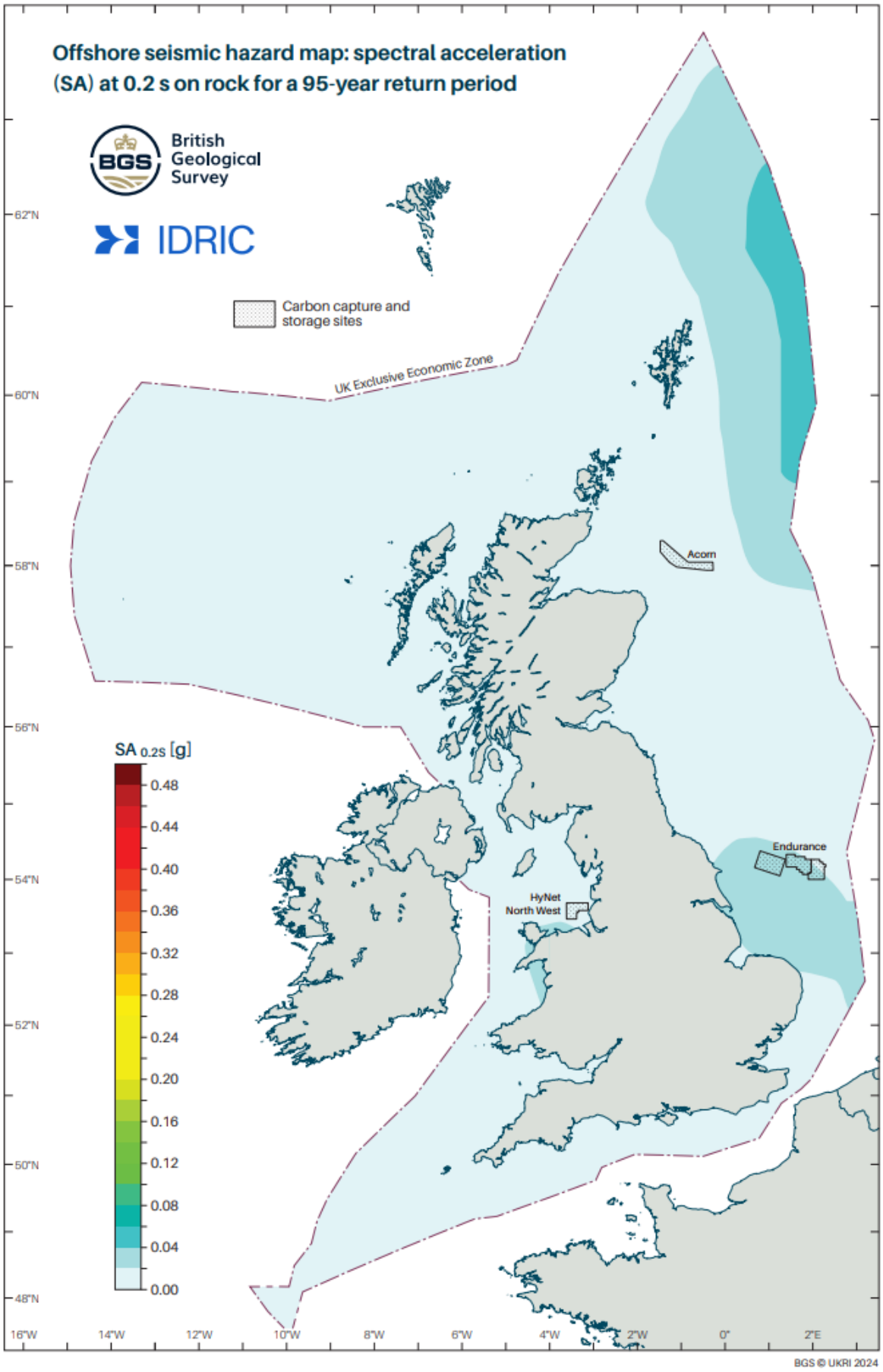

Figure 67: Hazard map for $SA_{0.2\ s}$ for a 95-year return period. The black polygon describes the UK offshore EEZ. Contains OS data © Crown copyright and database right 2024.

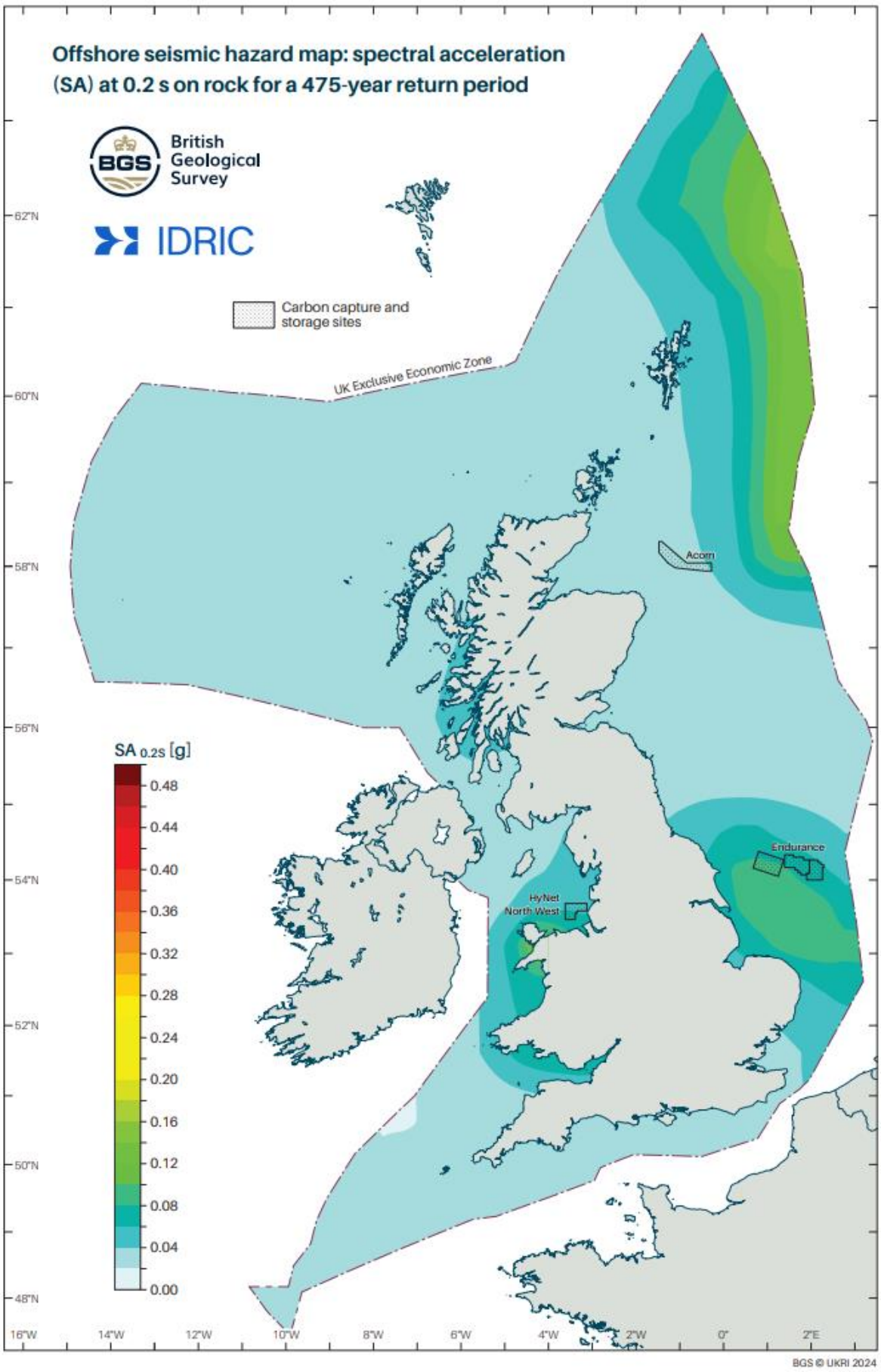

Figure 68: Hazard map for $SA_{0.2\,s}$ for a 475-year return period. The black polygon describes the UK offshore EEZ. Contains OS data © Crown copyright and database right 2024.

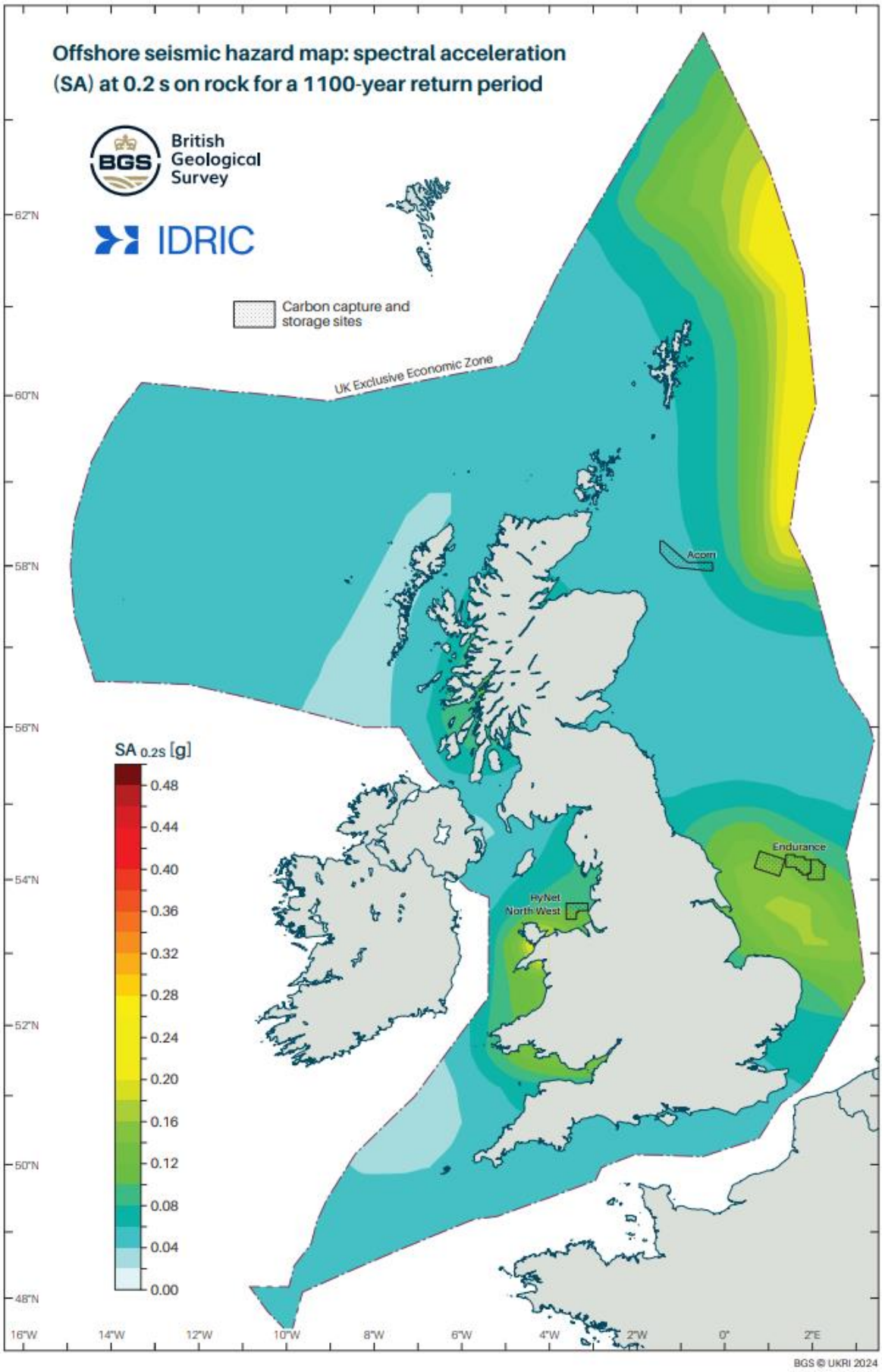

Figure 69: Hazard map for $SA_{0.2\ s}$ for a 1100-year return period. The black polygon describes the UK offshore EEZ. Contains OS data © Crown copyright and database right 2024.

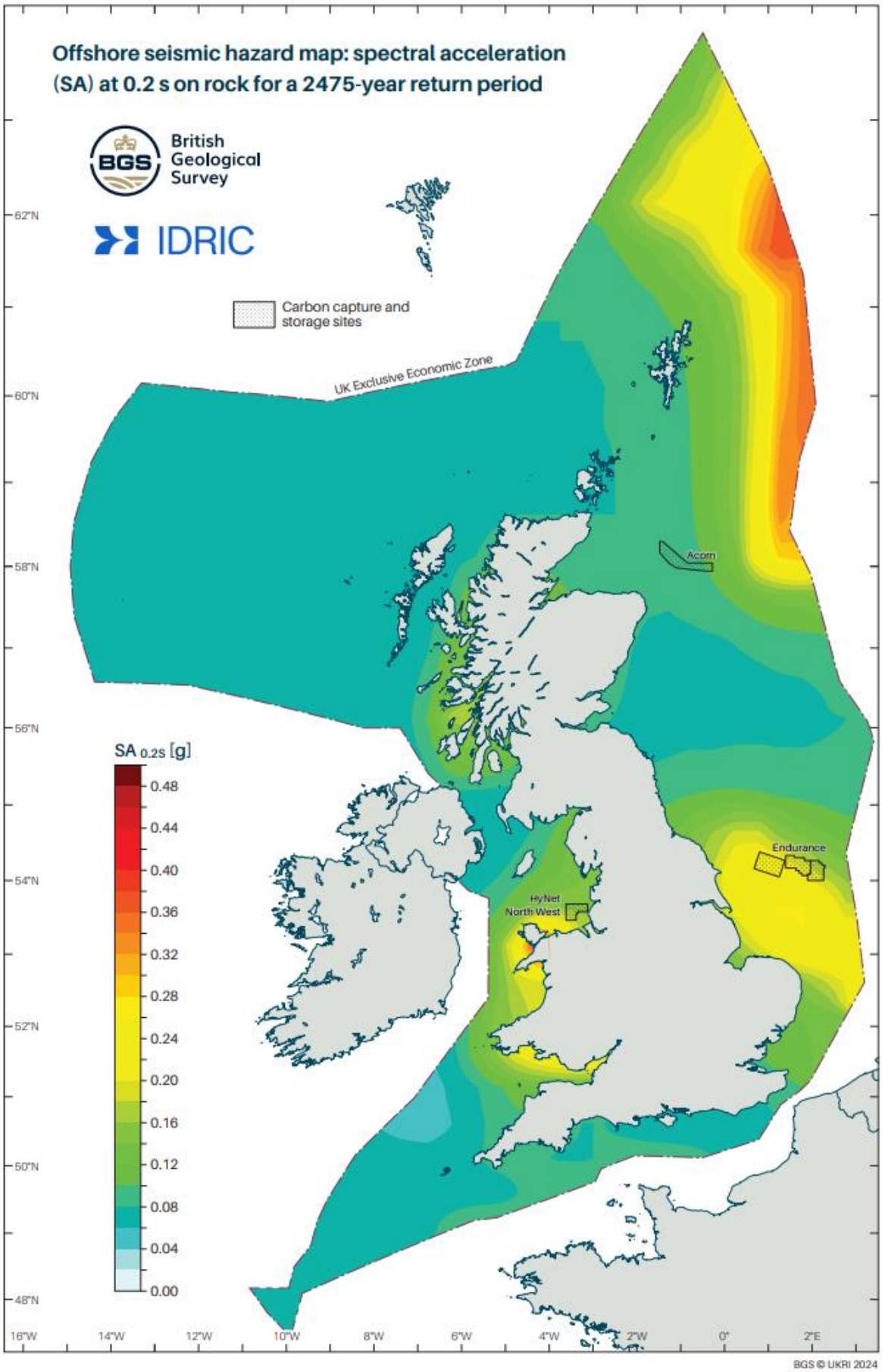

Figure 70: Hazard map for $SA_{0.2\ s}$ for a 2475-year return period. The black polygon describes the UK offshore EEZ. Contains OS data © Crown copyright and database right 2024.

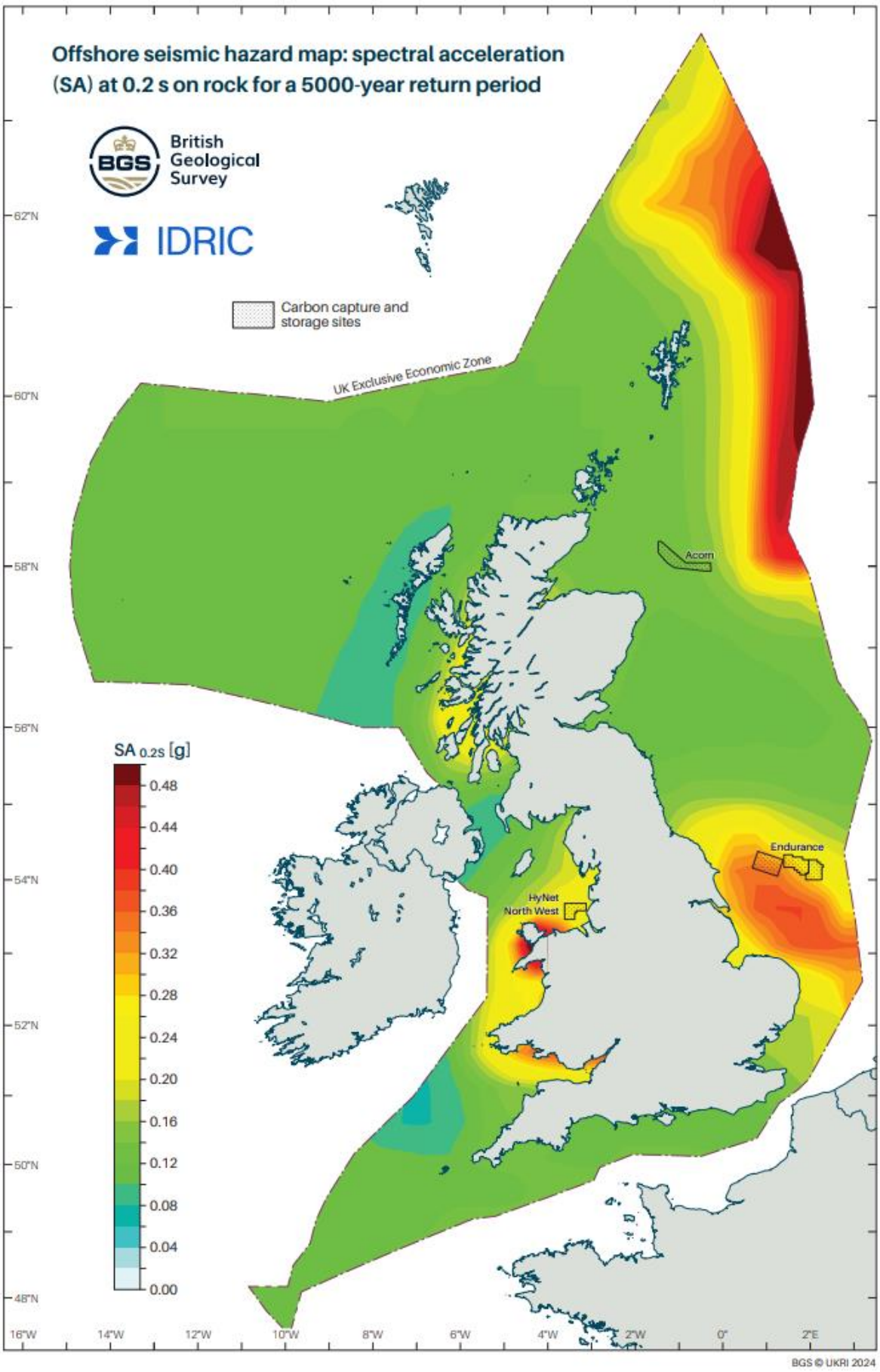

Figure 71: Hazard map for $SA_{0.2\ s}$ for a 5,000-year return period. The black polygon describes the UK offshore EEZ. Contains OS data © Crown copyright and database right 2024.

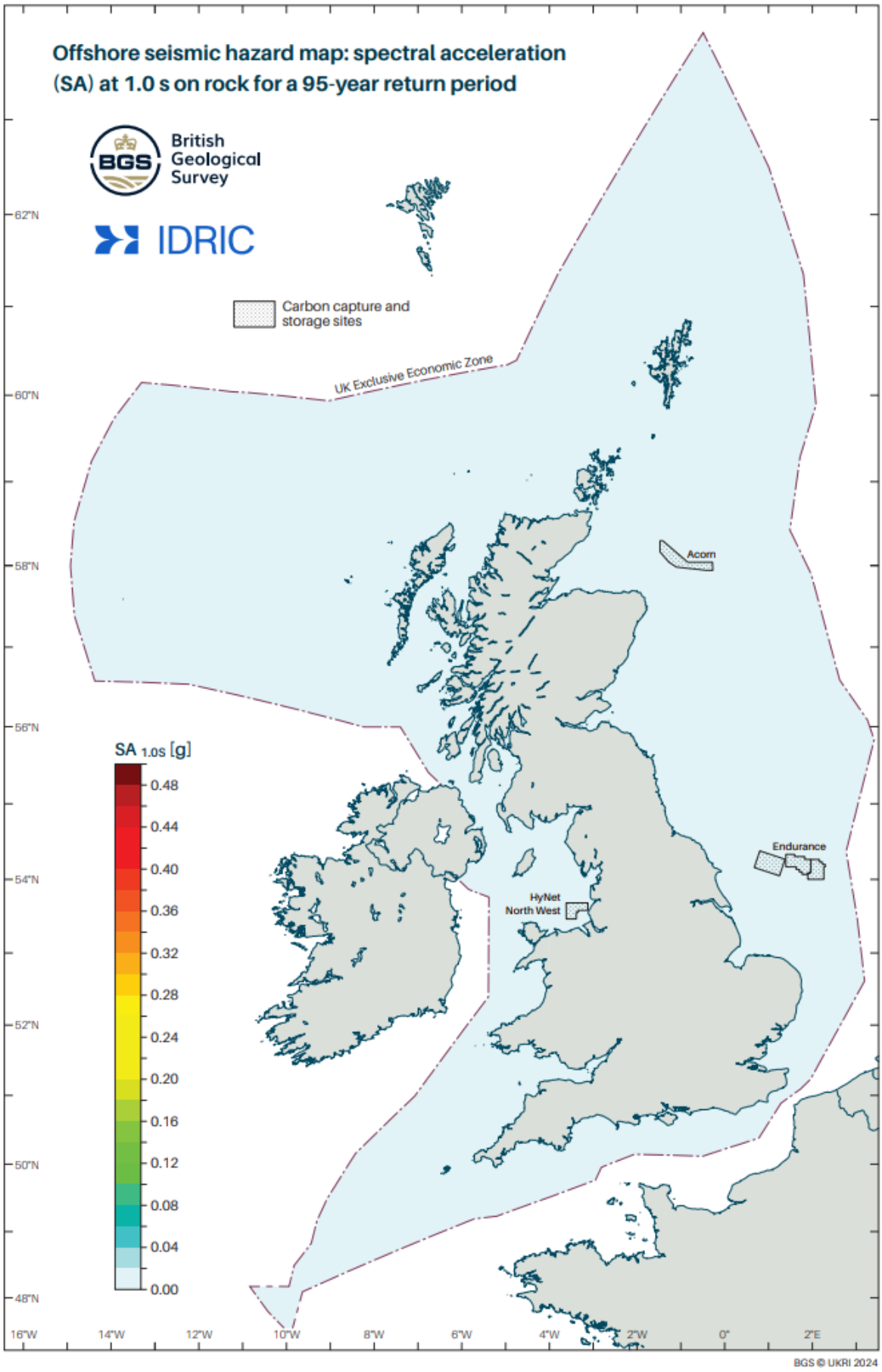

Figure 72: Hazard map for $SA_{1.0\ s}$ for a 95-year return period. The black polygon describes the UK offshore EEZ. Contains OS data © Crown copyright and database right 2024.

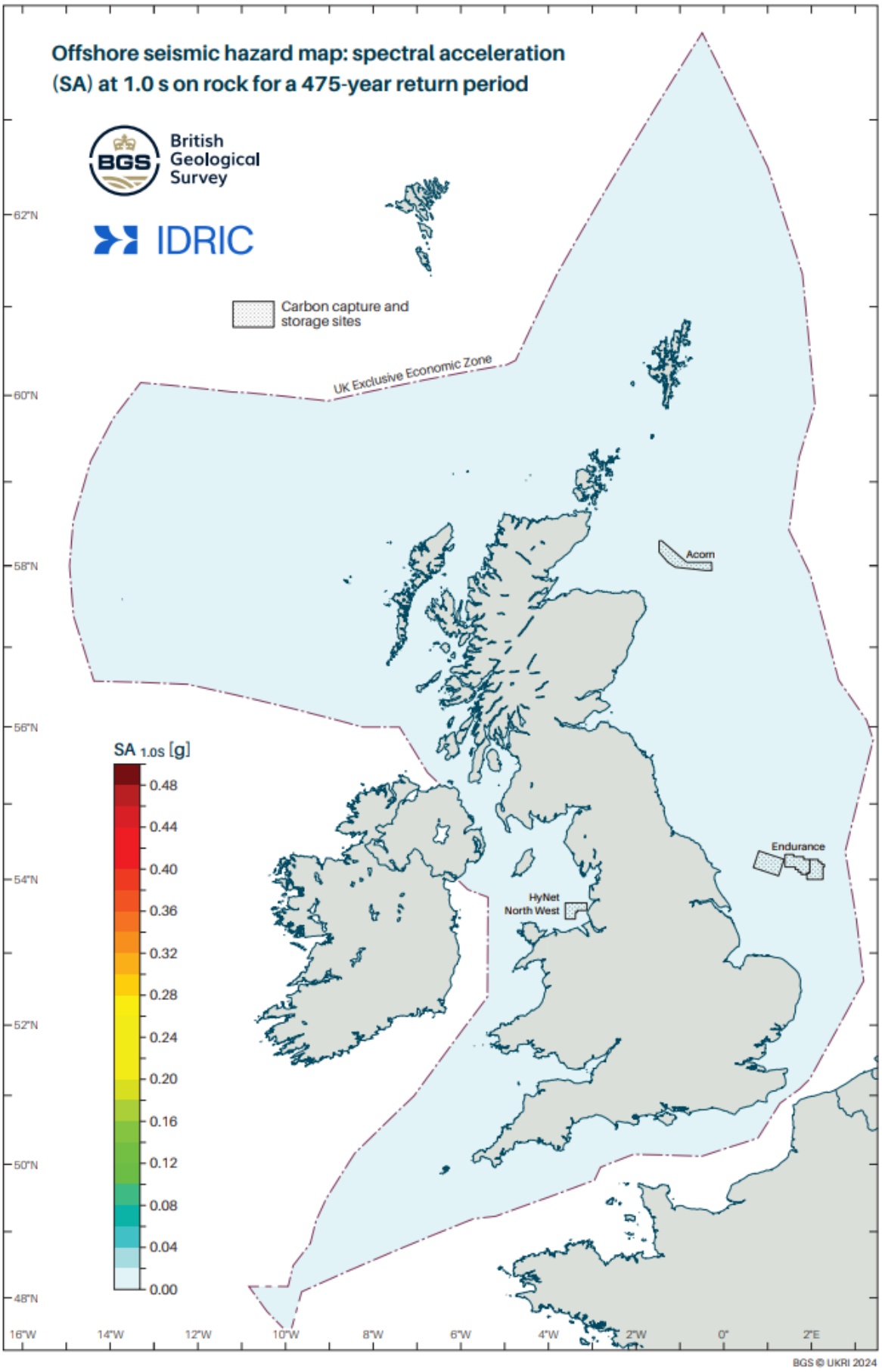

Figure 73: Hazard map for $SA_{1.0\,s}$ for a 475-year return period. The black polygon describes the UK offshore EEZ. Contains OS data © Crown copyright and database right 2024.

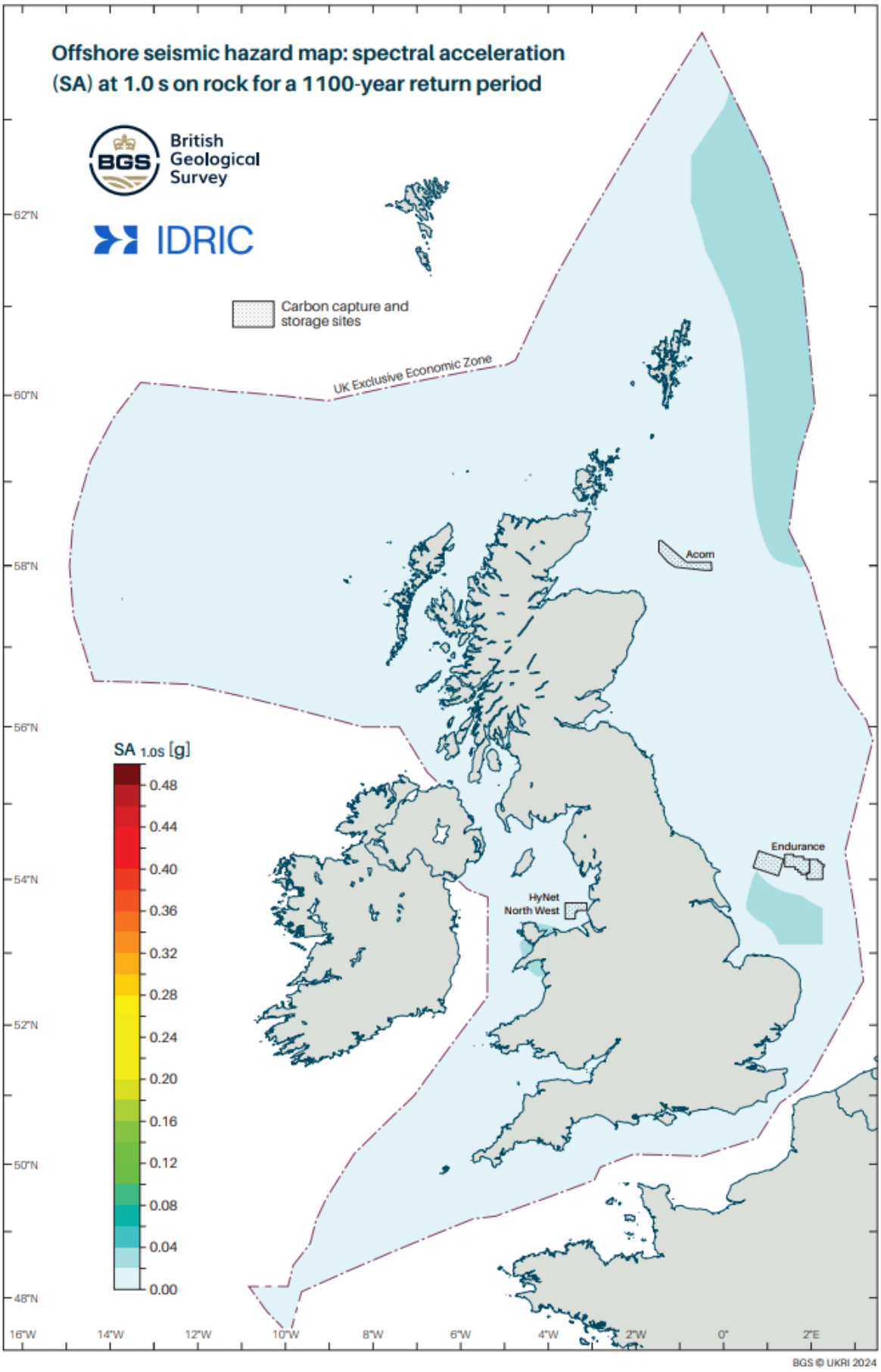

Figure 74: Hazard map for $SA_{1.0\ s}$ for a 1100-year return period. The black polygon describes the UK offshore EEZ. Contains OS data © Crown copyright and database right 2024.

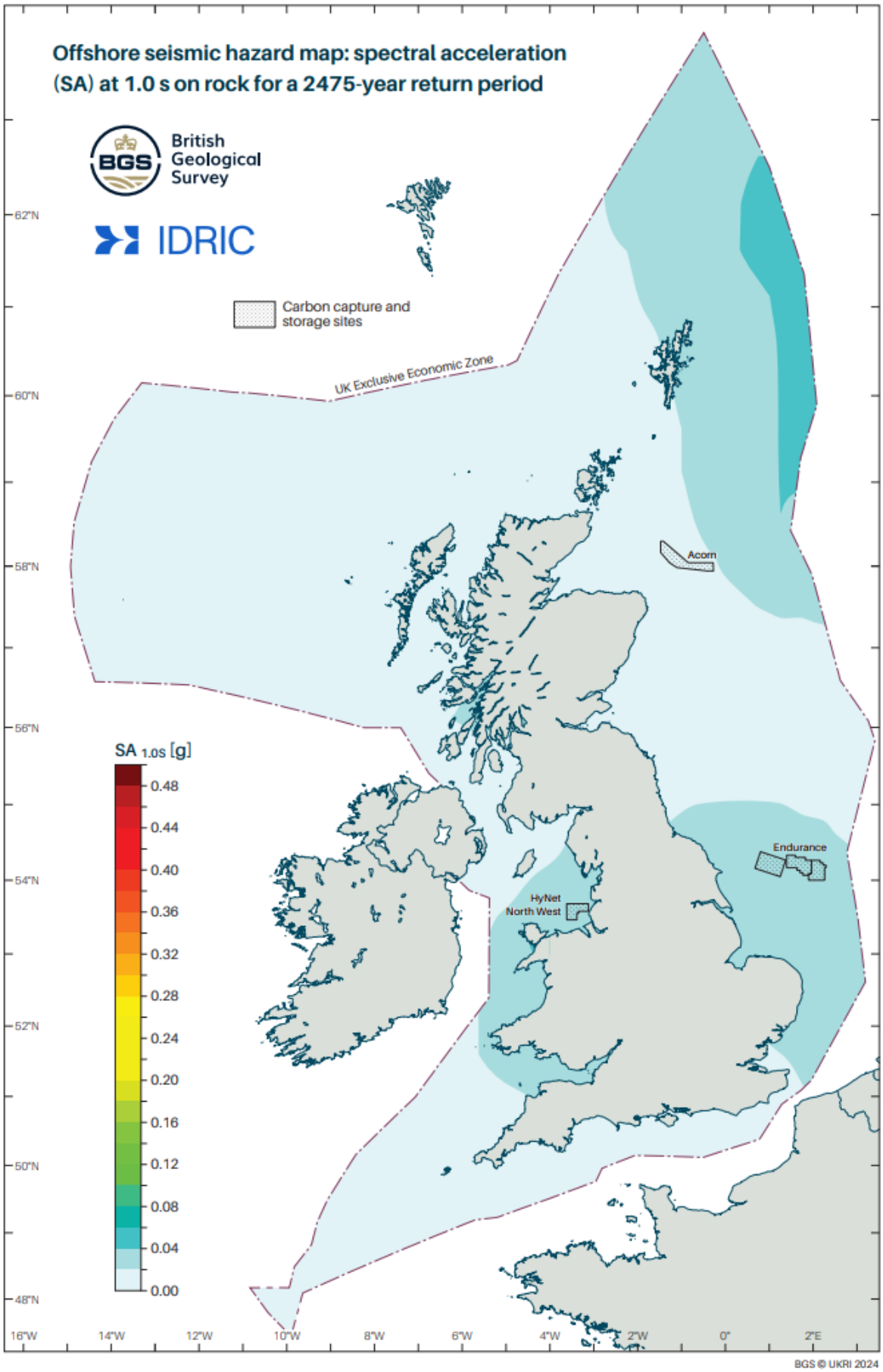

Figure 75: Hazard map for $SA_{1.0\ s}$ for a 2475-year return period. The black polygon describes the UK offshore EEZ. Contains OS data © Crown copyright and database right 2024.

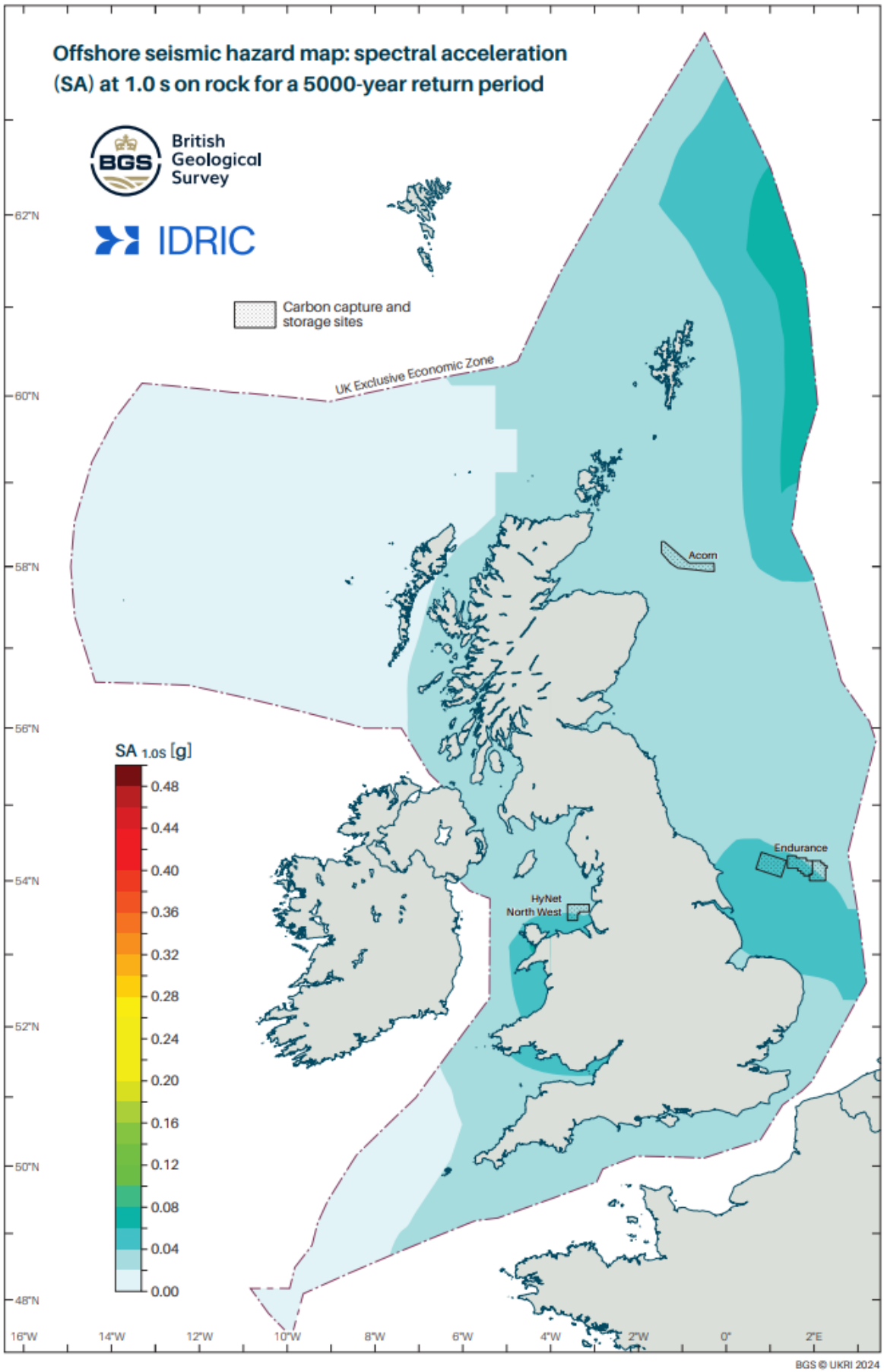

Figure 76: Hazard map for $SA_{1.0\ s}$ for a 5,000-year return period. The black polygon describes the UK offshore EEZ. Contains OS data © Crown copyright and database right 2024.

Appendix 4

This appendix describes the soil conditions of the boreholes at the Acorn, Endurance, and HyNet North West CCS areas.

Acorn

The Acorn site is primarily underlain by a modelled Quaternary sediment thickness of >50 m depth. The sediment thins towards the western end of the site to depths of 5-20 m (Figure 52).

A borehole (+57-002/345/BH/1), located at the western end of the site proved c.25 m of Quaternary sediments overlying c.17 m of bedrock. The Quaternary sediments consisted of fine-grained sand at the surface, underlain by interbeds of silty clay, sandy clay, sand and clay. The bedrock succession consisted of c. 4.5 m of volcanic tuff and interbedded tuff and clay (Eocene). This is underlain by c.12.5 m of interbedded clay, sandstone and coal with a thin conglomerate (Palaeocene) at the base of the borehole.

It should be noted that the borehole had intermittent recovery of material and this summary is based on an interpretation and is therefore not comprehensive.

Endurance 1

The Quaternary sediment thickness model shows a thickness of 5-20 m across most of the site with a patch of shallower (< 5 m) sediment at the western end. An area of deeper sediments (20-< 50 m) runs NW-SE through the western centre of the area with sediments thickening to > 50 m towards the NE (Figure 52).

A borehole (+54+000/598/BH/1) located 22 km west of the site proved c.4.5 m of Quaternary sediments overlying c. 27.5 m of bedrock. There was no recovery of Quaternary sediments, but they are assumed to consist of sand and gravel. The bedrock succession consisted of Kimmeridge Clay Formation (Jurassic mudstone and limestone).

Endurance 2

The majority of the Endurance B site has a modelled Quaternary sediment thickness of > 50 m, which shallows to the west in a NW-SE trending area of 30-50 m thick sediments, shallowing to 20 - 30 m at the NW end of the site (Figure 52).

A borehole (+54+001/190/BH/1) located 8 km south of the site proved c. 24 m of Quaternary sediments overlying c.26 m of bedrock. The Quaternary sediments consisted of c.4 m of sand and gravel at the surface underlain by c.16 m of dark greenish-grey, stiff clay with lenses and beds of calcareous silt. The base of the Quaternary sediments consisted of c.4 m of fine sand. The bedrock succession is composed of c.26 m of the Chalk Group (Cretaceous).

It should be noted that the borehole had intermittent recovery of material and this summary is based on an interpretation and is therefore not comprehensive.

Endurance 3

All of the Endurance C site has a modelled Quaternary sediment thickness of >50 m (Figure 52).

A borehole (+54+001/191/BH/1) located in the southwestern corner of the site proved >90 m of Quaternary sediments with no bedrock recovery. The Quaternary sediments consisted of c.6 m of shelly, gravelly sand at the surface, underlain by c.16 m of interbedded, shelly, fine sand and silty clay. This is underlain by c.16.5 m of stiff grey clay with interlaminated silt and sand followed by a thin bed (c.1 m) of muddy sand underlain by c. 11.5 m of stiff dark grey clay with silt laminations. This is underlain by c.22 m of muddy fine sand, underlain by c.11 m of stiff clay with lamination of silt and sand with a firm brown silt with rare shells at the base of the borehole.

It should be noted that the borehole had intermittent recovery of material and this summary is based on an interpretation and is therefore not comprehensive.

HyNet North West

The NW Offshore site has a much thinner sediment cover than the other sites in this study. The majority of the area is modelled to have a Quaternary sediment thickness of 5 - 20 m, with two isolated areas of deeper sediments, 30 - 50 m and > 50 m in the western portion of the site. The thickest sediments in the site are modelled in the eastern half of the site, with sediment depths of 30 - 50 m and > 50 m respectively (Figure 52).

A borehole (+53N-004W/85/BH/1), located at the western end of the site proved c.12.5 m of Quaternary sediments overlying c.8.5 m of bedrock. The Quaternary sediments consisted of coarse, shelly sand at the surface, underlain by gravel, boulders, pebbly sands and clayey silt. The bedrock succession consisted of c.8.5 m mudstone with localised pockets of gypsum (Permo-Triassic).

Glossary

The definitions included in this section are taken directly from various sources: Reiter (1990), Budnitz et al. (1997), Stein and Wysession (2003), McGuire (2004), Neuendorf et al. (2005), PNNL (2014), and https://earthquake.usgs.gov/learn/glossary/.

Activity rate: The logarithm of the number of earthquakes of magnitude zero or greater expected to occur in a specific period of time, such as a year.

Between-event variability: The portion of the total aleatory variability in ground motions that represents the variability in average level of ground motions from earthquake to earthquake. This is also referred to as inter-event variability.

b-value: The slope of a straight line describing the Gutenberg-Richter recurrence frequency-magnitude law. It expresses the proportion of large earthquakes to small earthquakes.

Declustering: A statistical approach that removes foreshocks and aftershocks to produce a catalogue of independent mainshocks consistent with the requirements of a PSHA model.

Deformation: The net effect of strain on rock mass or the components thereof.

Disaggregation: Statistical decomposition of the hazard to show the relative contribution by magnitude, distance, and ground motion deviation.

Displacement: Difference between the initial position of a reference point and any later position. The amount any point affected by an earthquake has moved from where it was before the earthquake.

Earthquake: Phenomenon of fault rupture releasing stored strain in the Earth's crust and propagating from the source through vibratory waves in all directions.

Epicentre: The point of the earthquake on the Earth's surface.

Fault: A fracture surface or zone in the earth across which there has been relative displacement.

Fault Zone: A system of related fracture segments that interact and link, and are restricted to a relatively narrow band, or volume.

Fracture: A deformation-break characterised by a discontinuous change in strength and/or stiffness, such that there is a stepwise change in the displacement distribution across it; the volume of deformed material associated with fractures typically has a negligible thickness at the scale of observation (hence their surfaces are perceived to be sharply defined); such features typically consist of two opposing surfaces in contact or close proximity.

Focal Mechanism: A geometrical representation of earthquake faulting expressed in terms of the strike and dip of the fault plane and the rake angle of the slip vector with respect to the fault plane.

Glacio-isostatic adjustment: Ongoing movement of land once burdened by ice-age glaciers.

Ground motion model: See *Ground motion prediction equation*.

Ground motion prediction equation (GMPE): An empirical model that relates a ground motion measure (e.g., peak ground acceleration and spectral acceleration) to a set of independent variables, such as distance, magnitude, source and path parameters. The GMPE predicts a lognormal distribution of values for the ground motion measure described by a median prediction and the standard deviation (sigma).

Gutenberg-Richter (recurrence) frequency-magnitude law: The relationship between magnitude and number of earthquakes in a given region and time period.

Hypocentre: The point in the earth at which an earthquake is initiated.

Inverse Random Vibration Theory: A technique to calculate the Fourier or power spectrum of the ground motion given the response spectrum and the duration of the motion.

Joyner-Boore distance (Rjb): The shortest distance from a site to the surface projection of the rupture surface of the earthquake.

Kappa (κ_0): A parameter that characterizes anelastic attenuation or damping through the uppermost part of the Earth's crust that acts as a filter on the high-frequency content of the seismic waves.

Local (or Richter) magnitude (ML): Common logarithm of the trace amplitude of a standard Wood-Anderson seismograph located on the firm ground 100 km from the epicentre.

Logic Tree: A series of branches to describe alternative models and parameter values. The weights, which must sum to unity at each node, are assigned to each branch using expert judgement that reflects the relative confidence in the models and parameters.

Magnitude: The size of the earthquake measured from the amplitude of the motion recorded on seismograms and expressed as logarithm with base 10.

Maximum magnitude (Mmax): The largest earthquake magnitude that a seismic source is capable of generating.

*Metasedimentary rock: T*ype of metamorphic rock that was first formed as a result of the deposition and solidification of sediment to form a sedimentary rock. Subsequently, that rock was deeply buried and was subjected to high pressures and temperatures (and likely deformed), causing the mineral in the original sedimentary rock to recrystallize under solid-state processes.

Moho: Boundary between the crust and the mantle in the earth.

Moment magnitude (Mw): Magnitude derived from the scalar seismic moment.

Normal fault: A dip-slip fault in which the block above the fault has moved downward relative to the block below. This type of fault represents crustal extension.

Orogeny: Continental deformation resulting from plate boundary-scale deformation leading to shortening and thickening, and associated metamorphism, which usually generates mountain belts (Dewey 2005: Orogeny can be very short. Proceedings of the National Academy of Sciences, 102(43), pp.15286-15293).

Poisson seismic model: The assumption that earthquakes have no memory, i.e. each earthquake occurs independently of any other earthquake.

Probabilistic seismic hazard analysis (PSHA): A methodology to quantify the frequency of exceeding various ground motion levels at a site given all possible earthquakes in a probabilistic framework.

Peak ground acceleration (PGA): Maximum value of acceleration displayed on an accelerogram.

Return period: The mean (average) time between occurrences of a seismic hazard. It is the reciprocal of the annual frequency of exceeding a particular ground motion level.

Reverse fault: A dip-slip fault in which the block above the fault has moved upward relative to the block below, and the fault dip >45°.

Seismic hazard: Potential for dangerous, earthquake-related natural phenomena such as ground shaking, fault rupture, or soil liquefaction.

Seismic source: Region or volume (zone or fault) where the seismic activity is considered to be of homogeneous earthquake potential.

Seismic hazard curve: A graphical curve depicting the frequency (the number of events per unit time, usually a year) with which selected values of a ground motion measure are expected to be exceeded.

Seismic source model: Mathematical representation of the spatial and temporal distribution of expected earthquakes within a magnitude range in a specific region.

Seismic Source zone: Area where the seismic activity is considered to be of homogeneous earthquake potential, and earthquakes have an equal chance of occurring at any point in the zone.

Seismogenic zone: Region of the crust capable of generating earthquakes. The base of the seismogenic zone is the top of the more ductile asthenosphere.

Shortening: See *Orogeny.*

Sigma model: Aleatory standard deviation in the ground motion model expressed in logarithm. It consists of the between-event standard deviation and the within-event standard deviation.

Spectral acceleration (SA): Pseudo-absolute response spectral acceleration, given as a function of period or frequency and damping ratio (typically 5%). It is equal to the peak relative displacement of a linear oscillator of frequency f attached to the ground, times the quantity $(2\pi f)^2$. It is expressed in g or cm/s^2.

Strain: Small changes in length and volume associated with deformation of the earth by tectonic stresses or by the passage of seismic waves.

Strain rate: How fast the lithosphere is being deformed from plate tectonic movement.

Stress: Force per unit area acting on a plane within a body. Six values are required to characterize completely the stress at a point: three normal components and three shear components.

Strike-slip fault: A fault in which the relative displacement is along the strike of the fault plane, either right- or left-lateral.

Terrane: A fault-bounded block containing rocks that have a distinct geological history when compared with the rocks making up contiguous blocks.

Thrust fault: A dip-slip fault in which the block above the fault has moved upward relative to the block below, and the fault dip < 45°. This type of fault represents crustal compression.

Uncertainty: In seismic hazard analysis there are two types of uncertainties: aleatory and epistemic uncertainty*. The aleatory uncertainty* is inherent in a random phenomenon and cannot be reduced by acquiring additional data or information. The future earthquake locations and magnitudes have aleatory uncertainty. The *epistemic uncertainty* is due to our lack of knowledge regarding the earthquake process and it can be reduced by the accumulation of additional information. The geometry of the seismic source model and the maximum magnitude have epistemic uncertainty.

Vs30: Time-averaged shear wave velocity for the top 30 m.

Within-event variability: The portion of the total aleatory variability in ground motions that is common to all recordings from an individual earthquake. This is also referred to as intra-event variability

References

ABRAHAMSON, NA, and YOUNGS, R. 1992. A stable algorithm for regression analyses using the random effects model, *Bulletin of the Seismological Society of America*, Vol. 82(1), 505–510.

ABRAHAMSON, NA, SILVA, WJ, and KAMAI, R. 2014. Summary of the ASK14 ground-motion relation for active crustal regions, *Earthquake Spectra*, Vol. 30(3), 1025–1055.

ABRAMOVITZ, T, and THYBO, H. 1999. Pre-Zechstein structures around the MONA LISA deep seismic lines in the southern Horn Graben area, *Bulletin of the Geological Society of Denmark*, Vol. 45, 99–116.

AKKAR, S, and CAĞNAN, Z. 2010. A local ground-motion predictive model for Turkey, and its comparison with other regional and global ground-motion, Bull Seismol Soc Am Vol. 100, 2978–2995.

AKKAR, S, SANDIKKAYA, MA, and BOMMER, JJ. 2014a. Empirical ground motion models for point- and extended-source crustal earthquake scenarios in Europe and the Middle East, *Bulletin of Earthquake Engineering,* Vol. 12**,** 359-387.

AKKAR, S, SANDIKKAYA, MA, S, ENYURT, M, SISI, AA, AY, BÖ, TRAVERSA, P, DOUGLAS, J, COTTON, F, LUZI, L, HERNANDEZ, B, and GODEY, S. 2014b. Reference database for seismic ground-motion in Europe (RESORCE), *Bulletin of Earthquake Engineering*, Vol. 12(1), 311–339.

AKKAR, S, KALE O, SANDIKKAYA, A, and YENIER, E. 2021. A procedure to develop backbone ground motion model: Its implementation to stable continental regions, *Earthquake Spectra*, Vol. 37(4), 2523–2544.

AL ATIK, L. 2015. NGA-East: Ground-Motion Standard Deviation Models for Central and Eastern North America, *Pacific Earthquake Engineering Research Center, PEER Report No. 2015/07*, Berkeley.

AL ATIK, L, ABRAHAMSON, NA, BOMMER, JJ, SCHERBAUM, F, COTTON, F, and KUEHN, N. 2010. The variability of ground-motion prediction models and its components, *Seismological Research Letters,* Vol. 81(5), 794–801.

AL ATIK, L, KOTTKE, A, ABRAHAMSON, NA, and HOLLENBACK, J. 2014. Kappa (κ) scaling of ground-motion prediction equations using an inverse random vibration theory approach, *Bulletin of the Seismological Society of America*, Vol. 104(1), 336–346.

AL ATIK, L, and ABRAHAMSON, NA. 2021. A methodology for the development of 1D reference Vs profiles compatible with ground-motion prediction equations: Application to NGA-West2 GMPEs, *Bulletin of the Seismological Society of America*, Vol. 111(4), 1765–1783.

ALDAMA-BUSTOS, G, DOUGLAS, J, STRASSER, FO, DAVÍ, M, and MACGREGOR, A. 2022. Methods for assessing the epistemic uncertainty captured in ground-motion models, *Bulletin of Earthquake Engineering,* Vol. 21, 1–26.

ALLEN, TI, Wald, DJ, and WORDEN, C. 2012. Intensity attenuation for active crustal regions, *Journal of Seismology*, Vol. 16, 409–433.

AMANTE, C, AND EAKINS, B. 2009. ETOPO1 1Arc-Minute Global Relief Model: Procedures, data resources and analysis, *NOAA (NOAA Technical Memorandum NESDIS NGDC-24.*

AMBRASEYS, NN, and MELVILLE, CP. 1982. A history of Persian earthquakes (Cambridge: Cambridge University Press).

AMBRASEYS, NN, SIMPSON, KA, and BOMMER, JJ. 1996. Prediction of horizontal response spectra in Europe, *Earthquake Engineering and Structural Dynamics*, Vol. 25, 371-400.

ANDERSON, JG, and HOUGH, SE. 1984. A model for the shape of the Fourier amplitude spectrum of acceleration at high frequencies, *Bulletin of the Seismological Society of America*, Vol. 74(5), 1969–1993.

ANDERSON, JG, and BRUNE, JN. 1999. Probabilistic seismic hazard assessment without the ergodic assumption, *Seismological Research Letters*, Vol. 70, 19–28.

ANDRESEN, KJ. 2020. The Norwegian–Danish Basin: a dynamic setting for subsurface sand remobilization – established concepts on distribution and controlling factors*, Geological Society, London, Special Publications*, Vol. 493, 47 – 68.

ANDREWS, I, LONG, D, RICHARDS, P, THOMSON, A, BROWN, S, CHESHER, J, and MCCORMAC, M. 1990. United Kingdom Offshore Regional Report: The geology of the Moray Firth. *British Geological Survey Regional Geology Series,* United Kingdom.

ARGENT, J, STEWART, S, GREEN, P, and UNDERHILL, J. 2002. Heterogeneous exhumation in the Inner Moray Firth, UK North Sea: constraints from the new AFTA® and seismic data, *Journal of Geological Society*, Vol. 159, 751-729.

ASSATOURIANS, K, and ATKINSON, GM. 2013. EqHaz - An open-source probabilistic seismic hazard code based on the Monte Carlo simulation approach, *Seismological Research Letters*, Vol. 84, DOI: 101785/0220120102

ASCH, K. 2003. *The 1 : 5 Million International Geological Map of Europe and Adjacent Areas: Development and Implementation of a GIS-enabled Concept*, (Geologisches Jahrbuch, SA 3, BGR, Stuttgart).

ATKINSON, GM. 2006. Single-station sigma, *Bulletin of the Seismological Society of America*, Vol. 96, 446–455.

ATKINSON, GM, and BOORE, DM. 2006. Earthquake ground motion prediction equations for eastern North America, *Bulletin of the Seismological Society of America,* Vol. 96(6), 2181–2205.

ATKINSON, GM, and BOORE, DM. 2011. Modifications to existing ground-motion prediction equations in light of new data, *Bulletin of the Seismological Society of America,* Vol. 10(3), 1121–1135.

ATKINSON, GM, BOMMER, JJ, and ABRAHAMSON, NA. 2014. Alternative approaches to modelling epistemic uncertainty in ground motions in probabilistic seismic-hazard analysis, *Seismological Research Letters,* Vol. 85(6), 1141–1144.

BAIZE, S, CUSHING, EM, LEMEILLE, F, and JOMARD, H. 2012. Updated seismotectonic zoning scheme of Metropolitan France, with reference to geologic and seismotectonic data, *Bulletin de la Société Géologique de France*, Vol. 184(3), 225–259.

BAKER, JW, BRADLEY, BA, AND STAFFORD, PJ. 2021. *Seismic Hazard and Risk Analysis*. (Cambridge University Press).

BAPTIE, B. 2010. State of stress in the UK from observations of local seismicity, *Tectonophysics*, Vol. 482, 150-159.

BAPTIE, B. 2012. UK earthquake monitoring 2011/2012: Twenty-third Annual Report, *British Geological Survey Commissioned Report,* OR/12/092, United Kingdom.

BAPTIE, B. 2020. Earthquake Seismology 2019/2020, BGS National Earthquake Information Service: Thirty-first Annual Report, *British Geological Survey Commissioned Report, OR/20/039*, United Kingdom.

BAPTIE, B. 2022. Earthquake Seismology 2021/2022, *British Geological Survey Open Report, OR/22/077,* United Kingdom.

BAPTIE, B, SEGOU, M, ELLEN, R, and MONAGHAN, A. 2016. Unconventional oil and gas development: Understanding and monitoring induced seismic activity, *British Geological Survey Open Report, OR/16/042*, United Kingdom.

BARBARAND, J, BOUR, I, PAGEL, M, QUESNEL, F, DELCAMBRE, B, DUPUIS, C, and YANS, J. 2018. Post-Paleozoic evolution of the northern Ardenne Massif constrained by apatite fission-track thermochronology and geological data, *BSGF - Earth Sciences Bulletin*, Vol. 189, 1-16.

BEAMISH, D, and SMYTHE, D. K. 1986. Geophysical images of the deep crust: The Iapetus suture, *Journal of the Geological Society*, Vol. 143, 489-497.

BEAUVAL, C, BARD, PY, and DANCIU, L. 2020. The influence of source- and ground-motion model choices on probabilistic seismic hazard levels at 6 sites in France, *Bulletin of Earthquake Engineering,* Vol. 18, 4551–4580.

BEST, G, KOCKEL, F, and SCHÖNEICH, H. 1983. Geological history of the Southern Horn Graben, *Geologie en Mijnbouw*, Vol. 62, 25–33.

BGS and ARUP. 1997. UK Continental Shelf Seismic Hazard, *OTH Report 93 416 for the Health & Safety Executive*.

BINDI, D, MASSA, M, LUZI, L, AMERI, G, PACOR, F, PUGLIA, R, and AUGIERA, P. 2014. Pan-European ground-motion prediction equations for the average horizontal component of PGA, PGV, and 5%-damped PSA at spectral periods up to 3.0 s using the RESORCE dataset, *Bulletin of Earthquake Engineering,* DOI:10.1007/s10518-013-9525-5.

BIRD, P. 2003. An updated digital model of plate boundaries, *Geochemistry Geophysics Geosystems*, Vol. 4, 1-52.

BLUCK, BJ, GIBBONS, W, and INGHAM, JK. 1992. Terranes. In *Atlas of Palaeogeography and Lithofacies,* COPE, JC, INGHAM, JK, RAWSON, PF (Editors), *Geological Society London*, Memoirs, Vol. 13, 1–4.

BLUNDELL, DJ, HOBBS, RW, KLEMPERER, SL, SCOTT-ROBINSON, R, LONG, RE, WEST, TE, and DUIN, E. 1991. Crustal Structure of the central and southern North Sea from BIRPS deep seismic reflection profiling, *Journal of the Geological Society*, Vol. 148, 445-458.

BOMMER, JJ, and ABRAHAMSON, NA. 2006. Why do modern probabilistic seismic hazard analyses lead to increased hazard estimates?, *Bulletin of the Seismological Society of America*, Vol. 96(6), 1967–1977.

BOMMER, JJ, and SCHERBAUM, F. 2008. The use and misuse of logic trees in probabilistic seismic hazard analysis, *Earthquake Spectra,* Vol. 24(4), 997-1009.

BOMMER, JJ, DOUGLAS, J, SCHERBAUM, F, COTTON F, BUNGUM, H, and FÄH, D. 2010. On the selection of ground-motion prediction equations for seismic hazard analysis, *Seismological Research Letters,* Vol. 81, 783-793.

BOMMER, JJ, PAPASPILIOU, M, and PRICE, W. 2011. Earthquake response spectra for seismic design of nuclear power plants in the UK, Elsevier Science SA, 968-977.

BOMMER JJ, COPPERSMITH KJ, COPPERSMITH RT, HANSON KL, MANGONGOLO A, NEVELING J, RATHJE EM, RODRIGUEZ-MAREK A, SCHERBAUM F, SHELEMBE R, STAFFORD PJ, and STRASSER FO. 2015. A SSHAC Level 3 probabilistic seismic hazard analysis for a new-build nuclear site in South Africa, *Earthquake Spectra*, Vol. 31(2), 661–698.

BOMMER, JJ, and CROWLEY, H. 2017. The purpose and definition of the minimum magnitude limit in PSHA calculations, *Seismological Research Letters,* Vol. 88, 1097-1106.

BOMMER JJ and STAFFORD PJ. 2020. Selecting ground-motion models for site-specific PSHA: Adaptability versus applicability, *Bulletin of the Seismological Society of America*, Vol. 110(6), 2801–2815.

BOORE, DM. 2003. Simulation of ground motion using the stochastic method, *Pure and Applied Geophysics*, Vol. 160, 635–676.

BOORE, DM, and JOYNER, WB. 1997. Site amplifications for Generic Rock Sites, *Bulletin of the Seismological Society of America*, Vol. 87, 327–341.

BOORE, D, STEWART, J, SEYHAN, E, and ATKINSON, G. 2014. NGA-West2 equations for predicting PGA, PGV, and 5% damped PSA for shallow crustal earthquakes, *Earthquake Spectra,* Vol. 30, 1057-1085.

BOORE, DM, YOUNGS, RR, KOTTKE, AR, BOMMER, JJ, DARRAGH, R, SILVA, WJ, STAFFORD, PJ, AL ATIK, L, RODRIGUEZ-MAREK, A, and KAKLAMANOS, J. 2022. Construction of a Ground-Motion Logic Tree through Host-to-Target Region Adjustments Applied to an Adaptable Ground-Motion Prediction Model, *Bulletin of the Seismological Society of America*, Vol. 112 (6):3063–3080.

BOOTH, DC, BOTT, JDJ, and O'MONGAIN, AM. 2001. The UK Seismic velocity model for earthquake location – a baseline review, *British Geological Survey Internal Report*, IR/01/188, United Kingdom.

BOZORGNIA, Y, ABRAHAMSON, NA, AL ATIK, L, ANCHETA, T, ATKINSON, G, BAKER, J, BALTAY, A, BOORE, D, CAMPBELL, K, CHIOU, B, DARRAGH, R, DAY, S, DONAHUE, J, GRAVES, R, GREGOR, N, HANKS, T, IDRISS, I, KAMAI, R, KISHIDA, T, KOTTKE, A, MAHIN, S, REZAEIAN, S, ROWSHANDEL, B, SEYHAN, E, SHAHI, S, SHANTZ, T, SILVA, W, SPUDICH, P, STEWART, J, WATSON-LAMPREY, J, WOODDELL, K, and YOUNGS, RR. 2014. NGA-West2 Research Project, *Earthquake Spectra*, Vol. 30, 973-987.

BRACKENRIDGE, RE, UNDERHILL, JR, JAMIESON, R, and BELL, A. 2020. Structural and stratigraphic evolution of the Mid North Sea High region of the UK Continental Shelf, *Petroleum Geoscience*, Vol. 26, 154 – 173.

BRAUNMILLER, J, DAHM, T, and BONJER, K-P. 1994. Source mechanism of the 1992 Roermond earthquake from surface-wave inversion of regional data, *Geophysical Journal International*, Vol. 116(3), 663–672.

BROOKS, C, DOUGLAS, J, and SHIPTON, Z. 2020. Improving earthquake ground-motion predictions for the North Sea, *Journal of Seismology*, Vol. 24, 343–362.

BROOKS, C. 2021. Improving the assessment of seismic hazard in the North Sea, PhD Thesis, University of Strathclyde.

BRUNE, JN. 1970. Tectonic stress and the spectra of seismic shear waves from earthquakes, *Journal of Geophysical Research*, Vol. 75, 4997–5009.

BS NA EN 1998-1. 2008. UK National Annex to Eurocode 8: Design of structures for earthquake resistance. BSI British Standards, London, United Kingdom.

BUDNITZ, RJ, APOSTOLAKIS, G, BOORE, DM, CLU, LS, COPPERSMITH, KJ, CORNELL, CA, and MORRIS, PA. 1997. Recommendations for probabilistic seismic hazard analysis: Guidance on uncertainty and use of experts, *NUREG/CR-6372, Volume 1,* US Nuclear Regulatory Commission, Washington, DC.

BUILDING SEISMIC SAFETY COUNCIL. 2009. NEHRP recommended seismic provisions for new buildings and other structures, FEMA P-750, 388.

BUNGUM, H, SWEARINGEN, PH, and WOO, G. 1986. Earthquake hazard assessment in the North Sea, *Physics of the Earth and Planetary Interiors*, Vol. 44(3), 201-210.

BUNGUM, H, ALSAKER, A, KVAMME, LB, and HANSEN, RA. 1991. Seismicity and seismotectonics of Norway and surrounding continental shelf areas, *Journal of Geophysical Research*, Vol. 96(2), 249-2,265.

BUNGUM, H, LINDHOLM, C, DAHLE, A, WOO, G, NADIM, F, HOLME, J, GUDMESTAD, O, HAGBERG, T, and KARTHIGEYAN, K. 2000. New Seismic Zoning Maps for Norway, the North Sea, and the United Kingdom, *Seismological Research Letters*, Vol. 71(6), 687-697.

BUNGUM, H, LINDHOLM, C, and FALEIDE, JI. 2005. Postglacial seismicity offshore mid-Norway with emphasis on spatio-temporal magnitude variations, *Marine Petroleum Geology*, Vol. 22, 137–148.

BURKHARD, M, and GRÜNTHAL, G. 2009. Seismic source zone characterization for the seismic hazard assessment project PEGASOS by the Expert Group 2 (EG1b*), Swiss Journal of Geosciences*, Vol. 102, 149–188.

BURTON, PW, and NEILSON, G. 1980. Annual catalogues of British earthquakes recorded on LOWNET (1967-1978), *Seismological Bulletin No. 7, Institute of Geological Sciences*, HMSO.

CAMPBELL, KW. 2003. Prediction of strong ground motion using the hybrid empirical method and its use in the development of ground motion (attenuation) relations in eastern North America, *Bulletin of the Seismological Society of America*, Vol. 93, 1012–1033.

CAMPBELL, KW, and BOZORGNIA, Y. 2014. NGA-West 2 ground motion model for the average horizontal components of PGA, PGV, and 5%-damped linear acceleration response spectra, *Earthquake Spectra*, Vol. 30(3), 1087–1115.

CAMELBEECK, T, VAN ECK, T, PELZING, R, AHORNER, L, LOOHUISZ, J, HAAK, HW, HOANG-TRONG, P, and HOLLNACK, D. 1994. The 1992 Roermond earthquake, the Netherlands, and its aftershocks, *Geologie en Mijnbouw*, Vol. 73, 181–197.

CAMELBEECK, T, ALEXANDRE, P, VANNESTE, K, and MEGHRAOUI, M. 2000. Long-term seismicity in regions of present day low seismic activity: the example of Western Europe, *Soil Dynamics and Earthquake Engineering*, Vol. 20, 405–414.

CAMELBEECK, T, VANNESTE, K, ALEXANDRE, P, VERBEECK, K, PETERMANS, T, ROSSET, P, EVERAERTS, M, WARNANT, R, and VAN CAMP, M. 2007. Relevance of active faulting and seismicity studies to assessments of long-term earthquake activity and maximum magnitude in intraplate northwest Europe, between the Lower Rhine Embayment and the North Sea, *Geological Society of America,* 425**,** 193–224.

CAMELBEECK, T, VAN NOTEN, K, LECOCQ, T, and HENDRICKX, M. 2022. The damaging character of shallow 20th century earthquakes in the Hainaut coal area (Belgium), *Solid Earth*, Vol. 13, 469–495.

CAMERON, IB, and STEPHENSON, D. 1985. *British regional geology: The Midland Valley of Scotland*. Third edition. Reprint 2014. Keyworth, Nottingham: British Geological Survey.

CAMERON, TDJ, CROSBY, A, BALSON, PS, JEFFERY, DH, LOTT, GK, BULAT, J, and HARRISON, DJ. 1992. *United Kingdom offshore regional report: the geology of the southern North Sea*. (London: HMSO for the British Geological Survey).

CAO, AM, and GAO, SS. 2002. Temporal variation of seismic *b*-values beneath northeastern Japan island arc, *Geophysical Research Letters,* Vol. 29**(**9), DOI:10.1029/2001GL013775.

CARA, M, CANSI, Y, SCHLUPP, A, ARROUCAU P, BÉTHOUX, N, BEUCLER, E, BRUNO, S, CALVET, M, CHEVROT, S, DEBOISSY, A, DELOUIS, B, DENIEUL, M, DESCHAMPS, A, DOUBRE, C, FRÉCHET, J, GODEY, S, GOLLE, O, GRUNBERG, M, GUILBERT, J, HAUGMARD, M, JENATTON, L, LAMBOTTE, S, LEOBAL, D, MARON, C, MENDEL, V, MERRER, S, MACQUET, M, MIGNAN, A, MOCQUET, A, NICOLAS, M, PERROT, J, POTIN, B, SANCHEZ, O, SANTOIRE, J-P, SÈBE, O, SYLVANDER, M, THOUVENOT, F, VAN DER WOERD, J, and VAN DER WOERD, K. 2015. SI-Hex: a new catalogue of instrumental seismicity for metropolitan France, *Bulletin de la Société Géologique de France*, Vol. 186 (1), 3–19.

CARLTON, B, BARWISE, A, and KAYNIA, AM. 2022. Seismic Hazard Assessment for aWind Farm Offshore England, *Geotechnics*, Vol. 2, 14–31.

CARTWRIGHT, JA. 1990. The structural evolution of the Ringkøbing-Fyn High, In Tectonic Evolution of the North Sea Rifts, BLUNDELL, DJ, and GIBBS, AD (Editors), Clarendon Press, Oxford, 200–216.

CAUZZI, C, FACCIOLI, E, VANINI, M, and BIANCHINI, A. 2015. Updated predictive equations for broadband (0.01–10s) horizontal response spectra and peak ground motions, based on a global dataset of digital acceleration records, *Bulletin of Earthquake Engineering,* Vol. 13, 1587-1612.

CAUZZI, C, and FACCIOLI, E. 2018. Anatomy of sigma of a global predictive model for ground motions and response spectra, *Bulletin of Earthquake Engineering,* Vol. 16, 1887–1905.

CESCA, S, DAHM, T, JURETZEK, C, and KÜHN, D. 2011. Rupture process of the 2001 May 7 Mw 4.3 Ekofisk induced earthquake, *Geophysical Journal International*, Vol. 187(1), 407-413.

CHADWICK, RA, EVANS, DJ, and HOLLIDAY, DW. 1993. The Maryport fault: the post-Caledonian tectonic history of southern Britain in microcosm, *Journal of Geological Society*, Vol. 150, 247–250.

CHADWICK, RA, PHARAOH, TC, WILLIAMSON, JP, and MUSSON, RMW. 1996. Seismotectonics of the UK, *British Geological Survey Technical Report,* WA/96/3C, United Kingdom.

CHADWICK, RA, and PHARAOH, TC. 1998. The seismic reflection Moho beneath the United Kingdom and adjacent areas, *Tectonophysics*, Vol. 299(4), 255–279.

CHIOU, B, and YOUNGS, RR. 2014. Update of the Chiou and Youngs NGA model for the average horizontal component of peak ground motion and response spectra, *Earthquake Spectra,* Vol. 30, 1117-1153.

CHRISTIANSSON, P, FALEIDE, J, and BERGE, A. 2000. Crustal structure in the northern North Sea: an integrated geophysical study. 15-40 in Dynamics of the Norwegian Margin. In: NØTTVEDT, A (Editor) Dynamics of the Norwegian Margin. *Geological Society, London, Special Publications*, Vol. 167.

CLARINGBOULD, JS, BELL, RE, JACKSON, CA-L, GAWTHORPE, RL, and ODINSEN, T. 2017. Pre-existing normal faults have limited control on the rift geometry of the northern North Sea, *Earth and Planetary Science Letters,* Vol. 475, 190-206.

CLAUSEN, OR, and KORSTGÅRD, JA. 1994. Displacement geometries along graben bounding faults in the Horn Graben, Offshore Denmark, *First Break*, Vol. 12, 305–315.

CLAUSEN, OR, NIELSEN, SB, EGHOLM, DL, and GOŁĘDOWSKI, B. 2012. Cenozoic structures in the eastern North Sea Basin – a case for salt tectonics*, Tectonophysics*, Vol. 514–517, 156–167.

COLBEAUX, J-P, SOMMÉ, J, and TUFFREAU, A. 1981. Tectonique quaternaire dans le Nord de la France: l'apport du gisement paléolithique de Biache – Saint-Vaast, *Bulletin de l'Association française pour l'étude du quaternaire*, Vol. 3-4, 183-192.

COPPERSMITH, K, and BOMMER, J. 2012. Use of the SSHAC methodology within regulated environments: cost-effective application for seismic characterization at multiple sites, *Nuclear Engineering Design*, Vol. 245, 233–240.

COPPERSMITH K, COPPERSMITH R, HANSON K, UNRUH J, WOLF L, BOMMER J, AL ATIK L, RODRIGUEZ-MAREK A, TORO G, YOUNGS R, and MONTALDO-FALERO V. 2014. Hanford sitewide probabilistic seismic hazard analysis, *Report Prepared for the U. S. Department of Energy under Contract DE-AC05-76RL01830*, Pacific Northwest National Laboratory, Richland, Washington, 99352.

CORNELL, CA. 1968. Engineering Seismic Risk Analysis, *Bulletin of the Seismological Society of America*, Vol. 58, 1583-1606.

CORNELL,CA, and VANMARCKE, EH. 1969. The Major Influences on Seismic Risk, *Proceedings of the Fourth World Conference on Earthquake Engineering*, Santiago, Chile.

COTTON, F, SCHERBAUM, F, BOMMER, JJ, and BUNGUM, H. 2006. Criteria for Selecting and Adjusting Ground-Motion Models for Specific Target Regions: Application to Central Europe and Rock Sites, *Journal of Seismology,* Vol. 10, 137-156.

DAHL, N, and SOLLIE, T. 1993. The structural evolution of the Snorre field and surrounding areas, *Geological Society London, Petroleum Geology Conference Series*, Vol. 4, 1159–1166.

DANCIU, L, NANDAN, S, REYES, C, BASILI, R, WEATHERILL, G, BEAUVAL, C, ROVIDA, A, VILANOVA, S, SESETYAN, K, BARD, P-Y, COTTON, F, WIEMER, S, and GIARDINI D. 2021. The 2020 update of the European Seismic Hazard Model: Model Overview, *EFEHR Technical Report 001, v1.0.0*.

DAVIS, JC. 1986. *Statistics and data analysis in geology* (New York: Wiley).

DAVIS, M, WHITE, N, PRIESTLY, K, BAPTIE, B, and TILMANN, F. 2012. Crustal structure of the British Isles and its epeirogenic consequences, *Geophysical Journal International*, Vol. 190(2), 705–725.

DELAVAUD E, SCHERBAUM F, KÜHN N, and ALLEN T (2012). Testing the global applicability of ground motion prediction equations for active shallow crustal regions, *Bulletin of the Seismological Society of America,* Vol. 102(2), 707-721.

DE LUGT, IR, VAN WEES, JB, WONG, THE. 2003. The tectonic evolution of the southern Dutch North Sea during the Palaeogene: basin inversion in distinct pulses, *Tectonophysics,* Vol. 373, 141 – 159.

DEMYTTENAERE, R, and LAGA, P. 1988. Breuken- en isohypsenkaarten van het Belgisch gedeelte van de Roerdal Slenk: Eerste resultaten van een seismisch onderzoek in het gebied van Poppel-Lommel-Maaseik, *Professional Paper Belgische Geologische Dienst*, 20 pp.

DEZES, P, and ZIEGLER, PA. 2002. Moho depth map of Western and Central Europe.

DNV. 2021. Seismic design of wind power plants – Recommended practice, *DNV-RP-0585*, Edition August 2021

DOUBRE, C, MEGHRAOUI, M, MASSON, F, LAMBOTTE, S,JUNDB, H, BÈS DE BERC, M, and GRUNBERG, M. 2021. Seismotectonics in Northeastern France and neighboring regions, *Comptes Rendus Géoscience—Sciences de la Planète*, Vol. 353(S1), 153-185.

DOUGLAS, J. 2018. Capturing geographically-varying uncertainty in earthquake ground-motion models or what we think we know may change, In *Recent Advances in Earthquake Engineering in Europe, Geotechnical, Geological and Earthquake Engineering*, PITILAKIS, K (Editor), Vol. 46, 153-181.

DOUGLAS, J. 2021. Ground motion prediction equations 1964–2021, available at http://www.gmpe.org.uk.

DOUGLAS, J, and EDWARDS, B. 2016. Recent and future developments in earthquake ground motion estimation*, Earth-Science Reviews,* Vol. 160, 203-219.

DOUGLAS, J, ALDAMA-BUSTOS, G, TALLET-WILLIAMS, S, DAVI', M, and TROMANS, IJ. 2024. Ground-motion models for earthquakes occurring in the United Kingdom, *Bulletin of Earthquake Engineering, DOI:*10.1007/s10518-024-01943-8*.*

DROUET, S, AMERI, G, LE DORTZ, K, SECANELL, R, and SENFAUTE, G. 2020. A probabilistic seismic hazard map for the metropolitan France, *Bulletin of Earthquake Engineering*, doi.org/10.1007/s10518-020-900790-7.

EBBING, J, ENGLAND, RW, KORJA, T, LAURITSEN, T, OLESEN, O, STRATFORD, W, and WEIDLE, C. 2012. Structure of the Scandes lithosphere from surface to depth, *Tectonophysics*, Vol. 536, 1-24.

EPRI. 2012. Technical report: Central and Eastern United States Seismic Source Characterization for Nuclear Facilities, *Electric Power Research Institute, Palo Alto, U.S. Nuclear Regulatory Commission, U.S. Department of Energy*.

EQE INTERNATIONAL LTD. 2002. Seismic hazard - UK continental shelf (2002), *Offshore Waters Report HSE-OTR OTH-2002/005,* UK and Health and Safety Executive, London, UK.

FÆRSETH, RB, GABRIELSEN, RH, and HURICH, CA. 1995. Influence of basement in structuring of the North Sea basin, offshore southwest Norway, *Norwegian Journal of Geology/Norsk Geologisk Tidsskrift*, Vol. 75, 105–119.

FÄH, D, GIARDINI, D, KÄSTLI, P, DEICHMANN, N, GISLER, M, SCHWARZ-ZANETTI, G, ALVAREZ-RUBIO, S, SELLAMI, S, EDWARDS, B, ALLMANN, B, BETHMANN, F, WÖSSNER, J, GASSNER-STAMM, G, FRITSCHE, S, and EBERHARD, D. 2011. ECOS-09 Earthquake Catalogue of Switzerland Release 2011 Report and Database, *Report SED/RISK/R/001/20110417*.

FIELITZ, W, and MANSY J-L. 1999. Pre- and synorogenic burial metamorphism in the Ardenne and neighbouring areas (Rhenohercynian zone, central European Variscides). In: *Palaeozoic to recent tectonics in the NW European Variscan front zone*, SINTUBIN, M, VANDYCKE, S, and CAMELBEECK, T (Editors), Tectonophysics 309: 227–256.

FJELDSKAAR, W, VOORDE, M, TER, JOHANSEN, H, CHRISTIANSSON, P, FALEIDE, JL, and CLOETINGH, SAPL. 2004. Numerical simulation of rifting in the Northern Viking Graben: the mutual effect of modelling parameters, *Tectonophysics*, Vol. 382, 189-212.

FREE, M. 1996. *The attenuation of earthquake strong-motion in intraplate regions*, PhD Thesis, University of London.

FROHLICH, C, and DAVIS, S. 1993. Teleseismic b-values - or, much ado about 1.0, *Journal of Geophysical Research-Solid Earth,* Vol. 98, 631-644.

FÜLÖP, L, JUSSILA, V, AAPASUO, R, VUORINEN, T, and MÄNTYNIEM, P. 2020. A Ground-Motion Prediction Equation for Fennoscandian Nuclear Installations, *Bulletin of the Seismological Society of America,* Vol. 110(3), 1211–1230.

GALLOWAY, D, BUKITS, J, and FORD, G. 2013. Bulletin of British Earthquakes 2012, *British Geological Survey Seismological Report, OR/13/54,* United Kingdom.

García-Moreno, D, Verbeeck, K, Camelbeeck, T, De Batist, M, Oggioni, F, Zurita Hurtado, O, Versteeg, W, Jomard, H, Collier, JS, Gupta, S, Trentesaux, A, and Vanneste, K. 2015. Fault activity in the epicentral area of the 1580 Dover Strait (Pas-de-Calais) earthquake (northwestern Europe), *Geophysical Journal International,* Vol. 201, 2, 528–542.

Gautier, DL. 2005. Kimmeridgian Shales Total Petroleum System of the North Sea Graben Province, *U.S. Geological Survey Report, Bulletin 2204-C*, Virginia.

Geluk, MC, Duin, EJT, Dusar, M, Rijkers, MH, Van Den Berg, MW, and Van Rooijen, P. 1994. Stratigraphy and tectonics of the Roer Valley Graben, *Geologie and Mijnbouw,* Vol. 73, 129–141.

Gerstenberger, MC, Marzocchi, W, Allen, T, Pagani, M, Adams, J, Danciu, L, Field, EH, Fujiwara, H, Luco, N, Ma, K-F, Meletti, C, and Petersen, MD. 2020. Probabilistic seismic hazard analysis at regional and national scales: state of the art and future challenges, *Review of Geophysics*, DOI:10.1029/2019RG000653.

Ghione, F, Kühn, D, and Oye, V. 2019. Site-specific seismic hazard study for the submarine Wreck U-864 location, Norway, *Report Prepared for The Norwegian Coastal Administration*.

Gibson, J. 2009. The United Kingdom's elusive exclusive economic zone, *Journal of Water Law*, Vol. 20, 179-185.

Glennie, KW, and Boegner, PLE. 1981. Sole Pit Inversion tectonics, In *Petroleum geology of the continental shelf of North-West Europe*. Illing, LV, and Hobson, GD (Editors). Heyden and Sons., 110-120.

Gölke, M, and Coblentz, D. 1996. Origins of the European regional stress field*, Tectonophysics*, Vol. 266(1–4), 11–24.

Goulet, CA, Kishida, T, Ancheta, TD, Cramer, CH, Darragh, RD, Silva, WJ, Hashash, YAM, Harmon, J, Stewart, JP, Wooddell, KE, and Youngs, RR. 2014. PEER NGA-East Database, *PEER Report No. 2014/17*, Pacific Earthquake Engineering Research Center, California.

Goulet, C, Bozorgnia, Y, Kuehn, N, Al Atik, L, Youngs, RR, Graves, RW, and Atkinson, GM. 2017. NGA-east ground-motion models for the U. S. geological survey national seismic hazard maps, *Technical Report No. 2017/03*, Pacific Earthquake Engineering Research Center.

Grünthal, G, and Stromeyer, D, 1992. The recent crustal stress field in central Europe: trajectories and finite element modelling, *Journal of Geophysical Research*, Vol. 97(B8), 11805-11820.

Grünthal, G, Wahlström, E, and Stromeyer, D. 2009. The unified catalogue of earthquakes in central, northern, and northwestern Europe (CENEC)—updated and expanded to the last millennium, *Journal of Seismology*, Vol. 13, 517-541.

Grünthal, G, Stromeyer, D, and Bosse, C. 2017. The data sets of the earthquake model for the probabilistic seismic hazard assessment of Germany, version 2016—report on supplementary material for the respective publication, *Scientific Technical Report STR 17/05, GFZ German Research Centre for Geosciences*, Potsdam.

Grünthal, G, Stromeyer, D, Bosse, C, Cotton, F, and Bindi, D. 2018. The probabilistic seismic hazard assessment of Germany—version 2016, considering the range of epistemic uncertainties and aleatory variability, *Bulletin of Earthquake Engineering,* Vol. 16(10)**,** 4339-4395.

Gutenberg, B, and Richter, C. 1954. *Seismicity of the Earth and Associated Phenomena* (New Jersey: Princeton University Press).

Guterch, A, Wybraniec, S, Grad, M., Chadwick, A., Krawczyk, C., Ziegler, P., Thybo, H., and De Vos, W. 2010. Crustal structure and structural framework. In *Petroleum Geological Atlas of the Southern Permian Basin Area*, Doornenbal JC, and Stevenson, AG. (Editors), *European Association of Geoscientists and Engineers*, Houten, The Netherlands, 11–23.

Hakimhashemi, AH, and Grünthal, G. 2012. A statistical method for estimating catalog completeness applicable to long-term nonstationary seismicity data, *Bulletin of the Seismological Society of America*, Vol. 102(6), 2530–2546.

Hall, J, Brewer, JA, Matthews, DH, and Warner, M. 1984. Crustal structure across the Caledonides from the WINCH seismic reflection profile: Influences on the evolution of the Midland Valley of Scotland, *Transactions of the Royal Society of Edinburgh-Earth Sciences*, Vol. 75, 97-109.

Hansen, RA, Bungum, H, and Alsaker, A. 1989. Three recent larger earthquakes offshore Norway, *Terra Nova,* Vol. 1, 284–295.

Hawthorn, D, Laughlin, J, and Baptie, B. 2023. The evolution of seismic monitoring in the UK and its effect on the earthquake catalogue and ground motion data, Paper ID69, SECED 2023 Conference, Cambridge, United Kingdom.

Heidbach, O, Rajabi, M, Reiter, K, Ziegler, M, and the WSM Team. 2016. World Stress Map Database Release 2016, *GFZ Data Services*.

Hitchen, K. 2004. The geology of the UK Hatton-Rockall margin, *Marine and Petroleum Geology*, Vol. 21(8), 993-1012

Holloway, S, Reay, DM, Donato, JA, and Beddoe-Stephens, B. 1991. Distribution of granite and possible Devonian sediments in part of the East Shetland Platform, North Sea, *Journal of the Geological Society of London*, Vol. 148, 635–638.

HOLSCHNEIDER, M, ZÖLLER, G, and HAINZL, S. 2011. Estimation of the maximum possible magnitude in the framework of a doubly truncated Gutenberg-Richter model, *Bulletin of the Seismological Society of America*, Vol. 101(4), 1649–1659.

HOLSCHNEIDER, M, ZÖLLER, G, CLEMENTS, R, and SCHORLEMMER, D. 2014. Can we test for the maximum possible earthquake magnitude?, *Journal of Geophysical Research-Solid Earth*, Vol. 119, 2019–2028.

HOUGH, SE, and PAGE, M. 2011. Toward a consistent model for strain accrual and release for the New Madrid Seismic Zone, central United States, *Journal of Geophysical Research*, Vol. 116(B03311), doi:10.1029/2010JB007783.

HOWELLS, MF. 2007. Wales British Regional Geology, *British Geological Survey* R*eport*, Keyworth, Nottingham.

IAEA. 2022. Seismic Hazards in Site Evaluation for Nuclear Installations, IAEA Specific Safety Guide Series No. SSG-9, International Atomic Energy Agency, Vienna.

IMBER, J, HOLDSWORTH, RE, BUTLER, CA, and STRACHAN, RA. 2001. A reappraisal of the Sibson-Scholz fault zone model: The nature of the frictional to viscous ('brittle-ductile') transition along a long-lived crustal-scale fault, Outer Hebrides, Scotland, *Tectonics,* Vol. 20, 601-624.

ISC. 2021. International Seismological Centre (2021), http://www.isc.ac.uk/, https://doi.org/10.31905/D808B830.

ISO 19901-2. 2022. Petroleum and Natural Gas Industries–Specific Requirements for Offshore Structures–Part 2: Seismic Design Procedures and Criteria, *International Organization for Standardization*: Geneva, Switzerland.

JACKSON, DI, JACKSON, AA, EVANS, D, WINGFIELD, RTR, BARNES, RP, and ARTHUR, MJ. 1995. *United Kingdom offshore regional report: the geology of the Irish Sea* (London: HMSO for the British Geological Survey).

JAPSEN, P. 1997. Regional Neogene exhumation of Britain and the western North Sea, *Journal of the Geological Society*, Vol. 154, 239-247.

JERKINS, AE, OYE, V, ALVIZURI, C, HALPAAP, F, and KVÆRNA, T. 2023. The 21 March 2022 Mw 5.1 Tampen Spur Earthquake, North Sea: Location, Moment Tensor, and Context, *Bulletin of Seismological Society of America,* DOI: 10.1785/0120230163.

JOHNSTON, AC. 1996. Seismic moment assessment of earthquakes in stable continental regions—III. New Madrid 1811–1812, Charleston 1886 and Lisbon 1755, *Geophysical Journal International*, Vol. 126(2), 314–344.

JOHNSTON, AC, COPPERSMITH, KJ, KANTER, LR, and CORNELL, CA. 1994. The earthquakes of stable continental regions, *EPRI Report, Electric Power Research Institute*, Palo Alto, California.

JOHNSTON, AC, and SCHWEIG, ES. 1996. The enigma of the New Madrid earthquakes of 1811–1812, *Annual Review of Earth and Planetary Sciences*, Vol. 24, 339-384.

KALE, Ö, and AKKAR, S. 2013. A new procedure for selecting and ranking ground-motion prediction equations (GMPEs): the Euclidean distance-based ranking (EDR) method, *Bulletin of Seismological Society of America,* Vol. 103(2A), 1069–1084.

KENT, PE. 1974. Structural History, In: *The geology and mineral resources of Yorkshire*, RAYNER, DH, and HEMMINGWAY, JE (Editors), Yorkshire Geological Society, 13-28.

KENT, PE. 1980. Subsidence and uplift in East Yorkshire and Lincolnshire: a double inversion, *Proceedings of the Yorkshire Geological Society*, 42, 505-524.

KILHAMS, B, STEVANOVIC, S, AND NICOLAI, C. 2010. The 'Buntsandstein' gas play of the Horn Graben (German and Danish offshore): dry well analysis and remaining hydrocarbon potential, *Geological Society, London, Special Publications*, Vol. 469, 169 – 192.

KLEMPERER, SL, and HOBBS, R. 1991. *The BIRPS atlas. Deep seismic reflection profiles around the British Isles* (Cambridge University Press).

KLOSE, M, WANG, J, and KU, A. 2021. Seismic Design for Offshore Wind Farms–Lessons Learnt from the ACE Joint Industry Project, In *Proceedings of the ASME 2021 Conference on Ocean, Offshore and Arctic Engineering*, Virtual Online.

KOTHA, SR, WEATHERILL, GA, BINDI, D, and COTTON, F. 2020 A regionally-adaptable ground-motion model for shallow crustal earthquakes in Europe. *Bulletin of Earthquake Engineering*, Vol. 18, 4091–4125.

KOWSARI, M and GHASEMI, S. 2021. A backbone probabilistic seismic hazard analysis for the North Tehran Fault scenario, *Soil Dynamics and Earthquake Engineering*, Vol. 144, 106672.

KRISTIANSEN, TG, BARKVED, O, and PATILLO, PD. 2000. Use of passive seismic monitoring in well and casing design in the compacting and subsiding Valhall field, North Sea, *Society of Petroleum Engineering SPE, 65134.*

LAMBECK, K. 1993. Glacial rebound of the British-Isles - 1. Preliminary model results, *Geophysical Journal International*, Vol. 115(3), 941–959.

LANZANO, G, SGOBBA, S, LUZI, L, PUGLIA, R, PACOR, F, FELICETTA, C, D'AMICO, M, COTTON, F, and BINDI, D. 2019. The pan-European engineering strong motion (ESM) flatfile: compilation criteria and data statistics, *Bulletin of Earthquake Engineering*, Vol. 17, 561–582.

LARUE, J-P. 2005. The status of ravine-like incisions in the dry valleys of the Pays de Thelle (Paris basin, France), *Geomorphology*, Vol. 68, 242-256.

LEBEDEV,S, GRANNELL, J, ARROUCAU, P, BONADIO, R, PIANA AGOSTINETTI, N, and BEAN, CJ. 2023. Seismicity of Ireland, and why it is so low: How the thickness of the lithosphere controls intraplate seismicity, *Geophysical Journal International*, Vol. 235, 431–447.

LEEDER, MR, and HARDMAN, M. 1990. Carboniferous of the Southern North Sea Basin and controls on hydrocarbon prospectivity, In *Tectonic events responsible for Britain's oil and gas reserves*. HARDMAN, RFP, and BROOKS, J (Editors), Special Publication of the Geological Society of London, Vol. 55, 87-105.

LEONARD, M. 2014. Self-consistent earthquake fault-scaling relations: update and extension to stable continental strike-slip faults, *Bulletin of the Seismological Society of America*, Vol. 104(6), 2953-2965.

LE ROY, P, GRACIA-GARAY, C, GUENNOC, P, BOURILLET, J-F, REYNAUD, J-Y, THINON, I, KERVEVAN, P, PAQUET, F, MENIER, D, and BULOIS, C. 2011. Cenozoic tectonics of the Western Approaches Channel basins and its control of local drainage systems, *Bulletin de la Société Géologique de France*, Vol. 182(5), 451–463.

LICCIARDI, A, ENGLAND. RW, PIANA AGOSTINETTI, N, and GALLAGHER, K. 2020. Moho depth of the British Isles: a probabilistic perspective, *Geophysical Journal International*, Vol. 221, 1384–1401.

LINDHOLM, CD, BUNGUM, H, HICKS, E, and VILLAGRAN, M. 2000. Crustal stress and tectonics in Norwegian regions determined from earthquake focal mechanisms. In: NØTTVEDT, A (Editor) Dynamics of the Norwegian Margin. *Geological Society, London, Special Publications*, Vol. 167, 429-440.

LINDHOLM, CD, BUNGUM, H, GHIONE, F, MESLEM, A, HUANG, C, and OYE, V. 2024. Earthquakes and Seismic Hazard for Norway and Svalbard, *Journal of Seismology,* Under review.

LUBKOWSKI, Z, BOMMER, J, BAPTIE, B, BIRD, J, DOUGLAS, J, FREE, M, HANCOCK, J, and SARGEANT, S. 2004. An evaluation of attenuation relationships for seismic hazard assessment in the UK, *13th World Conference on Earthquake Engineering*, Vancouver, B.C., Canada, Paper No. 1422.

LUCKETT, R, OTTEMÖLLER, L, BUTCHER, A, and BAPTIE, B. 2019. Extending local magnitude ML to short distances, *Geophysical Journal International*, Vol. 216(2), 1145–1156.

MAGUIRE, P, ENGLAND, R, and HARDWICK, A. 2011. LISPB DELTA, a lithospheric seismic profile in Britain: analysis and interpretation of Wales and southern England section, *Journal of the Geological Society London*, Vol. 168, 61–82.

MAIN, ID, IRVING, D, MUSSON, RMW, and READING, A. 1999. Constraints on the frequency-magnitude relation and maximum magnitudes in the UK from observed seismicity and glacio-isostatic recovery rates, *Geophysical Journal International,* Vol 137(2), 535–550.

MALLARD, D, SKIPP, W, and ASPINALL, W. 2003. *An appraisal of existing seismic hazard estimates for the UK Continental Shelf,* (Sudbury: HSE Books).

MANCHUEL, K, TRAVERSA, P, BAUMONT, D, CARA, M, NAYMAN, E, and DUROUCHOUX, C, 2018. The French seismic CATalogue (FCAT-17), *Bulletin of Earthquake Engineering*, Vol. 16, 2227-2251.

MANSY, J-L, MANBY, GM, AVERBUCH, O, EVERAERTS, M, BERGERAT, F, VAN VLIET-LANOË, B, LAMARCHE, J, and VANDYCKE, S. 2003. Dynamics and inversion of the Mesozoic Basin of the Weald-Boulonnais area: role of basement reactivation, *Tectonophysics,* Vol. 373, 161–179.

MARROW, P. 1992. Seismic monitoring of the North Sea, *Offshore Technology Report, OTO 90 323*.

MARROW, PC, and WALKER, AB. 1988. LLeyn earthquake of 1984 July 19: Aftershock sequence and focal mechanism, *Geophysical Journal International,* Vol 92, 487–493.

MAZZOTTI, S, AUBAGNAC, C, BOLLINGER, L, COCA OSCANOA, K, DELOUIS, B, DO PACO, D, DOUBRE, C, GODANO, M, JOMARD, H, LARROQUEET, C, LAURENDEAU, A, MASSON, F, SYLVANDER, M, and TRILLA, A. 2021. FMHex20: An earthquake focal mechanism database for seismotectonic analyses in metropolitan France and bordering regions, *Bulletin de la Société Géologique de France*, Vol. 192, pp.10.

MCCOMB, HE, and WEST, CJ. 1931. List of seismological stations of the world, *Bulletin of the National Research Council, Number 82*, National Academy of Sciences, Washington, D.C.

MCCULLY, R, KOULOURI, I, LUBKOWSKI, Z, and PAPPIN, J. 2014. Comparison of Eurocode 8 site class amplification factors with non-linear site response analysis, Second European Conference on Earthquake Engineering and Seismology, Istanbul, Turkey.

MCGUIRE, RK. 1974. Seismic Structural Response Risk Analysis, Incorporating Peak Response Regressions on Earthquake Magnitude and Distance, *Report R74-51, Department of Civil Engineering, Massachusetts Institute of Technology*, Cambridge, U.S.A.

MCGUIRE, RK. 1995. Probabilistic seismic hazard analysis and design earthquakes: closing the loop, *Bulletin of the Seismological Society of America*, Vol. 85, 1275-1284.

MCGUIRE, RK. 2004. *Seismic Hazard and Risk Analysis*. (Oakland CA: Earthquake Engineering Research Institute).

MELETTI, C, D'AMICO, V, and MARTINELLI, F. 2009. Homogeneous determination of maximum magnitude, *SHARE* Deliverable 3.3.

MILLER, AC, and RICE, TR. 1983. Discrete approximations of probability distributions, *Management Science*, Vol 29(3), 352–362.

MOEIN, MJA, LANGENBRUCH, C, SCHULTZ, R, GRIGOLI, F, ELLSWORTH, WL, WANG, R, RINALDI, AP, and SHAPIRO, S. 2023. The physical mechanisms of induced earthquakes, *Nature Review Earth and Environment*, Vol. 4, 847–863.

MOLYNEUX, SG. 1991. The contribution of palaeontological data to an understanding of the Early Palaeozoic framework of eastern England. In: *Proceedings of the International Meeting on the Caledonides of the Midlands and the Brabant Massif*. ANDRE, L, HERBOSCH A, VANGUESTAINE, M, and VERNIERS, J. (editors), Annales de la Société Géologique de Belgique, Vol. 114, 93-106.

MOSCA, I. 2019. Comparing seismic hazard software: M3C vs. OpenQuake, *British Geological Survey Open Report, OR/19/038,* United Kingdom.

MOSCA, I, SARGEANT, S, BAPTIE, B, MUSSON, RMW, and PHARAOH, T. 2020. National seismic hazard maps for the UK: 2020 update, *British Geological Survey Seismological Report, OR/20/053*, United Kingdom.

MOSCA, I, SARGEANT, S, BAPTIE, B, MUSSON, RMW, and PHARAOH, T. 2022. The 2020 national seismic hazard model for the United Kingdom, *Bulletin of Earthquake Engineering*, Vol. 20, 633–675.

MOSCA, I, BAPTIE, B, FOWLER, R, and STAFFORD, PJ. 2023a. Preliminary results on the development of an adjustable backbone model approach for ground-motion prediction within the UK, Paper ID159, SECED 2023 Conference, Cambridge, United Kingdom.

MOSCA, I, BAPTIE, B, and Luckett, R. 2023b. Comparing observed and modelled ground motions using adjustments for specific sites in the UK, Paper ID57, SECED 2023 Conference, Cambridge, United Kingdom.

MUIR-WOOD, R. 2000. Deglaciation seismotectonics: A principal influence on intraplate seismogenesis at high latitudes, *Quaternary Science Reviews*, Vol. 19(14–15), 1399–1411.

MUSSON, RMW. 1986. The use of newspaper data in historical earthquake studies, *Disasters*, Vol. 10, 217–223.

MUSSON, RMW. 1994. A catalogue of British earthquakes, *British Geological Survey Global Seismology Report*, WL/94/04, United Kingdom.

MUSSON, RMW. 1996. Determination of parameters for historical British earthquakes, *Annali di Geofisica*, Vol. 39, 1041-1048.

MUSSON, RMW. 1999. Determination of design earthquakes in seismic hazard analysis through Monte Carlo simulation, *Journal of Earthquake Engineering*, Vol. 3, 463-474.

MUSSON, RMW. 2000. The use of Monte Carlo simulations for seismic hazard assessment in the UK, *Annali di Geofisica,* Vol. 43, 1-9.

MUSSON, RMW. 2007. British earthquakes, *Proceedings of the Geologists' Association*, Vol. 118, 305-337.

MUSSON, RMW. 2012a. PSHA validated by quasi observational means, *Seismological Research Letters*, Vol. 83, 130-134.

MUSSON, RMW. 2012b. The effect of magnitude uncertainty on earthquake activity rates, *Bulletin of the Seismological Society of America*, Vol. 102(6), 2771–2775.

MUSSON, RMW. 2012c. Interpreting intraplate tectonics for seismic hazard: A UK historical perspective, *Journal of Seismology*, Vol. 16, 261–273.

MUSSON, RMW. 2013. Updated intensity attenuation for the UK, *British Geological Survey Open Report OR/13/029*. 19pp.

MUSSON, RWM. 2015. What was the largest British earthquake?, *SECED 2015 Conference*, Cambridge, United Kingdom.

MUSSON, RMW, and SARGEANT, S. 2007. Eurocode 8 seismic hazard zoning maps for the UK, *British Geological Survey Report, CR/07/125.*

NAYLOR, D, SHANNON, P, and MURPHY, NJ. 1999. Irish Rockall Basin region—a standard structural nomenclature system Petroleum Affairs Division, Ireland, *Special Publication*, 1-99.

NGI, NORSAR, and PML. 1988. Earthquake loading of the Norwegian Continental Shelf, *ELOCS Report*.

NEILSON, G, MUSSON, RMW, and BURTON, PW. 1984. Macroseismic reports on historical British earthquakes V: The South and South West of England, *British Geological Survey Report*, 231, United Kingdom.

NORSAR. 2020. Seismic Zonation and Earthquake loading for Norway and Svalbard; Load estimates as basis for Eurocode 8 applications, *Internal Report No. 19-005*.

NORSAR, and NGI. 1998. Seismic Zonation for Norway, *Report prepared for the Norwegian Council for Building Standardization*, Oslo, Norway.

ODINSON, T, CHRISTIANSSON, P, GABRIELSEN, R, FALEIDE, J, and BERGE, A. 2000. The geometries and deep structure of the northern North Sea rift system. 41-58 in Dynamics of the Norwegian Margins. In: NØTTVEDT, A (Editor) Dynamics of the Norwegian Margin. *Geological Society, London, Special Publications*, Vol. 167.

ÓLAVSDÓTTIR, J, STOKER, MS, RIISHUUS, MS, and EIDESGAARD, ÓR. 2017. Discovery of Two Sub-Volcanic Basins Below the North Atlantic Igneous Province (NAIP), Faroe Platform, NE Atlantic Ocean, *Tectonics*, Vol. 4, DOI:10.1029/2020TC006589.

OTTEMÖLLER, L, NIELSEN, HH, ATAKAN, K, BRAUNMILLER, J, and HAVSKOV, J. 2005. The 7 May 2001 induced seismic event in the Ekofisk oil field, North Sea, *Journal of Geophysical Research*, Vol. 110(B10), B10301, doi: 10.1029/2004JB003374.

OTTEMÖLLER, L, and THOMAS, CW. 2007. Highland Boundary Fault Zone: Tectonic implications of the Aberfoyle earthquake sequence of 2003, *Tectonophysics*, Vol. 430, 83–95.

OTTEMÖLLER, L, BAPTIE, B, and SMITH, NJ P. 2009. Source parameters for the 28 April 2007 Mw 4.0 earthquake in Folkestone, United Kingdom, *Bulletin of the Seismological Society of America*, Vol. 99(3), 1853-1867.

OTTEMÖLLER, L, and SARGEANT, S. 2010. Ground-motion difference between two moderate-size intraplate earthquakes in the United Kingdom. *Bulletin of the Seismological Society of America*, Vol. 100(4), 1823–1829.

PAGANI, M, MONELLI, D, WEATHERILL, G, DANCIU, L, CROWLEY, H, SILVA, V, HENSHAW, P, NASTASI, M, PANZERI, L, and VIGANÒ, D. 2014. OpenQuake engine: An open hazard (and risk) software for Global Earthquake Model. *Seismological Research Letters*, Vol. 85, 692-702.

PATRUNO, S, KOMBRINK, H, and ARCHER, SG. 2022. Cross-border stratigraphy of the Northern, Central and Southern North Sea: a comparative tectono-stratigraphic mega-sequence synthesis, In *Cross-Border Themes in Petroleum Geology I: The North Sea*, PATRUNO, S, ARCHER, SG, CHIARELLA, D, HOWELL, JA, JACKSON, CA-L, and KOMBRINK, H. (Editors). Geological Society, London, Special Publications, 494, 13–83.

PEER. 2015. NGA-east: median ground-motion models for the Central and Eastern North America region, *Technical report PEER report no. 2015/04*, Pacific Earthquake Engineering Research Center.

PEKOT, LJ, and GERSIB, GA. 1987. Ekofisk, in Geology of the Norwegian Oil and Gas Fields. In SPENCER, AM, et al., *Grahamand Trotman, London*, 73-78.

PETERSEN, MD, MOSCHETTI, MP, POWERS, PM, MUELLER, CS, HALLER, KM, FRANKEL, AD, ZENG, Y, YUEHUA, REZAEIAN, S, HARMSEN, SC, BOYD, OS, FIELD, N, CHEN, R, RUKSTALES, KS, LUCO, N, WHEELER, RL, WILLIAMS, RA, and OLSEN, AH. 2014. Documentation for the 2014 update of the United States national seismic hazard maps, *U.S. Geological Survey Open-File Report 2014–1091,* California.

PERROT, J, ARROUCAU, P, GUILBERT, J, DÉVERCHÈRE, J, MAZABRAUD, Y, ROLET, J, MOCQUET, A, MOUSSEAU, M, and MATIAS, L. 2005. Analysis of the Mw 4.3 Lorient earthquake sequence: a multidisciplinary approach to the geodynamics of the Armorican Massif, westernmost France, *Geophysical Journal International,* Vol. 162, 935–950.

PEZESHK, S, ZANDIEH, A, CAMPBELL, KW, and TAVAKOLI, B. 2018. Ground-Motion Prediction Equations for Central and Eastern North America Using the Hybrid Empirical Method and NGA-West2 Empirical Ground-Motion Models, *Bulletin of the Seismological Society of America*, Vol. 108(4), 2278–2304.

PHARAOH, TC. 2018. The Anglo-Brabant Massif: persistent but enigmatic palaeo-relief at the heart of Western Europe, *Proceedings of the Geologists' Association*, Vol. 129(3), 278-328.

PHARAOH, TC. 2019. The complex tectonic evolution of the Malvern region: crustal accretion followed by multiple extensional and compressional reactivation, *Proceedings of the Open University Geological Society*.

PHARAOH, TC, BREWER, TS, and WEBB, PC. 1993. Subduction-related magmatism of late Ordovician age in eastern England, *Geological Magazine*, Vol. 130, 647-656.

PHARAOH, TC, ENGLAND, R, and LEE, MK. 1995. The concealed Caledonide Basement of Eastern England and the Southern North Sea – A review, In The Trans-European Suture Zone: EUROPROBE in Liblice 1993, GEE, DG, and BECKHOLMEN, M. (Editors), Studia Geophysica et Geodaetica, 39, 85-97.

PLATT, NH. 1992. Structure and tectonics of the northern North Sea: new insights from deep penetration regional seismic data. In: LAMBIASE, JJ (Editor). Hydrocarbon Habitat in Rift Basins, *Geological Society, London, Special Publications*, Vol. 80, 103-113.

PLATT, NH, and CARTWRIGHT, JA. 1998. Structure of the East Shetland Platform, northern North Sea, *Petroleum Geoscience,* Vol. 4 (4), 353–362.

PML. 1985. Seismological Studies for UK Hazard Analysis, *Report No 346/85* by Principia Mechanica Ltd for CEGB.

PML. 1988. UK uniform risk spectra, *Technical Report HPC-IP-096013*, Principia Mechanica Ltd., London. Report for National Nuclear Corporation.

PNNL - PACIFIC NORTHWEST NATIONAL LABORATORY. 2014. Hanford Sitewide Probabilistic Seismic Hazard Analysis, *U.S. Department of Energy under contract DE-AC06076RL01830 and Energy Northwest.*

PRINCIPIA MECHANICA LTD. 1986. North Sea seismicity, *UK Dept. of Energy Offshore Technology Report No. OTH 86 219*, HMSO, London.

RAVNÅS, NØTTVEDT, A, STEEL, RJ, and WINDELSTAD, J. 2000. Syn-rift sedimentary architectures in the Northern North Sea, *Geological Society London Special Publications,* Vol. 167(1), 133-177.

REITER, L. 1990. *Earthquake Hazard Analysis* (New York: Columbia University Press).

RESTREPO-VELEZ, LF, and BOMMER JJ. 2003. An exploration of the nature of the scatter in ground-motion prediction equations and the implications for seismic hazard assessment, *Journal of Earthquake Engineering*, Vol. 7(SI1), 171–199.

REZAEIAN, S, POWERS, PM, SHUMWAY, AM, PETERSEN, MD, LUCO, N, FRANKEL, AD, MOSCHETTI, MP, THOMPSON, EM, and MCNAMARA, DE. 2021. The 2018 update of the US National Seismic Hazard Model: Ground motion models in the central and eastern US, *Earthquake Spectra*, Vol. 37(1), DOI: 10.1177/8755293021993837.

RIETBROCK, A, STRASSER, FO, and EDWARDS, B. 2013. A stochastic earthquake ground motion prediction model for the United Kingdom, *Bulletin of the Seismological Society of America*, Vol. 103(1), 57-77.

RIETBROCK, A, and EDWARDS, B. 2019. Update of the UK stochastic ground motion model using a decade of broadband data, *SECED 2019 Conference*, Greenwich, United Kingdom.

RITCHIE, MEA, MUSSON, RMW, and WOODCOCK, NH. 1990. The Bishop's Castle (UK) Earthquake of 2 April 1990, *Terra Nova*, Vol. 2(4), 390–400.

RITCHIE, JD, ZISKA, H, KIMBELL, G, QUINN, M, and CHADWICK, A. 2011. Geology of the Faroe–Shetland Basin and Adjacent Are*as*, *British Geological Survey Research Report, RR/11/01*, 9–70.

RITZ, J-F, BAIZE, S, AUDIN, L, AUTHÉMAYOU, C, GRAVELEAU, F, KAUB, C, LACAN, P, LECLERC, F, LARROQUE,C, MANCHUEL, K, MUGNIER, J-L, ORTUÑO, M, RIZZA, M, VASSALLO, R, ANTOINE, P, ARROUCAU, P, BILLANT, J, BOLLINGER, L, FERRY, M, FILLON, C, GEOFFROY, L, JOMARD, H, LE ROY, P, LOCHT, J-L, MIGEONG, S, PERRIN, C, PERROT, J, RATZOV, G, REICHERTER, K, SOUBIGOU, O, VERGNIAULTH, C, VIAPLANA-MUZAS, M, and VAN DERWOERD, J. 2021. New perspectives in studying active faults in metropolitan France: the "Active faults France" (FACT/ATS) research axis from the Resif-Epos consortium, *Comptes Rendus Géoscience—Sciences de la Planète*, Vol. 353(S1), 381-412.

ROBERTS, NS, BELL, AF, and MAIN, I. 2015. Are volcanic seismic *b*-value high, and if so when?, *Journal of Volcanology and Geothermal Research,* Vol. 308, 127-141.

RODRIGUEZ-MAREK, A, RATHJE, EM, BOMMER, JJ, SCHERBAUM, F, and STAFFORD, PJ. 2014. Application of Single-Station Sigma and Site-Response Characterization in a Probabilistic Seismic-Hazard Analysis for a New Nuclear Site, *Bulletin of the Seismological Society of America*, Vol. 104(4), 1601–1619.

RYDELEK, PA, and SACKS, IS. 1989. Testing the completeness of earthquake catalogs and the hypothesis of self-similarity, *Nature*, Vol. 337, 251–253.

SARGEANT, SL, STAFFORD, PJ, LAWLEY, R, WEATHERILL, G, WESTON, A-JS, BOMMER, JJ, BURTON, PW, FREE, M, MUSSON, RMW, KUUYUOR, T, and ROSSETTO, T. 2008. Observations from the Folkestone, UK, earthquake of 28 April 2007, *Seismological Research Letters*, Vol. 79 (5), 672-687.

SARGEANT, S, and OTTEMÖLLER, L. 2009. Lg wave attenuation in Britain, *Geophysical Journal International*, Vol. 179(3), 1593–1606.

SCHLAPHORST, D, KENDALL, J-M, COLLIER, JS, VERDON, JP, BLUNDY, J, BAPTIE, B, LATCHMAN, JL, MASSIN, F, and BOUIN, M-P. 2016. Water, oceanic fracture zones and the lubrication of subducting plate boundaries—insights from seismicity, *Geophysical Journal International,* Vol. 204(3), 1405–1420.

SCHERBAUM, F, DELAVAUD, W, and RIGGELSEN, C. 2009. Model selection in seismic hazard analysis: An information–theoretic perspective, *Bulletin of the Seismological Society of America*, Vol. 99(6), 3234–3247.

SCHMID, SM, and KISSLING, E. 2000. The arc of the western Alps in the light of geophysical data on deep crustal structure, *Tectonics*, Vol. 19, 62–85.

SHENNAN, I, BRADLEY, S, MILNE, G, BROOKS, A, BASSETT, S, and HAMILTON, S.2006. Relative sea-level changes, glacial isostatic modelling and ice-sheet reconstructions from the British Isles since the Last Glacial Maximum, *Journal of Quaternary Science*, Vol. 21(6), 585–599.

SICHIEN, E, HENRIET, JP, CAMELBEECK, T, and DE BAETS, B. 2012. Estimating crustal thickness in Belgium and surrounding regions from Moho-reflected waves, *Tectonophysics*, Vol. 560-561, 105-119.

SISSINGH, W. 2006. Syn-kinematic palaeogeographic evolution of the West European platform: correlation with Alpine plate collision and foreland deformation, *Geologie and Mijnbouw,* Vol. 85(2), 131–180.

SMYTHE, DK, DOBINSON, A, MCQUILLIN, R, BREWER, JA, MATTHEWS, DH, BLUNDELL, DJ, and KELK, B. 1982. Deep structure of the Scottish Caledonides revealed by the MOIST reflection profile, *Nature*, Vol. 299, 338-340.

SØRENSEN, MB, VOSS, PH, HAVSKOV, J, GREGERSEN, S, and ATAKAN, K. 2011. The seismotectonics of western Skagerrak, *Journal of Seismology*, Vol. 15, 599–611.

STAFFORD, PJ. 2022. A model for the distribution of response spectral ordinates from New Zealand crustal earthquakes based upon adjustments to the Chiou and Youngs (2014) response spectral model, *GNS Science Report 2022/15*, GNS Science, Lower Hutt, New Zealand.

STAFFORD, PJ, BOORE, D, YOUNGS, R, and BOMMER, J. 2022. Host-region parameters for an adjustable model for crustal earthquakes to facilitate the implementation of the backbone approach to building ground-motion logic trees in probabilistic seismic hazard analysis, *Earthquake Spectra*, Vol. 38(2), DOI10.1177/87552930211063221.

STEIN, AM. 1988. Basement controls upon basin development in the Caledonian foreland, *Basin Research*, Vol. 1, 107-119.

STEIN, S, and WYSESSION, M. 2003. *An Introduction to Seismology, Earthquakes, and Earth Structure* (Oxford: Wiley-Blackwell Publishing).

STEPHAN, T, KRONER, U, HAHN, T, HALLAS, P, and HEUSE, T. 2016. Fold/cleavage relationships as indicator for late Variscan sinistral transpression at the Rheno-Hercynian-Saxo-Thuringian boundary zone, Central European Variscides, *Tectonophysics,* Vol. 681, 250–262.

STEWART, M, STRACHAN, RA, MARTIN, MW, and HOLDSWORTH, RE. 2001. Dating early sinistral displacements along the Great Glen Fault Zone, Scotland: structural setting, emplacement and U–Pb geochronology of the syn-tectonic Clunes Tonalite, *Journal of the Geological Society, London*, Vol. 158, 821–830.

STOKER MS, HITCHEN K, and GRAHAM, CC. 1993. *United Kingdom offshore regional report. The geology of the Hebrides and West Shetland shelves, and adjacent deep-water areas*. (London: HMSO for the British Geological Survey.)

STONE P, MCMILLAN AA, FLOYD JD, BARNES RP, and PHILLIPS, ER. 2012. *British regional geology: South of Scotland*. Fourth edition. Keyworth, Nottingham: British Geological Survey.

STRACHAN, RA, HARRIS, AL, FETTES, DJ, AND SMITH, M. 2002. The Northern Highland and Grampian terranes. In: TREWIN, NH (Ed.). The Geology of Scotland. (4th edition), *The Geological Society, London*, 81–148.

STRATFORD, W, THYBO, H, FALEIDE, JI, OLESEN, O, and TRYGGVASON, A. 2009. New Moho map for onshore southern Norway, *Geophysical Journal International*, Vol. 178(3), 1755-1765.

STRASSER, FO, ABRAHAMSON, NA, and BOMMER JJ. 2009. Sigma: Issues, insights and challenges, *Seismological Research Letters,* Vol. 80(1), 40–54.

TAMAS, A, HOLDSWORTH, RE, UNDERHILL, JR, TAMAS, DM, DEMPSEY, ED, MCCARTHY, DJ, MCCAFFREY, KJ, and SELBY, D. 2022. Correlating deformation events onshore and offshore in superimposed rift basins: the Lossiemouth Fault Zone, Inner Moray Firth Basin, Scotland, *Basin Research*, Vol. 34(4), 1314-1340.

THYBO, H. 1997. Geophysical characteristics of the Tornquist Fan area, northwest Trans-European Suture Zone: indication of late Carboniferous to early Permian dextral transtension, *Geological Magazine,* Vol. 134, 597–606.

TORO, GR, AND ABRAHAMSON, NA, and SCHNEIDER, JE. 1997. Model of strong ground motions from earthquakes in central and eastern North America: Best estimates and uncertainties, *Seismological Research Letters*, Vol. 68, 41-57.

TREWIN, NH, and ROLLIN, M. 2002. Geology history and structure of Scotland. In: *The Geology of Scotland* (4th edition), TREWIN, NH (Editor), The Geological Society, London, 1–26.

TRODD, H, WARBURTON, P, and POOLEY, CI. 1985. The Great British Earthquake of 1984 seen from afar*, Geophysical Journal of Royal Astronomical Society*, Vol. 83, 809–812.

TROMANS, IJ, ALDAMA-BUSTOS, G, DOUGLAS, J, LESSI-CHEIMARIOU, A, HUNT, S, DAVI, M, MUSSON, RMW, GARRARD, G, STRASSER, FO, and ROBERTSON, C. 2019. Probabilistic seismic hazard assessment for a new-build nuclear power plant site in the UK, *Bulletin of Earthquake Engineering*, Vol. 17(1), 1-36.

TURBITT, T, BARKER, EJ, BROWITT, CWA, HOWELLS, M, MARROW, PC, MUSSON, RMW, NEWMARK, RH, REDMAYNE, DW, WALKER, AB, JACOB, AWB, RYAN, E, and WARD, V. 1985. The North Wales earthquake of 19 July 1984, *Journal of the Geological Society*, Vol. 142(3), 567–571.

UNDERHILL, JR. 1991. Implications of Mesozoic - Recent basin development in the western Inner Moray Firth, UK, *Marine and Petroleum Geology*, Vol. 8, 359–369.

UNDERHILL, J, and PARTINGTON, M. 1993. Jurassic thermal doming and deflation in the North Sea: implications of sequence stratigraphic evidence. 337-345 in Petroleum Geology of North-west Europe. In Proceedings of the 4th Conference. PARKER, J (Editor), *The Geological Society, London*.

USGS. 2017. U.S. Geological Survey, Earthquake Hazards Program, Advanced National Seismic System (ANSS) Comprehensive Catalog of Earthquake Events and Products: Various, https://doi.org/10.5066/F7MS3QZH.

USNRC. 2012. Practical implementation guidelines for SSHAC level 3 and 4 hazard studies, *U.S. Nuclear Regulatory Commission,* NUREG-2117, Rev. 1.

VAN DEN BERG, MW. 1994. Neotectonics of the Roer Valley rift system: Style and rate of crustal deformation inferred from syn-tectonic sedimentation, *Geologie and Mijnbouw,* Vol. 73, 143–156.

VAN ECK, T, GOUTBEEK, F, HAAK, H, and DOST, B. 2006. Seismic hazard due to small-magnitude, shallow-source, induced earthquakes in The Netherlands, *Engineering Geology*, Vol. 87(1-2), 105-121.

VAN EIJS, R, MULDERS, F, NEPVEU, M, KENTER, C, and SCHEFFERS, B. 2006. Correlation between hydrocarbon reservoir properties and induced seismicity in the Netherlands, *Engineering Geology*, Vol. 84(3-4), 99-111.

VAN HOORN, B. 1987. Structural evolution, timing and tectonic style of the Sole Pit Inversion, *Tectonophysics*, Vol. 137, 239–284.

VAN HOUTTE, C, DROUET, S, and COTTON, F. 2011. Analysis of the origins of κ (Kappa) to compute hard rock to rock adjustment factors for GMPEs, *Bulletin of the Seismological Society of America*, Vol. 101(6), 2926–2941.

VAN NOTEN, K, LECOCQ, T, SHAH, AK, and CAMELBEECK, T. 2015. Seismotectonic significance of the 2008–2010 Walloon Brabant seismic swarm in the Brabant Massif, Belgium, *Tectonophysics*, Vol. 656, 20-38.

VAN VLIET-LANOË, B, LAURENT, M, BAHAIN, JL, BALESCU, S, FALGUÉRES, C, FIELD, M, HALLÉGOUËT, B, and KEEN, D.H. 2000. Middle Pleistocene raised beach anomalies in the English Channel: regional and global stratigraphic implications, *Journal of Geodynamics*, Vol. 29, 15–41.

VAN VLIET-LANOË, B, VANDENBERGHE, N, BERGERAT, F, and HENRIET, J-P. 2002. Cenozoic evolution of the Channel and southern North Sea areas (Western Europe). The neotectonic control on sedimentation and rivers, in Contributions to the Geology of Belgium and Northwest Europe, *Proceedings of the First Geologica Belgica International Meeting*, Leuven, Vol. 12, 21–24.

VANNESTE, K, CAMELBEECK, T, and VERBEECK, K. 2013. A Model of Composite Seismic Sources for the Lower Rhine Graben, Northwest Europe, *Bulletin of the Seismological Society of America*, Vol. 103(2A), 984–1007.

VERSEY, HC. 1939. The North Sea Earthquake of 1931 June 7, *Geophysical Supplements to the Monthly Notices of the Royal Astronomical Society*, Vol. 4(6), 416–423.

VERWEIJ, JM, and SIMMELINK, HK. 2002. Geodynamic and hydrodynamic evolution of the Broad Fourteens Basin (The Netherlands) in relation to its petroleum systems, *Marine and Petroleum Geology,* Vol. 19, 339-359.

VILLANI, M, POLIDORO, B, ADER, T, MCCULLY, R, LUBKOWSKI, Z, COURTNEY, TJ, and WALSH, M. 2019. A selection of GMPEs for the UK based on ground motion and macroseismic datasets, *Bulletin of the Seismological Society of America*, Vol. 109(4), 1378–1400.

VILLANI, M, LUBKOWSKI, Z, FREE, M, MUSSON, RWM, POLIDORO B, MCCULLY R, KOSKOSIDI, A, OAKMAN, C, COURTNEY TJ, and WALSH M. 2020. A probabilistic seismic hazard assessment for Wylfa Newydd, a new nuclear site in the United Kingdom, *Bulletin of Earthquake Engineering*, Vol. 18, 4061–4089.

YENIER, E, and ATKINSON, GM. 2015. Regionally adjustable generic ground-motion prediction equation based on equivalent point-source simulations: Application to central and eastern North America, *Bulletin of the Seismological Society of America*, Vol.105, 1898–2009.

WALKER, AB. 1991. The Jersey Earthquake of 30th April 1990. *Annual Bulletin of Society Jersiaise*, Vol. 25 (3), 529–538.

WEATHERILL, G, and COTTON, F. 2020. A ground motion logic tree for seismic hazard analysis in the stable cratonic region of Europe: regionalisation, model selection and development of a scaled backbone approach, *Bulletin of Earthquake Engineering*, Vol. 18, 6119–6148.

WEATHERILL GA, KOTHA SR, and COTTON F. 2020. A regionally-adaptable "scaled-backbone" ground motion logic tree for shallow seismicity in Europe: application to the 2020 European Seismic Hazard Model, *Bulletin of Earthquake Engineering*, Vol. 18(11), 5087–5117.

WEICHERT, D.H. 1980. Estimation of the Earthquake Recurrence Parameters for Unequal Observation Periods for Different Magnitudes, *Bulletin of the Seismological Society of America*, Vol. 70(4), 1337-1346.

WESSEL, P, LUIS, JF, UIEDA, L, SCHARROO, R, WOBBE, F, SMITH, WHF, and TIAN, D. 2019. The Generic Mapping Tools Version 6, *Geochemistry, Geophysics, Geosystems*, Vol. 20(11), 5556–5564.

WESTHEAD, RK, MCCARTHY, DJ, COLLIER, JS, and SANDERSON, DJ. 2018. Spatial variability of the Purbeck–Wight Fault Zone—a long-lived tectonic element in the southern UK, *Proceedings of the Geologists' Association*, Vol. 129(3), 436-451.

WHEELER, RL. 2009. Methods of Mmax Estimation East of the Rocky Mountains*, U.S. Geological Survey Open-File Report 2009–1018*.

WIEMER, S, and WYSS, M. 2000. Minimum magnitude of complete reporting in earthquake catalogs: examples from Alaska, the Western United States, and Japan, *Bulletin of the Seismological Society of America*, Vol. 90**,** 859–869.

WIEMER, S, DANCIU, L, EDWARDS, B, MARTI, M, FÄH, D, HIEMER, S, WÖSSNER, J, CAUZZI, C, KÄSTLI, P, and KREMER, K. 2016. Seismic Hazard Model 2015 for Switzerland (SUIhaz2015). *Swiss Seismological Service*, Zurich, Switzerland.

WILSON, MP, DAVIES, RJ, FOULGER, GR, JULIAN, BR, STYLES, P, GLUYAS, JG, and ALMOND, S. 2015. Anthropogenic earthquakes in the UK: A national baseline prior to shale exploitation, *Marine and Petroleum Geology*, Vol. 68(A), 1-17.

WINTER, PW. 1995. A stochastic ground motion model for UK earthquakes, *Technical Report GNSR(DTI)/P(96)275 Milestone ECS 0263, AEA/16423530/R003*, AEA Technology.

WOESSNER, J, and WIEMER, S. 2005. Assessing the Quality of Earthquake Catalogues: Estimating the Magnitude of Completeness and Its Uncertainty, *Bulletin of the Seismological Society of America*, Vol. 95(2), 684–698.

WOESSNER, J, DANCIU, L, GIARDINI, D., CROWLEY, H, COTTON, F, GRÜNTHAL, G, VALENSISE, G, ARVIDSSON, R, BASILI, R, BETÜL DEMIRCIOGLU, M, HIEMER, S, MELETTI, C, MUSSON, RWM, ROVIDA, AN, SESETYAN, K, STUCCHI, and THE SHARE CONSORTIUM. 2015. The 2013 European seismic hazard model: key components and results, *Bulletin of Earthquake Engineering,* Vol. 13, 3553–3596.

WOO, G, and MUIR-WOOD, R. 1986. North Sea seismicity. *Offshore Technology Report, OTO 86 219*.

WOODCOCK, N, and STRACHAN, R. 2012. *Geological History of Britain and Ireland*. (Oxford: Blackwell Publishing).

WYNS, R. 1977. Tectonique récente dans l'Ouest du bassin de Paris: méthodes d'étude et bilan des déformations plio-quaternaires, Bulletin de la Société géologique de France, Vol. (7) XIX, 1093-1101.

ZARIFI, Z, KÖHLER. A, RINGROSE. P, OTTEMÖLLER, L, FURRE, A-K, HANSTEEN, F, JERKINS, A, OYE, V, DEHGHAN NIRI, R, and BAKKE, R. 2022. Background seismicity monitoring to prepare for large scale CO2 storage offshore Norway, *Seismological Research Letters,* Vol. 94, 775–791.

ZANELLA, E, and COWARD, MP. 2003. Structural framework, In *The Millennium Atlas: Petroleum geology of the Central and Northern North Sea,* EVANS, D, GRAHAM, C, ARMOUR, A, and BATHURST, P (Editors), Geological Society, London, 45–59.

ZIEGLER, PA. 1987. Evolution of the Western Approaches trough, *Tectonophysics*, Vol. 137, 341-346.

ZIEGLER, PA. 1990. *Geological Atlas of Western and Central Europe* (Elsevier: The Hague).

ZIEGLER, PA. 1992. North Sea rift system, *Tectonophysics*, Vol. 208, 55-75.

ZIEGLER, PA. 1994. Cenozoic rift system of Eastern and Central Europe: an overview, *Geologie and Mijnbouw*, Vol. 73(2), 99–127.

ZIEGLER, PA, and DÉZES, P. 2005. Evolution of the lithosphere in the area of the Rhine Rift System, *International Journal of Earth Sciences*, Vol. 94, 594–614.

ZIEGLER, PA, and DÉZES, P. 2006. Crustal evolution of Western and Central Europe, In: *European Lithosphere Dynamics*, GEE, DG, and STEPHENSON, RA (Editors), Geological Society of London, Vol. 32(1), 43-56.